Leveraging Forward Detectors at CERN to Investigate Properties and Extensions of the Standard Model

Dissertation

zur

Erlangung der naturwissenschaftlichen Doktorwürde
(Dr. sc. nat.)

vorgelegt der

Mathematisch-naturwissenschaftlichen Fakultät

der

Universität Zürich

von

Martina Ferrillo

aus

Italien

Promotionskommission

Prof. Dr. Nicola Serra (Vorsitz)

Prof. Dr. Marta Calvi

Prof. Dr. Gino Isidori

Dr. Patrick Owen

Zürich, 2024

Abstract

The remarkable success of the Standard Model (SM) of particle physics lies in its comprehensive description of the dynamics governing the behaviour of microscopic constituents of our Universe, ultimately translated into the discovery of a Higgs boson-like particle at CERN. Despite its predictive power, several SM shortcomings suggest the existence of more complete theory, solving long-standing issues like Dark Matter, baryon-antibaryon asymmetry, and neutrino oscillations, currently unexplained within the framework. As a result, the SM could represent a sensible approximation valid in the low-energy limit below the energy scale of new phenomena. The lack of a New Physics (NP) observation in the high energy domain has broadened the interest of the scientific community, now turning to complementary approaches.

High precision measurements with heavy flavour decays represent the strategy of choice when looking for indirect effects of NP at high energy scales, contributing to SM processes. The research conducted in this PhD project follows this approach at first. In this manuscript, we present a sensitivity evaluation for NP in semileptonic $\Lambda_b^0 \to \Lambda_c^+ \mu^- \bar{\nu}_\mu$ transitions, alongside its first angular analysis performed with data collected by the LHCb experiment during the Run 2 of the Large Hadron Collider (LHC). Furthermore, novel enhancements to the offline LHCb software framework intended for the new LHC conditions are discussed.

High energy neutrinos produced at the LHC present an unmatched opportunity to test unexplored regions of the SM where NP could manifest. We describe the observation of muon collider neutrinos with the SND@LHC experiment, paving the way for a new frontier for testing the SM.

Under the assumption of NP interacting feebly with the SM, experiments running with high intensity beams could have a privileged access portal to a wealth of hidden particles, potentially including dark matter. In this context, we discuss the sensitivity of the SHiP experimental proposal to light dark matter, focusing on the case of elastic scattering off electrons.

Contents

Chapter 1

Introduction

Contents

1.1 Motivation and problem statement

Almost twelve years after the groundbreaking discovery of the Higgs boson [1, 2], the landscape in high energy physics remains unchanged. The Standard Model (SM) is still the most successful theory explaining the complex microscopic phenomena that regulate the interaction between particles, ultimately constituting the building blocks of our Universe. However, it has known limitations, leaving many observed phenomena outside its scope in particle physics, astrophysics and cosmology [3]. In addition, certain theoretical features of the SM deserve serious investigation as they are not deeply understood within its framework. As a result, the SM is considered to be an incomplete theory, due to the following aspects:

(a) *Neutrino oscillations*
   The mutating flavour of propagating neutrinos is clear evidence that these enigmatic leptons have a rather small, although non-zero mass [4, 5], therefore signalling an incompatibility with the SM postulation of a zero neutrino mass value.

(b) *Baryon Asymmetry* of the *Universe*
   A fundamental puzzle arises from the prevalence of matter over anti-matter despite a hypothetically perfect balance in the early Universe within the Big Bang theory. The departure from the equilibrium in the amount of baryons and anti-baryons, formulated by Sakharov [6], could explain the observed imbalance. It implies a violation of the baryon number B, of the C and CP symmetries, alongside a departure from thermal equilibrium, assuming CPT

conservation. Unfortunately, the amount of CP violation predicted by the SM is still many orders of magnitude too small to account for the baryon asymmetry currently observed in the Universe.

(c) *Dark Matter* (DM)

Ordinary matter constitutes only a scarce fraction of our Universe, approximately $4 - 5\%$. The remaining component is divided between Dark Matter, accounting for around 25%, and Dark Energy, constituting circa 70% of the total Universe [7]. This understanding originates from observations of galaxy rotational dynamics and the Cosmic Microwave Background, indicating the presence of additional, unobserved matter with a cold and non-relativistic nature. The existence of Dark Matter does not find an explanation within the SM.

(d) *Cosmological inflation* and *Dark Energy*

The SM fails to explain the origin of the accelerated expansion of our Universe both in its primordial and current expansion phases. A commonly regarded hypothesis involves an unknown form of energy (Dark energy) that drives inflation dynamics.

(e) *Fine tuning of the Higgs mass*

Understanding how to protect the mass of the Higgs boson from diverging quadratic corrections is a challenge within the SM [8, 9]. Depending on the energy scale Λ at which gravitational effect becomes sizeable, and the SM validity terminates, *i.e.* the Planck scale $M_P \sim 10^{19}$ GeV, these corrections could exceed by orders of magnitude the measured Higgs mass, undermining the stability of the model and ultimately requiring fine-tuning.

(f) *Strong CP problem*

CP violation is yet experimentally unobserved in the strong sector of the SM without a plausible explanation within the model. To address this issue, large fine-tuning and extensions to the SM framework are required [10].

The absence of a plausible explanation for these unresolved issues within the SM motivates endeavours to observe signals of New Physics (NP). This quest is being pursued in research facilities worldwide, with the CERN complex at the forefront of exploring several domains. Despite that, clear evidence for NP is currently lacking, raising questions about the research direction to be pursued. In the following, we discuss approaches to the search for physics *beyond* the SM, explicitly focusing on the fields where a contribution was made in the context of this PhD work.

1.1.1 The High Precision Frontier

A possible explanation for the absence of new particles might reside in the energy scale required to access their production (multi-TeV), beyond the Electroweak (EW) one and the reach of current experiments at the Large Hadron Collider (LHC) chasing the so-called *energy frontier*. Nevertheless, high precision measurements performed in the field of *flavour physics* (Kaon and B physics) can probe the existence of NP effects at a larger scale than the one potentially accessible by present and future collider experiments, *e.g.* by constraining the flavour dynamics behind SM processes.

The structure of the SM can be ultimately connected to the gauge and Higgs sectors [11], where the former is completely specified by the local $SU(3)_C \times SU(2)_L \times U(1)_Y$ symmetry and the five fermionic fields of flavour i:

$$Q_L^i(3,2)_{+1/6}, \quad U_R^i(3,1)_{+2/3}, \quad D_R^i(3,1)_{-1/3}, \quad L_L^i(1,2)_{-1/2}, \quad E_R^i(1,1)_{-1}, \quad i \in \{1, 2, 3\},$$
(1.1)

where the terms in Eq. 1.1 illustrate the invariance of the Lagrangian under three flavour replicas, corresponding to a global flavour symmetry $L_{\text{gauge}}^{\text{SM}}$. Global and local symmetries are broken with the introduction of the scalar Higgs field ϕ. In particular, the global flavour symmetry, $L_{\text{gauge}}^{\text{SM}}$, is broken explicitly by the interaction of the Higgs with fermionic fields, giving rise to the non-unitary Yukawa terms Y_α^{ij} [11]:

$$-L_{\text{Yukawa}}^{\text{SM}} = Y_d^{ij} \bar{Q}_L^i \phi D_R^j + Y_u^{ij} \bar{Q}_L^i \tilde{\phi} U_R^j + Y_e^{ij} \bar{L}_L^i \tilde{\phi} E_R^j + \text{h.c.} \qquad (\tilde{\phi} = i\tau_2 \phi^\dagger)$$
(1.2)

While the diagonalisation of the Yukawa matrix Y_e in the lepton sector can occur without breaking gauge invariance, the flavour symmetry is broken in the quark sector as a transformation V yielding a simultaneous diagonalisation of Y_u and Y_d in the flavour space does not exist. The resulting misalignment between the Yukawa matrices Y_u and Y_d is the non-trivial CKM quark flavour mixing matrix [12–14], entirely determined by three real angles and one complex CP-violating phase. The structure of the CKM matrix follows a hierarchical pattern, with the diagonal elements, indication of quark mixing within the same multiplet, receiving a value close to unity and the off-diagonal ones ranging from $\mathscr{O}(10^{-1})$ to $\mathscr{O}(10^{-3})$, as clearly highlighted in the Wolfenstein parameterisation [15]:

$$V = \begin{pmatrix} V_{ud} & V_{us} & V_{ub} \\ V_{cd} & V_{cs} & V_{cb} \\ V_{td} & V_{ts} & V_{tb} \end{pmatrix} =$$

$$= \begin{pmatrix} 1 - \frac{\lambda^2}{2} & \lambda & A\lambda^3(\varrho - i\eta) \\ -\lambda & 1 - \frac{\lambda^2}{2} & A\lambda^2 \\ A\lambda^3(1 - \varrho - i\eta) & -A\lambda^2 & 1 \end{pmatrix} + \mathscr{O}(\lambda^4),$$
(1.3)

with $\lambda = |V_{us}| \sim 0.22$ denoting the Cabibbo angle, instead A, ρ, η defined as parameters with value close to unity. The unitarity of the CKM matrix yields a series of relations between its terms. Some of these equations translate into interesting measurable observables known as *unitarity triangles*, used to help constrain experimentally the flavour sector of the SM.

The field of flavour physics extends beyond the study of CKM elements. As discussed in Sec. 1.1, many observations suggest that the SM might be an approximate, low-energy limit of a more comprehensive theory. Following the effective theory approach, we can extend the SM Lagrangian by including contributions from operators with dimensions $d > 4$, suppressed by the inverse power

of an effective energy scale Λ[1]:

$$L_{\text{EFT}} = L_{d<4}^{\text{SM}} + \Delta L_{d>4} \tag{1.4}$$

with:

$$\Delta L_{d>4} = \sum_{d>4} \sum_{n=1}^{N_d} \frac{c_n^{(d)}}{\Lambda^{d-4}} \mathcal{O}_n^{(d)}(\psi_{\text{SM}}). \tag{1.5}$$

The introduction of new operators $\mathcal{O}_n$, governed by the short-distance coupling terms c_n known as *Wilson coefficients*, results from the integration of the heavy degrees of freedom beyond the effective scale. Accessing the value of the Wilson coefficients is a way to probe and constrain the existence of NP indirectly in a model-agnostic way.

In addition to the discussed motivations fuelling the exploration of flavour physics as a venue to unveil the structure of NP, another piece of experimental evidence stands out. The so-called *flavour anomalies* [16], *e.g.* an observed pattern of deviations in tree-level $b \rightarrow c\ell\nu_\ell$ transitions, hint at a non-universal electroweak gauge coupling to leptons[2], suggesting the presence of physics beyond the SM. As previously underlined, in the SM, the Yukawa terms represent the only interaction breaking the flavour symmetry and differentiating between lepton species. The deviations show up in the R observables (Fig. 1.1), defined as the ratio:

$$R(X_c) = \frac{\mathscr{B}\left(X_b \rightarrow X_c \tau^- \bar{\nu}_\tau\right)}{\mathscr{B}\left(X_b \rightarrow X_c \ell^- \bar{\nu}_\ell\right)} \qquad \ell \in \{e, \mu\} \tag{1.6}$$

offering the advantage of reduced theoretical and experimental uncertainties, mitigated in the ratio. The observed discrepancy of the world average from the predicted SM value [17] corresponds to an excess at the 3.34σ level (Fig. 1.1) [18].
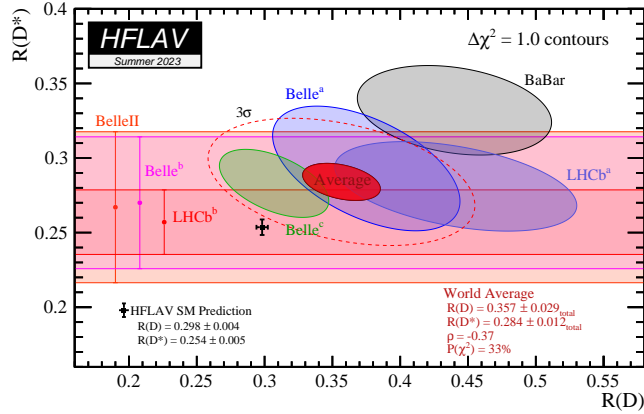

FIGURE 1.1: Experimental results on flavour anomalies represented in the $R(D) - R(D^*)$ plane [18]. Simultaneous measurements are shown as an ellipse.

---

[1]The energy scale Λ must be significantly larger than the scale of the investigated process occurring in the SM.
[2]In literature this is often referred to as Lepton Flavour Universality (LFU) violation.

To unravel the flavour anomalies highlighted so far, the scientific community has extensively delivered in the context of semileptonic transitions with studies of *B* meson decays, either with LFU ratios or angular measurements. Many experiments have contributed to the wealth of observations, with particular emphasis provided by the *B* factories (BaBar [19, 20], Belle [21–24], Belle II [25]) and the LHCb [26, 27] experiment at the Large Hadron Collider. Notably, investigations of the same underlying tree-level transition in the baryon sector, *e.g.* $\Lambda_b^0 \to \Lambda_c^+ \ell^- \bar{\nu}_\ell$, are limited [28] and angular studies completely absent. However, they could provide additional sensitivity to NP. The work presented in this manuscript aims to fill this gap and to provide the first measurement of the full angular distribution of $\Lambda_b^0 \to \Lambda_c^+ \mu^- \bar{\nu}_\mu$ decays with data collected by the LHCb experiment, delivering on the determination of the muonic Wilson coefficients. The thesis extends to every analysis stage, ranging from a preliminary sensitivity assessment to the factual realisation of the measurement.

1.1.2 The Intensity Frontier

Another viable reason for the absence of NP observations so far might reside not in their unreachable masses but rather in the exceptionally weak coupling to the SM. Such Feebly Interacting Particles (FIPs), populating the energy regime below the EW scale, could be linked to the SM via *hidden portals*, thus requiring high intensity accelerator beams to be produced at a detectable rate [3, 29]. This regime is commonly called the *intensity frontier*.

FIPs and their corresponding force carriers are singlets under the SM gauge interactions and solely couple to SM fields not carrying any electromagnetic charge via *portal* operators. The literature is rich in proposals of hidden sector portals improving on several of the SM known limitations. Nevertheless, a classification exists based on the composition and dimension of the introduced NP operators. Let us consider L_{portal}, the interaction lagrangian between the SM and the hidden sector (HS), which reads as [3]:

$$L_{\text{portal}} = \mathcal{O}_{\text{SM}} \times \mathcal{O}_{\text{HS}}, \tag{1.7}$$

where the terms $\mathcal{O}$ denote the operators of the SM and HS, respectively. When restricting the portal framework to renormalisable interactions, four main categories arise.

1. *Vector portal*
   This model generates FIPs from an extra gauge symmetry $U'(1)$. The new force carrier is a vector state, A'_μ, named *dark photon* (DP), interacting with the SM via a dimensionless kinetic mixing coupling ϵ:

   $$L_{\text{vector}} = L_{\text{SM}} + L_{\text{HS}} - \epsilon F'_{\mu\nu} B^{\mu\nu}, \tag{1.8}$$

   with $B^{\mu\nu}$ and $F'_{\mu\nu}$ denoting the SM and new gauge group $U'(1)$ hypercharge strength field, respectively. In Eq. 1.8, the term L_{HS} can include additional fields χ, charged under $U'(1)$. These particles, originating from the decay of the DP A'_μ, represent a WIMP dark matter candidate [30], with possible rescattering on electrons or nucleons mediated by the mixed

propagator $A^{\mu} A'_{\mu}$ [29, 31]. Additional models, formulated within the framework of vector portals, postulate a leptophobic or leptophylic DP coupling to the total baryon or lepton current [32].

2. *Scalar portal*

Prompted by the discovery of the Higgs boson, these models associate new (pseudo)scalar singlets S_i to the SM bilinear operator $\phi^{\dagger}\phi$, with ϕ denoting the Higgs field [33]:

$$L_{\text{scalar}} = L_{\text{SM}} + L_{\text{HS}} - (\mu S + \lambda S^2)\phi^{\dagger}\phi \,, \tag{1.9}$$

where μ and λ represent small, dimensionful coupling parameters. A non-zero value of the coupling constant μ results in mixing between the dark scalar and Higgs fields, which implies that the portal coupling occurs with all SM fields interacting with the Higgs. As a result, flavour-changing transitions in the decays of Kaons and B hadrons can occur [33]. Additionally, the presence of the λ parameter denotes pair production of scalars originating from the Higgs [33]. The interest of the scientific community towards this portal originates from the need to fully explain the structure of the Higgs sector, comprising a single scalar SM-like field to current knowledge but possibly extended to multiple doublets.

3. *Neutrino portal*

The introduction of dark fermions, referred to as *Heavy Neutral Leptons* (HNL), is a popular solution to the neutrino mass generation problem. A generic lagrangian associated with the neutrino portal reads as:

$$L_{\text{neutrino}} = L_{\text{SM}} + L_{\text{HS}} + \sum F_{\alpha I}(\bar{L}_{\alpha} \cdot \tilde{\phi})N_I \,, \tag{1.10}$$

where the summation term runs over all the possible $SU(2)$ lepton doublets L_{α} and number of HNL N_I, while the dimensionless factors $F_{\alpha I}$ denote the Yukawa couplings. The mass terms for HNL, either of Dirac or Majorana type, originate within the hidden sector lagrangian and could compensate for the smallness of the SM neutrino mass [29]. The phenomenology of the neutrino portal implies the mixing between SM neutrinos and HNL modulated by elements of a mixing matrix U, controlling the production and decay mechanisms within the SM [29].

4. *Axion portal*

Models including pseudoscalar QCD axion-like particles (ALP) offer a compelling solution to the apparent absence of CP violation in the strong sector of the SM. If considering only diagonal interaction terms between a pseudoscalar axion field A and the SM, higher

dimension operators originate in the corresponding lagrangian [3]:

$$L_{\text{axion}} = L_{\text{SM}} + L_{\text{HS}} + \frac{A}{4f_\gamma} F_{\mu\nu} \tilde{F}^{\mu\nu} + \frac{A}{4f_G} \text{Tr}\, G_{\mu\nu} \tilde{G}^{\mu\nu} \tag{1.11}$$

$$+ \frac{\partial_\mu A}{f_\ell} \sum_\alpha \bar{\ell}_\alpha \gamma_\mu \gamma_5 \ell_\alpha + \frac{\partial_\mu A}{f_q} \sum_\beta \bar{q}_\beta \gamma_\mu \gamma_5 q_\beta \,, \tag{1.12}$$

with $F_{\mu\nu}$ hypercharge field, $G_{\mu\nu}$ gluon field; ℓ_α and q_β lepton and quark fields, respectively. A corresponding effective, non-renormalisable coupling modulates each term in the summation, as the ALP model requires external UV completion unlike the vector, scalar and neutrino portals [3]. A popular solution to the strong CP and renormalisation problem is introducing additional QCD axion states to the HS lagrangian [34].

Many ongoing experiments contribute to the rich set of measurements performed to confirm or refute the existence of FIPs [3], offering sensitivity in a region of parameters compatible with their acceptance. Remarkably, no evidence for NP has been found yet. Several novel experimental proposals have appeared in recent years, aiming to reach an unprecedented sensitivity [3]. Among them stands out the Search for Hidden Particles (SHiP) experiment [35, 36] proposed at CERN as an unprecedented opportunity to probe multiple HS models and signatures. The research conducted in this thesis occurs within the framework of the SHiP experiment. It focuses on a simulation-based estimate of SHiP sensitivity to light dark matter particles χ originating from the decay of DP A'. The work performed within this PhD project lies in the realisation of Monte Carlo simulation infrastructure and samples utilised in the analysis, as well as in estimating the background sources.

1.1.3 Neutrino physics at the High Energy Frontier

Neutrinos are the most enigmatic particle of the SM and, even though they have been tested precisely [37–40], they offer opportunities to probe the existence of NP [41]. So far, experimental observations have been limited to energies below a few hundreds of GeV for human-made muon neutrinos, with just a handful of events from ultra-high energy astrophysical sources [42]. The scenario significantly worsens for the electron neutrino and tau neutrino species, similarly limited in energy and signal yields [43–45]. High energy neutrinos in the TeV range could open up the scene to the exploration of non-standard and flavour-specific interactions, including exotic scenarios foreseeing oscillations into sterile neutrinos (HNL) and interactions with dark matter [41, 46], as discussed in Sec. 1.1.2.

The LHC is the most powerful neutrino-generating machine currently in operation, producing high intensity and unprecedented high energy (anti)neutrino fluxes of all flavours in the so-far unexplored TeV energy region. Given the need to complement NP searches occurring in the high energy, precision and intensity frontiers, the scientific community has recently shown increased interest towards proposals of neutrino experiments covering forward rapidities at the LHC [46]. The two main playing actors in the current experimental scene are FASER(ν) [47, 48]

and SND@LHC [49]. They exploit the concept of hybrid detectors[3] located $\sim 500\,\mathrm{m}$ away from the ATLAS pp collision point, covering complementary pseudo-rapidity regions and therefore neutrino energies and fluxes: on-axis ($\eta > 9.2$) for FASER; off-axis ($7.2 < \eta < 8.4$) for SND@LHC. The research project described in this manuscript has been performed within the SND@LHC experiment. The primary objective of the measurement is the observation of muon neutrino interactions occurring at the uncharted TeV energy scale, paving the way for a new era of explorations in the field. The work performed in this thesis extends uniformly to every detailed stage of the corresponding analysis.

1.2 Organisation of the thesis

This manuscript is arranged into three main parts, including six independent chapters:

- Part I - **The High Precision Frontier: flavour physics**

  - **Chapter 2** introduces the computation of the complete differential decay density expression for semileptonic decays $\Lambda_b^0 \to \Lambda_c^+ \ell^- \bar{\nu}_\ell$. Additionally, it presents the assessment of the experimental precision on the Wilson Coefficients of the New Physics operators in semimuonic transitions $\Lambda_b^0 \to \Lambda_c^+ \mu^- \bar{\nu}_\mu$.

  - **Chapter 3** provides a comprehensive description of the angular measurement conducted on baryon decays $\Lambda_b^+ \to \Lambda_c^+ \mu^- \bar{\nu}_\mu$, with data collected with the LHCb detector.

  - **Chapter 4** details the enhancements implemented into the offline software of the LHCb experiment, resulting from upgrades in both the detector and trigger for the Run 3 of the LHC.

- Part II - **Neutrino physics at the High Energy Frontier**

  - **Chapter 5** presents the measurement leading to the direct observation of muon neutrino interactions with the SND@LHC experiment.

- Part III - **The Intensity Frontier**

  - **Chapter 6** outlines the sensitivity study conducted to assess the potential of the SHiP experiment to detect the elastic scattering on electrons of light dark matter particles.

---

[3]Ensemble of tungsten and nuclear emulsion-based heavy target, and electronic tracking devices.

1.3 Published work

The outcome of the research work conducted within this PhD has resulted in the following peer-reviewed publications:

- Chapter 2:

  M. Ferrillo, A. Mathad, P. Owen, N. Serra, "*Probing effects of new physics in $\Lambda_b^0 \rightarrow \Lambda_c^+ \mu^- \bar{\nu}_\mu$ decays*", JHEP 12(2019)148, [arXiv:1909.04608].

- Chapter 4:

  M. Ferrillo et al., "*FunTuple: A new N-tuple algorithm for offline data processing at the LHCb experiment*", Comput. Softw. Big Sci. 8 (2024) 1, 6, [arXiv:2310.02433].

- Chapter 5:

  SND@LHC Collaboration, "*Observation of Collider Muon Neutrinos with the SND@LHC experiment*", Phys. Rev. Lett. **131** (2023), no. 3 031802, [arXiv:2305.09383].

- Chapter 6:

  SHiP Collaboration, "*Sensitivity of the SHiP experiment to light dark matter*", JHEP04(2021)199, [arXiv:2010.11057].

The research that led to the publication:

- M. Ferrillo et al., "*Improving the potential of BDF@SPS to search for new physics with the liquid argon time projection chambers*", JHEP 02(2024)196, [arXiv:2312.14868]

was also conducted as part of this PhD project. However, due to brevity, it is not elaborated within this manuscript.

References

[1]   G. Aad et al. "Observation of a new particle in the search for the Standard Model Higgs boson with the ATLAS detector at the LHC". In: *Physics Letters B* 716.1 (2012), pp. 1–29. ISSN: 0370-2693. DOI: https://doi.org/10.1016/j.physletb.2012.08.020. URL: https://www.sciencedirect.com/science/article/pii/S037026931200857X.

[2]   S. Chatrchyan et al. "Observation of a new boson at a mass of 125 GeV with the CMS experiment at the LHC". In: *Physics Letters B* 716.1 (2012), pp. 30–61. ISSN: 0370-2693. DOI: https://doi.org/10.1016/j.physletb.2012.08.021. URL: https://www.sciencedirect.com/science/article/pii/S0370269312008581.

[3]   J Beacham et al. "Physics beyond colliders at CERN: beyond the Standard Model working group report". In: *Journal of Physics G: Nuclear and Particle Physics* 47.1 (Dec. 2019), p. 010501. ISSN: 1361-6471. DOI: 10.1088/1361-6471/ab4cd2. URL: http://dx.doi.org/10.1088/1361-6471/ab4cd2.

[4]   Y. Fukuda et al. "Evidence for oscillation of atmospheric neutrinos". In: *Phys. Rev. Lett.* 81 (1998), pp. 1562–1567. DOI: 10.1103/PhysRevLett.81.1562. arXiv: hep-ex/9807003.

[5]   Q. R. Ahmad et al. "Measurement of day and night neutrino energy spectra at SNO and constraints on neutrino mixing parameters". In: *Phys. Rev. Lett.* 89 (2002), p. 011302. DOI: 10.1103/PhysRevLett.89.011302. arXiv: nucl-ex/0204009.

[6]   A. D. Sakharov. "Violation of CP Invariance, C asymmetry, and baryon asymmetry of the universe". In: *Pisma Zh. Eksp. Teor. Fiz.* 5 (1967), pp. 32–35. DOI: 10.1070/PU1991v034n05ABEH002497.

[7]   P. A. R. Ade et al. "Planck2013 results. XVI. Cosmological parameters". In: *Astronomy amp; Astrophysics* 571 (Oct. 2014), A16. ISSN: 1432-0746. DOI: 10.1051/0004-6361/201321591. URL: http://dx.doi.org/10.1051/0004-6361/201321591.

[8]   Steven Weinberg. "Implications of dynamical symmetry breaking". In: *Phys. Rev. D* 13 (4 Feb. 1976), pp. 974–996. DOI: 10.1103/PhysRevD.13.974. URL: https://link.aps.org/doi/10.1103/PhysRevD.13.974.

[9]   S. Weinberg. "Implications of dynamical symmetry breaking: An addendum". In: *Phys. Rev. D* 19 (4 Feb. 1979), pp. 1277–1280. DOI: 10.1103/PhysRevD.19.1277. URL: https://link.aps.org/doi/10.1103/PhysRevD.19.1277.

[10] Roberto D. Peccei. "The Strong CP Problem and Axions". In: *Axions*. Springer Berlin Heidelberg, 2008, pp. 3–17. ISBN: 9783540735182. DOI: 10.1007/978-3-540-73518-2_1. URL: http://dx.doi.org/10.1007/978-3-540-73518-2_1.

[11] Gino Isidori. *B physics in the LHC era*. 2010. arXiv: 1001.3431 [hep-ph].

[12]   Nicola Cabibbo. "Unitary Symmetry and Leptonic Decays". In: *Phys. Rev. Lett.* 10 (12 June 1963), pp. 531–533. DOI: 10.1103/PhysRevLett.10.531. URL: https://link.aps.org/doi/10.1103/PhysRevLett.10.531.

[13]   S. L. Glashow, J. Iliopoulos, and L. Maiani. "Weak Interactions with Lepton-Hadron Symmetry". In: *Phys. Rev. D* 2 (7 Oct. 1970), pp. 1285–1292. DOI: 10.1103/PhysRevD.2.1285. URL: https://link.aps.org/doi/10.1103/PhysRevD.2.1285.

[14]   Makoto Kobayashi and Toshihide Maskawa. "CP Violation in the Renormalizable Theory of Weak Interaction". In: *Prog. Theor. Phys.* 49 (1973), pp. 652–657. DOI: 10.1143/PTP.49.652.

[15]   Lincoln Wolfenstein. "Parametrization of the Kobayashi-Maskawa Matrix". In: *Phys. Rev. Lett.* 51 (1983), p. 1945. DOI: 10.1103/PhysRevLett.51.1945.

[16]   Bernat Capdevila, Andreas Crivellin, and Joaquim Matias. "Review of Semileptonic B Anomalies". In: *Eur. Phys. J. ST* 1 (2023), p. 20. DOI: 10.1140/epjs/s11734-023-01012-2. arXiv: 2309.01311 [hep-ph].

[17]   C. S. Kim et al. "Remarks on the Standard Model predictions for $R(D)$ and $R(D^*)$". In: *Phys. Rev. D* 95 (1 Jan. 2017), p. 013003. DOI: 10.1103/PhysRevD.95.013003. URL: https://link.aps.org/doi/10.1103/PhysRevD.95.013003.

[18]   Y. Amhis et al. "Averages of b-hadron, c-hadron, and τ-lepton properties as of 2021". In: *Phys. Rev. D* 107 (2023), p. 052008. DOI: 10.1103/PhysRevD.107.052008. arXiv: 2206.07501 [hep-ex].

[19]   J. P. Lees et al. "Evidence for an excess of $\bar{B} \to D^{(*)}\tau^-\bar{\nu}_\tau$ decays". In: *Phys. Rev. Lett.* 109 (2012), p. 101802. DOI: 10.1103/PhysRevLett.109.101802. arXiv: 1205.5442 [hep-ex].

[20]   J. P. Lees et al. "Measurement of an Excess of $\bar{B} \to D^{(*)}\tau^-\bar{\nu}_\tau$ Decays and Implications for Charged Higgs Bosons". In: *Phys. Rev. D* 88.7 (2013), p. 072012. DOI: 10.1103/PhysRevD.88.072012. arXiv: 1303.0571 [hep-ex].

[21]   M. Huschle et al. "Measurement of the branching ratio of $\bar{B} \to D^{(*)}\tau^-\bar{\nu}_\tau$ relative to $\bar{B} \to D^{(*)}\ell^-\bar{\nu}_\ell$ decays with hadronic tagging at Belle". In: *Phys. Rev. D* 92.7 (2015), p. 072014. DOI: 10.1103/PhysRevD.92.072014. arXiv: 1507.03233 [hep-ex].

[22]   S. Hirose et al. "Measurement of the τ lepton polarization and $R(D^*)$ in the decay $\bar{B} \to D^*\tau^-\bar{\nu}_\tau$". In: *Phys. Rev. Lett.* 118.21 (2017), p. 211801. DOI: 10.1103/PhysRevLett.118.211801. arXiv: 1612.00529 [hep-ex].

[23]   S. Hirose et al. "Measurement of the τ lepton polarization and $R(D^*)$ in the decay $\bar{B} \to D^*\tau^-\bar{\nu}_\tau$ with one-prong hadronic τ decays at Belle". In: *Phys. Rev. D* 97.1 (2018), p. 012004. DOI: 10.1103/PhysRevD.97.012004. arXiv: 1709.00129 [hep-ex].

[24]   Y. Sato et al. "Measurement of the branching ratio of $\bar{B}^0 \to D^{*+}\tau^-\bar{\nu}_\tau$ relative to $\bar{B}^0 \to D^{*+}\ell^-\bar{\nu}_\ell$ decays with a semileptonic tagging method". In: *Phys. Rev. D* 94.7 (2016), p. 072007. DOI: 10.1103/PhysRevD.94.072007. arXiv: 1607.07923 [hep-ex].

[25]   Belle II Collaboration et al. *A test of lepton flavor universality with a measurement of $R(D^*)$ using hadronic B tagging at the Belle II experiment*. 2024. arXiv: 2401.02840 [hep-ex].

[26] "Measurement of the ratios of branching fractions $\mathscr{R}(D^*)$ and $\mathscr{R}(D^0)$". In: *Phys. Rev. Lett.* 131 (2023), p. 111802. DOI: 10.1103/PhysRevLett.131.111802. arXiv: 2302.02886 [hep-ex].

[27] Roel Aaij et al. "Test of lepton flavor universality using B0→D*-τ+$\nu\tau$ decays with hadronic τ channels". In: *Phys. Rev. D* 108.1 (2023), p. 012018. DOI: 10.1103/PhysRevD.108.012018. arXiv: 2305.01463 [hep-ex].

[28] R. Aaij et al. "Observation of the decay $\Lambda_b^0 \rightarrow \Lambda_c^+ \tau^- \overline{\nu}_\tau$". In: *Phys. Rev. Lett.* 128 (2021), p. 191803. DOI: 10.1103/PhysRevLett.128.191803. arXiv: 2201.03497 [hep-ex].

[29] Sergey Alekhin et al. "A facility to search for hidden particles at the CERN SPS: the SHiP physics case". In: *Reports on Progress in Physics* 79.12 (Oct. 2016), p. 124201. ISSN: 1361-6633. DOI: 10.1088/0034-4885/79/12/124201. URL: http://dx.doi.org/10.1088/0034-4885/79/12/124201.

[30] Maxim Pospelov, Adam Ritz, and Mikhail Voloshin. "Secluded WIMP dark matter". In: *Physics Letters B* 662.1 (2008), pp. 53–61. ISSN: 0370-2693. DOI: https://doi.org/10.1016/j.physletb.2008.02.052. URL: https://www.sciencedirect.com/science/article/pii/S0370269308002402.

[31] Brian Batell, Maxim Pospelov, and Adam Ritz. "Exploring portals to a hidden sector through fixed targets". In: *Phys. Rev. D* 80 (9 Nov. 2009), p. 095024. DOI: 10.1103/PhysRevD.80.095024. URL: https://link.aps.org/doi/10.1103/PhysRevD.80.095024.

[32] Martin Bauer, Patrick Foldenauer, and Joerg Jaeckel. "Hunting all the hidden photons". In: *Journal of High Energy Physics* 2018.7 (July 2018). ISSN: 1029-8479. DOI: 10.1007/jhep07(2018)094. URL: http://dx.doi.org/10.1007/JHEP07(2018)094.

[33] Donal O'Connell, Michael J. Ramsey-Musolf, and Mark B. Wise. "Minimal extension of the standard model scalar sector". In: *Phys. Rev. D* 75 (3 Feb. 2007), p. 037701. DOI: 10.1103/PhysRevD.75.037701. URL: https://link.aps.org/doi/10.1103/PhysRevD.75.037701.

[34] R. D. Peccei and Helen R. Quinn. "CP Conservation in the Presence of Pseudoparticles". In: *Phys. Rev. Lett.* 38 (25 June 1977), pp. 1440–1443. DOI: 10.1103/PhysRevLett.38.1440. URL: https://link.aps.org/doi/10.1103/PhysRevLett.38.1440.

[35] C. Ahdida et al. "The SHiP experiment at the proposed CERN SPS Beam Dump Facility". In: *Eur. Phys. J. C* 82.5 (2022), p. 486. DOI: 10.1140/epjc/s10052-022-10346-5. arXiv: 2112.01487 [physics.ins-det].

[36] O Aberle et al. *BDF/SHiP at the ECN3 high-intensity beam facility*. Tech. rep. Geneva: CERN, 2022. URL: https://cds.cern.ch/record/2839677.

[37] Janet M. Conrad, Michael H. Shaevitz, and Tim Bolton. "Precision measurements with high-energy neutrino beams". In: *Reviews of Modern Physics* 70.4 (Oct. 1998), pp. 1341–1392. ISSN: 1539-0756. DOI: 10.1103/revmodphys.70.1341. URL: http://dx.doi.org/10.1103/RevModPhys.70.1341.

[38] J. A. Formaggio and G. P. Zeller. "From eV to EeV: Neutrino cross sections across energy scales". In: *Reviews of Modern Physics* 84.3 (Sept. 2012), pp. 1307–1341. ISSN: 1539-0756.

DOI: `10.1103/revmodphys.84.1307`. URL: `http://dx.doi.org/10.1103/RevModPhys.84.1307`.

[39]   Raymond Brock et al. "Handbook of perturbative QCD: Version 1.0". In: *Rev. Mod. Phys.* 67 (1995), pp. 157–248. DOI: `10.1103/RevModPhys.67.157`.

[40]   Giovanni De Lellis, Pasquale Migliozzi, and Pietro Santorelli. "Charm physics with neutrinos". In: *Phys. Rept.* 399 (2004). [Erratum: Phys.Rept. 411, 323–324 (2005)], pp. 227–320. DOI: `10.1016/j.physrep.2005.02.001`.

[41]   D. Marfatia, D.W. McKay, and T.J. Weiler. "New physics with ultra-high-energy neutrinos". In: *Physics Letters B* 748 (Sept. 2015), pp. 113–116. ISSN: 0370-2693. DOI: `10.1016/j.physletb.2015.07.002`. URL: `http://dx.doi.org/10.1016/j.physletb.2015.07.002`.

[42]   "Measurement of the multi-TeV neutrino interaction cross-section with IceCube using Earth absorption". In: *Nature* 551.7682 (Nov. 2017), pp. 596–600. ISSN: 1476-4687. DOI: `10.1038/nature24459`. URL: `http://dx.doi.org/10.1038/nature24459`.

[43]   K. Kodama et al. "Final tau-neutrino results from the DONuT experiment". In: *Physical Review D* 78.5 (Sept. 2008). ISSN: 1550-2368. DOI: `10.1103/physrevd.78.052002`. URL: `http://dx.doi.org/10.1103/PhysRevD.78.052002`.

[44]   N. Agafonova et al. "Final Results of the OPERA Experiment on ν_τ Appearance in the CNGS Neutrino Beam". In: *Phys. Rev. Lett.* 120 (21 May 2018), p. 211801. DOI: `10.1103/PhysRevLett.120.211801`. URL: `https://link.aps.org/doi/10.1103/PhysRevLett.120.211801`.

[45]   OPERA Collaboration et al. *Final results of the search for $\nu_\mu \rightarrow \nu_e$ oscillations with the OPERA detector in the CNGS beam*. 2018. arXiv: `1803.11400 [hep-ex]`.

[46]   Jonathan L Feng et al. "The Forward Physics Facility at the High-Luminosity LHC". In: *Journal of Physics G: Nuclear and Particle Physics* 50.3 (Jan. 2023), p. 030501. DOI: `10.1088/1361-6471/ac865e`. URL: `https://dx.doi.org/10.1088/1361-6471/ac865e`.

[47]   Akitaka Ariga et al. "FASER: ForwArd Search ExpeRiment at the LHC". In: (Jan. 2019). arXiv: `1901.04468 [hep-ex]`.

[48]   Henso Abreu et al. "Technical Proposal: FASERnu". In: (Jan. 2020). arXiv: `2001.03073 [physics.ins-det]`.

[49]   G. Acampora et al. "SND@LHC: The Scattering and Neutrino Detector at the LHC". In: (Oct. 2022). arXiv: `2210.02784 [hep-ex]`.

Part I

The High Precision Frontier: flavour physics

Chapter 2

Probing effects of new physics in $\Lambda_b^0 \to \Lambda_c^+ \mu^- \bar{\nu}_\mu$ decays

Contents

We present, for the first time, the six-fold differential decay density expression for $\Lambda_b^0 \to \Lambda_c^+ \ell^- \bar{\nu}_l$, taking into account the polarisation of the Λ_b^0 baryon and a complete basis of new physics operators. Using the expected yield in the current dataset collected at the LHCb experiment, we present sensitivity studies to determine the experimental precision on the Wilson coefficients of the new physics operators with $\Lambda_b^0 \to \Lambda_c^+ \mu^- \bar{\nu}_\mu$ decays in two scenarios. In the first case, unpolarised $\Lambda_b^0 \to \Lambda_c^+ \mu^- \bar{\nu}_\mu$ decays with $\Lambda_c^+ \to pK^-\pi^+$ are considered, whereas polarised $\Lambda_b^0 \to \Lambda_c^+ \mu^- \bar{\nu}_\mu$ decays with $\Lambda_c^+ \to pK_S^0$ are studied in the second. For the latter scenario, the experimental precision that can be achieved on the determination of Λ_b^0 polarisation and Λ_c^+ weak decay asymmetry parameter is also presented.

2.1 Introduction

Semileptonic b-hadron decays are highly promising avenues to search for New Physics (NP) due to their large signal yields and controllable theoretical uncertainties. The hint of lepton flavour universality violation in $B \to D^{(*)}\ell\nu$ decays [1–8][1] has led to the proposal of various NP

---

[1] As no CP violation is considered in this paper, the inclusion of charge conjugate processes is implied.

scenarios that could affect decays involving $b \to c\ell\nu$ transitions [9–11]. In addition, numerous studies involving $B \to D^{(*)}\tau\nu$ decays have shown the effects of these NP contributions on the corresponding angular distributions [12–18]. Global fits to $b \to c\tau\nu$ transitions have also been conducted to determine the Wilson coefficients of the NP operators [19–22]. A recent global fit to $b \to c\mu\nu$ and $b \to ce\nu$ transitions [22] has proven that a good sensitivity to various different NP operators can be achieved through studies of b-meson decays involving lighter leptons in the final state.

The baryonic equivalent of these decays, $\Lambda_b^0 \to \Lambda_c^+ \ell^- \bar{\nu}_l$, is a good candidate to complement the NP sensitivity of the mesonic counterparts, due to the large production cross section of Λ_b^0 baryons and the well measured form factors [23–26]. The literature is rich in studies of the possible effect of NP contributions in unpolarised $\Lambda_b^0 \to \Lambda_c^+ \tau^- \bar{\nu}_\tau$ decays [27–31], as well as in subsequent $\Lambda_c \to \Lambda\pi$ decays [32, 33]. More recently, the same investigation has been extended to Λ_b^0 unpolarised semileptonic decays to lighter leptons [33, 34].

In this study, we present for the first time an expression for the six-fold differential decay density of $\Lambda_b^0 \to \Lambda_c^+ \ell^- \bar{\nu}_l$ transitions, including the effects of Λ_b^0 polarisation and all the relevant NP contributions which are encapsulated by Wilson coefficients. These decays can currently be studied only at the LHCb experiment and present several experimental challenges. On one side, in the $\Lambda_b^0 \to \Lambda_c^+ \tau^- \bar{\nu}_\tau$ case multiple missing neutrinos in the final state drastically dilute the resolution on the kinematic variables in addition to contributions from irreducible backgrounds (such as feed-down $\Lambda_b^0 \to \Lambda_c^{+*} \ell^- \bar{\nu}_l$ and $\Lambda_b^0 \to \Lambda_c^+ X_c$, where X_c is a charmed meson). Furthermore, $\Lambda_b^0 \to \Lambda_c^+ e^- \bar{\nu}_e$ decays are challenging to reconstruct at LHCb due to the poor electron reconstruction efficiency [35]. Therefore, we conduct sensitivity studies to determine the experimental precision on the Wilson coefficients with $\Lambda_b^0 \to \Lambda_c^+ \mu^- \bar{\nu}_\mu$ channel in two different scenarios, using the expected yield from Run I and II data collected at the LHCb experiment.

In the first scenario, the Λ_b^0 is unpolarised and the Λ_c^+ decay kinematics are integrated over and is assumed to be reconstructed using the $\Lambda_c^+ \to pK^-\pi^+$ channel. This is an experimentally favourable signature due to the presence of three charged particles in the final state and the large branching fraction, which ensure a cleaner reconstruction with small background contributions at LHCb.

In the second scenario we allow for a non-zero Λ_b^0 polarisation, with a subsequent $\Lambda_c^+ \to pK_S^0$ decay accounting for the involved kinematics of the process. The interest in this case lies in the achievable sensitivity not only to the polarisation of Λ_b^0 ($P_{\Lambda_b^0}$), but also to the Λ_c^+ decay asymmetry parameter ($\alpha_{\Lambda_c^+}$). So far, at the LHC no hint for a non-zero value of $P_{\Lambda_b^0}$ has been observed [36–38], whereas the Λ_c^+ decay asymmetry has been very recently measured at the BESIII experiment, but with a large uncertainty [39]. Therefore, we present an estimate on the experimental precision which could be achieved on $P_{\Lambda_b^0}$ and $\alpha_{\Lambda_c^+}$ at the LHCb, relying on the large signal yields of semileptonic decays.

The paper is organised in the following way. In section 2.2, the effective Lagrangian expression for $b \to c\ell\nu$ transitions is reported, including all the relevant NP operators. The decay amplitude of $\Lambda_b^0 \to \Lambda_c^+ (\to p\, K_S^0)(\ell^- \bar{\nu}_l)$ is presented in section 2.3. Section 2.4 contains the expression for

the six-fold differential decay density for the polarised $\Lambda_b^0 \to (pK_S^0)(\ell^- \bar{\nu}_l)$ decays in the context of NP. In section 2.5, the results of the sensitivity studies undertaken on the Wilson coefficients in the two working assumptions are reported. The conclusions of this work are given in section 2.6.

2.2 Effective Lagrangian for $b \to c\ell\nu$

The most generic effective Lagrangian of the four-fermion interaction, extending the Standard Model (SM) within the NP scenario and governing semileptonic $b \to c\ell\nu$ transitions, is given by:

$$\mathscr{H}_{\text{eff}} = \frac{4G_F}{\sqrt{2}} V_{cb} \left[(1 + C_{V_L}) \mathscr{O}_{C_{V_L}} + C_{V_R} \mathscr{O}_{C_{V_R}} + C_{S_L} \mathscr{O}_{C_{S_L}} + C_{S_R} \mathscr{O}_{C_{S_R}} + C_{T_L} \mathscr{O}_{C_{T_L}} \right] + h.c., \qquad (2.1)$$

where the four-fermion operators $\mathscr{O}_{C_i}$ are defined as:

$$\mathscr{O}_{C_{V_L}} = \bar{c}_L \gamma^\mu b_L \, \bar{\ell}_L \gamma_\mu \nu_L , \qquad (2.2)$$

$$\mathscr{O}_{C_{V_R}} = \bar{c}_R \gamma^\mu b_R \, \bar{\ell}_L \gamma_\mu \nu_L , \qquad (2.3)$$

$$\mathscr{O}_{C_{S_L}} = \bar{c}_R b_L \, \bar{\ell}_R \nu_L , \qquad (2.4)$$

$$\mathscr{O}_{C_{S_R}} = \bar{c}_L b_R \, \bar{\ell}_R \nu_L , \qquad (2.5)$$

$$\mathscr{O}_{C_{T_L}} = \bar{c}_R \sigma^{\mu\nu} b_L \, \bar{\ell}_R \sigma_{\mu\nu} \nu_L .$$

Here the factors $C_{V_{L,R}}, C_{S_{L,R}}, C_{T_L}$ denote the Wilson coefficients of their respective operators, that take a value of zero within the SM. The symbol ℓ represents the lepton flavour involved in the interaction. It is noted here that the right-handed tensor operator $\mathscr{O}_{T_R} = \bar{q}_L \sigma^{\mu\nu} b_R \, \bar{\ell}_R \sigma_{\mu\nu} \nu_L$ vanishes [13]. As in the case of SM, we assume the absence of right-handed ν_l and left-handed $\bar{\nu}_l$ [2]. Since the flavour of the neutrino is not observed, neutrino mixing effects are also not considered.

2.3 Decay amplitude

The transition matrix elements for $\Lambda_b^0 \to (pK_S^0)(\ell^- \bar{\nu}_l)$ can be expressed as the product of amplitudes of unstable particles involved in the decay, *i.e.* Λ_b^0, Λ_c^+, W^{*-}:

$$T_{\lambda_l, \lambda_{\bar{\nu}_l}, \lambda_p, \lambda_{K_S^0}}^{\lambda_{\Lambda_b}} = \frac{4G_F V_{cb}}{\sqrt{2}} BW(m_{pK_S^0}^2) \sum_{i, \lambda_{\Lambda_c}, \lambda_W} T_{\lambda_{\Lambda_c}, \lambda_W}^{i, \lambda_{\Lambda_b}}(q^2) T_{\lambda_l, \lambda_{\bar{\nu}_l}}^{i, \lambda_W}(q^2) T_{\lambda_p, \lambda_{K_S^0}}^{i, \lambda_{\Lambda_c}} . \qquad (2.6)$$

In Eq.(2), the term q^2 denotes the squared transferred four momentum, defined as $q^2 = (P_{\Lambda_b} - P_{\Lambda_c})^2 = (P_{\ell^-} + P_{\bar{\nu}_l})^2$; $m_{pK_S^0}$ is the combined mass of the system pK_S^0; G_F represents the Fermi constant; the index λ refers to the helicity of the particle involved in the transition. The propagator term for intermediate Λ_c^+ particle is parametrised as the relativistic Breit-Wigner and is denoted by BW. Using the narrow-width approximation for BW_{Λ_c}, the $m_{pK_S^0}^2$ dependence is integrated out in

---

[2]Operators involving right-handed neutrino are considered in Ref. [40, 41]

the expression of the differential decay density. In Eq.(2.6), we have also summed over i, denoting the operator $\mathcal{O}_i$ (Eq.(2.1)) involved in the transition, and the helicities of the intermediate unstable particles. In the following the helicity index $\lambda_{K_S^0}$ is dropped as it is null and $\lambda_{\bar{\nu}_l}$ is fixed to $1/2$ for Λ_b^0 decays (or $\lambda_{\nu_l} = -1/2$ for $\overline{\Lambda}_b^0$ decays). Since the weak decay of $\Lambda_c^+ \to pK_S^0$ involves the charged current transition of $c \to su\bar{d}$, we express the total decay density in terms of the weak decay asymmetry parameter, $\alpha_{\Lambda_c^+}$ [39].

The transition amplitude shown in Eq.(2.6) can be expanded in terms of the helicity amplitudes of the involved decay processes as follows:

$$
T_{\lambda_l,\lambda_p}^{\lambda_{\Lambda_b}} = \frac{4G_F|V_{cb}|}{\sqrt{2}} BW(m_{pK_S^0}^2)
$$

$$
\left[\sum_{\lambda_{\Lambda_c},\lambda_W} \eta_{\lambda_W} \left(\sum_{j=SM,C_{V_L},C_{V_R}} H_{\lambda_{\Lambda_c},\lambda_W}^{j;\lambda_{\Lambda_b}} \right) L_{\lambda_l}^{SM;\lambda_W} G_{\lambda_p}^{\lambda_{\Lambda_c}} \right.
$$

$$
+ \sum_{\lambda_{\Lambda_c}} \left(\sum_{k=C_{S_L},C_{S_R}} H_{\lambda_{\Lambda_c}}^{k;\lambda_{\Lambda_b}} \right) L_{\lambda_l}^{C_{S_L}} G_{\lambda_p}^{\lambda_{\Lambda_c}}
$$

$$
\left. + \sum_{\lambda_{\Lambda_c},\lambda_W,\lambda_W'} \eta_{\lambda_W} \eta_{\lambda_W'} H_{\lambda_{\Lambda_c},\lambda_W,\lambda_W'}^{C_{T_L};\lambda_{\Lambda_b}} L_{\lambda_l}^{C_{T_L};\lambda_W,\lambda_W'} G_{\lambda_p}^{\lambda_{\Lambda_c}} \right]. \tag{2.7}
$$

Here H, L and G represent the helicity amplitudes of Λ_b^0, W^{*-} and Λ_c^+ decays, respectively, retaining dependence on all the angular degrees of freedom. In this study the two lowest allowed spins for W^{*-}, i.e. $(J_W = 0, \lambda_W = 0)$ and $(J_W = 1, \lambda_W = -1,0,1)$, are being considered. To distinguish the former helicity configuration from the latter, we denote $\lambda_W = t$ when $J_W = 0$. The term η_λ denotes a metric factor that originates when we replace the metric tensor with the polarisation vectors of the virtual W^{*-} i.e. $g^{\mu\nu} = \sum_\lambda \eta_\lambda \epsilon^{\dagger\mu}(\lambda)\epsilon^\nu(\lambda)$ where $\eta_{0,\pm1} = -\eta_t = -1$.

The hadronic amplitudes expressed above in Eq.(2.7) are related to those involving vector (V), axial-vector (A), scalar (S), pseudo-scalar (PS), tensor (T) and pseudo-tensor (PT) currents through the following relations:

$$
H_{\lambda_{\Lambda_c},\lambda_W}^{SM;\lambda_{\Lambda_b}} = \frac{1}{2}\left(H_{\lambda_{\Lambda_c},\lambda_W}^{V;\lambda_{\Lambda_b}} - H_{\lambda_{\Lambda_c},\lambda_W}^{A;\lambda_{\Lambda_b}} \right), \tag{2.8}
$$

$$
H_{\lambda_{\Lambda_c},\lambda_W}^{C_{V_L};\lambda_{\Lambda_b}} = \frac{C_{V_L}}{2}\left(H_{\lambda_{\Lambda_c},\lambda_W}^{V;\lambda_{\Lambda_b}} - H_{\lambda_{\Lambda_c},\lambda_W}^{A;\lambda_{\Lambda_b}} \right), \tag{2.9}
$$

$$
H_{\lambda_{\Lambda_c},\lambda_W}^{C_{V_R};\lambda_{\Lambda_b}} = \frac{C_{V_R}}{2}\left(H_{\lambda_{\Lambda_c},\lambda_W}^{V;\lambda_{\Lambda_b}} + H_{\lambda_{\Lambda_c},\lambda_W}^{A;\lambda_{\Lambda_b}} \right), \tag{2.10}
$$

$$
H_{\lambda_{\Lambda_c}}^{C_{S_L};\lambda_{\Lambda_b}} = \frac{C_{S_L}}{2}\left(H_{\lambda_{\Lambda_c}}^{S;\lambda_{\Lambda_b}} - H_{\lambda_{\Lambda_c}}^{PS;\lambda_{\Lambda_b}} \right), \tag{2.11}
$$

$$
H_{\lambda_{\Lambda_c}}^{C_{S_R};\lambda_{\Lambda_b}} = \frac{C_{S_R}}{2}\left(H_{\lambda_{\Lambda_c}}^{S;\lambda_{\Lambda_b}} + H_{\lambda_{\Lambda_c}}^{PS;\lambda_{\Lambda_b}} \right), \tag{2.12}
$$

$$
H_{\lambda_{\Lambda_c},\lambda_W,\lambda_W'}^{C_{T_L};\lambda_{\Lambda_b}} = \frac{C_{T_L}}{2}\left(H_{\lambda_{\Lambda_c},\lambda_W,\lambda_W'}^{T;\lambda_{\Lambda_b}} - H_{\lambda_{\Lambda_c},\lambda_W,\lambda_W'}^{PT;\lambda_{\Lambda_b}} \right). \tag{2.13}
$$

In Appendix 2.A the expressions for these amplitudes are provided in the rest frame of Λ_b, where Λ_c momentum has spherical coordinates $(p_{\Lambda_c}^{[\Lambda_b]}, \theta_{\Lambda_c}^{[\Lambda_b]}, \phi_{\Lambda_c}^{[\Lambda_b]} = 0)$. In further discussions, we drop superscript '$[\Lambda_b]$' for brevity, specifying that the quantity has been defined in the Λ_b^0 rest frame.

The polar angle and momentum of Λ_c^+ in this frame are depicted in Figure 2.1. It is worth noting that these hadronic helicity amplitudes are functions of q^2 and θ_{Λ_c}.
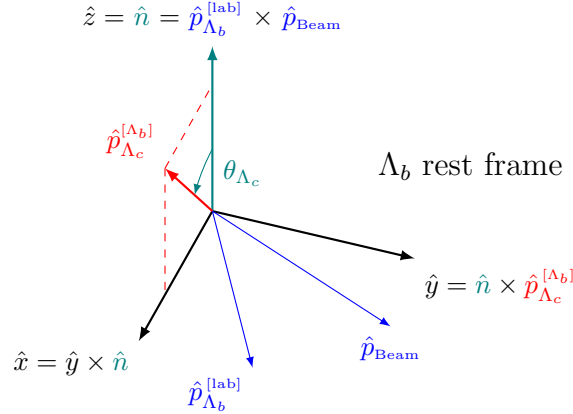

FIGURE 2.1: Pictorial representation of the frame $(\hat{x}, \hat{y}, \hat{z})$ in which the hadronic helicity amplitudes related to $\Lambda_b^0 \to \Lambda_c^+ W^{*-}$ decay are defined. The axis $\hat{n}$ represents the polarisation axis of Λ_b^0, chosen to be perpendicular to the production plane $(\hat{p}_{\Lambda_b}^{[lab]} \times \hat{p}_{Beam})$.

The leptonic amplitudes, shown in Eq.(2.7), are defined as:

$$L_{\lambda_l}^{SM;\lambda_W} = \frac{1}{2} \epsilon^\mu(\lambda_W) \bar{u}_l(\lambda_l) \gamma_\mu (1-\gamma_5) v_{\bar{\nu}_l} \,, \tag{2.14}$$

$$L_{\lambda_l}^{C_{S_L}} = \frac{1}{2} \bar{u}_l(\lambda_l)(1-\gamma_5) v_{\bar{\nu}_l} \,, \tag{2.15}$$

$$L_{\lambda_l}^{C_{T_L};\lambda_W,\lambda_W'} = \frac{-i}{2} \epsilon^\mu(\lambda_W) \epsilon^\nu(\lambda_W') \bar{u}_l(\lambda_l) \sigma_{\mu\nu}(1-\gamma_5) v_{\bar{\nu}_l} \,. \tag{2.16}$$

Here $\bar{u}_l$, $v_{\bar{\nu}_l}$ and ϵ^μ represents the particle helicity spinor of the lepton, the anti-particle helicity spinor for neutrino and the polarisation vector of W, respectively. In Appendix 2.B, we present the expressions for the leptonic amplitudes defined in the helicity frame of W^{*-} [3], $(\hat{x}_\ell, \hat{y}_\ell, \hat{z}_\ell)$, where the ℓ^- momentum has spherical coordinates $(p_\ell^{[W]}, \theta_\ell^{[W]}, \phi_\ell^{[W]})$. As before, the superscript '$[W]$' is dropped in further discussions for brevity. The angles and momentum of the ℓ^-, defined in the W^{*-} helicity frame, are shown in Figure 2.2. The leptonic helicity amplitudes expressed above are functions of q^2, θ_l and ϕ_l.

---

[3]In the decay of $A \to BC$, the helicity frame of A forms the rest frame of A in which the z-axis is in the direction of its polarisation axis. The latter is chosen to be in direction of the momentum of A in the rest frame of its parent particle.
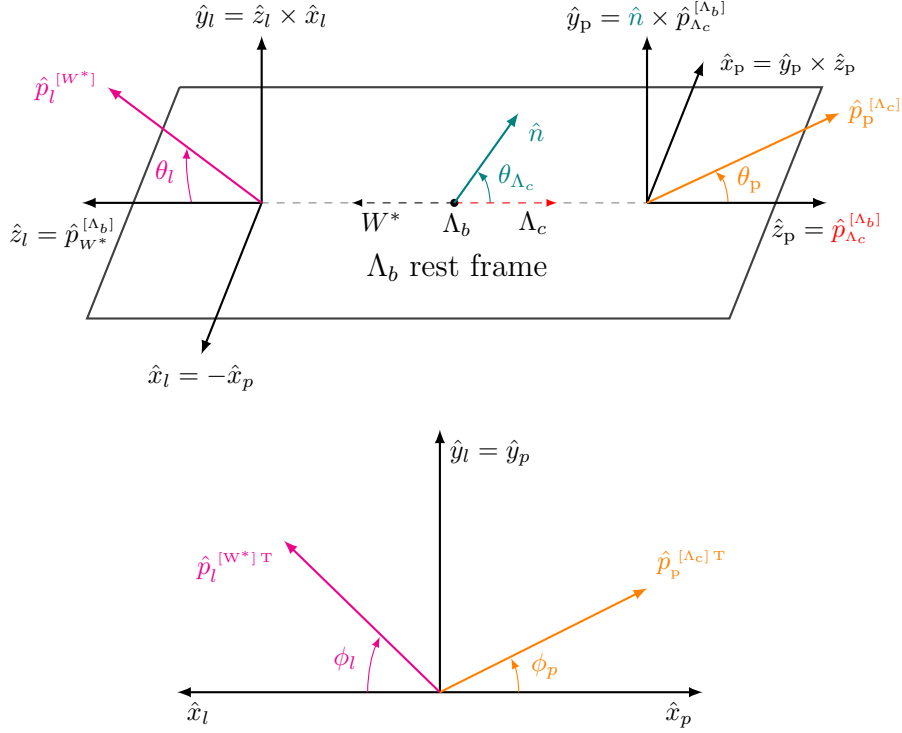
FIGURE 2.2: Pictorial representation of W^{*-} helicity frame $(\hat{x}_l, \hat{y}_l, \hat{z}_l)$ and Λ_c^+ helicity frame $(\hat{x}_p, \hat{y}_p, \hat{z}_p)$. (Top) The unit vectors $\hat{p}_W^{[\Lambda_b]}$ and $\hat{p}_{\Lambda_c}^{[\Lambda_b]}$ denote the direction of propagation of W^{*-} and Λ_c^+ in the Λ_b^0 rest frame, respectively. (Bottom) The unit vector $\hat{p}_l^{[W]\text{T}}$ and $\hat{p}_p^{[\Lambda_c]\text{T}}$ denote the direction of the transverse momentum components of ℓ^- and p in W^{*-} and Λ_c^+ helicity frames, respectively.

The amplitudes corresponding to the weak decay $\Lambda_c^+ \to pK_S^0$ are given as:

$$G_{\lambda_\text{p}}^{\lambda_{\Lambda_c}} = D_{\lambda_{\Lambda_c}, \lambda_\text{p}}^{1/2*}(\phi_\text{p}, \theta_\text{p}, -\phi_\text{p}) g_{\lambda_\text{p}}, \tag{2.17}$$

where g_{λ_p} denotes the rotationally invariant amplitude of the Λ_c decay, defined in the rest frame of Λ_c with the proton moving in positive direction of the z-axis. The Wigner-D elements, $D_{\lambda_{\Lambda_c}, \lambda_\text{p}}^{1/2*}$, specify the rotation of the helicity states into the helicity frame of Λ_c. In this frame, the proton momentum has spherical coordinates $(p_p^{[\Lambda_c]}, \theta_p^{[\Lambda_c]}, \phi_p^{[\Lambda_c]})$. The superscript '$[\Lambda_c]$' in further discussions is omitted for brevity. As noted above, after incoherent sum over λ_p, we can express the decay density in terms of the weak decay asymmetry parameter $\alpha_{\Lambda_c^+}$, through the substitution:

$$\widehat{|g_{+\frac{1}{2}}|^2} = \frac{|g_{+\frac{1}{2}}|^2}{\sum_{\lambda_p} |g_{\lambda_p}|^2} = \frac{1}{2}(1 + \alpha_{\Lambda_c}), \quad \widehat{|g_{-\frac{1}{2}}|^2} = \frac{|g_{-\frac{1}{2}}|^2}{\sum_{\lambda_p} |g_{\lambda_p}|^2} = \frac{1}{2}(1 - \alpha_{\Lambda_c}). \tag{2.18}$$

The expressions for the amplitude shown in Eq.(2.17), when expanding out the Wigner-D elements, are given in Appendix 2.C.

The transition amplitudes shown in Eq.(2.6) apply to the $\Lambda_b^0 \to (pK_S^0)(\ell^- \bar{\nu}_l)$ decay channel. To obtain the amplitude of the *CP* conjugate process, we complex conjugate all the Wilson co-efficients ($\{C\}$) that carry the weak phase, change the sign of all the azimuthal angles involved ($\{\phi\}$) and change the set of final state particles helicities to those of their *CP* conjugate partner $\{\bar{\lambda}\}$ [12], *i.e.*:

$$T_{\overline{\Lambda}_b^0 \to \overline{\Lambda}_c^- \ell^+ \nu_l} = T_{\Lambda_b^0 \to \Lambda_c^+ \ell^- \overline{\nu}_l}(\{\lambda\} \to \{\bar{\lambda}\}, \{\phi\} \to \{-\phi\}, \{C\} \to \{C^*\}).$$

2.4 Decay density

The full six-fold normalised angular differential decay density considering the Λ_b^0 polarisation effects is given by:

$$d^6\Gamma = \frac{N}{\Gamma}|T|^2 d\Omega', \tag{2.19}$$

with

$$\Gamma = \int (d^6\Gamma/d\Omega')d\Omega', \tag{2.20}$$

$$N = \frac{G_F^2 |V_{cb}|^2 p_l \, \mathscr{B}_{\Lambda_c} \left[p_{\Lambda_c}\right]^{m_{pK_S^0}^2 = m_{\Lambda_c}^2}}{2^{12}\pi^5 m_{\Lambda_b}^2 \sqrt{q^2}}, \quad d\Omega' = dq^2 d\cos\theta_{\Lambda_c} d\cos\theta_p d\phi_p d\cos\theta_l d\phi_l, \tag{2.21}$$

and

$$|T|^2 = (1 + P_{\Lambda_b}) \sum_{\lambda_p, \lambda_{\ell^-}} |T_{\lambda_{\ell^-}, \lambda_p}^{\lambda_{\Lambda_b^0} = \frac{1}{2}}|^2 + (1 - P_{\Lambda_b}) \sum_{\lambda_p, \lambda_{\ell^-}} |T_{\lambda_{\ell^-}, \lambda_p}^{\lambda_{\Lambda_b^0} = -\frac{1}{2}}|^2,$$

$$= K_1(1 - P_{\Lambda_b}\cos\theta_{\Lambda_c}) + K_2(1 + P_{\Lambda_b}\cos\theta_{\Lambda_c}) + K_3 P_{\Lambda_b}\sin\theta_{\Lambda_c}. \tag{2.22}$$

More details are provided in Appendix 2.D. In Eq. 2.21, $\mathscr{B}_{\Lambda_c}$ denotes the branching fraction of $\Lambda_c^+ \to pK_S^0$ decay; m_{Λ_b} and m_{Λ_c} are the masses of Λ_b^0 and Λ_c^+; p_{Λ_c}, p_p and p_l denote the three-momentum magnitudes of Λ_c^+, proton and lepton respectively, all defined in the rest frame of their parent particle and expressed in terms of Lorentz invariant quantities in Eq.(2.40). In Eq. 2.22, P_{Λ_b} refers to the polarisation of Λ_b^0; the terms K_i depend on all the phase space observables with the exception of θ_{Λ_c}, which are given in Appendix 2.E.

The expression of the decay density intrinsically depends on the assumptions made on Λ_b^0 polarisation and Λ_c^+ decay kinematics. When Λ_b^0 is produced unpolarised and the two-body decay $\Lambda_c^+ \to pK_S^0$ is considered, the decay density is independent of $\cos\theta_{\Lambda_c}$ and ϕ_p (Eq.(2.45)), and the variable ϕ_l can be expressed in terms of χ, defined as the angle between pK_S^0 and $\ell^- \bar{\nu}_l$ decay planes. Conversely, if Λ_b^0 is produced polarised and the degrees of freedom related to Λ_c^+ decay are integrated out, the decay density exhibits dependence on q^2, $\cos\theta_{\Lambda_c}$, $\cos\theta_l$ and ϕ_l (Eq.(2.46)),

where ϕ_l can be expressed in terms of the angle between the Λ_b^0 polarisation plane (*i.e.* the one containing $\hat{n}$ and $\hat{p}_{\Lambda_c}$) and $\ell^- \bar{\nu}_l$ decay plane. In the case that the Λ_b^0 baryon is unpolarised and degrees of freedom related to the Λ_c^+ decay are integrated out, the decay density depends only on q^2 and $\cos\theta_l$.

2.5 Experimental sensitivity

In this section the sensitivity that can be achieved on the Wilson coefficients, by studying the differential decay density in different scenarios, is presented.

In the first case, Λ_b^0 baryons are considered to be produced unpolarised. The angular distribution of the Λ_c^+ decay is integrated over and the q^2 and $\cos\theta_l$ distributions are measured. The expression for the employed fit model is shown in Eq.(2.48) of Appendix 2.F. The expected signal yield is determined from Ref. [26], where the $\Lambda_c^+ \to pK^+\pi^-$ decay mode is adopted. When extrapolated to the current LHCb dataset of $9\,\text{fb}^{-1}$, this gives 7.5M expected signal candidates $\Lambda_b^0 \to \Lambda_c^+ \mu^- \bar{\nu}_\mu$. The abundant signal yield suggests that the $\Lambda_c^+ \to pK^+\pi^-$ decay mode is the most sensitive to NP operators, as favoured by the experimental signature.

For the second scenario the $\Lambda_c^+ \to pK_S^0$ decay is reconstructed and a non-zero polarisation of Λ_b^0 is foreseen. In this case, the angles $\cos\theta_p$ and ϕ_p are additionally included in the differential decay density and thus the four-dimensional distribution is fitted. The expression for the complete fit model is shown in Eq.(2.49) of Appendix 2.F. It is worth noting that the low reconstruction efficiency of long-lived K_S^0 mesons and the smaller Λ_c^+ branching fraction translates into a signal yield which is reduced by approximately a factor 20 with respect to the $\Lambda_c^+ \to pK^+\pi^-$ three-body decay case.

The background level for $\Lambda_b^0 \to \Lambda_c^+ \mu^- \bar{\nu}_\mu$ decays is small, as reported in Ref. [26]. Furthermore, the acceptance is not expected to be a strong function of the decay variables as the muon trigger selection at LHCb is efficient [26]. As a result, these effects are neglected in the following studies. One aspect that cannot be ignored, however, is the dilution of resolution on q^2 and $\cos\theta_l$ variables due the unreconstructed neutrino. To take this into account, we generate the $\Lambda_b^0 \to \Lambda_c^+ \mu^- \bar{\nu}_\mu$ signal sample using Pythia [42, 43], requiring the signal events to be approximately within the LHCb acceptance (*i.e.* $2 < \eta < 5$). The Λ_b^0 vertex position is then smeared according a spatial resolution inspired in Ref. [44]. Data migration between kinematic bins in q^2 and $\cos\theta_l$ is included in the fit by convoluting the decay density with a migration matrix, which is described in more detail in Appendix. 2.G.

In order to assess the sensitivity to the Wilson coefficients, pseudo-experiments have been generated with the expected signal yield and experimental resolution. A binned maximum likelihood fit, with 20 bins employed in each dimension, is then performed. A Gaussian constraint is applied to the $\Lambda_b^0 \to \Lambda_c^+$ hadronic form factors, using lattice QCD results from [24, 30]. The 95% CL intervals obtained from this study are compared with those inferred from $B \to D^{(*)}\ell\nu$ decays [22]. No

effects of *CP* violation have been considered, therefore the Wilson coefficients in this study are assumed to be real.

At first, only one Wilson coefficient at a time is varied; the results are shown in Fig. 2.3. As the production fraction of Λ_b^0 decays has a relatively large uncertainty [45], the normalised differential distribution is fitted which has no sensitivity to the Wilson coefficient C_{V_L} and the CKM matrix element V_{cb}. The sensitivity to other NP operators is expected to be significantly better than that of the current constraints, mainly due to the huge signal yields expected at LHCb.
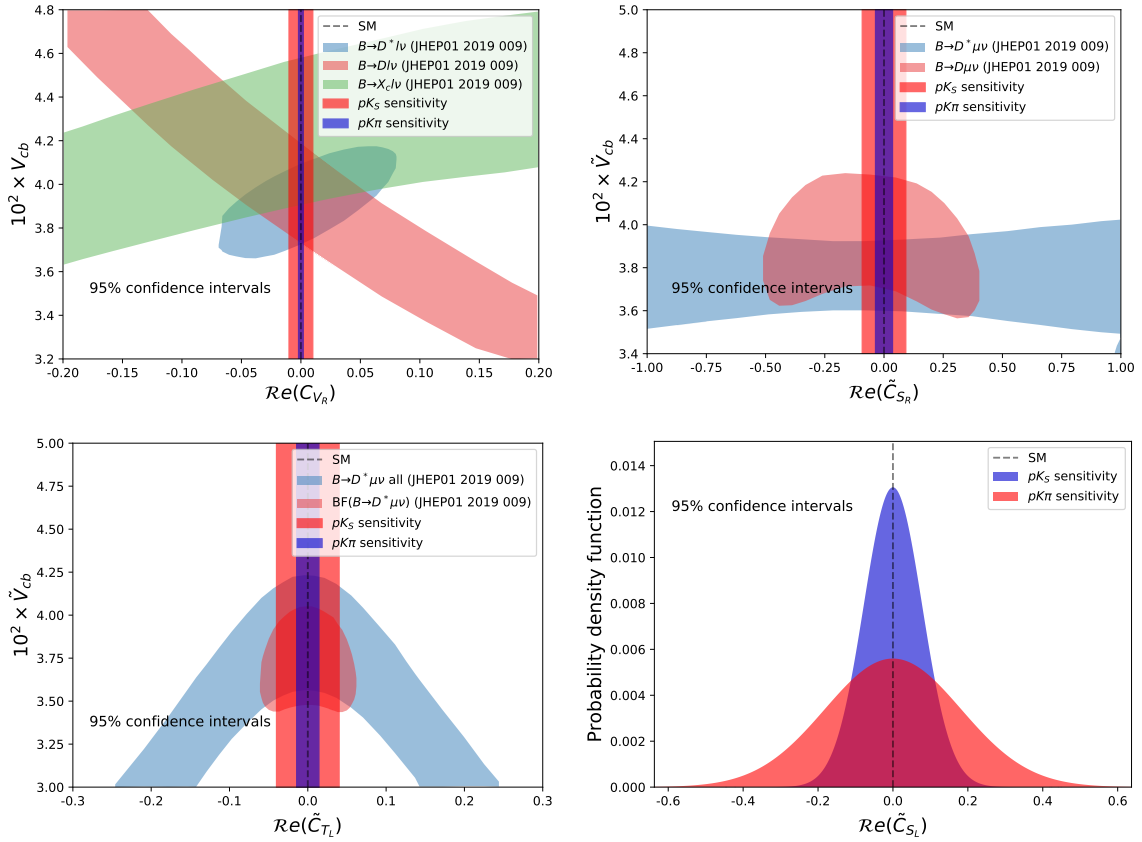
FIGURE 2.3: Expected sensitivity to the Wilson coefficients of the NP operators individually fitted and compared to the constraints obtained from the corresponding mesonic semileptonic decays [22]. As done in Ref.([22]), we define here $\tilde{C}_i = C_i/(1 + C_{V_L})$ and $\tilde{V}_{cb} = V_{cb}/(1 + C_{V_L})$.

The interplay between different Wilson coefficients is explored in Fig. 2.4 and compared to Ref. [22]. Large non-Gaussian correlations are observed, affecting both the 2D and 4D differential widths. When all the Wilson coefficients are fitted at once, then the observed correlations between the tensor and scalar currents become even larger, implying that contributions from these operators are difficult to disentangle from the explored distributions alone.

The four-dimensional decay density distribution involving $\Lambda_c^+ \to pK_S^0$ is sensitive to both the $P_{\Lambda_b^0}$
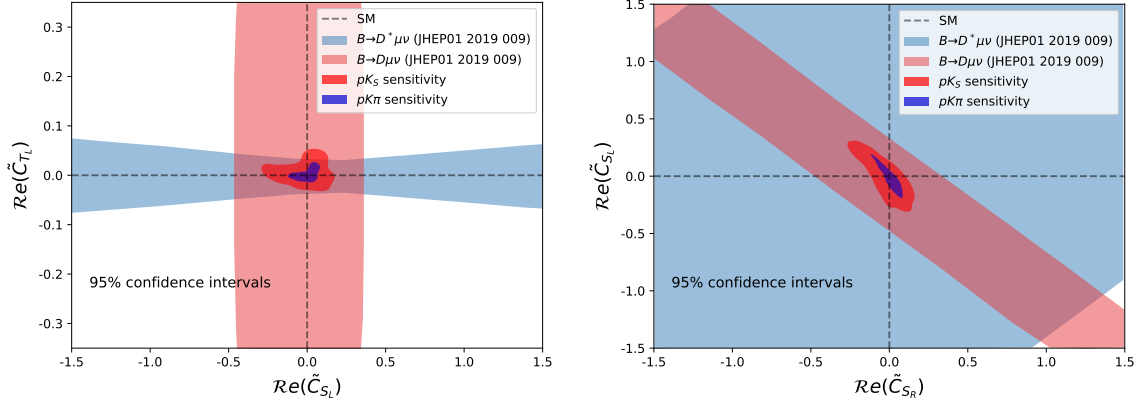
FIGURE 2.4: Two-dimensional sensitivity plot between the Wilson coefficients $\tilde{C}_{T_L}$, $\tilde{C}_{S_L}$ and $\tilde{C}_{S_R}$ when compared to the limits obtained from mesonic semileptonic decays [22]. As done in Ref.([22]), we define here $\tilde{C}_i = C_i / (1 + C_{V_L})$.

and $\alpha_{\Lambda_c^+}$. A comparison of the results of this study with existing measurements from BES III [39] and LHCb [36] is illustrated in Fig. 2.5. The expected sensitivity to $\alpha_{\Lambda_c^+}$ is currently a world-leading value, whereas the sensitivity to $P_{\Lambda_b^0}$ is slightly less precise than previous measurements [36–38], but could be improved in the future with a full angular analysis of $\Lambda_b^0 \to \Lambda_c^+ (\to pK_S^0) \mu^- \bar{\nu}_\mu$ decays. A summary of the sensitivity for the various cases can be found in Table 2.1.
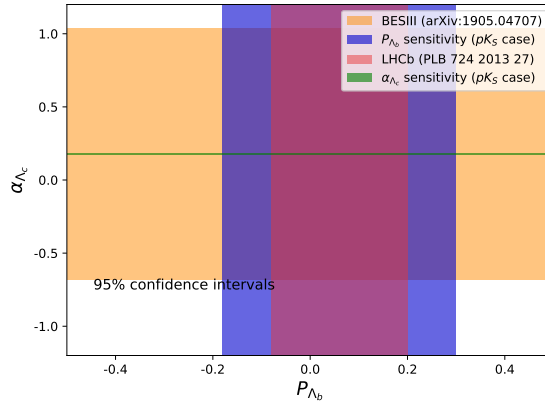
FIGURE 2.5: Sensitivity on $P_{\Lambda_b^0}$ and $\alpha_{\Lambda_c^+}$ as obtained from a four-dimensional fit to the $\Lambda_b^0 \to \Lambda_c^+ (\to pK_S^0) \mu \nu$ differential distribution.

2.6 Conclusions

In this study a general expression for the effective Lagrangian governing $b \to c\ell\nu_l$ transitions has been considered, including NP contributions through a complete basis of dimension-six operators

The 68% confidence intervals for the parameters of interest for various cases.

Free parameters	pK$_S^0$ case	pK$^- \pi^+$ case
C_{V_R}	0.005	0.001
C_{S_R}	0.046	0.018
C_{T_L}	0.020	0.007
C_{S_L}	0.091	0.039
$P_{\Lambda_b^0}$	0.13	–
$\alpha_{\Lambda_c^+}$	0.003	–

and assuming only left-handed neutrinos. Using this formalism, we presented for the first time an expression for the six-fold differential decay density for polarised $\Lambda_b^0 \to \Lambda_c^+ \ell^- \bar{\nu}_l$ decays, with subsequent $\Lambda_c^+ \to pK_S^0$ decay.

In addition, we carried out sensitivity studies to determine the experimental precision on the Wilson coefficients which can be achieved through the analysis of $\Lambda_b^0 \to \Lambda_c^+ \mu^- \bar{\nu}_\mu$ decays at the LHCb experiment. When considering the integrated Run I and Run II data samples collected at LHCb. The first case considered was the decay channel $\Lambda_b^0 \to \Lambda_c^+ (\to pK^- \pi^+) \mu^- \bar{\nu}_\mu$, where the 2D distribution in q^2 and $\cos\theta_l$ was studied. The second explored scenario focused on $\Lambda_b^0 \to \Lambda_c^+ (\to pK_S^0) \mu^- \bar{\nu}_\mu$ decays, including polarisation effects on the production of Λ_b^0. At this purpose, the 4D distributions in q^2, $\cos\theta_l$, $\cos\theta_p$ and ϕ_p variables were inspected. Since a missing unreconstructed neutrino in the final state spoils the experimental resolution on q^2 and $\cos\theta_l$, in both of the mentioned cases the resolution effects were folded into the fit model through a migration matrix.

The results of the sensitivity studies show that the best precision on the Wilson coefficients can be achieved by probing the q^2 and $\cos\theta_l$ distributions of $\Lambda_b^0 \to \Lambda_c^+ (\to pK^- \pi^+) \mu^- \bar{\nu}_\mu$ decays collected at LHCb, leading to a good sensitivity to C_{V_R}, C_{T_L}, C_{S_R} and C_{S_L}. No sensitivity is expected to overall global factors, such as V_{cb} and C_{V_L}, as the present study is performed on the normalised differential decay distributions.

Although no enhanced sensitivity to the Wilson coefficients could be achieved through the investigation of 4D kinematic distributions of $\Lambda_b^0 \to \Lambda_c^+ (\to pK_S^0) \mu^- \bar{\nu}_\mu$ decay channel, they do however provide a prospect of measuring $\alpha_{\Lambda_c^+}$ and $P_{\Lambda_b^0}$. The parameter $\alpha_{\Lambda_c^+}$ is particularly promising, with a precision which is two orders of magnitude smaller than that measured by the BESIII experiment. The precision on $P_{\Lambda_b^0}$ could also be improved by performing a full six-dimensional angular analysis. That would require large signal yields expected at the LHCb upgrades and a different treatment of the resolution.

In this paper we have assumed *CP* conservation and considered the Wilson coefficients to be real variables. To further distinguish NP models, one could easily extend the present study allowing Wilson coefficients to be complex to probe *CP* violation in $\Lambda_b^0 \to \Lambda_c^+ \mu^- \bar{\nu}_\mu$ decays. The results of the sensitivity studies have been compared to the model-independent constraints obtained in global

fits to $B \to D^{(*)} \ell^- \nu_l$ semileptonic decays, presented in Ref. [22], and have shown a significant improvement in the achievable experimental precision. As a consequence, it can be concluded that studying $\Lambda_b^0 \to \Lambda_c^+ \mu^- \bar{\nu}_\mu$ decays at the LHCb experiment will not only lead to a more precise measurement on Λ_c^+ decay asymmetry parameter, but also allows to place stringent world leading constraints on the Wilson coefficients of the corresponding NP operators.

Appendix

Contents

2.A Hadronic amplitudes of $\Lambda_b^0 \to \Lambda_c^+ W^{*-}$ decay

In this section, we give expressions of the hadronic helicity amplitudes for $\Lambda_b^0 \to \Lambda_c^+ W^{*-}$ decay. The hadronic matrix elements shown in Eqs.(2.8–2.13) are expressed as:

$$H^{V;\lambda_{\Lambda_b}}_{\lambda_{\Lambda_c},\lambda_W} = \epsilon^{\dagger\mu}(\lambda_W)\langle \Lambda_c, \lambda_{\Lambda_c} | \bar{c}\gamma_\mu b | \Lambda_b, \lambda_{\Lambda_b}\rangle \,, \tag{2.23}$$

$$H^{A;\lambda_{\Lambda_b}}_{\lambda_{\Lambda_c},\lambda_W} = \epsilon^{\dagger\mu}(\lambda_W)\langle \Lambda_c, \lambda_{\Lambda_c} | \bar{c}\gamma_\mu \gamma_5 b | \Lambda_b, \lambda_{\Lambda_b}\rangle \,, \tag{2.24}$$

$$H^{S;\lambda_{\Lambda_b}}_{\lambda_{\Lambda_c}} = \langle \Lambda_c, \lambda_{\Lambda_c} | \bar{c} b | \Lambda_b, \lambda_{\Lambda_b}\rangle \,, \tag{2.25}$$

$$H^{PS;\lambda_{\Lambda_b}}_{\lambda_{\Lambda_c}} = \langle \Lambda_c, \lambda_{\Lambda_c} | \bar{c}\gamma_5 b | \Lambda_b, \lambda_{\Lambda_b}\rangle \,, \tag{2.26}$$

$$H^{T;\lambda_{\Lambda_b}}_{\lambda_{\Lambda_c},\lambda_W,\lambda'_W} = \epsilon^{\dagger\mu}(\lambda_W)\epsilon^{\dagger\nu}(\lambda'_W)\langle \Lambda_c, \lambda_{\Lambda_c} | \bar{c} i\sigma_{\mu\nu} b | \Lambda_b, \lambda_{\Lambda_b}\rangle \,, \tag{2.27}$$

$$H^{PT;\lambda_{\Lambda_b}}_{\lambda_{\Lambda_c},\lambda_W,\lambda'_W} = \epsilon^{\dagger\mu}(\lambda_W)\epsilon^{\dagger\nu}(\lambda'_W)\langle \Lambda_c, \lambda_{\Lambda_c} | \bar{c} i\sigma_{\mu\nu}\gamma_5 b | \Lambda_b, \lambda_{\Lambda_b}\rangle \,.$$

Here '$\epsilon^{\dagger\mu}$' denotes the polarisation vector of W^{*-}. The definitions of the matrix elements in terms of the form factors are given in Ref.[30].

When considering the transverse polarisation of Λ_b, the common choice of a Λ_b rest frame is the one where the polarisation axis ($\hat{n}$) is perpendicular to the production plane, *i.e.*:

$$\hat{z} = \hat{n} = \hat{p}^{lab}_{\Lambda_b} \times \hat{p}^{lab}_{Beam} \,, \ \hat{y} = \hat{p}_{\Lambda_c} \times \hat{z} \,, \ \hat{x} = \hat{y} \times \hat{z} \,, \tag{2.28}$$

where $\hat{\ }$ refers to the unit vector, the superscript 'lab' indicates the lab frame and $\hat{p}_{\Lambda_c}$ is the unit vector of Λ_c momentum in Λ_b rest frame (Figure 2.1). In such a frame, the choice of azimuthal angle for $\hat{p}_{\Lambda_c}^{[\Lambda_b]}$ is arbitrary and is set to zero. Therefore, Λ_c momentum is oriented in the direction $(\theta_{\Lambda_c}, \phi_{\Lambda_c} = 0)$ with magnitude p_{Λ_c} and the virtual W^{*-} moves in the opposite direction, which is $(\pi - \theta_{\Lambda_c}, \pi)$ with $p_{W^{*-}} = p_{\Lambda_c}$.

The generic expression for the polarisation vector, helicity spinors and the representation of gamma matrices used in this work follow Ref. [46, 47]. We show below the expression for helicity spinors of Λ_b^0 (u_{Λ_b}) with mass m_{Λ_b}, Λ_c^+ (u_{Λ_c}) with mass m_{Λ_c} and polarisation vector of W^{*-} (ϵ^μ) in the Λ_b rest frame.

$$
u_{\Lambda_b}\left(\lambda_{\Lambda_b} = \tfrac{1}{2}\right) = \begin{pmatrix} \sqrt{2m_{\Lambda_b}} \\ 0 \\ 0 \\ 0 \end{pmatrix}
\qquad
u_{\Lambda_c}\left(\lambda_{\Lambda_c} = \tfrac{1}{2}\right) = \begin{pmatrix} \sqrt{E_{\Lambda_c} + m_{\Lambda_c}}\cos\frac{\theta_{\Lambda_c}}{2} \\ \sqrt{E_{\Lambda_c} + m_{\Lambda_c}}\sin\frac{\theta_{\Lambda_c}}{2} \\ \sqrt{E_{\Lambda_c} - m_{\Lambda_c}}\cos\frac{\theta_{\Lambda_c}}{2} \\ \sqrt{E_{\Lambda_c} - m_{\Lambda_c}}\sin\frac{\theta_{\Lambda_c}}{2} \end{pmatrix},
$$

$$
u_{\Lambda_b}\left(\lambda_{\Lambda_b} = -\tfrac{1}{2}\right) = \begin{pmatrix} 0 \\ \sqrt{2m_{\Lambda_b}} \\ 0 \\ 0 \end{pmatrix},
\qquad
u_{\Lambda_c}\left(\lambda_{\Lambda_c} = -\tfrac{1}{2}\right) = \begin{pmatrix} -\sqrt{E_{\Lambda_c} + m_{\Lambda_c}}\sin\frac{\theta_{\Lambda_c}}{2} \\ \sqrt{E_{\Lambda_c} + m_{\Lambda_c}}\cos\frac{\theta_{\Lambda_c}}{2} \\ \sqrt{E_{\Lambda_c} - m_{\Lambda_c}}\sin\frac{\theta_{\Lambda_c}}{2} \\ -\sqrt{E_{\Lambda_c} - m_{\Lambda_c}}\cos\frac{\theta_{\Lambda_c}}{2} \end{pmatrix},
$$

$$
\epsilon^\mu(\lambda_W = t) = \begin{pmatrix} \frac{E_W}{\sqrt{q^2}} \\ -\frac{p_{\Lambda_c}\sin\theta_{\Lambda_c}}{\sqrt{q^2}} \\ 0 \\ -\frac{p_{\Lambda_c}\cos\theta_{\Lambda_c}}{\sqrt{q^2}} \end{pmatrix},
\qquad
\epsilon^\mu(\lambda_W = 1) = \begin{pmatrix} 0 \\ \frac{\cos\theta_{\Lambda_c}}{\sqrt{2}} \\ \frac{-i}{\sqrt{2}} \\ -\frac{\sin\theta_{\Lambda_c}}{\sqrt{2}} \end{pmatrix},
$$

$$
\epsilon^\mu(\lambda_W = 0) = \begin{pmatrix} \frac{p_{\Lambda_c}}{\sqrt{q^2}} \\ -\frac{E_W\sin\theta_{\Lambda_c}}{\sqrt{q^2}} \\ 0 \\ -\frac{E_W\cos\theta_{\Lambda_c}}{\sqrt{q^2}} \end{pmatrix},
\qquad
\epsilon^\mu(\lambda_W = -1) = \begin{pmatrix} 0 \\ -\frac{\cos\theta_{\Lambda_c}}{\sqrt{2}} \\ -\frac{i}{\sqrt{2}} \\ \frac{\sin\theta_{\Lambda_c}}{\sqrt{2}} \end{pmatrix},
$$

where

$$
E_{\Lambda_c} = \sqrt{p_{\Lambda_c}^2 + m_{\Lambda_c}^2}, \qquad\qquad E_W = \sqrt{p_{\Lambda_c}^2 + q^2} = \frac{1}{2m_{\Lambda_b}}\left(m_{\Lambda_b}^2 - m_{\Lambda_c}^2 + q^2\right),
$$

$$
p_{\Lambda_c} = \frac{1}{2m_{\Lambda_b}}\sqrt{Q_+ Q_-}, \qquad\qquad Q_\pm = (M_\pm^2 - q^2), \quad M_\pm = (m_{\Lambda_b} \pm m_{\Lambda_c}).
$$

The vector ($H_{\lambda_{\Lambda_c},\lambda_W}^{V;\lambda_{\Lambda_b}}$) and axial vector ($H_{\lambda_{\Lambda_c},\lambda_W}^{A;\lambda_{\Lambda_b}}$) amplitudes can then be expressed as:

$$H_{\frac{1}{2},t}^{V;\frac{1}{2}} = H_{-\frac{1}{2},t}^{V;-\frac{1}{2}} = \cos\frac{\theta_{\Lambda_c}}{2}a_V \qquad , H_{-\frac{1}{2},t}^{V;\frac{1}{2}} = -H_{\frac{1}{2},t}^{V;-\frac{1}{2}} = -\sin\frac{\theta_{\Lambda_c}}{2}a_V \,,$$

$$H_{\frac{1}{2},0}^{V;\frac{1}{2}} = H_{-\frac{1}{2},0}^{V;-\frac{1}{2}} = \cos\frac{\theta_{\Lambda_c}}{2}b_V \qquad , H_{-\frac{1}{2},0}^{V;\frac{1}{2}} = -H_{\frac{1}{2},0}^{V;-\frac{1}{2}} = -\sin\frac{\theta_{\Lambda_c}}{2}b_V \,,$$

$$H_{-\frac{1}{2},-}^{V;\frac{1}{2}} = H_{\frac{1}{2},+}^{V;-\frac{1}{2}} = -\cos\frac{\theta_{\Lambda_c}}{2}c_V \qquad , H_{-\frac{1}{2},-}^{V;-\frac{1}{2}} = -H_{\frac{1}{2},+}^{V;\frac{1}{2}} = -\sin\frac{\theta_{\Lambda_c}}{2}c_V \,,$$

$$H_{\frac{1}{2},t}^{A;\frac{1}{2}} = -H_{-\frac{1}{2},t}^{A;-\frac{1}{2}} = \cos\frac{\theta_{\Lambda_c}}{2}a_A \qquad , H_{-\frac{1}{2},t}^{A;\frac{1}{2}} = H_{\frac{1}{2},t}^{A;-\frac{1}{2}} = \sin\frac{\theta_{\Lambda_c}}{2}a_A \,,$$

$$H_{\frac{1}{2},0}^{A;\frac{1}{2}} = -H_{-\frac{1}{2},0}^{A;-\frac{1}{2}} = \cos\frac{\theta_{\Lambda_c}}{2}b_A \qquad , H_{-\frac{1}{2},0}^{A;\frac{1}{2}} = H_{\frac{1}{2},0}^{A;-\frac{1}{2}} = \sin\frac{\theta_{\Lambda_c}}{2}b_A \,,$$

$$H_{-\frac{1}{2},-}^{A;\frac{1}{2}} = -H_{\frac{1}{2},+}^{A;-\frac{1}{2}} = \cos\frac{\theta_{\Lambda_c}}{2}c_A \qquad , H_{-\frac{1}{2},-}^{A;-\frac{1}{2}} = H_{\frac{1}{2},+}^{A;\frac{1}{2}} = \sin\frac{\theta_{\Lambda_c}}{2}c_A \,,$$

$$H_{\frac{1}{2},-}^{V(A);\frac{1}{2}} = H_{-\frac{1}{2},+}^{V(A);-\frac{1}{2}} = 0 \qquad , H_{-\frac{1}{2},+}^{V(A);\frac{1}{2}} = H_{\frac{1}{2},-}^{V(A);-\frac{1}{2}} = 0 \,,$$

where the q^2 dependent quantities are expressed in terms of the form factors $F_{0,+,\perp}$ and $G_{0,+,\perp}$ as:

$$a_V = \frac{F_0\sqrt{Q_+}M_-}{\sqrt{q^2}}, \quad b_V = \frac{F_+\sqrt{Q_-}M_+}{\sqrt{q^2}}, \quad c_V = \sqrt{2}F_\perp\sqrt{Q_-},$$

$$a_A = \frac{G_0\sqrt{Q_-}M_+}{\sqrt{q^2}}, \quad b_A = \frac{G_+\sqrt{Q_+}M_-}{\sqrt{q^2}}, \quad c_A = \sqrt{2}G_\perp\sqrt{Q_+}. \tag{2.29}$$

Similarly, the scalar ($H_{\lambda_{\Lambda_c}}^{S;\lambda_{\Lambda_b}}$) and pseudo-scalar ($H_{\lambda_{\Lambda_c}}^{PS;\lambda_{\Lambda_b}}$) amplitudes are given by:

$$H_{\frac{1}{2}}^{S;\frac{1}{2}} = H_{-\frac{1}{2}}^{S;-\frac{1}{2}} = \cos\frac{\theta_{\Lambda_c}}{2}a_S \qquad , H_{-\frac{1}{2}}^{S;\frac{1}{2}} = -H_{\frac{1}{2}}^{S;-\frac{1}{2}} = -\sin\frac{\theta_{\Lambda_c}}{2}a_S \,,$$

$$H_{\frac{1}{2}}^{PS;\frac{1}{2}} = -H_{-\frac{1}{2}}^{PS;-\frac{1}{2}} = -\cos\frac{\theta_{\Lambda_c}}{2}a_P \qquad , H_{-\frac{1}{2}}^{PS;\frac{1}{2}} = H_{\frac{1}{2}}^{PS;-\frac{1}{2}} = -\sin\frac{\theta_{\Lambda_c}}{2}a_P \,,$$

where

$$a_S = \frac{F_0\sqrt{Q_+}M_-}{m_b - m_c}, \quad a_P = \frac{G_0\sqrt{Q_-}M_+}{m_b + m_c}. \tag{2.30}$$

The tensor ($H^{T;\lambda_{\Lambda_b}}_{\lambda_{\Lambda_c},\lambda_W,\lambda'_W}$) and pseudo-tensor ($H^{PT;\lambda_{\Lambda_b}}_{\lambda_{\Lambda_c},\lambda_W,\lambda'_W}$) amplitudes can be expressed as follows:

$$H^{T;\pm\frac{1}{2}}_{\pm\frac{1}{2},t,0} = H^{PT;\pm\frac{1}{2}}_{\pm\frac{1}{2},1,-1} = \cos\frac{\theta_{\Lambda_c}}{2}a_T \qquad ,H^{T;\pm\frac{1}{2}}_{\mp\frac{1}{2},t,0} = H^{PT;\pm\frac{1}{2}}_{\mp\frac{1}{2},1,-1} = \mp\sin\frac{\theta_{\Lambda_c}}{2}a_T\,,$$

$$H^{T;\mp\frac{1}{2}}_{\pm\frac{1}{2},t,\pm1} = H^{PT;\frac{1}{2}}_{-\frac{1}{2},0,-1} = -\cos\frac{\theta_{\Lambda_c}}{2}b_T \qquad ,H^{T;-\frac{1}{2}}_{-\frac{1}{2},t,-1} = H^{PT;\pm\frac{1}{2}}_{\pm\frac{1}{2},0,\pm1} = -\sin\frac{\theta_{\Lambda_c}}{2}b_T\,,$$

$$H^{T;-\frac{1}{2}}_{-\frac{1}{2},0,-1} = H^{PT;\pm\frac{1}{2}}_{\pm\frac{1}{2},t,\pm1} = -\sin\frac{\theta_{\Lambda_c}}{2}c_T \qquad ,H^{T;\mp\frac{1}{2}}_{\pm\frac{1}{2},0,\pm1} = H^{PT;\frac{1}{2}}_{-\frac{1}{2},t,-1} = -\cos\frac{\theta_{\Lambda_c}}{2}c_T\,,$$

$$H^{T;\pm\frac{1}{2}}_{\mp\frac{1}{2},1,-1} = H^{PT;\pm\frac{1}{2}}_{\mp\frac{1}{2},t,0} = -\sin\frac{\theta_{\Lambda_c}}{2}d_T \qquad ,H^{T;\pm\frac{1}{2}}_{\pm\frac{1}{2},1,-1} = H^{PT;\pm\frac{1}{2}}_{\pm\frac{1}{2},t,0} = \mp\cos\frac{\theta_{\Lambda_c}}{2}d_T\,,$$

$$H^{(P)T;\pm\frac{1}{2}}_{-\frac{1}{2},t,1} = H^{(P)T;\pm\frac{1}{2}}_{\frac{1}{2},t,-1} = 0 \qquad ,H^{(P)T;\pm\frac{1}{2}}_{-\frac{1}{2},0,1} = H^{(P)T;\pm\frac{1}{2}}_{\frac{1}{2},0,-1} = 0\,.$$

The remaining (pseudo-)tensor amplitudes can be obtained through the relations:

$$H^{T;\frac{1}{2}}_{\frac{1}{2},t,1} = -H^{T;-\frac{1}{2}}_{-\frac{1}{2},t,-1}\,,\quad H^{T;\frac{1}{2}}_{\frac{1}{2},0,1} = -H^{T;-\frac{1}{2}}_{-\frac{1}{2},0,-1}\,,\quad H^{PT;-\frac{1}{2}}_{\frac{1}{2},t,1} = -H^{PT;\frac{1}{2}}_{-\frac{1}{2},t,-1}\,,H^{PT;-\frac{1}{2}}_{\frac{1}{2},0,1} = -H^{PT;\frac{1}{2}}_{-\frac{1}{2},0,-1}\,,$$

$$H^{(P)T;\lambda_{\Lambda_b}}_{\lambda_{\Lambda_c},\lambda_W,\lambda'_W} = -H^{(P)T;\lambda_{\Lambda_b}}_{\lambda_{\Lambda_c},\lambda'_W,\lambda_W}\,,H^{(P)T;\lambda_{\Lambda_b}}_{\lambda_{\Lambda_c},\lambda_W,\lambda_W} = 0\,.$$

In the above expressions, the q^2 dependent quantities are given in terms of the tensor form factors h_+, $h_\perp$, $\tilde{h}_+$ and $\tilde{h}_\perp$ as:

$$a_T = h_+\sqrt{Q_-}\,,\quad b_T = \frac{\sqrt{2}h_\perp M_+\sqrt{Q_-}}{\sqrt{q^2}}\,,$$

$$c_T = \frac{\sqrt{2}\tilde{h}_\perp M_-\sqrt{Q_+}}{\sqrt{q^2}}\,,d_T = \tilde{h}_+\sqrt{Q_+}\,, \tag{2.31}$$

It is worth noting that when $\theta_{\Lambda_c} = 0$ we recover the expressions as quoted in Ref.[27, 28, 30].

The helicity amplitudes presented in this section are expressed in terms of the form factors $F_{0,+,\perp}$, $G_{0,+,\perp}$, $h_{+,\perp}$ and $\tilde{h}_{+,\perp}$, which are defined in such a way that they correspond to time-like (scalar), longitudinal and transverse polarisation with respect to the momentum-transfer q^μ. An alternate parameterisation of form factors (denoted by $f_{1,2,3}$, $g_{1,2,3}$, $f^T_{1,2}$ and $g^T_{1,2}$) that are based on the large and small projections of massive fermion spinors, can often be found in the literature [27, 28]. The relation between these two form factor parameterisation is given in Appendix B of Ref.[48].

2.B   Leptonic amplitudes of $W^{*-} \to \ell^- \bar{\nu}_l$ decay

In this section, we give the expressions of the leptonic helicity amplitudes for $W^{*-} \to \ell^- \bar{\nu}_l$ decay, shown in Eqs.(2.14–2.16). The choice of the lepton azimuthal angle in the W^* rest frame is now

fixed by $\hat{n}$, *i.e.* the Λ_b polarisation axis (Eq. 2.28):

$$\hat{z}_l = \hat{p}_W^{[\Lambda_b]}, \ \hat{y}_l = \hat{n} \times \hat{z}_l, \ \hat{x}_l = \hat{y}_l \times \hat{z}_l. \tag{2.32}$$

Therefore, the lepton ℓ^- momentum is oriented in the direction (θ_l, ϕ_l) with magnitude p_l, whereas the neutrino $\bar{\nu}_l$ moves in the opposite direction, which is $(\pi - \theta_l, \pi + \phi_l)$ with $p_{\bar{\nu}_l} = p_l$. This frame of reference is depicted in Figure 2.2.

We show below the expressions for helicity spinors of ℓ^- (u_l) with mass m_l, $\bar{\nu}_l$ ($u_{\bar{\nu}_l}$) and polarisation vector of W^{*-} (ϵ^μ) in the above defined frame:

$$\epsilon^\mu(\lambda_W = t) = \begin{pmatrix} 1 \\ 0 \\ 0 \\ 0 \end{pmatrix}, \qquad \epsilon^\mu(\lambda_W = 1) = \begin{pmatrix} 0 \\ \frac{1}{\sqrt{2}} \\ -\frac{i}{\sqrt{2}} \\ 0 \end{pmatrix},$$

$$\epsilon^\mu(\lambda_W = 0) = \begin{pmatrix} 0 \\ 0 \\ 0 \\ -1 \end{pmatrix}, \qquad \epsilon^\mu(\lambda_W = -1) = \begin{pmatrix} 0 \\ -\frac{1}{\sqrt{2}} \\ -\frac{i}{\sqrt{2}} \\ 0 \end{pmatrix},$$

$$u_l\left(\lambda_l = \frac{1}{2}\right) = \begin{pmatrix} \sqrt{m + E_l} \cos\left(\frac{\theta_l}{2}\right) \\ e^{i\phi_l} \sqrt{m + E_l} \sin\left(\frac{\theta_l}{2}\right) \\ \sqrt{E_l - m} \cos\left(\frac{\theta_l}{2}\right) \\ e^{i\phi_l} \sqrt{E_l - m} \sin\left(\frac{\theta_l}{2}\right) \end{pmatrix}, \quad u_l\left(\lambda_l = -\frac{1}{2}\right) = \begin{pmatrix} -e^{-i\phi_l} \sqrt{m + E_l} \sin\frac{\theta_l}{2} \\ \sqrt{m_l + E_l} \cos\frac{\theta_l}{2} \\ e^{-i\phi_l} \sqrt{E_l - m} \sin\frac{\theta_l}{2} \\ -\sqrt{E_l - m_l} \cos\frac{\theta_l}{2} \end{pmatrix},$$

$$v_{\bar{\nu}_l}\left(\lambda_{\bar{\nu}_l} = \frac{1}{2}\right) = \begin{pmatrix} e^{-i\phi_l} \sqrt{p_l} \cos\frac{\theta_l}{2} \\ \sqrt{p_l} \sin\frac{\theta}{2} \\ -e^{-i\phi_l} \sqrt{p_l} \cos\frac{\theta_l}{2} \\ -\sqrt{p_l} \sin\frac{\theta}{2} \end{pmatrix},$$

where

$$p_l = \sqrt{q^2} v^2 / 2, \ E_l = p_l + m_l^2 / \sqrt{q^2}, \ v = \sqrt{1 - \frac{m_l^2}{q^2}}. \tag{2.33}$$

The vector and axial-vector amplitudes ($L^{SM;\lambda_W}_{\lambda_l, \lambda_{\bar{\nu}_l} = \frac{1}{2}}$) are then given by:

$$L^{SM;t}_{\frac{1}{2}} = e^{-i\phi_l} a_l \qquad\qquad , L^{SM;0}_{\frac{1}{2}} = -e^{-i\phi_l} \cos\theta_l a_l \,,$$

$$L^{SM;1}_{\frac{1}{2}} = e^{-2i\phi_l} \sin\theta_l \frac{a_l}{\sqrt{2}} \qquad\qquad , L^{SM;-1}_{\frac{1}{2}} = -\sin\theta_l \frac{a_l}{\sqrt{2}} \,,$$

$$L^{SM;0}_{-\frac{1}{2}} = \sin\theta_l b_l \qquad\qquad , L^{SM;\pm 1}_{\mp \frac{1}{2}} = e^{\mp i\phi_l} (1 \pm \cos\theta_l) \frac{b_l}{\sqrt{2}} \,,$$

$$L^{SM;t}_{-\frac{1}{2}} = 0 \qquad\qquad .$$

The scalar and pseudo-scalar leptonic helicity amplitudes ($L^{S_L}_{\lambda_l}$) become:

$$L^{S_L}_{\frac{1}{2}} = e^{-i\phi_l} b_l \,, \quad L^{S_L}_{-\frac{1}{2}} = 0 \,. \tag{2.34}$$

The tensor amplitudes ($L^{T_L;\lambda_W,\lambda'_W}_{\lambda_l}$) are given by:

$$L^{T_L;t,0}_{-\frac{1}{2}} = L^{T_L;1,-1}_{-\frac{1}{2}} = \sin\theta_l a_l \qquad\qquad , L^{T_L;0,-1}_{-\frac{1}{2}} = L^{T_L;t,-1}_{-\frac{1}{2}} = e^{i\phi_l} (1 - \cos\theta_l) \frac{a_l}{\sqrt{2}} \,,$$

$$L^{T_L;t,1}_{-\frac{1}{2}} = -L^{T_L;0,1}_{-\frac{1}{2}} = e^{-i\phi_l} (1 + \cos\theta_l) \frac{a_l}{\sqrt{2}} \qquad , L^{T_L;t,0}_{\frac{1}{2}} = L^{T_L;1,-1}_{\frac{1}{2}} = -e^{-i\phi_l} \cos\theta_l b_l \,,$$

$$L^{T_L;t,1}_{\frac{1}{2}} = -L^{T_L;0,1}_{\frac{1}{2}} = e^{-2i\phi_l} \sin\theta_l \frac{b_l}{\sqrt{2}} \qquad , L^{T_L;t,-1}_{\frac{1}{2}} = L^{T_L;0,-1}_{\frac{1}{2}} = -\sin\theta_l \frac{b_l}{\sqrt{2}} \,.$$

The rest of the tensor amplitudes can be obtained using the relations:

$$L^{T_L;\lambda_W,\lambda_W}_{\lambda_l} = 0 \,, \quad L^{T_L;\lambda_W,\lambda'_W}_{\lambda_l} = -L^{T_L;\lambda'_W,\lambda_W}_{\lambda_l} \,. \tag{2.35}$$

The q^2 dependent terms that appear in the above equations are given by:

$$a_l = 2m_l v \,, \quad b_l = 2\sqrt{q^2} v \,. \tag{2.36}$$

We note that the relations obtained here match that of Ref.[30] when $\phi_l = 0$. As done in Ref.[30], in the definition of the polarisation vector the Euler angle has been set to $\gamma = -\phi_l$, contrary to $\gamma = 0$ as done in Ref.[14]. As a result, the expressions presented in Ref.[14], differ from ours and those presented in Ref.[30] by an unimportant overall phase factor, $e^{-\pi}$.

2.C   Hadronic amplitudes of $\Lambda_c^+ \to pK_S^0$ decay

In this section, we expand out the Wigner-D elements and provide expressions of the hadronic amplitudes for $\Lambda_c^+ \to pK_S^0$ decay, which is shown in Eqs.(2.17). These amplitudes are defined in the Λ_c^+ rest frame where the choice of azimuthal angle for the proton is fixed by $\hat{n}$ defined in

Eq.(2.28):

$$\hat{z_p} = \hat{p}_{\Lambda_c}^{[\Lambda_b]}, \ \hat{y_p} = \hat{n} \times \hat{z_p}, \ \hat{x_p} = \hat{y_p} \times \hat{z_p}, \tag{2.37}$$

Therefore, in this frame, p momentum is oriented in the direction (θ_p, ϕ_p) with magnitude p_p and K_S^0 moves in the opposite direction *i.e.* $(\pi - \theta_p, \pi + \phi_p)$ with $p_{K_S^0} = p_p$. A transformation from this frame to the frame defined in Eq.(2.32) can be achieved through rotation by angle π about y_p-axis. This frame of reference is depicted in Figure 2.2.

The hadronic amplitudes $(G_{\lambda_p}^{\lambda_{\Lambda_c}})$, in this frame, are then given by [4]

$$G_{\frac{1}{2}}^{\frac{1}{2}} = \cos\frac{\theta_p}{2} g_{\frac{1}{2}} \qquad\qquad , G_{-\frac{1}{2}}^{\frac{1}{2}} = -e^{i\phi_p} \sin\frac{\theta_p}{2} g_{-\frac{1}{2}},$$

$$G_{\frac{1}{2}}^{-\frac{1}{2}} = e^{-i\phi_p} \sin\frac{\theta_p}{2} g_{\frac{1}{2}} \qquad\qquad , G_{-\frac{1}{2}}^{-\frac{1}{2}} = \cos\frac{\theta_p}{2} g_{-\frac{1}{2}}.$$

2.D Phase space

The differential decay rate can be written as:

$$d\Gamma = \frac{|T|^2}{2m_{\Lambda_b}} d\Phi_4(P_{\Lambda_b}; P_p, P_{K_S^0}, P_l, P_{\bar{\nu}_l}) \tag{2.38}$$

where T denotes the complex transition amplitude, 'P_A' is the four-momentum of the particle 'A' in Λ_b rest frame, m_{Λ_b} is mass of Λ_b^0 and $d\Phi_4$ is the four-body phase space element that can be written as the product of two-body phase space elements as follows:

$$d\Phi_4 = (2\pi)^4 \delta^{(4)}(P_{\Lambda_b} - \sum_i^4 P_i) \prod_{i=1}^4 \frac{d^3 p_i}{(2\pi)^3 2E_i}$$

$$= \frac{dm_{pK_S^0}^2}{2\pi} \frac{dq^2}{2\pi} d\Phi_2(P_{\Lambda_b}; P_{\Lambda_c}, q) \, d\Phi_2(P_{\Lambda_c}; \hat{P}_p, \hat{P}_{K_S^0}) \, d\Phi_2(q; \hat{P}_l, \hat{P}_{\bar{\nu}_l}).$$

Here $m_{pK_S^0}^2 = (P_p + P_{K_S^0})^2$, $q^2 = (P_l + P_{\bar{\nu}_l})^2$ and ^denotes that the four-momenta are now defined in the rest frame of the parent particle. The two-body phase space is given by:

$$d\Phi_2(\hat{P}_i, \hat{P}_j) = \frac{1}{2^4 \pi^2} \frac{p_i}{m_{ij}} d\cos\theta_i \, d\phi_i,$$

---

[4] We employ Wigner sign convention, where Wigner-D elements are defined as $D_{m',m}^J(\alpha, \beta, \gamma) = e^{-im'\alpha} d_{m',m}^J(\beta) e^{-im\gamma}$ with the property $D_{m',m}^{J*}(\alpha, \beta, \gamma) = (-1)^{m'-m} D_{-m',-m}^J(\gamma, \beta, \alpha)$, where α, β, γ are Euler angles and $d_{m',m}^J(\beta)$ are small-d Wigner elements.

where p_i denotes the magnitude of three-momentum of particle i in the ij rest frame. The full four-body phase space element then becomes:

$$d\Phi_4 = \frac{1}{2^{14}\pi^8} dm^2_{\mathrm{pK}_S^0} dq^2 \frac{p_{\Lambda_c}}{m_{\Lambda_b}} d\cos\theta_{\Lambda_c} d\phi_{\Lambda_c} \frac{p_p}{m_{\mathrm{pK}_S^0}} d\cos\theta_p d\phi_p \frac{p_l}{\sqrt{q^2}} d\cos\theta_l d\phi_l, \tag{2.39}$$

where p_{Λ_c}, p_{p}, p_l with their corresponding angles are defined in the Λ_b^0, Λ_c^+ and W^{*-} rest frames, respectively. These momenta can be expressed as:

$$p_{\Lambda_c} = \frac{\sqrt{\lambda(m^2_{\Lambda_b}, m^2_{\mathrm{pK}_S^0}, q^2)}}{2m_{\Lambda_b}} \quad p_{\mathrm{p}} = \frac{\sqrt{\lambda(m^2_{\mathrm{pK}_S^0}, m^2_{\mathrm{p}}, m^2_{\mathrm{K}_S^0})}}{2m_{\mathrm{pK}_S^0}} \quad p_l = \frac{q^2 - m^2_l}{2\sqrt{q^2}}, \tag{2.40}$$

where $\lambda(a,b,c) = a^2 + b^2 + c^2 - 2(ab + ac + bc)$.

The differential density shown in Eq.(2.38) then becomes:

$$d\Gamma_{4-body} = \frac{p_{\Lambda_c} \, p_p \, p_l}{2^{15}\pi^8 m^2_{\Lambda_b} m_{\mathrm{pK}_S^0} \sqrt{q^2}} \, |T|^2 d\Omega. \tag{2.41}$$

where $d\Omega = dm^2_{\mathrm{pK}_S^0} dq^2 d\cos\theta_{\Lambda_c} d\phi_{\Lambda_c} d\cos\theta_p d\phi_p d\cos\theta_l d\phi_l$.

In the main text, it is highlighted that the choice of ϕ_{Λ_c} is arbitrary and has been set to zero, removing its dependence from $|T|^2$. It can also be seen in Eq.(2.7) that, for a given helicity of initial and final state, $|T|^2$ would have dependence on $m^2_{\mathrm{pK}_S^0}$ through the propagation terms $BW_{\Lambda_c} BW^\dagger_{\Lambda_c}$. Since the total width of Λ_c^+ is far below its mass ($\Gamma_{\Lambda_c} << m_{\Lambda_c}$), we can use here the narrow width approximation to give:

$$BW_{\Lambda_c} BW^\dagger_{\Lambda_c} = \frac{\pi}{m_{\Lambda_c}\Gamma_{\Lambda_c}} \delta(m^2_{\mathrm{pK}_S^0} - m^2_{\Lambda_c}). \tag{2.42}$$

We can also factor out the term $(|g_{+\frac{1}{2}}|^2 + |g_{-\frac{1}{2}}|^2)$ from $|T|^2$ and normalise Λ_c^+ decay density using the relation:

$$\frac{p_p}{2^6 \pi^2 m^2_{\Lambda_c}} \left(|g_{+\frac{1}{2}}|^2 + |g_{-\frac{1}{2}}|^2\right) = \frac{\mathcal{B}_{\Lambda_c}\Gamma_{\Lambda_c}}{4\pi}. \tag{2.43}$$

Substituting all the above three relations in Eq.(2.41) and integrating over $m^2_{\mathrm{pK}_S^0}$ and ϕ_{Λ_c}, the differential decay density becomes:

$$d\Gamma_{4-body} = \frac{p_l \, \mathcal{B}_{\Lambda_c} \, [p_{\Lambda_c}]^{m^2_{\mathrm{pK}_S^0} = m^2_{\Lambda_c}}}{2^{10}\pi^5 m^2_{\Lambda_b} \sqrt{q^2}} \, |T|^2 d\Omega', \tag{2.44}$$

where $d\Omega' = dq^2 d\cos\theta_{\Lambda_c} d\cos\theta_p d\phi_p d\cos\theta_l d\phi_l$ and $\mathcal{B}_{\Lambda_c}$ denotes the branching fraction of $\Lambda_c^+ \to \mathrm{pK}_S^0$ decay.

When the Λ_b^0 is unpolarised ($P_{\Lambda_b} = 0$), it is clear from Eq.(2.22), that the dependence of $|T|^2$ on

θ_{Λ_c} is inherently removed. Also the choice of the azimuthal angle ϕ_p that was previously fixed by the definition of the Λ_b^0 polarisation axis ($\hat{n}$), now becomes arbitrary. We therefore set the Λ_c^+ helicity frame (x_p, y_p, z_p) in such a way that angle $\phi_p = 0$, *i.e.* the proton momentum always lies in the x_p–z_p plane and, as before, $\hat{x}_l = -\hat{x}_p$. In this case, the differential decay density becomes:

$$d\Gamma_{4-body} = \frac{p_l \; \mathcal{B}_{\Lambda_c} [p_{\Lambda_c}]^{m^2_{pK_S^0} = m^2_{\Lambda_c}}}{2^8 \pi^4 m^2_{\Lambda_b} \sqrt{q^2}} \left[|T|^2\right]^{P_{\Lambda_b}=0, \phi_p=0} d\Omega'' , \qquad (2.45)$$

where $d\Omega'' = dq^2 d\cos\theta_p d\cos\theta_l d\phi_l$. Note that with the choice of $\phi_p = 0$, one can also express angle ϕ_l (Figure 2.2) in terms of the relative angle between the (pK_S^0) and $(\ell^- \bar{\nu}_l)$ decay planes, χ. Either of the two relations that are often employed in the literature can be used, *i.e.* either $\phi_l = \pi + mod(2\pi) - \chi$ [49] or $\phi_l = \chi$ [14] (However, when chosen the definition should be adopted consistently throughout the analysis).

When integrating out the Λ_c^+ dynamics, the three-body phase space element is considered. This case is very similar to setting Λ_c^+ decay asymmetry to zero ($\alpha_{\Lambda_c} = 0$), where the dependency of $|T|^2$ on $\cos\theta_p$ and ϕ_p is inherently removed. The differential decay density then takes the form:

$$d\Gamma_{3-body} = \frac{p_{\Lambda_c} p_l}{2^9 \pi^4 m^2_{\Lambda_b} \sqrt{q^2}} \left[|T|^2\right]^{\alpha_{\Lambda_c}=0} d\Omega''' , \qquad (2.46)$$

where $d\Omega''' = dq^2 d\cos\theta_{\Lambda_c} d\cos\theta_l d\phi_l$. The choice of angle ϕ_l in the above case is now fixed through the choice of W^{*-} helicity frame, defined with respect to the Λ_b^0 polarisation plane (*i.e.* $\hat{y}_l = \hat{n} \times \hat{p}_{\Lambda_c}$). Additionally, if Λ_b^0 is unpolarised, the dependence of $\left[|T|^2\right]^{\alpha_{\Lambda_c}=0}$ on $\cos\theta_{\Lambda_c}$ and ϕ_l is inherently removed, leaving the dependence of decay density on only q^2 and $\cos\theta_l$ (with an additional factor 4π from integration over the element $d\cos\theta_{\Lambda_c} d\phi_l$).

2.E   Terms of differential decay density

We present below explicit expressions for K_i terms defined in the full angular differential density in Eq.(2.22):

$$
\begin{aligned}
K_1 = \frac{1}{8}\Bigg[& \cos\theta_p (\widehat{|g_{-\frac{1}{2}}|^2} - \widehat{|g_{+\frac{1}{2}}|^2})\Big\{ -2(1-\cos^2\theta_l)(|I_1|^2 - 2|I_8|^2) - 2|I_4|^2(\cos\theta_l + 1)^2 + \\
& 2I_5^*(I_5(2\cos^2\theta_l - 1) + 2I_9\cos\theta_l) + 4I_9^*(I_5\cos\theta_l + I_9)\Big\} + 4\cos\theta_l \\
& \Big\{|I_4|^2 + I_9 I_5^* + I_5 I_9^*\Big\} + 2|I_5|^2\Big\{\widehat{|g_{-\frac{1}{2}}|^2}(\cos\theta_p + 1) - \widehat{|g_{+\frac{1}{2}}|^2}\cos\theta_p\Big\} + \widehat{|g_{-\frac{1}{2}}|^2}\Big\{|I_1|^2 + 3|I_4|^2 + \\
& 2|I_8|^2 + 4|I_9|^2\Big\} + \widehat{|g_{+\frac{1}{2}}|^2}\Big\{|I_1|^2 + 3|I_4|^2 + 2|I_5|^2 + 2|I_8|^2 + 4|I_9|^2\Big\} + (2\cos^2\theta_l - 1) \\
& \Big\{-|I_1|^2 + |I_4|^2 + 2|I_5|^2 - 2|I_8|^2\Big\}\Bigg] + \frac{1}{2\sqrt{2}}\Bigg[e^{-i(\phi_l + \phi_p)}\sqrt{1-\cos^2\theta_l}\sqrt{1-\cos^2\theta_p} \\
& (\widehat{|g_{-\frac{1}{2}}|^2} - \widehat{|g_{+\frac{1}{2}}|^2})\Big\{e^{2i\phi_l}I_1^*(I_5\cos\theta_l + I_9) - e^{2i\phi_l}I_8 I_4^*(\cos\theta_l + 1) + \\
& e^{2i\phi_p}(I_1(I_5^*\cos\theta_l + I_9^*) - I_4 I_8^*(\cos\theta_l + 1))\Big\}\Bigg].
\end{aligned}
$$

$$
\begin{aligned}
K_2 = \frac{1}{16}\Bigg[& 2\widehat{|g_{-\frac{1}{2}}|^2}\Big\{4(1-\cos\theta_p)\Big(I_6^*\cos\theta_l(I_6\cos\theta_l + I_{10}) + |I_7|^2(1-\cos^2\theta_l)\Big) - \\
& 4I_{10}^*(\cos\theta_p - 1)(I_6\cos\theta_l + I_{10}) + 2(\cos\theta_p + 1)\Big(|I_2|^2(1-\cos^2\theta_l) + |I_3|^2 \\
& (1-\cos\theta_l)^2\Big)\Big\} + e^{-i\phi_l}\Big\{4\sqrt{2}\sqrt{1-\cos^2\theta_l}\sqrt{1-\cos^2\theta_p}(\widehat{|g_{-\frac{1}{2}}|^2} - \widehat{|g_{+\frac{1}{2}}|^2}) \\
& \Big(-e^{2i\phi_l - i\phi_p}\Big\{I_2 I_6^*\cos\theta_l + I_3 I_7^*(\cos\theta_l - 1) + I_2 I_{10}^*\Big\} - e^{i\phi_p}\Big\{I_2^*(I_6\cos\theta_l + I_{10}) + \\
& I_7 I_3^*(\cos\theta_l - 1)\Big\}\Big) + 4e^{i\phi_l}\widehat{|g_{+\frac{1}{2}}|^2}\Big(2(\cos\theta_p + 1)(I_6\cos\theta_l + I_{10}) \\
& (I_6^*\cos\theta_l + I_{10}^*) + (1-\cos^2\theta_l)\Big\{I_2^*(I_2 - I_2\cos\theta_p) + 2|I_7|^2(\cos\theta_p + 1)\Big\} + \\
& |I_3|^2(1-\cos\theta_l)^2(1-\cos\theta_p)\Big)\Big\}\Bigg].
\end{aligned}
$$

$$K_3 = \frac{1}{16}\left[4e^{-i(2\phi_l+\phi_p)}\sqrt{1-\cos^2\theta_p}(\widehat{|g_{-\frac{1}{2}}|^2} - \widehat{|g_{+\frac{1}{2}}|^2})\left\{e^{2i\phi_p}\left((1-\cos^2\theta_l)(I_1 I_2^* - I_4 I_3^*)-\right.\right.\right.$$

$$\left.2e^{2i\phi_l}\left\{(I_6\cos\theta_l + I_{10})(I_5^*\cos\theta_l + I_9^*) - I_7 I_8^*(1-\cos^2\theta_l)\right\}\right)+$$

$$\left.\left.e^{2i\phi_l}\left(-2(I_5\cos\theta_l + I_9)(I_6^*\cos\theta_l + I_{10}^*) + (1-\cos^2\theta_l)\left\{2I_8 I_7^* + e^{2i\phi_l}(I_2 I_1^* - I_3 I_4^*)\right\}\right)\right\}+$$

$$4\sqrt{2}e^{-i\phi_l}\sqrt{1-\cos^2\theta_l}\cos\theta_p(\widehat{|g_{-\frac{1}{2}}|^2} - \widehat{|g_{+\frac{1}{2}}|^2})\left\{e^{2i\phi_l}\left(I_1^*(I_6\cos\theta_l + I_{10})+\right.\right.$$

$$\left.I_2(I_5^*\cos\theta_l + I_9^*) - I_3 I_8^*(\cos\theta_l - 1) + I_7 I_4^*(\cos\theta_l + 1)\right) + \cos\theta_l\left(I_1 I_6^* + I_5 I_2^*-\right.$$

$$\left.\left.I_8 I_3^* + I_4 I_7^*\right) + I_1 I_{10}^* + I_9 I_2^* + I_8 I_3^* + I_4 I_7^*\right\} + 4\sqrt{2}e^{-i\phi_l}\sqrt{1-\cos^2\theta_l}$$

$$\left\{e^{2i\phi_l}\left(-I_1^*(I_6\cos\theta_l + I_{10}) + I_2(I_5^*\cos\theta_l + I_9^*) - I_3 I_8^*(\cos\theta_l - 1) - I_7 I_4^*(\cos\theta_l + 1)\right)+\right.$$

$$\left.\left.\cos\theta_l\left(-I_1 I_6^* + I_5 I_2^* - I_8 I_3^* - I_4 I_7^*\right) - I_1 I_{10}^* + I_9 I_2^* + I_8 I_3^* - I_4 I_7^*\right\}\right].$$

In the above expression, the normalised helicity amplitudes for Λ_c^+ decay, $\widehat{|g_{-\frac{1}{2}}|^2}$ and $\widehat{|g_{+\frac{1}{2}}|^2}$, can be expressed in terms of the Λ_c^+ weak decay asymmetry parameter given by Eq.(2.18).

In all the above expressions the I_i depend on the complex Wilson coefficients and terms that are functions of q^2, *i.e.*:

$$I_1 = a_l c_A (1 + C_{V_L} - C_{V_R}) - a_l c_V (1 + C_{V_L} + C_{V_R}) - 4b_l(b_T + c_T)C_{T_L},$$
$$I_2 = a_l c_A (1 + C_{V_L} - C_{V_R}) + a_l c_V (1 + C_{V_L} + C_{V_R}) + 4b_l(b_T - c_T)C_{T_L},$$
$$I_3 = b_l c_A (1 + C_{V_L} - C_{V_R}) + b_l c_V (1 + C_{V_L} + C_{V_R}) + 4a_l(b_T - c_T)C_{T_L},$$
$$I_4 = b_l c_A (1 + C_{V_L} - C_{V_R}) - b_l c_V (1 + C_{V_L} + C_{V_R}) - 4a_l(b_T + c_T)C_{T_L},$$
$$I_5 = a_l b_A (1 + C_{V_L} - C_{V_R}) + a_l b_V (1 + C_{V_L} + C_{V_R}) + 4b_l(a_T - d_T)C_{T_L},$$
$$I_6 = a_l b_A (1 + C_{V_L} - C_{V_R}) - a_l b_V (1 + C_{V_L} + C_{V_R}) - 4b_l(a_T + d_T)C_{T_L},$$
$$I_7 = -b_A b_l (1 + C_{V_L} - C_{V_R}) + b_l b_V (1 + C_{V_L} + C_{V_R}) + 4a_l(a_T + d_T)C_{T_L},$$
$$I_8 = b_A b_l (1 + C_{V_L} - C_{V_R}) + b_l b_V (1 + C_{V_L} + C_{V_R}) + 4a_l(a_T - d_T)C_{T_L},$$
$$I_9 = a_A a_l (1 + C_{V_L} - C_{V_R}) + a_l a_V (1 + C_{V_L} + C_{V_R}) - a_P b_l(C_{S_L} - C_{S_R}) + a_S b_l(C_{S_L} + C_{S_R}),$$
$$I_{10} = a_A a_l (1 + C_{V_L} - C_{V_R}) - a_l a_V (1 + C_{V_L} + C_{V_R}) - a_P b_l(C_{S_L} - C_{S_R}) - a_S b_l(C_{S_L} + C_{S_R}). \tag{2.47}$$

Here the q^2 dependent terms $a_{V,A,S,P,T,l}$, $b_{V,A,T,l}$, $c_{V,A,T}$ and d_T are defined in Eqs.(2.29),(2.30),(2.31) and (2.36). Note that in literature [28, 50], the relations $(C_{S_L} - C_{S_R}) = g_P$, $(C_{S_L} + C_{S_R}) = g_S$,

$(C_{V_R} - C_{V_L}) = g_A$ and $(C_{V_R} + C_{V_L}) = g_V$ are often used.

2.F Decay density for two considered cases

For the first case studied in this paper, we present below the decay density as a function of q^2 and $\cos\theta_l$, after integrating Eq.(2.19) over all other phase space variables:

$$
\frac{d^2\Gamma}{dq^2\, d\cos\theta_l} = \frac{N}{\Gamma}\bigg[2\pi^2 \bigg\{ \cos\theta_l \bigg(-2\cos\theta_l(|I_7|^2 + |I_8|^2) + 2I_6^*(\cos\theta_l I_6 + I_{10}) - \cos\theta_l I_2 I_2^* +
$$

$$
(\cos\theta_l - 2)I_3 I_3^* + (\cos\theta_l + 2)I_4 I_4^* + 2I_5^*(\cos\theta_l I_5 + I_9) \bigg) + |I_2|^2 + |I_3|^2 + |I_4|^2 +
$$

$$
I_1^*(I_1 - \cos\theta_l^2 I_1) + 2I_{10}^*(\cos\theta_l I_6 + I_{10}) + 2I_9^*(\cos\theta_l I_5 + I_9) + 2I_7 I_7^* + 2I_8 I_8^* \bigg\} \bigg],
$$

$$
(2.48)
$$

where the q^2 dependent terms I_i are defined Eqs.(2.47). It can be seen from the above equation that the decay density is independent of P_{Λ_b} and α_{Λ_c}. The shape of this decay density is similar to the case when Λ_c^+ is considered stable and Λ_b^0 is unpolarised.

For the second case studied in this paper, we present below the decay density as a function of q^2, $\cos\theta_l$, $\cos\theta_p$ and ϕ_p, after integrating Eq.(2.19) over all other phase space variables

$$
\begin{aligned}
\frac{d^4\Gamma}{d\omega} = \frac{N}{\Gamma}\Bigg[\frac{1}{8}\pi\Bigg\{ & -\alpha_{\Lambda_c}\sqrt{1-\cos\theta_p^2}\,e^{-i\phi_p}P_{\Lambda_b}\Bigg(-2\pi e^{2i\phi_p}\Big\{ (\cos\theta_l^2-1)I_7 I_8^* \\
& + (\cos\theta_l I_6 + I_{10})(\cos\theta_l I_5^* + I_9^*)\Big\} - 2\pi(\cos\theta_l^2-1)I_8 I_7^* \\
& - 2\pi(\cos\theta_l I_5 + I_9)(\cos\theta_l I_6^* + I_{10}^*)\Bigg) - 4(\cos\theta_l^2-1)|I_1|^2(\alpha_{\Lambda_c}\cos\theta_p+1) \\
& + 4\alpha_{\Lambda_c}\cos\theta_l^2\cos\theta_p|I_2|^2 - 4\alpha_{\Lambda_c}\cos\theta_l^2\cos\theta_p|I_3|^2 \\
& - 8(\alpha_{\Lambda_c}\cos\theta_p-1)\Bigg(|I_8|^2(1-\cos\theta_l^2) + \cos\theta_l I_5^*(\cos\theta_l I_5 + I_9) \\
& + I_9^*(\cos\theta_l I_5 + I_9)\Bigg) + 8\alpha_{\Lambda_c}\cos\theta_l^2\cos\theta_p|I_6|^2 - 8\alpha_{\Lambda_c}\cos\theta_l^2\cos\theta_p|I_7|^2 \\
& + 8\alpha_{\Lambda_c}\cos\theta_l\cos\theta_p I_6 I_{10}^* + 8\alpha_{\Lambda_c}\cos\theta_l\cos\theta_p I_{10}I_6^* + 8\alpha_{\Lambda_c}\cos\theta_l\cos\theta_p|I_3|^2 \\
& + 4(\cos\theta_l+1)^2|I_4|^2(\alpha_{\Lambda_c}\cos\theta_p+1) + 8\alpha_{\Lambda_c}\cos\theta_p|I_{10}|^2 - 4\alpha_{\Lambda_c}\cos\theta_p|I_2|^2 \\
& - 4\alpha_{\Lambda_c}\cos\theta_p|I_3|^2 + 8\alpha_{\Lambda_c}\cos\theta_p|I_7|^2 - 4\cos\theta_l^2|I_2|^2 + 4\cos\theta_l^2|I_3|^2 \\
& + 8\cos\theta_l^2|I_6|^2 - 8\cos\theta_l^2|I_7|^2 + 8\cos\theta_l I_6 I_{10}^* + 8\cos\theta_l I_{10}I_6^* \\
& - 8\cos\theta_l|I_3|^2 + 8|I_{10}|^2 + 4|I_2|^2 + 4|I_3|^2 + 8|I_7|^2 \Bigg\}\Bigg],
\end{aligned}
\tag{2.49}
$$

where $d\omega = dq^2 d\cos\theta_l d\cos\theta_p d\phi_p$ and the q^2 dependent terms I_i are defined Eqs.(2.47). In the above equation, ϕ_p dependence is removed when either P_{Λ_b} or α_{Λ_c} is zero. The $\cos\theta_p$ dependence on the above equation only exists when α_{Λ_c} is non-zero.

2.G   Response Matrix

In this section the migration/response matrix is discussed, which is convolved with the fit model to account for finite resolution effects on q^2 and $\cos\theta_l$ variables. It is a four dimensional object that is a function of the reconstructed and true variables. To obtain this matrix, we generate a signal sample according to SM using PYTHIA [42, 43] and require that the signal events lie within the LHCb acceptance of $2 < \eta < 5$. The Λ_b^0 vertex position is then smeared according the resolution discussed in Ref. [44]. To avoid any model dependence, we bin the reconstructed and true variables very finely. In this study a binning scheme of $20 \times 20 \times 20 \times 20$ is employed.

The migration matrix of reconstructed (q^2_{rec}, $\cos(\theta_l)_{reco}$) versus true (q^2_{true},$\cos(\theta_l)_{true}$) variables is illustrated in Figure 2.G.1, where the 2D projections are shown. The effect of migration is pretty uniform for the q^2 variable except for the corners. On the contrary, for $\cos(\theta_l)$ the migration

effects are prominent at lower $\cos(\theta_l)_{reco}$ and $\cos(\theta_l)_{true}$ values. In Figure 2.G.2, the effects of migration on SM-like Monte Carlo sample are illustrated.
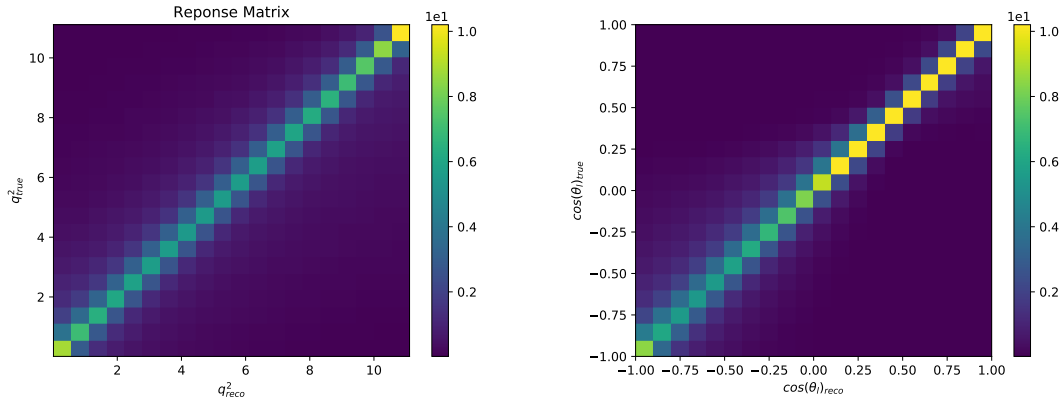
FIGURE 2.G.1: 2D projection of the 4D migration matrix of reconstructed versus true variables for (left) q^2 and (right) $\cos(\theta_l)$.
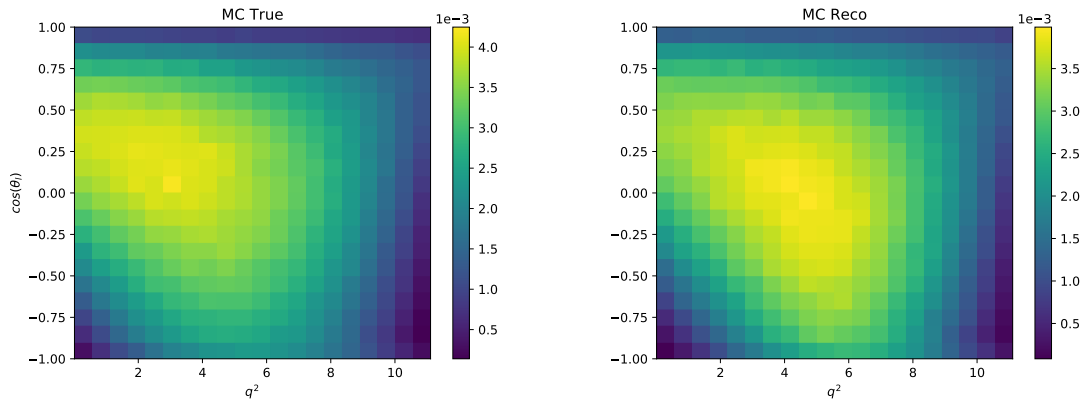
FIGURE 2.G.2: (Left) The true distribution of q^2 and $\cos(\theta_l)$ generated according to SM and (right) the result of the convolution of the true distribution with the migration matrix.

References

[1] J. P. Lees et al. "Evidence for an excess of $\bar{B} \to D^{(*)}\tau^-\bar{\nu}_\tau$ decays". In: *Phys. Rev. Lett.* 109 (2012), p. 101802. DOI: 10.1103/PhysRevLett.109.101802. arXiv: 1205.5442 [hep-ex].

[2] J. P. Lees et al. "Measurement of an Excess of $\bar{B} \to D^{(*)}\tau^-\bar{\nu}_\tau$ Decays and Implications for Charged Higgs Bosons". In: *Phys. Rev. D* 88.7 (2013), p. 072012. DOI: 10.1103/PhysRevD.88.072012. arXiv: 1303.0571 [hep-ex].

[3] M. Huschle et al. "Measurement of the branching ratio of $\bar{B} \to D^{(*)}\tau^-\bar{\nu}_\tau$ relative to $\bar{B} \to D^{(*)}\ell^-\bar{\nu}_\ell$ decays with hadronic tagging at Belle". In: *Phys. Rev. D* 92.7 (2015), p. 072014. DOI: 10.1103/PhysRevD.92.072014. arXiv: 1507.03233 [hep-ex].

[4] Y. Sato et al. "Measurement of the branching ratio of $\bar{B}^0 \to D^{*+}\tau^-\bar{\nu}_\tau$ relative to $\bar{B}^0 \to D^{*+}\ell^-\bar{\nu}_\ell$ decays with a semileptonic tagging method". In: *Phys. Rev. D* 94.7 (2016), p. 072007. DOI: 10.1103/PhysRevD.94.072007. arXiv: 1607.07923 [hep-ex].

[5] S. Hirose et al. "Measurement of the τ lepton polarization and $R(D^*)$ in the decay $\bar{B} \to D^*\tau^-\bar{\nu}_\tau$". In: *Phys. Rev. Lett.* 118.21 (2017), p. 211801. DOI: 10.1103/PhysRevLett.118.211801. arXiv: 1612.00529 [hep-ex].

[6] Roel Aaij et al. "Measurement of the ratio of branching fractions $\mathcal{B}(\bar{B}^0 \to D^{*+}\tau^-\bar{\nu}_\tau)/\mathcal{B}(\bar{B}^0 \to D^{*+}\mu^-\bar{\nu}_\mu)$". In: *Phys. Rev. Lett.* 115.11 (2015). [Erratum: Phys.Rev.Lett. 115, 159901 (2015)], p. 111803. DOI: 10.1103/PhysRevLett.115.111803. arXiv: 1506.08614 [hep-ex].

[7] R. Aaij et al. "Measurement of the ratio of the $B^0 \to D^{*-}\tau^+\nu_\tau$ and $B^0 \to D^{*-}\mu^+\nu_\mu$ branching fractions using three-prong τ-lepton decays". In: *Phys. Rev. Lett.* 120.17 (2018), p. 171802. DOI: 10.1103/PhysRevLett.120.171802. arXiv: 1708.08856 [hep-ex].

[8] A. Abdesselam et al. "Measurement of $\mathcal{R}(D)$ and $\mathcal{R}(D^*)$ with a semileptonic tagging method". In: (Apr. 2019). arXiv: 1904.08794 [hep-ex].

[9] M. Tanaka. "Charged Higgs effects on exclusive semitauonic B decays". In: *Z. Phys. C* 67 (1995), pp. 321–326. DOI: 10.1007/BF01571294. arXiv: hep-ph/9411405.

[10] Sacha Davidson, David C. Bailey, and Bruce A. Campbell. "Model independent constraints on leptoquarks from rare processes". In: *Z. Phys. C* 61 (1994), pp. 613–644. DOI: 10.1007/BF01552629. arXiv: hep-ph/9309310.

[11] W. Buchmuller, R. Ruckl, and D. Wyler. "Leptoquarks in Lepton - Quark Collisions". In: *Phys. Lett. B* 191 (1987). [Erratum: Phys.Lett.B 448, 320–320 (1999)], pp. 442–448. DOI: 10.1016/0370-2693(87)90637-X.

[12] Zoltan Ligeti, Michele Papucci, and Dean J. Robinson. "New Physics in the Visible Final States of $B \rightarrow D^{(*)}\tau\nu$". In: *JHEP* 01 (2017), p. 083. DOI: 10.1007/JHEP01(2017)083. arXiv: 1610.02045 [hep-ph].

[13] Minoru Tanaka and Ryoutaro Watanabe. "New physics in the weak interaction of $\bar{B} \rightarrow D^{(*)}\tau\bar{\nu}$". In: *Phys. Rev. D* 87.3 (2013), p. 034028. DOI: 10.1103/PhysRevD.87.034028. arXiv: 1212.1878 [hep-ph].

[14] Damir Bečirević et al. "Lepton Flavor Universality tests through angular observables of $\overline{B} \rightarrow D^{(*)}\ell\overline{\nu}$ decay modes". In: (July 2019). arXiv: 1907.02257 [hep-ph].

[15] Murugeswaran Duraisamy and Alakabha Datta. "The Full $B \rightarrow D^*\tau^-\bar{\nu}_\tau$ Angular Distribution and CP violating Triple Products". In: *JHEP* 09 (2013), p. 059. DOI: 10.1007/JHEP09(2013)059. arXiv: 1302.7031 [hep-ph].

[16] Donal Hill et al. "Model-independent method for measuring the angular coefficients of $B^0 \rightarrow D^{*-}\tau^+\nu_\tau$ decays". In: *JHEP* 11 (2019), p. 133. DOI: 10.1007/JHEP11(2019)133. arXiv: 1908.04643 [hep-ph].

[17] Atasi Ray, Suchismita Sahoo, and Rukmani Mohanta. "Model independent analysis of $B^* \rightarrow P\ell\bar{\nu}_\ell$ decay processes". In: *Eur. Phys. J. C* 79.8 (2019), p. 670. DOI: 10.1140/epjc/s10052-019-7183-8. arXiv: 1907.13586 [hep-ph].

[18] Ashutosh Kumar Alok et al. "Resolution of R_D/R_{D^*} puzzle". In: *Phys. Lett. B* 784 (2018), pp. 16–20. DOI: 10.1016/j.physletb.2018.07.001. arXiv: 1804.08078 [hep-ph].

[19] Clara Murgui et al. "Global fit to $b \rightarrow c\tau\nu$ transitions". In: *JHEP* 09 (2019), p. 103. DOI: 10.1007/JHEP09(2019)103. arXiv: 1904.09311 [hep-ph].

[20] Ashutosh Kumar Alok et al. "New physics solutions for R_D and R_{D^*}". In: *JHEP* 09 (2018), p. 152. DOI: 10.1007/JHEP09(2018)152. arXiv: 1710.04127 [hep-ph].

[21] Ashutosh Kumar Alok et al. "Solutions to R_D-R_{D^*} in light of Belle 2019 data". In: *Nucl. Phys. B* 953 (2020), p. 114957. DOI: 10.1016/j.nuclphysb.2020.114957. arXiv: 1903.10486 [hep-ph].

[22] Martin Jung and David M. Straub. "Constraining new physics in $b \rightarrow c\ell\nu$ transitions". In: *JHEP* 01 (2019), p. 009. DOI: 10.1007/JHEP01(2019)009. arXiv: 1801.01112 [hep-ph].

[23] Florian U. Bernlochner et al. "New predictions for $\Lambda_b \rightarrow \Lambda_c$ semileptonic decays and tests of heavy quark symmetry". In: *Phys. Rev. Lett.* 121.20 (2018), p. 202001. DOI: 10.1103/PhysRevLett.121.202001. arXiv: 1808.09464 [hep-ph].

[24] William Detmold, Christoph Lehner, and Stefan Meinel. "$\Lambda_b \rightarrow p\ell^-\overline{\nu}_\ell$ and $\Lambda_b \rightarrow \Lambda_c\ell^-\overline{\nu}_\ell$ form factors from lattice QCD with relativistic heavy quarks". In: *Phys. Rev. D* 92 (3 Aug. 2015), p. 034503. DOI: 10.1103/PhysRevD.92.034503. URL: https://link.aps.org/doi/10.1103/PhysRevD.92.034503.

[25] Florian U. Bernlochner et al. "Precise predictions for $\Lambda_b \rightarrow \Lambda_c$ semileptonic decays". In: *Phys. Rev. D* 99.5 (2019), p. 055008. DOI: 10.1103/PhysRevD.99.055008. arXiv: 1812.07593 [hep-ph].

[26] R. Aaij et al. "Measurement of the shape of the $\Lambda_b^0 \to \Lambda_c^+ \mu^- \overline{\nu}_\mu$ differential decay rate". In: *Phys. Rev.* D96 (2017), p. 112005. DOI: 10.1103/PhysRevD.96.112005. arXiv: 1709.01920 [hep-ex].

[27] Atasi Ray, Suchismita Sahoo, and Rukmani Mohanta. "Probing new physics in semileptonic Λ_b decays". In: *Phys. Rev. D* 99.1 (2019), p. 015015. DOI: 10.1103/PhysRevD.99.015015. arXiv: 1812.08314 [hep-ph].

[28] Xin-Qiang Li, Ya-Dong Yang, and Xin Zhang. "$\Lambda_b \to \Lambda_c \tau \overline{\nu}_\tau$ decay in scalar and vector leptoquark scenarios". In: *JHEP* 02 (2017), p. 068. DOI: 10.1007/JHEP02(2017)068. arXiv: 1611.01635 [hep-ph].

[29] E. Di Salvo, F. Fontanelli, and Z. J. Ajaltouni. "Detailed Study of the Decay $\Lambda_b \to \Lambda_c \tau \bar{\nu}_\tau$". In: *Int. J. Mod. Phys. A* 33.29 (2018), p. 1850169. DOI: 10.1142/S0217751X18501695. arXiv: 1804.05592 [hep-ph].

[30] Alakabha Datta et al. "Phenomenology of $\Lambda_b \to \Lambda_c \tau \overline{\nu}_\tau$ using lattice QCD calculations". In: *JHEP* 08 (2017), p. 131. DOI: 10.1007/JHEP08(2017)131. arXiv: 1702.02243 [hep-ph].

[31] Rupak Dutta. "$\Lambda_b \to (\Lambda_c, p) \tau \nu$ decays within standard model and beyond". In: *Phys. Rev. D* 93.5 (2016), p. 054003. DOI: 10.1103/PhysRevD.93.054003. arXiv: 1512.04034 [hep-ph].

[32] Shanmuka Shivashankara, Wanwei Wu, and Alakabha Datta. "$\Lambda_b \to \Lambda_c \tau \bar{\nu}_\tau$ Decay in the Standard Model and with New Physics". In: *Phys. Rev. D* 91.11 (2015), p. 115003. DOI: 10.1103/PhysRevD.91.115003. arXiv: 1502.07230 [hep-ph].

[33] Philipp Böer et al. "Angular Analysis of $\Lambda_b \to \Lambda_c (\to \Lambda \pi) \ell \bar{\nu}$". In: *JHEP* 12 (2019), p. 082. DOI: 10.1007/JHEP12(2019)082. arXiv: 1907.12554 [hep-ph].

[34] Neus Penalva, Eliecer Hernández, and Juan Nieves. "Further tests of lepton flavour universality from the charged lepton energy distribution in $b \to c$ semileptonic decays: The case of $\Lambda_b \to \Lambda_c \ell \bar{\nu}_\ell$". In: *Phys. Rev. D* 100.11 (2019), p. 113007. DOI: 10.1103/PhysRevD.100.113007. arXiv: 1908.02328 [hep-ph].

[35] R. Aaij et al. "Angular analysis of the $\mathscr{B}^0 \to K^* e^+ e^-$ decay in the low-q^2 region". In: *JHEP* 04 (2015), p. 064. DOI: 10.1007/JHEP04(2015)064. arXiv: 1501.03038 [hep-ex].

[36] Georges Aad et al. "Measurement of the parity-violating asymmetry parameter α_b and the helicity amplitudes for the decay $\Lambda_b^0 \to J/\psi + \Lambda^0$ with the ATLAS detector". In: *Phys. Rev. D* 89.9 (2014), p. 092009. DOI: 10.1103/PhysRevD.89.092009. arXiv: 1404.1071 [hep-ex].

[37] Roel Aaij et al. "Differential branching fraction and angular analysis of $\Lambda_b^0 \to \Lambda \mu^+ \mu^-$ decays". In: *JHEP* 06 (2015). [Erratum: JHEP 09, 145 (2018)], p. 115. DOI: 10.1007/JHEP06(2015)115. arXiv: 1503.07138 [hep-ex].

[38] Albert M Sirunyan et al. "Measurement of the Λ_b polarization and angular parameters in $\Lambda_b \to J/\psi \Lambda$ decays from pp collisions at $\sqrt{s} = 7$ and 8 TeV". In: *Phys. Rev. D* 97.7 (2018), p. 072010. DOI: 10.1103/PhysRevD.97.072010. arXiv: 1802.04867 [hep-ex].

[39] Medina Ablikim et al. "Measurements of Weak Decay Asymmetries of $\Lambda_c^+ \to pK_S^0$, $\Lambda\pi^+$, $\Sigma^+\pi^0$, and $\Sigma^0\pi^+$". In: *Phys. Rev. D* 100.7 (2019), p. 072004. DOI: 10.1103/PhysRevD. 100.072004. arXiv: 1905.04707 [hep-ex].

[40] Svjetlana Fajfer et al. "Implications of Lepton Flavor Universality Violations in B Decays". In: *Phys. Rev. Lett.* 109 (2012), p. 161801. DOI: 10.1103/PhysRevLett.109.161801. arXiv: 1206.1872 [hep-ph].

[41] Xiao-Gang He and German Valencia. "*B* decays with τ leptons in nonuniversal left-right models". In: *Phys. Rev. D* 87.1 (2013), p. 014014. DOI: 10.1103/PhysRevD.87.014014. arXiv: 1211.0348 [hep-ph].

[42] Torbjorn Sjostrand, Stephen Mrenna, and Peter Z. Skands. "PYTHIA 6.4 Physics and Manual". In: *JHEP* 05 (2006), p. 026. DOI: 10.1088/1126-6708/2006/05/026. arXiv: hep-ph/0603175 [hep-ph].

[43] Torbjorn Sjostrand, Stephen Mrenna, and Peter Z. Skands. "A Brief Introduction to PYTHIA 8.1". In: *Comput. Phys. Commun.* 178 (2008), pp. 852–867. DOI: 10.1016/j.cpc.2008. 01.036. arXiv: 0710.3820 [hep-ph].

[44] "LHCb VELO TDR: Vertex locator. Technical design report". In: (May 2001).

[45] R. Aaij et al. "Measurement of b-hadron fractions in 13 TeV pp collisions". In: *Phys. Rev. D100* (2019), 031102(R). DOI: 10.1103/PhysRevD.100.031102. arXiv: 1902.06794 [hep-ex].

[46] Howard E. Haber. "Spin formalism and applications to new physics searches". In: *21st Annual SLAC Summer Institute on Particle Physics: Spin Structure in High-energy Processes (School: 26 Jul - 3 Aug, Topical Conference: 4-6 Aug) (SSI 93)*. Apr. 1994, pp. 231–272. arXiv: hep-ph/9405376.

[47] P. R. Auvil and J. J. Brehm. "Wave Functions for Particles of Higher Spin". In: *Phys. Rev.* 145.4 (1966), p. 1152. DOI: 10.1103/PhysRev.145.1152.

[48] Thorsten Feldmann and Matthew W. Y. Yip. "Form factors for $\Lambda_b \to \Lambda$ transitions in the soft-collinear effective theory". In: *Phys. Rev. D* 85 (2012). [Erratum: Phys.Rev.D 86, 079901 (2012)], p. 014035. DOI: 10.1103/PhysRevD.85.014035. arXiv: 1111.1844 [hep-ph].

[49] A. Kadeer, J. G. Korner, and U. Moosbrugger. "Helicity analysis of semileptonic hyperon decays including lepton mass effects". In: *Eur. Phys. J. C* 59 (2009), pp. 27–47. DOI: 10. 1140/epjc/s10052-008-0801-5. arXiv: hep-ph/0511019.

[50] Tanmoy Bhattacharya et al. "Probing Novel Scalar and Tensor Interactions from (Ultra)Cold Neutrons to the LHC". In: *Phys. Rev. D* 85 (2012), p. 054512. DOI: 10.1103/PhysRevD.85. 054512. arXiv: 1110.6448 [hep-ph].

Chapter 3

Angular analysis of the decay $\Lambda_b^0 \to \Lambda_c^+ \mu^- \bar{\nu}_\mu$

Contents

The scientific interest in semileptonic $b \to c\ell\,\nu_\ell$ processes has been discussed in Chapter 2.1. We here focus on the experimental aspects of the angular measurement of decays involving heavy baryon $\Lambda_b^0 \to \Lambda_c^+ \mu^- \bar{\nu}_\mu$ transitions[1], illustrated in Fig. 3.0.1, with a Λ_c^+ reconstructed in the three-body $pK^+\pi^-$ final state. We perform the analysis with data collected with the LHCb detector during the years 2016 to 2018 of the LHC Run 2[2], amounting to the integrated luminosity $\mathscr{L} = 5.57\,\text{fb}^{-1}$ collected at the centre-of-mass energy $\sqrt{s} = 13\,\text{TeV}$. The goal of the analysis is to extract the hadronic form factors and Wilson Coefficients in $\Lambda_b^0 \to \Lambda_c^+ \mu^- \bar{\nu}_\mu$ decays by measuring the dependence of the double differential decay density on the squared di-lepton invariant mass q^2 and cosine of the muon helicity angle $\cos\theta_\mu$.

---

[1]The inclusion of the charge-conjugate process is implied throughout the whole Chapter.

[2]To keep consistency between semimuonic and semitauonic angular analyses of Λ_b decays, we discard data collected during Run 1 of the LHC due to missing trigger lines to select semitauonic transitions. This choice has a negligible impact on this analysis which is dominated by systematic uncertainties.
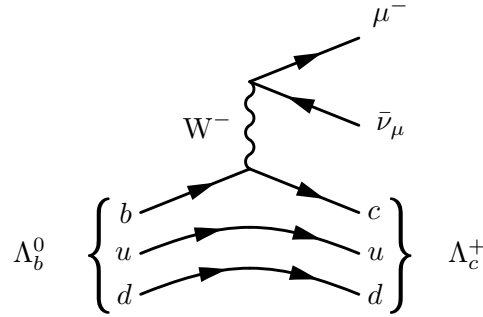
FIGURE 3.0.1: Diagram depicting the $\Lambda_b^0 \to \Lambda_c^+ \mu^- \bar{\nu}_\mu$ decay via a tree-level $b \to c \mu^- \bar{\nu}_\mu$ transition.

3.1 Introduction

The experimental advantage of dealing with Λ_b baryons is multi-fold. The different spin structure ($J^P = 1/2^+$) from the mesonic system of pseudo-scalar B hadrons complements the sensitivity to a number of New Physics scenarios, as discussed in Chapter 2. As the e^+e^- colliders are currently tuned for the on-shell production of the $\Upsilon(4S)$ resonance, these baryonic states are inaccessible and a unique prerogative of hadron collider experiments.

Λ_b baryons are copiously produced at hadron colliders in an unpolarised state [1]. Unprecedented statistics collected at the LHCb experiment stems from the large $b\bar{b}$ pairs production cross section, $\sigma(pp \to b\bar{b}X) \sim 154\,\mu$b at $\sqrt{s} = 13$ TeV within the experiment pseudo-rapidity η range [2]. In $5.57\,\text{fb}^{-1}$, corresponding to the data taking period $2016-2018$, at the LHCb experiment got produced a number of $b\bar{b}$ pairs $N_{b\bar{b}} = \sigma L \approx 10^{12}$. The hadronisation process yields a variety of b-flavoured hadrons, which are Λ_b particles in $\sim 20\%$ of the cases [3]. As semileptonic $b \to c\ell\nu_\ell$ are favoured transitions occurring at tree-level in the SM (Table 3.2.1), the analysis dataset is dominated by $\Lambda_b^0 \to \Lambda_c^+ \mu^- \bar{\nu}_\mu$ signal events. The yields are even larger than in the mesonic partner transitions, *e.g.* $\bar{B}^0 \to D^+ \mu^- \bar{\nu}_\mu$, given the larger branching fractions by a factor ca. three [4].

In addition, Λ_b decays are affected by reduced backgrounds if compared to the mesonic case, following conservation of both baryon number and isospin. As the ground state of b-baryon resonances, they primarily compete with additional decay modes of the Λ_b. Backgrounds from weak decays of higher mass resonances to the ground state imply multiple missing (charged) particles in the final state (see Table 3.2.1).

While dealing with large yields is undoubtedly an advantage, there are limitations to the hadronic environment in which the measurement takes place, including undetectable neutrinos in the final state of the signal decay. The rest frame of the decaying Λ_b cannot be fully reconstructed, given the unknown energy and momentum of colliding partons in the initial state, resulting in the

impossibility of constraining the direction of the neutrino with respect to the Λ_b^0 orientation in the laboratory system. The Λ_b system can be approximately recovered in case of a single missing mass-less particle [5] by imposing momentum conservation against the visible decay products, which returns a two-fold ambiguous solution for the neutrino momentum as described in App. 3.B. Picking up the solution randomly with $\sim 50\%$ efficiency is the standard of choice but inevitably degrades the Λ_b momentum resolution. A method to increase the selection rate for the correct solution with Gaussian Process Regression has been developed in this analysis and is discussed in Sec. 3.8.

The LHCb collaboration has previously published measurements involving semi-muonic Λ_b decays, either in the ratio $|V_{ub}/V_{cb}|$ [6] or in the shape of the single differential decay spectrum in bins of the di-lepton invariant mass [7], both with Run 1 data. This LHCb analysis is the first to study and the first to perform an angular analysis of $\Lambda_b^0 \to \Lambda_c^+ \mu^- \bar{\nu}_\mu$ decays with the Run 2 dataset. As a result of the large yields involved, measuring the shape of the decay density opens the venue to unprecedented precision on hadronic form factors and muonic Wilson Coefficients.

3.2 Measurement strategy

The approach of the analysis is to perform a full angular measurement of the decay products of unpolarised exclusive $\Lambda_b^0 \to \Lambda_c^+ \mu^- \bar{\nu}_\mu$ transitions with Run 2 data while integrating over the kinematics of the Λ_c^+ three-body decay reconstructed in the $pK^-\pi^+$ final state. The abundance of signal processes translates into the ability to disentangle the contribution of the hadronic current, encapsulated in the value of form factors, from the leptonic one, described by the Wilson coefficients of their corresponding SM/NP operator. The double differential decay density is therefore defined in the 2D-dimensional phase space described by the following variables:

- The squared invariant mass transferred to the lepton-neutrino system:

$$q^2 = (\hat{P}_{\Lambda_b} - \hat{P}_{\Lambda_c})^2 \, ;$$

- The helicity angle of the muon, defined as the angle between the muon direction in the W^* rest frame and the original W^* flight direction in the Λ_b rest frame (Fig. 3.2.1):

$$\cos\theta_\mu = -\frac{P_\mu^{[W^*]} \cdot P_{W^*}^{[\Lambda_b]}}{|P_\mu^{[W^*]}||P_{W^*}^{[\Lambda_b]}|} \, .$$

The complete expression of the decay density for NP contributions in the CP-conserving limit and for unpolarised Λ_bs has been computed in Sec. 2.D.
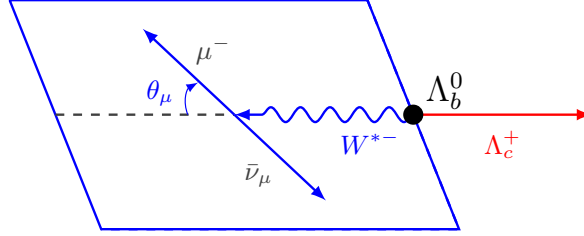
FIGURE 3.2.1: Schematic picture of a Λ_b^0 semileptonic decay, with a detail of the decay plane of the virtual W^* boson. We integrate over the degrees of freedom of the Λ_c^+ three-body transition, which is equivalent to assuming a stable Λ_c^+ resonance.

Partially reconstructed final state signatures are particularly challenging to isolate in the busy LHCb hadronic environment: this is mainly due to ineffective background rejection, given lacking information based on complete kinematic closure on a event-by-event basis. Missing momentum in the final state translates into both the incapability to recover the exact pointing to the primary vertex, and a flawed invariant mass resolution. Strategies have been developed to recover the kinematics of the parent Λ_b hadron and therefore the neutrino, ultimately improving the resolution and maximising the ability to perform a differential decay density measurement. In the case of semileptonic decays with a single neutrino in the final state, momentum conservation with respect to the Λ_b flight direction is imposed, which leads to a two-fold ambiguous solution for the parallel neutrino momentum component (see App. 3.B). The achieved resolution on phase space quantities q^2 and $\cos\theta_\mu$ is at the level of 30% (Fig. 3.2.2) when adopting Gaussian Process Regression techniques to guide the choice among one of the two solutions. We refer to Sec. 3.8 and App. 3.E for a detailed discussion on resolution effects.

Imposing momentum conservation in the orthogonal direction to the Λ_b direction of flight allows reconstructing an auxiliary variable, the corrected mass $M_{\text{corr}}(\Lambda_b^0)$ (Fig. 3.2.3):

$$M_{\text{corr}}(\Lambda_b^0) = \sqrt{m_{\text{vis}}^2 + p_\perp^2} + p_\perp \tag{3.1}$$

which relies on the knowledge of the orthogonal component of the momentum of the visible decay products $\Lambda_c^+ \mu^-$, $P_\perp$, and its invariant mass m_{vis}. The corrected mass is the fit variable of choice in this analysis to determine the signal yields, as it offers good discriminatory power between signal and backgrounds while granting good model independence due to its small sensitivity to the physics model prior. Fig. 3.2.4 illustrates the separation power of the corrected mass between the signal, peaking at the mass of the Λ_b^0, and backgrounds of the type $\Lambda_b^0 \to \Lambda_c^+ \mu^- \bar{\nu}_\mu X$ with unreconstructed massive X particles, instead exhibiting a broader distribution at the lower end
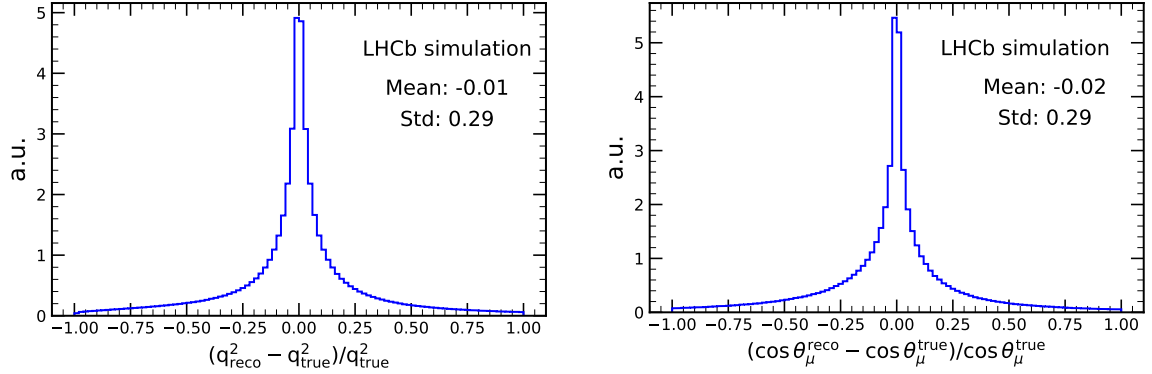
FIGURE 3.2.2: Fractional resolution on the phase space variables q^2 (left) and $\cos\theta_\mu$ (right) for $\Lambda_b^0 \to \Lambda_c^+ \mu^- \bar{\nu}_\mu$ simulated decays by picking one of the two solutions to the neutrino momentum.

of the spectrum[34]. It follows that the uncertainty on the Λ_b flight direction, and thus on the resolution of the reconstructed primary (PV) and secondary vertex (SV) positions, are the driving factors affecting the corrected mass width.

Signal candidates $\Lambda_b^0 \to \Lambda_c^+ \mu^- \bar{\nu}_\mu$ are identified by pairing $\Lambda_c^+ \to pK^-\pi^+$ decays with a particle identified as a muon. Background contributions arise from transitions of the type $\Lambda_b^0 \to \Lambda_c^+ \mu^- \bar{\nu}_\mu X$ with any combination of missing particles X in the final state, therefore referred to as *partially reconstructed*. A complete list of signal and background decays to current knowledge [4], with associated decay rate probabilities and quantum numbers, have been reported in Table 3.2.1. Three main components can be identified:

1. Λ_b^0 semi-tauonic decays, occurring with a similar branching ratio and followed by a muonic decay of the tau lepton. Three missing neutrinos are present in the final state and add up to

---

[3]If ignoring resolution effects, $M_{\text{corr}}(\Lambda_b^0) < m(\Lambda_b^0)$

[4]Throughout this chapter, we have adopted natural units ($\hbar = c = 1$) if not stated otherwise.
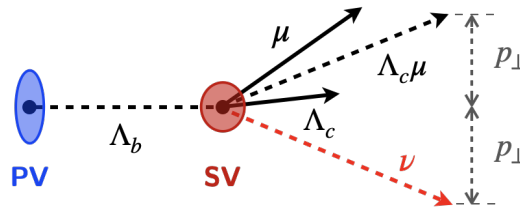
FIGURE 3.2.3: Schematics of momentum conservation in the orthogonal direction to the Λ_b^0 direction of flight (FD), defined as the vector linking the parent hadron primary vertex (PV) and decay vertex (SV). The orthogonal component of the neutrino momentum, $p_\perp$, is constrained by the momentum of the visible decay products.

a non-negligible missing momentum contribution;

2. Λ_b^0 decays to excited resonances of the $\Lambda_c^{+(*)}$ baryon. They are regarded as *feed-down* contributions because of the higher mass resonance feeding into the Λ_c^+ ground state with two low momentum charged or neutral pions. They represent by far the most abundant background contribution;

3. Doubly-charmed decays of the Λ_b^0 to a $\Lambda_c^{+(*)}$ plus a charmed hadron X_c, *e.g.* the short-lived D_s meson. The topology of their semileptonic decay is indistinguishable from that of the tau lepton.

We rely heavily on simulation to estimate the kinematic properties and relative contributions of these background sources, as further discussed in Sec. 3.9.1. Given the large amount of missing momentum in the final state, they are well separated from the signal shape in corrected mass while contributing to the lower end of the spectrum.

Other possible backgrounds arise when a hadron is reconstructed and wrongly classified as a muon in the combination $\Lambda_c^+ \mu^-$, giving rise to the *misID* component (Sec. 3.9.1). Furthermore, particles belonging to unrelated processes could get paired to form a fake Λ_b^0 vertex candidate, thus known as *combinatorial* backgrounds (Sec. 3.9.1). These cannot be studied with simulation and must be characterised with data-driven methods.

This analysis utilises proton-proton collision data recorded with the LHCb detector between the years 2016 to 2018. The dataset undergoes a detailed offline selection procedure (Sec. 3.5) tuned on the simulation, aimed at enriching the sample in $\Lambda_b^0 \to \Lambda_c^+ \mu^- \bar{\nu}_\mu$ signal candidates. Any known misalignment between simulations and data has been taken into account and corrected, as discussed in Sec. 3.6.

The normalised yields of the signal decay, *i.e.* $d^2N/(dq^2 d\cos\theta_\mu)$, are retrieved from independent likelihood binned fits to the corrected mass in bins of the reconstructed phase space variables. Using the forward folding approach [8], we convolve the experimental effects (selection efficiency and resolution-induced bin migration) to the true differential decay model. The shape of the offline selection efficiency as a function of phase space (see Sec. 3.7), together with detector resolution effects (see Sec. 3.8), has been modelled with simulation. Ultimately, parameters of interest of the analysis, *i.e.* the hadronic Form Factors and the muonic Wilson Coefficients, can be extracted from a folded binned maximum likelihood fit to the normalised reconstructed data shape. We remark that, according to the analysis strategy, we lose sensitivity to the absolute decay density normalisation by considering merely the shape of $\Lambda_b^0 \to \Lambda_c^+ \mu^- \bar{\nu}_\mu$ decays in phase space. The choice unfolds from poor knowledge about Λ_b^0 baryons production and given the absence of a suitable normalisation channel to reduce the associated systematic uncertainty. Additional details on the corrected mass and phase space fits have been provided in Sec. 3.9 and 3.10, respectively, while Sec. 3.10.4 and 3.10.5 presents the analysis results. The common variables used in this work and related to the quantities measured by the LHCb detector are defined in App. 3.A.

Baryon	Mass	J^P	(I, I_3)	Decay modes	
Λ_b^0	$5619.60 \pm 0.17\,\text{MeV}/\text{c}^2$	$\left(\frac{1}{2}\right)^+$	$(0, 0)$	$\Lambda_c^+ \ell^- \bar{\nu}_\ell$	$\left(6.2^{+1.4}_{-1.3}\right)\%$
				$\Lambda_c^+(2595)\ell^- \bar{\nu}_\ell$	$\left(7.9^{+4.0}_{-3.5}\right) \times 10^{-3}\,\%$[5]
				$\Lambda_c^+(2625)\ell^- \bar{\nu}_\ell$	$\left(1.3^{+0.6}_{-0.5}\right)\%$[5]
				$\Lambda_c^+ D_s$	$(1.10 \pm 0.10)\%$
				$\Sigma_c^0(2455)\pi^+ \ell^- \bar{\nu}_\ell$	—
				$\Sigma_c^{++}(2455)\pi^- \ell^- \bar{\nu}_\ell$	—
Λ_c^+	$2286.46 \pm 0.14\,\text{MeV}/\text{c}^2$	$\left(\frac{1}{2}\right)^+$	$(0, 0)$	$pK^- \pi^+$ non resonant	$(3.5 \pm 0.4)\%$
				$p\bar{K}^*(892)^0$	$(1.95 \pm 0.27)\%$
				$\Delta(1232)^{++}K^-$	$(1.08 \pm 0.25)\%$
				$\Lambda(1520)\pi^+$	$(2.2 \pm 0.5)\%$
$\Lambda_c^+(2595)$	$2592.25 \pm 0.28\,\text{MeV}/\text{c}^2$	$\left(\frac{1}{2}\right)^-$	$(0, 0)$	$\Lambda_c^+ \pi^+ \pi^-$	$\sim 18.5\%$ [9]
				$\Lambda_c^+ \pi^0 \pi^0$	$\sim 81.5\%$ [9]
$\Lambda_c^+(2625)$	$2628.11 \pm 0.19\,\text{MeV}/\text{c}^2$	$\left(\frac{3}{2}\right)^-$	$(0, 0)$	$\Lambda_c^+ \pi^+ \pi^-$	$\sim 55\%$ [9]
				$\Lambda_c^+ \pi^0 \pi^0$	$\sim 45\%$ [9]

TABLE 3.2.1: List of signal and partially reconstructed backgrounds in Λ_b^0 semileptonic decays with a muon and a three-body $\Lambda_c^+ \to pK^- \pi^+$ in the final state. Quantum numbers and experimental knowledge to date [4] on masses and decay rate probabilities are also reported.

---

[5] These fractions rely on the assumption of exact isospin symmetry in the Λ_c^* decays in charged and neutral pions [10]. We refer to [9] for the-state-of-the-art calculation for the $\Lambda_c(2595)$ and $\Lambda_c(2625)$ partial widths.
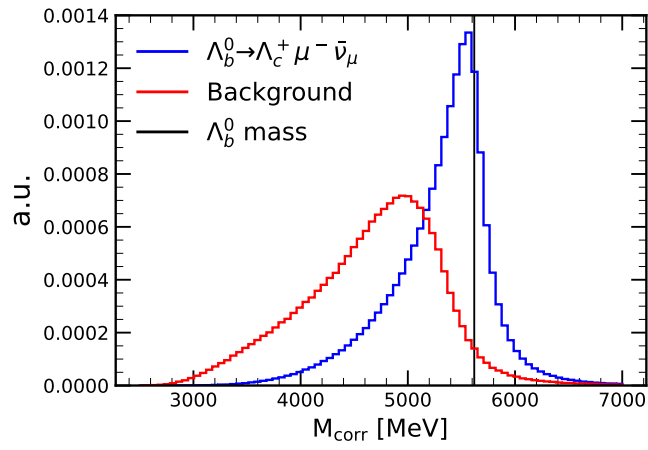
FIGURE 3.2.4: Reconstructed corrected mass distribution over the full phase space spectrum: comparison between simulated signal (blue) and background decays (red) of the type $\Lambda_b^0 \to \Lambda_c^+ \mu^- \bar{\nu}_\mu X$, with unreconstructed massive X in the final state. The value of the Λ_b^0 mass is superimposed, to further stress the separation of the signal peaking distribution from the broad shape of partially reconstructed backgrounds.

3.3 The LHCb experiment

3.3.1 The Large Hadron Collider at CERN

The European Organisation for Nuclear Research (CERN), located at the Swiss-French border, is the physics facility hosting the most powerful and recognised proton collider in the world: the Large Hadron Collider (LHC) [11]. Among its collection of multiple achievements since starting its operational time in 2011, the discovery of the Higgs boson [12, 13] stands above all as the last missing tile in the spectrum of particles of the Standard Model.

This machine of wonder is a proton-proton accelerator and collider, structured in two separate superconducting rings [11], achieving today the record centre-of-mass energy of 14 TeV. It is hosted in a tunnel with a circumference of 27 km at a max depth of 170 m, previously utilised for the Large Electron-Positron Collider (LEP) dismantled in 2001. The reason for two separate rings stems from the requirement of separate allocations for circulating beams of the same particle, curved under the action of disjoint magnetic and vacuum systems. This feature is unnecessary in the case of LEP, whose particle-antiparticle beams share the phase space in a single ring. Each beam is accelerated using 16 radio-frequency (RF) cavities, then curved with over 12300 superconducting dipole magnets of Niobium-Titanium alloy kept at 1.9 K. The beam focusing and stability are ensured through 392 magnetic quadrupoles. Most of the RF cavities present along the straight particle segments, designed for LEP to compensate for synchrotron radiation energy loss, have been dismissed in the LHC configuration, thus reducing the number of beam crossing points. This choice led to the definition of only four interaction points, each hosting an underground experiment (Fig. 3.3.1): ATLAS [14], CMS [15], LHCb [16] and ALICE [17][6]. Fig. 3.3.1 additionally highlights the exploitation of the whole CERN accelerator complex as the injection facility into the LHC rings.

The operational time of the LHC machine is defined in terms of *runs*, characterised by distinct achievements of centre-of-mass energy $\sqrt{s}$ and peak luminosity L. The first run of the LHC (Run 1) occurred between 2011 and 2013, leading to the maximal recorded energy $\sqrt{s} = 8$ TeV. A period of technical stop to commission and upgrade the accelerating machine, also known as *Long Shutdown 1*, followed until the beginning of 2015 when the LHC became operational again. The years from 2015 to 2018 (Run 2) witnessed an unprecedented success, reaching the maximum energy $\sqrt{s} = 13$ TeV, with a record peak luminosity of 2.07×10^{34} cm^{-2} s^{-1} [18] corresponding to more than twice the design value (Fig. 3.3.2). During the stable configuration of Run 2, the LHC delivered beams with more than 2800 proton bunches and a 25 ns bunch spacing (corresponding to the event rate of 30 MHz). The peak luminosity estimates shown in Fig. 3.3.2 represent the high luminosity ATLAS and CMS experiments. Instead, the LHCb experiment aims at a lower instantaneous luminosity[7], by operating a beam separation technique known as *luminosity levelling* [19] to achieve a lower constant collision rate. Running at lower luminosity carries the

---

[6]The ALICE experiment is designed to operate with ion beams.
[7]$L_{\text{LHCb}} = 4 \times 10^{32}$ cm^{-2} s^{-1}.

advantage of producing a single pp interaction per bunch crossing within the LHCb acceptance, consequently corresponding to a low detector occupancy and reduced radiation damage.

At the time of this work, the LHC machine delivers beams at $\sqrt{s} = 13.6$ TeV in the Run 3 of operation after the Long Shutdown 2, lasting between the end of 2018 and 2022. During this period, the LHCb detector has undergone a significant commissioning phase for its first Upgrade [20], including its detector and software infrastructure, as discussed in Chap. 4 and Ref. [20].
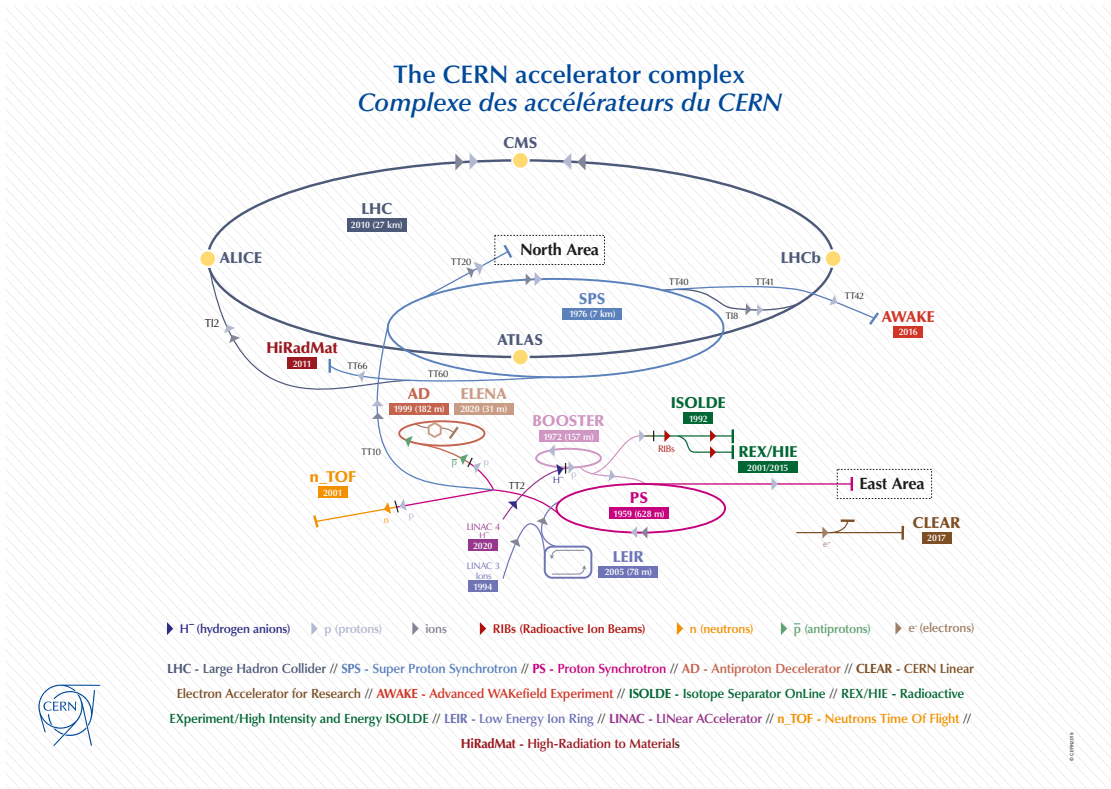
FIGURE 3.3.1: Illustration of the CERN accelerator complex, highlighting the injection system to the LHC ring and the four LHC experiments, corresponding to a proton-proton collision point.
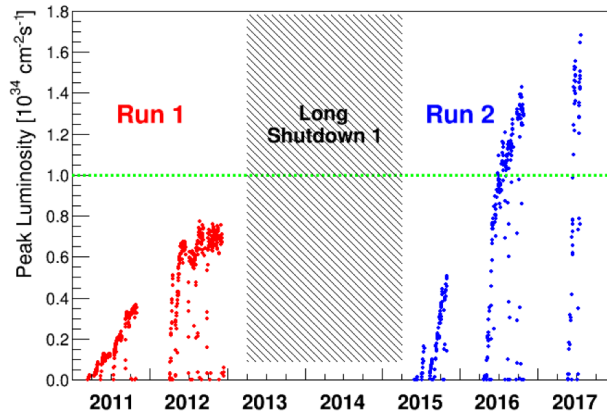
FIGURE 3.3.2: Evolution of the peak luminosity of the LHC during the Run 1 and Run 2. The design value is superimposed in green.

3.3.2 The LHCb detector layout

LHCb is the experiment devoted to detecting and investigating heavy flavour decays at the LHC, the factory with the most abundant production of b hadrons in the world. In the following, we describe the experimental setup of the LHCb experiment during Run 1(2) of the LHC used for the data taking relevant to this analysis. We refer to [21] for the Upgrade I version of the LHCb detector, currently in operation.

The detector design derives *in-primis* from acceptance considerations, as the production of $b\bar{b}$ pairs from pp collisions occur almost collinearly to the beam axis, with a high correlation between the two quarks emission angles. The system of two quarks can be emitted in the forward[8] region of rapidity $\eta = -\ln \tan \theta/2$, with θ polar angle between the particle and the beam direction. For this reason, the LHCb detector is a single-arm forward spectrometer (Fig. 3.3.3) with an angular coverage (15, 300) mrad in the bending and (15, 250) mrad in the non-bending plane, corresponding to the rapidity region $2 < \eta < 5$.

In addition to constraints derived from acceptance considerations, the core of the LHCb design is dictated by the required physics delivery: a deep understanding of the flavour properties of the SM by studying primarily CP violation sources and rare B-hadron processes with high precision[9]. For this purpose, the detector has been equipped with subsystems designed to have a high track reconstruction efficiency and good separation capabilities between distinct particle species in a wide momentum range while achieving high trigger efficiencies [22]. These different components have been described in the following Sections.

---

[8]The production can occur either in the forward or the backward region, which falls outside the LHCb angular acceptance.

[9]This is by far not an exhaustive list of the LHCb physics potential. The current exploration programme includes semi-leptonic, electroweak, heavy-ion, and exotica physics, among others.
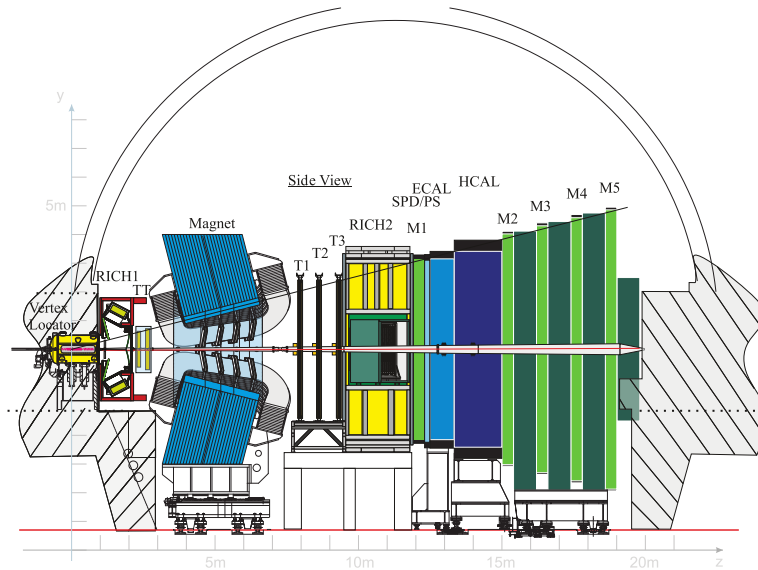
FIGURE 3.3.3: Layout of the LHCb detector [16] operating during Run 1 and Run 2 of the LHC (side view). The horizontal axis corresponds to the z coordinate, aligned with the beam direction, while the vertical axis denotes the y coordinate in a right-handed defined coordinate system.

3.3.3 Tracking system

LHCb tracking detectors are devoted to reconstructing the position and momentum of charged particles (*tracks*) crossing their fiducial volume in the presence of a deflection induced by a magnetic field. Starting from the beam interaction point, the first encountered device is the Vertex Locator (VELO) [22, 23], followed by four planar spectrometer stations: placed upstream of the $\sim 4\,\mathrm{Tm}$ dipole magnet, the Tracker Turicensis (TT) [22, 24]; downstream of the magnet, the tracking stations T1-T3 [22, 24, 25].

The primary capability of the VELO detector is the reconstruction of vertices in the proximity of the interaction point with extreme precision. The ability to locate displaced primary and secondary vertices plays a crucial role in beauty and charm hadron decays, where an accurate measurement of hadron lifetime and impact parameter is required to perform flavour identification [22]. The cylindrical geometry of the VELO is illustrated in Fig. 3.3.4: it was structured in two retractable halves, moved close to the beam during pp collisions time while keeping at a distance during beam injection. A series of 21, $300\,\mu$m-thick, silicon microstrip sensors were displaced in the radial direction (R-sensor) and the azimuthal direction around the beam (ϕ-sensor) for a total length of 1 m, hence covering the $r\phi z$ 3D space to achieve a fast reconstruction during trigger time. An additional set of two tracking stations perpendicular to the beam axis, the *pileup system*, was placed upstream of the beam crossing point to constrain the number of pp interactions for bunch crossing. In terms of spatial resolution, the detector achieved a performance of $13\,\mu$m in the transverse plane to the beam direction, and $71\,\mu$m along the beam line for vertices with 25

tracks [26].
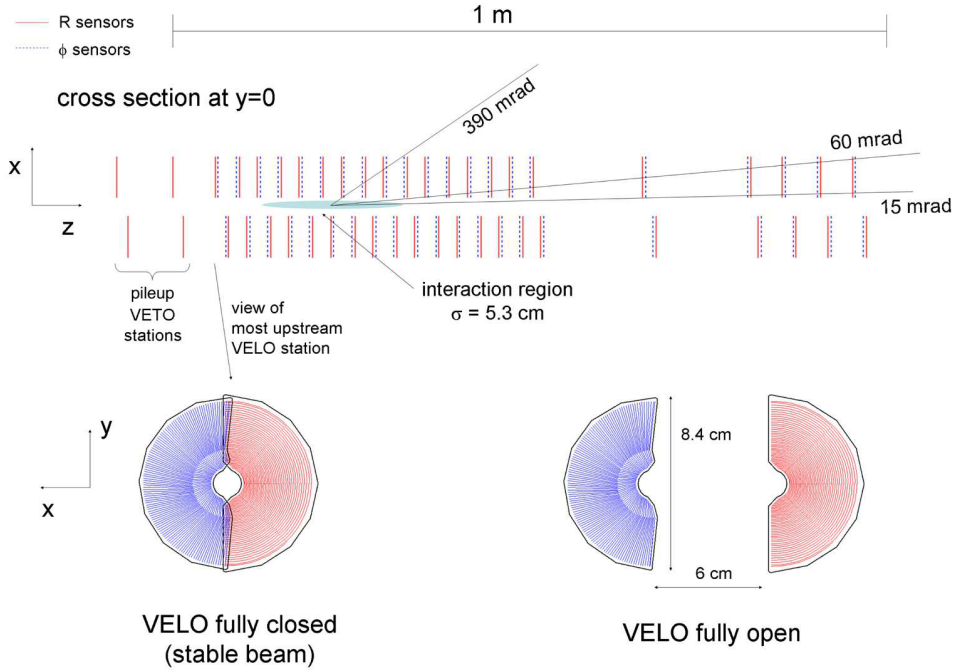
FIGURE 3.3.4: Schematic view of the LHCb Vertex Locator (VELO) from the side
(top panel) and from the front (bottom panel) [22].

The TT detector comprised 500 μm-thick silicon microstrip sensors covering the full LHCb acceptance, upstream of the magnet. Fig. 3.3.5 demonstrates the geometry of TT layers, oriented in four stereo-views (x, u, v, x) tilted by 5° to the vertical direction [27]. The T1-T3 tracking stations constrained the position of tracks resulting from the deflecting action of the dipole magnet exploiting two different technologies: silicon microstrips were used for the inner area surrounding the beam (Inner Tracker, IT) to withstand the intense radiation, while straw tubes covered the external area (Outer Tracker, OT) amounting to more than 99% of the whole surface. Each station comprised four modules arranged in stereo views, similar to the TT. The layout of one of the three IT stations is schematically represented in Fig. 3.3.6: silicon microstrips were staggered along the x and z directions to avoid acceptance gaps. With more than a 99% single hit efficiency, the achieved performance in spatial resolution was 50 μm [27]. The OT geometry is illustrated in Fig. 3.3.7. The filling gas mixture was chosen to achieve a spatial resolution of 200 μm [29].
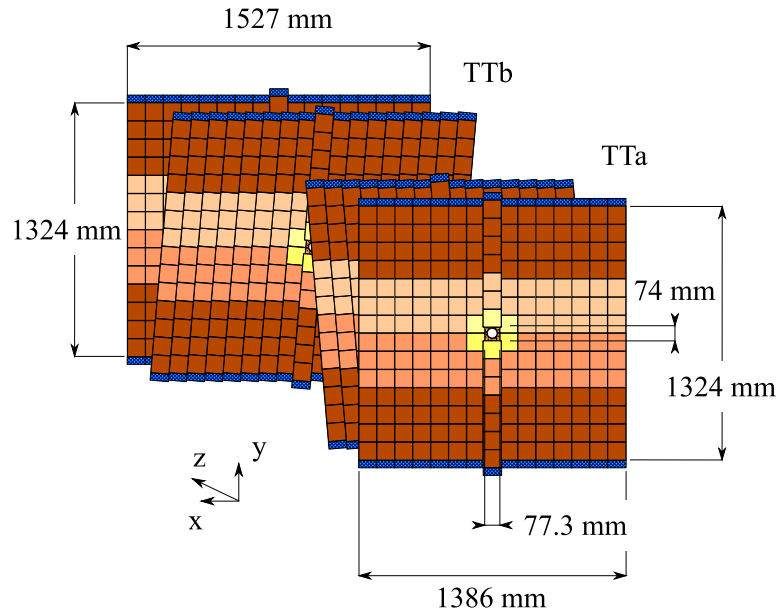
FIGURE 3.3.5: Schematic layout of the four layers of the Tracker Turicensis (TT) detector, detailing the different readout sectors in distinct colours [28].
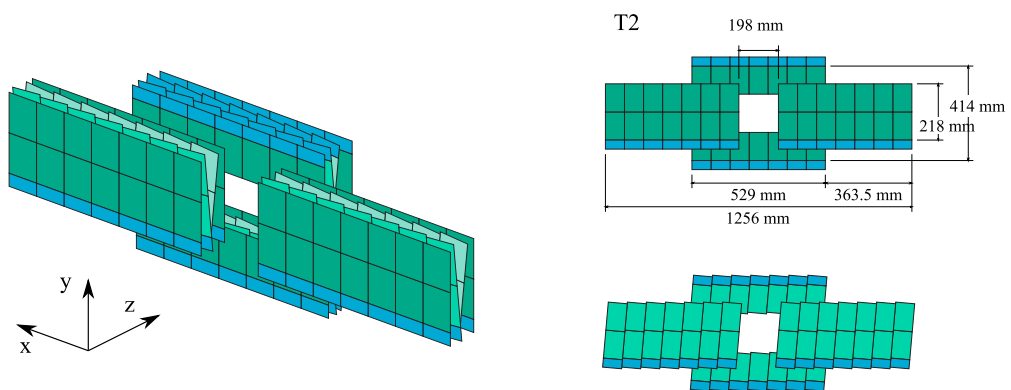
FIGURE 3.3.6: Geometry of the LHCb Inner Tracker, detailing the sensors (green) and readout (blue).
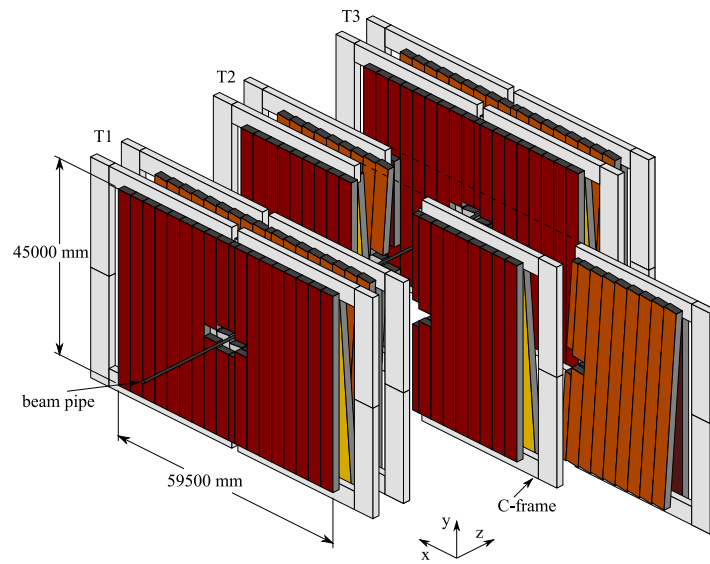
FIGURE 3.3.7: Illustration of the LHCb Outer Tracker geometry. The empty area surrounding the beam pipe hosts the Inner Tracker modules.

3.3.4 Particle Identification system

Particle identification (PID) is a critical task for every analysis conducted in LHCb, where a clear separation between particle species (p, K, π, μ, e) is required to unambiguously select $b-$hadron decays. The momentum spectrum of particles produced in pp collisions is harder in the proximity of the beam direction, whereas substantially softer at large polar angles, following closely the trend in the detector occupancy. The design of the LHCb PID system accommodates these features to cover the full momentum range by combining several granularity zones and different technologies: two Ring Imaging Cherenkov detectors (RICH1 and RICH2), an Electromagnetic Calorimeter (ECAL), and a Hadronic Calorimeter (HCAL); a Muon System (MUON).

RICH detectors [30] represent the first system devoted to the PID, performed across the full spectrum of particle momentum. They exploit the principle of Cherenkov radiation emission in a dielectric medium with refractive index n, in which the velocity of the crossing particle v is larger than the velocity of light c/n. The choice of the radiating medium impacts the resulting emission angle of Cherenkov photons, at the same time dependent on the crossing particle momentum, as shown in Fig. 3.3.8 for RICH radiators. Cherenkov photons are subsequently focused outside of the LHCb acceptance through a system of reflecting mirrors and then collected on Hybrid Photon Detectors (HPD) encased within an iron shield against edge effects from the magnetic field. The RICH1 detector (Fig. 3.3.9a) was located upstream of the dipole magnet, right before the TT. It covered the softer particles momentum spectrum up to $\sim 60\,\text{GeV}$ with fluorobutane (C_4F_{10}) and aerogel (Run 1 only) radiators [31]. The RICH2 system was instead placed downstream of the magnet and the T3 tracking station, covering a smaller angular acceptance which corresponds to the harder momentum spectrum above $100\,\text{GeV}$ [31] with a CF_4 gas as radiator.
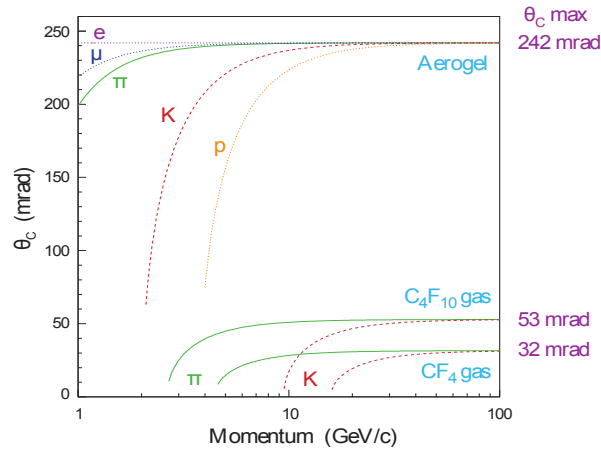
FIGURE 3.3.8: Distribution of Cherenkov radiation angle per particle species, as a function of the particle momentum, for several radiators.

The role of ECAL and HCAL [32] was multifold: they aided the identification of electrons, photons, and π^0 by providing information about their position and energy loss in the traversed medium. As the response of the calorimeters was used in the first hardware stage of the LHCb trigger
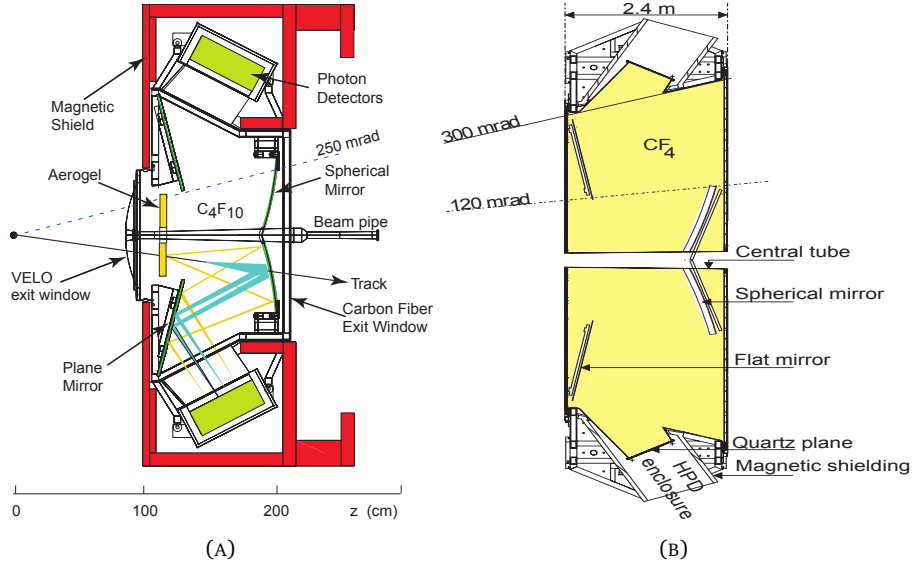
FIGURE 3.3.9: Schematic layout of the LHCb Ring Imaging Cherenkov detectors for the identification of particles: (A) RICH1 (side view), for the softer momentum spectrum; (B) RICH2 (top view), for the harder momentum spectrum.

(Sec. 3.3.5), yielding the rejection of almost 99% of inelastic pp collisions [31], the detected signal must have been processed rapidly. For this purpose, it was crucial to achieve optimal separation between electrons and photons, which was enforced by placing two additional detectors before the ECAL to enable earlier shower development: a plastic Scintillating Pad Detector (SPD), interleaved with a 15mm-thick lead converter and an almost identical Pre-Shower (PS) detector. The ECAL and HCAL layout and segmented designs are illustrated in Fig. 3.3.10. The choice to arrange sections with different granularity mostly depended on the hit occupancy variation across the calorimeter surface, amounting to more than two orders of magnitude [31]. The structure of the ECAL detector consisted of an alternation between 4 mm-thick plastic scintillator and 2 mm-thick lead absorber (*shashlik* [32]), for a total length of $\sim 25 \, X_0$ for full electromagnetic shower containment. Similarly, the HCAL was based on a periodic sampling detector technology, alternating scintillating pads to layers of lead as absorbing medium, for a length corresponding to $5.6 \, \lambda_I$. The measured energy resolution for ECAL and HCAL was [31]:

$$
\left(\frac{\sigma_E}{E} \right)_{\text{ECAL}} = \frac{10\%}{\sqrt{E}} \, ,
$$
$$
\left(\frac{\sigma_E}{E} \right)_{\text{HCAL}} = \frac{69 \pm 5\%}{\sqrt{E}} \, ,
$$

(3.2)

where we include only the term related to intrinsic fluctuations in the sampled energy and the number of particles contributing to the signal in the active detector area.

The very downstream section of the LHCb detector hosted the MUON system [33], comprising five
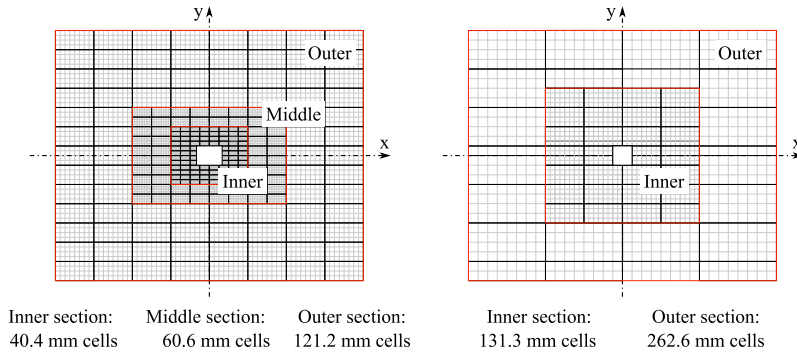
FIGURE 3.3.10: Schematic view of the cross section of the LHCb ECAL (left) and HCAL (right), highlighting the difference in granularity as a function of the distance to the beam axis, here taken as the origin of the coordinate system.

stations (M1 to M5) along the beam axis used for the task of muon reconstruction and triggering, fundamental to most LHCb analyses. Not least, it assumes a primary role in this work, analysing reconstructed decays with a muon signature in the final state. As a consequence, we employ a trigger selection requiring the presence of a clear, high p_T muon track from the very first stages of reconstruction (hardware trigger, see Sec. 3.3.5). While the first station, M1, was placed in front of the calorimeters to improve on the trigger p_T estimate, the M2-M5 occupied the section immediately downstream of the HCAL. Fig. 3.3.11 illustrates the segmented geometry of each station, increasing in transverse dimensions moving away from the interaction point. The chosen technology for the MUON was a combination of 80 cm-thick lead absorber interleaved with stations of Multi Wire Proportional Chambers (MWPC) and triple Gas Electron Multipliers (GEM) detectors, the latter for the area surrounding the beam pipe to withstand the larger particle flux. The used filling gas mixture was $Ar/CO_2/CF_4$ with variable concentrations, designed to achieve a fast trigger decision within 25 ns [31]. The first stations, M1-M3, had an improved (x, y) spatial resolution compared to M4-M5, which combined to a $\sim 20\%$ transverse momentum resolution [31]. The additional stations, M4 and M5, aimed to tag penetrating particles reaching the downstream end of the LHCb detector.
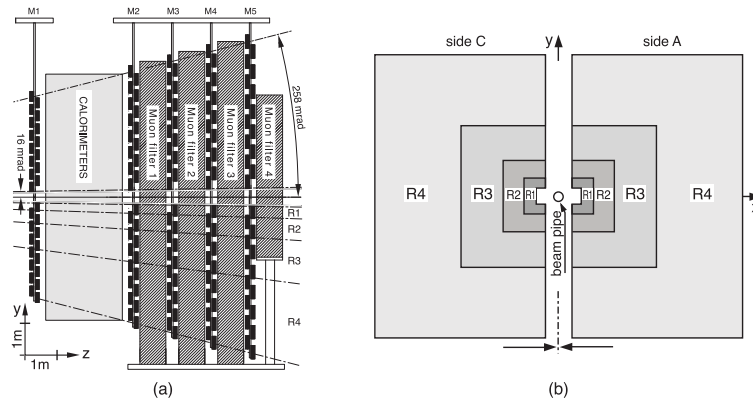
FIGURE 3.3.11: Layout of the LHCb MUON system: (a) side view; (b) front view. The regions R1-R4 correspond to areas with different segmentation, decreasing with the distance from the beam axis.

3.3.5 Trigger

The raw event rate at particle physics experiments, particularly at colliders, is typically too high to be fully allocated to physical storage and, most times, comprises a significant fraction of uninteresting processes. A trigger system is designed to overcome both issues with algorithms that select only signal-like transitions, reducing the data rate to a manageable level.

The general Run 1 and Run 2 design of the LHCb trigger is articulated in two separate stages [34]: a first hardware L0 level, followed by a software High-Level Trigger HLT. However, the Run 1 trigger version suffered from substantial limitations, given not only the low efficiency for low-momentum charged tracks at the L0 but also large resolution differences between online and offline reconstruction [35]. A novel design for the LHCb trigger was introduced for the Run 2 phase, enabling real-time detector alignment and calibration. This change of paradigm aimed at achieving two primary goals: on one side, to enable a full offline event reconstruction at the trigger level with increased efficiency; on another side, to achieve offline alignment and calibration of Run 1 performances at the trigger level, with the advantage of being able to perform a final event selection within the trigger.

The logic of the implemented Run 2 LHCb trigger is illustrated in Fig. 3.3.12. Its structure is shaped by the requirement of minimal readout downtime at the full bunch crossing rate of 40 MHz. The hard limit of the L0 hardware readout is dictated by the front-end and bandwidth features of the LHCb detectors which are being read out. During Run 2, the detector was operated at a rate of visible interactions per bunch crossing $\mu = 1.1$, corresponding to the readout rate of 1 MHz. The L0 trigger, implemented on Field-Programmable Gate Arrays (FPGA), operates on information collected from the calorimeters and the muon system after removing the busiest events from the processing chain. Reducing the event complexity ensures a faster reconstruction and yields a higher rejection power on prompt backgrounds. The L0 muon trigger decision is the set of selections used in this analysis for the first stage of the trigger (Sec. 3.6.4). Muon candidates are

searched for in the muon stations as straight-line tracks, originating from the collision point and receiving a single kick from the magnetic field. The selection is enforced on the value of the muon transverse momentum p_T, required to be above a defined threshold, estimated with an average resolution of 25%.

Events selected by the L0 stage are transferred to the High-Level Trigger (HLT), running on the Event Filter Farm (EFF). The EFF, with its approximately 30×10^3 physical cores and a disk buffer size of 10 PB, allows for event processing and real-time detector alignment and calibration *before* performing the full event reconstruction. The HLT software framework is shared with the offline analysis tools, making it possible to integrate selections directly at the trigger level. The first level HLT1 reduces the event rate to a few hundred kHz by selecting single or multi-body signatures after a preliminary fast track and a precise primary vertex (PV) reconstruction. The HLT1 requirements used in this analysis correspond to inclusive selections aimed at identifying good quality tracks and secondary vertices. They are further discussed in Sec. 3.6.5. The full event reconstruction is performed in the HLT2 stage, occurring when all the sub-detectors are calibrated and aligned, thus enabling the identification of particles and the most precise momentum estimate. Event rates are further reduced to 12.5 kHz, ready to be permanently saved on disk storage. The set of HLT2 selections relevant for this analysis is summarised in Sec. 3.6.5. An event candidate is identified by requiring high-momentum hadronic tracks, forming a good-quality displaced vertex, and a muon with a large impact parameter to the production vertex of the parent particle.
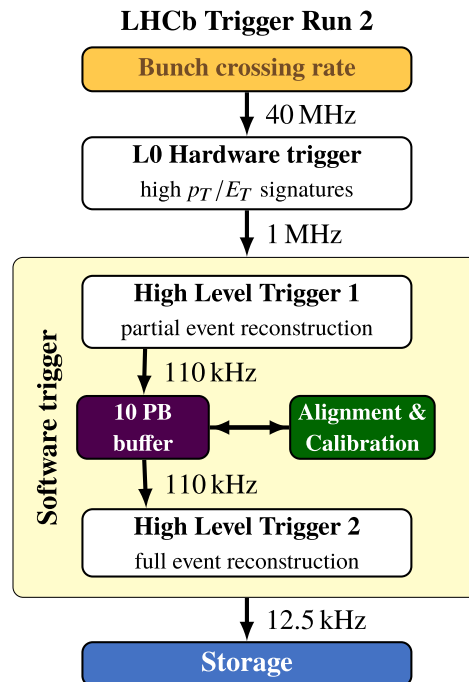
FIGURE 3.3.12: Schematic layout of the LHCb trigger logic during Run 2 [34].

The trigger strategy has been revised in light of the LHCb detector makeover during the Long

Shutdown 2 to accommodate a higher recorded luminosity in the LHC Run 3 and 4. The topic, which falls outside the objectives of this Chapter, has been treated in Chap. 4.

3.4   Data and Monte Carlo samples

This analysis is performed on data collected by the LHCb experiment during the data-taking periods from 2016 to 2018. A summary of the centre of mass energy, $\sqrt{s}$, and integrated luminosity $\mathscr{L}$ associated with each year is provided in Tab. 3.4.1. Particles compatible with the hypothesis of a μ^- or Λ_c^+ baryon are grouped to shape Λ_b^0 candidates, from here on defined as *signal sample*. In addition to building signal neutral candidates by pairing particles of the opposite sign, we make use of couples with the same sign (*e.g.* $\mu^- \Lambda_c^- + h.c.$, defined as *same sign sample*) as a proxy to investigate the behaviour of backgrounds due to tracks misidentification or arising from random combinations.

Year	$\sqrt{s}$	$\mathscr{L}$
2016	13 TeV	$1.67\,\mathrm{fb}^{-1}$
2017	13 TeV	$1.71\,\mathrm{fb}^{-1}$
2018	13 TeV	$2.19\,\mathrm{fb}^{-1}$

TABLE 3.4.1: Specifics of the data sample used in this analysis, detailing the centre-of-mass energy $\sqrt{s}$ and integrated luminosity $\mathscr{L}$.

A large number of $\Lambda_b^0 \to \Lambda_c^+ \mu^- \bar{\nu}_\mu$ signal candidates is expected in the data. Large simulation samples are therefore required to model the signal efficiency variation over the phase space precisely, as well as the response matrix and corrected mass shapes of both the signal and background. To achieve this, fast simulation techniques, such as the *tracker-only* one, are employed to generate larger samples in a shorter amount of time compared to the complete LHCb simulation set. In the tracker-only MC samples, only the response from the tracking systems (Velo, TT, and T1-T3) and the magnet are included. An in-depth discussion about tracker-only MC simulations is presented in Sec. 3.4.1. Nonetheless, MC samples, which include the entirety of the LHCb detector (*full simulation*), have been produced and used to compare and validate tracker-only samples. The proton-proton collision dynamics have been simulated with the software Pythia v8 [36], while we use the tool EvtGen [37] for the decay of hadrons produced in the fragmentation of partons. The software Geant4 [38] handles the final particle propagation step within the LHCb detectors and surrounding materials. Every MC generation step has been tuned to reproduce the experimental conditions of its corresponding data-taking period. Once produced, simulated events are reconstructed using the same software setup and versions as the corresponding data. Moreover, reconstructed candidates in simulation undergo equivalent selections as those placed upon the data. The number of generated MC events for the signal and background channels is

summarised in Table 3.4.2 after a basic set of pre-selections, the *filtering*[10] and *generator-level* cuts. It is worth noting the calibre of MC statistics handled by this analysis, amounting to more than one billion events, which poses non-trivial challenges in processing speed and memory allocation. For this reason, the software framework handling the analysis pipeline has been designed in a parallel, multi-thread-oriented way.

Decay	2016		2017		2018	
	MagUp	MagDown	MagUp	MagDown	MagUp	MagDown
$\Lambda_b^0 \rightarrow \Lambda_c^+ \mu^- \bar{\nu}_\mu$	18.2M	18.2M	15.5M	15.5M	18.5M	18.5M
$\Lambda_b^0 \rightarrow \Lambda_c^+ \tau^- \bar{\nu}_\tau$	2.2M	2.2M	1.9M	1.9M	2.2M	2.2M
$\Lambda_b^0 \rightarrow \Lambda_c^+(2595)\mu^- \bar{\nu}_\mu$	1.1M	1.1M	0.9M	0.9M	1.1M	1.1M
$\Lambda_b^0 \rightarrow \Lambda_c^+(2595)\tau^- \bar{\nu}_\tau$	161k	161k	100k	100k	163k	180k
$\Lambda_b^0 \rightarrow \Lambda_c^+(2625)\mu^- \bar{\nu}_\mu$	5.9M	5.9M	4.9M	4.9M	5.9M	5.9M
$\Lambda_b^0 \rightarrow \Lambda_c^+(2625)\tau^- \bar{\nu}_\tau$	650k	660k	540k	560k	690k	670k
$\Lambda_b^0 \rightarrow \Lambda_c^+(2765)\mu^- \bar{\nu}_\mu$	1M	1M	450k	440k	505k	550k
$\Lambda_b^0 \rightarrow \Lambda_c^+(2880)\mu^- \bar{\nu}_\mu$	730k	520k	270k	273k	290k	323k
$\Lambda_b^0 \rightarrow \Lambda_c^+ D_s^- X$	18M	18M	15M	15M	18M	18M
$\Lambda_b^0 \rightarrow \Lambda_c^+(2595)D_s^- X$	1.3M	1.3M	1M	1M	1.3M	1.3M
$\Lambda_b^0 \rightarrow \Lambda_c^+(2625)D_s^- X$	5.4M	5.9M	4.5M	4.5M	5.5M	5.5M
Total	~ 400M		~ 360M		~ 400M	

TABLE 3.4.2: Breakdown of generated Monte Carlo events for each data-taking year and magnet polarity after the filtering and generator level cuts.

3.4.1 Tracker-only simulation

As discussed in Sec 3.1, signal $\Lambda_b^0 \rightarrow \Lambda_c^+ \mu^- \bar{\nu}_\mu$ decays dominate the analysed data sample with large yields, amounting to ca. 6 M events in 6 fb^{-1}. In order to keep the systematic uncertainty associated with the statistics of our simulation to a negligible level, we require high statistics MC samples. The assessment strategy of this source of systematic uncertainty has been described in Sec 3.11.1. Fig. 3.11.2 illustrates the comparison, as a ratio, between the statistical uncertainty and MC statistics associated systematic in fits to the corrected mass, clearly highlighting the similarity in size between the two. We aim at a minimum of a hundred-fold increase in MC statistics from the nominal scenario (fully simulated LHCb detector) for a sizeable reduction in the systematic component, which corresponds to approximately one billion events for each data-taking year prior to any pre-selection stage.

---

[10]Filtering selection constitute requirements enforced on the generated Monte Carlo in order to skim the candidates, thus saving to storage only those likely to pass the full selection. In this specific case, they overlap with the stripping selections discussed in Sec. 3.5.2 and summarised in Tab. 3.5.6

Simulating very large statistics samples with the minutiae of the LHCb detector is not a straightforward task, as it corresponds to computationally demanding processes reaching unfeasible processing times within the available computing resources. For this reason, we make use of a fast simulation with a modified detector description, merely including the tracking system and therefore known as *tracker-only* simulation[11] (Fig. 3.4.1). As the bottleneck of the MC processing resides in simulating the event dynamics happening in RICH detectors and calorimeters, the immediate advantage of excluding these components is a 90% reduction in simulation time and a more compact disk usage, smaller by ca. $\sim 40\%$. However, a simplified detector description comes at the cost of missing particle identification and trigger selection unavailability, which must be emulated offline in a data-driven way uniquely via the response of the LHCb tracking system. The emulation procedure has been described within the correction to MC simulation in Sec. 3.6.

3.5 Candidate selection

This section introduces the complete set of selection criteria, as applied to the data and simulation, to select a clean sample of reconstructed $(\Lambda_c^+ \mu^-)$ candidates.

Concurrently with data acquisition, recorded events undergo the first two stages of trigger selections (L0 and HLT1). While these focus on the reconstruction of single muon and Λ_c^+ candidates, the last trigger phase (HLT2) consists of a dedicated selection line for processes with final state $H_b \to H_c \mu X$. The complete set of used trigger lines has been described in Sec. 3.5.1.

---

[11]In tracker-only MC simulation calorimeters and muon system are not present in the detector description. RICH detectors, instead, have been included, but the generation of optical photons has been switched off.
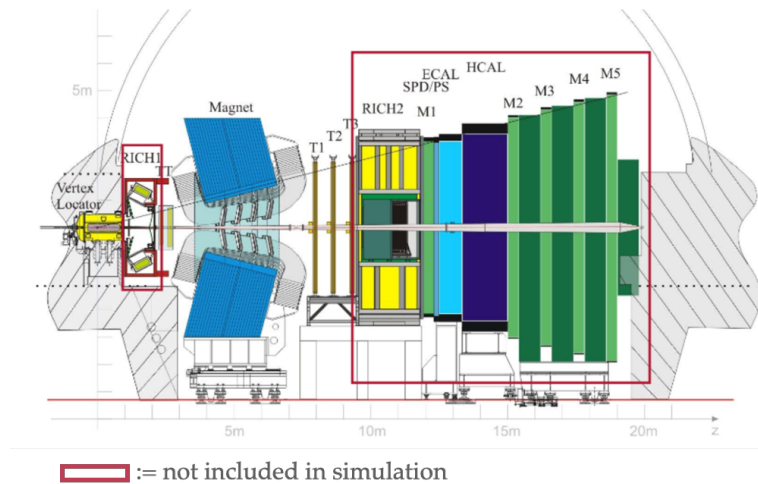
FIGURE 3.4.1: Illustration of the reduced LHCb detector description used for tracker-only MC simulations, with excluded components highlighted in red.

In Sec. 3.5.2, selection criteria applied at the offline *Stripping* stage have been detailed. They correspond to loose and centralised selection cuts, applied straight after the event reconstruction.

Finally, a discussion on the offline analysis selections follows from Sec. 3.5.3 onward, including the Multivariate classifier against fake Λ_c^+ backgrounds (Sec. 3.5.4), and the Multivariate charged track isolation against feed-down and doubly-charmed backgrounds (Sec. 3.5.5).

3.5.1 Trigger

The trigger selection is performed in two stages, as discussed in Sec. 3.3: the first is entirely hardware-based (Level 0, L0), while the second is built on software (High Level Trigger, HLT).

At the hardware trigger stage, we require L0Muon to be triggered by the Λ_b^0 signal candidate itself (Trigger On Signal, TOS). The corresponding selection implies the presence of at least one penetrating straight track, with transverse momentum above a defined value, whose trajectory is compatible with a muon candidate hitting the muon stations (M1-M5). Besides, it is required that the Scintillating Pad Detector (SPD) occupancy of the associated event must not exceed a certain threshold, aiming at rejecting saturated events taking up most of the computing resources in the reconstruction phase. Each data-taking year condition defines the associated thresholds for L0 trigger selections. A summary for Run 2 is available in Tab. 3.5.2. Corrections to mis-alignments between L0 trigger response in data and Monte Carlo have been discussed in Sec. 3.6.4.

Prior to the software trigger (HLT), a set of cuts is enforced to remove the busiest events from the processing chain (Global Event Cuts): variables describing the occupancy in the Velo, Inner, and Outer Tracker must fall within a fiducial range, as summarised in Tab. 3.5.1.

The next step in the trigger filtering chain consists of two separate stages: the first level, HLT1; the second and last level, HLT2. The reconstruction of signal Λ_c^+ candidates (TOS) involves the logical OR between two HLT1 lines, HLT1TrackMVA and HLT1TwoTrackMVA, as described in detail in Sec. 3.6.5. While HLT1TrackMVA requirements ensure high-quality track reconstruction, HLT1TwoTrackMVA selects two-track combinations, yielding a good quality vertexing. The HLT1 selection cuts for each of the trigger lines are listed in Tables 3.5.3 and 3.5.4. The final stage of the software trigger (HLT2) comprises a full reconstruction of tracks in the event, alongside loose selection requirements on decay products kinematics and parent $b-$hadron vertex quality. Λ_b^0 signal events are required to satisfy selection requirements imposed by the line Hlt2XcMuXForTauB2XcMu (TOS) listed in Table 3.5.5.

3.5.2 Stripping

Following the trigger stage, our data and simulation samples undergo additional event filtering in the *stripping*, according to requirements specified in the stripping selection listed in Tab. 3.5.6. In Run 2, the stripping stage corresponds to a set of specialised algorithms aimed at enhancing the signal content of recorded data by rejecting candidates arising from random or ghost track combinations and misidentified particles.

Global Event Cuts
$50 <$ VeloHits < 6000
$50 <$ ITHits < 3000
$50 <$ OTHits < 15000

TABLE 3.5.1: Selection corresponding to Global Event Cuts (GEC), running prior to the HLT filtering stage.

Year	p_T threshold	nSPDHits threshold
2016	$> 1.8 \,\text{GeV}$	< 450
2017	$> 1.35 \,\text{GeV}$	< 450
2018	$> 1.8 \,\text{GeV}$	< 450

TABLE 3.5.2: L0Muon trigger requirements in transverse momentum of the muon candidate and number of hits in the SPD per event, detailed for each of the analysed Run 2 years.

In the stripping selection, Λ_c^+ three-body decays are built from a combination of pions, protons and Kaons which pass a loose selection, encased in algorithms known as *standard particle containers*, including a specific set of cuts for each particle species. In addition, Λ_c^+ decay product candidates are subject to extra selections aimed at reducing misidentification and tracks ghost rates. Once constructed, Λ_c^+ candidates are subject to *combination* requirements (i.e. selection cuts applied before vertexing of decay products) and *parent* requirements (i.e. selection cuts applied after vertexing) to tackle the contribution from combinatorics of tracks.

The so-formed Λ_c candidates are combined with muon candidates, then subject to additional particle identification and track quality cuts to form parent Λ_b^0s. The latter also undergo *combination* and *parent* selection cuts in order to reduce the contribution of combinatorial backgrounds.

At last, the stripping line includes selections on the event level, as the event occupancy, the presence of at least one primary vertex (PV), and the triggering of the Hlt2 line (Tab. 3.5.5). As a consequence, data is required to contain the complete set of Λ_b^0 candidates categories: Trigger On Signal (TOS); Trigger Independent of Signal (TIS); Trigger On Both (TOB). Nonetheless, for this analysis, we exclusively focus on TOS candidates due to their higher signal purity.

3.5.3 Offline selection

An additional cut-based offline selection has been placed upon Λ_b^0 candidates selected by the stripping line. The corresponding cuts are listed in Table 3.5.7. We remark that a comprehensive list of variables used in this analysis, alongside a short description, is available in App. 3.A.

Description	Selection
Fiducial	

Description	Selection
Track transverse momentum	$0 < p_T < 60$ GeV
Track momentum	$0 < p < 200$ GeV
Track pseudo-rapidity	$2 < \eta < 4.9$
Event track multiplicity	`nTracks`< 700
Linear sum of Λ_c decay products p	$\sum_{i=p,K,\pi} p_i > 15$ GeV
Event occupancy	`nSPDHits`< 450
Λ_c mass	$2240 < m(pK^-\pi^+) < 2330$ MeV
Impact parameter Λ_c	$-7 < \log(\text{IP}(\Lambda_c)) < 2$
Λ_b mass	$2391 < m(\Lambda_c\mu) < 5620$ MeV
Λ_b corrected mass	$2500 < \text{M}_{\text{corr}}(\Lambda_b) < 7000$ MeV
Phase space edges	$0.01 < q^2 < 11.11$ GeV^2
	$-1 < \cos\theta_\mu < 1$
Additional	
	$\Delta\log\mathfrak{L}(\mu-\pi) > 2$
	$\Delta\log\mathfrak{L}(\mu-K) > 2$
Muon PID and track quality	$\Delta\log\mathfrak{L}(\mu-p) > 2$
	`isMuon == 1`
	`GhostProb` < 0.2
MVA classifier (against fake Λ_c bkg.)	MVA > 0.5
MVA classifier (against Λ_c^* bkg.)	MVA < 0.35

TABLE 3.5.7: Fiducial and additional offline selection requirements for the signal decay $\Lambda_b^0 \to \Lambda_c^+ \mu^- \bar{\nu}_\mu$, placed upon candidates after the stripping stage.

Later in this Section, fiducial requirements, including particle identification (PID) and track quality requirements have been discussed. The selection strategy against fake Λ_c^+ backgrounds has been detailed in Sec. 3.5.4, while the reduction of partially reconstructed Λ_c^* backgrounds (charged track *isolation* multivariate selection) has been described in subsection 3.5.5.

Fiducial requirements

Particles compatible with a Λ_b candidate undergo a dedicated series of fiducial cuts, as listed in Table 3.5.7, which comprise kinematic and track multiplicity selections. The main motivation for their existence resides in defining a fiducial region where to compute corrections to Monte Carlo samples, mostly involving the particle identification response modelled with data (described in Sec. 3.6.1). Furthermore, requirements on the linear sum of the momenta of Λ_c decay products and detector occupancy are aligned with cuts placed at the generation level or in the context of correction to simulation. Besides, the Λ_c mass and Λ_c impact parameter requirements correspond to the fit range used to evaluate the contribution from prompt Λ_c and to subtract the fake Λ_c background contribution. A loose requirement on the Λ_b mass is applied to minimise the contribution from fake candidates. Moreover, the selection enforced on the Λ_b corrected mass

Variable	Selection requirement
track preselection	
p_T	$> 0.6\,\text{GeV}$
p	$> 5\,\text{GeV}$
χ_{trk}^2/ndof	< 4
χ_{trk}^2/ndof	< 2.5
GhostProb	< 0.2
p_T, IP_{χ^2}	$\left(p_T > 25\,\text{GeV} \wedge \text{IP}_{\chi^2} > 7.4\right) \vee \left[\left(1 < p_T < 25\,\text{GeV}\right) \wedge \right.$
	$\left. \log \text{IP}_{\chi^2} > \left(\frac{1}{p_T\,[\text{GeV}]-1}\right)^2 + \left(\frac{1.1}{25\,[\text{GeV}]}\right)\left(25\,[\text{GeV}] - p_T\right) + \log(7.4)\right]$

TABLE 3.5.3: Requirements for the one-track HLT1 selection, acting on $\Lambda_c^+(\rightarrow pK^-\pi^+)$ decay products.

mirrors the fit range used to evaluate the signal yield in bins of q^2 and $\cos\theta_\mu$. Lastly, cuts on the phase space observables (q^2 and $\cos\theta_\mu$) correspond to the physical limits of the $\Lambda_b^0 \rightarrow \Lambda_c^+ \mu^- \bar{\nu}_\mu$ decay phase space.

Particle identification and track ghost rate

The tightest particle identification and track ghost probability requirements for hadrons, here including pions, kaons, and protons, are enforced at the stripping stage as reported in Tab.3.5.6. No further PID requirements have been defined for hadrons in the offline selection stage. Nevertheless, loose PID and track ghost probability requirements have been placed upon muon candidates, as described in Table 3.5.7, in order to discard possible fake tracks.

3.5.4 Multivariate classifier against fake Λ_c backgrounds

Despite the above selection cuts, reconstructed Λ_c decays are still polluted with misidentified and random track combinations in $pK^-\pi^+$ final states. In order to tame this component, from here onward defined as *fake* Λ_c background contribution, a dedicated multivariate classification (MVA) has been developed. Several approaches have been pursued, which resulted in the choice of XGBoost [40], a classifier based on gradient tree boosting [41], as the fastest-to-train and best-performing model.

The classifier has been trained separately for each data-taking year using $\Lambda_b^0 \rightarrow \Lambda_c^+ \mu^- \bar{\nu}_\mu$ decays. To model the signal component, we use MC simulation in the $m(pK^-\pi^+)$ region within $3\,\sigma$ from the Λ_c resonance mass[12] (Fig. 3.5.1a). The upper and lower data sidebands have been defined considering $m(pK^-\pi^+)$ values outside the $3\,\sigma$ peaking region to model fake Λ_c backgrounds (Fig. 3.5.1b) with negligible signal contamination. Input features to characterise signal and background samples

---

[12] $1\,\sigma = 8\,\text{MeV}$ is taken as reference LHCb mass resolution in $B \rightarrow J/\Psi X$ decays.

Variable	Selection requirement
track preselection	
p_T	$> 0.6\,\mathrm{GeV}$
p	$> 5\,\mathrm{GeV}$
$\chi^2_{trk}/\mathrm{ndof}$	< 2.5
GhostProb	< 0.2
IP_{χ^2}	>4
2-body combination	
$\sum p_T$	$> 2\,\mathrm{GeV}$
DOCA_{χ^2}	< 10
χ^2_{vtx}	< 10
$\mathrm{M}_{\mathrm{corr}}$	$> 1\,\mathrm{GeV}$
DIRA	> 0
MatrixNet [39] MVA score	> 0.95

TABLE 3.5.4: Requirements for the two-track HLT1 selection, acting on $\Lambda_c^+(\to pK^-\pi^+)$ decay products.

Particle	Variable	Selection requirement
K, π, p	p	$> 5\,\mathrm{GeV}$
Λ_c^+	$\geq 1\,\mathrm{decay\ prod.}\ p_T$	$> 0.8\,\mathrm{GeV}$
Λ_c^+	DOCA (combination)	$< 0.10\,\mathrm{mm}$
Λ_b^0	FD_{χ^2}	> 50
Λ_b^0	DOCA (parent)	$< 0.50\,\mathrm{mm}$

TABLE 3.5.5: Requirements for the HLT2 selection, acting on the Λ_b^0 and its decay products.

have been chosen in order to provide the maximum discriminating power, although there is a null correlation between MVA output and phase space, fit variables q^2, $\cos\theta_\mu$, $\mathrm{M}_{\mathrm{corr}}(\Lambda_b)$. Table 3.5.8 summarises the full set of input variables to the MVA classifier. All the particle identification quantities have been corrected to remove any data/MC differences, following the approach described in Sec. 3.6.1. A compendium of comparison plots (Fig. 3.C.1) and linear correlation coefficients (Fig. 3.C.2) for 2016 input features can be found in Appendix 3.C.

Before its supervised training, the MVA model undergoes a preliminary input parameter (*hyper-parameters*) tuning phase, aiming to optimise its performance. The optimal parameter space point is identified by maximising a defined metric through a grid-search strategy. For this study, we have selected the Area Under the Curve (AUC) of the Receiver Operator Characteristic (ROC) to measure the model classification power between the signal and background.

For the training procedure and a final, unbiased evaluation of the MVA classification performance, input samples get divided into *training* and *test* sets, respectively. To reduce the representation imbalance in the input features for each class between the two splits, the model gets iteratively trained and sequentially tested on distinct sampled portions, or *folds*, of the provided samples (Stratified k-Folding Cross Validation). The uniformity in the proportion of input features for each class across separate folds translates into a consistent performance of the MVA classifier, as demonstrated in the ROC curve for the test set in Fig. 3.5.2a. Neural Network-based PID variables dominate when generating the classification, followed by the linear sum of the transverse momentum of Λ_c decay products (Fig. 3.5.2b). The MVA output distributions are illustrated in Fig. 3.5.3, featuring a good separation and no sign of discrepancy between the classifier response on train and test sets (*over-training*). Moreover, the absence of correlation in the output classification score with phase space and fit variables has been assessed for both the data and MC samples. Additional plots have been included in Appendix 3.C.

Identifying the optimal MVA selection point corresponds to maximising the significance of the Λ_c signal observation. The chosen metric is the Figure of Merit, FoM $= S / \sqrt{S + B}$, evaluated as a function of the MVA threshold score. The numerator $S = N_{\text{pred}}^{\text{sig}} \cdot \epsilon_{\text{sel}}$ is the predicted signal $N_{\text{pred}}^{\text{sig}}$ rescaled by the selection efficiency ϵ_{sel}. In an extended form:

$$S = 2 \cdot \sigma_{pp}(\sqrt{s}) \cdot \mathscr{L} \cdot f_{\Lambda_b} \cdot \mathscr{B}(\Lambda_b^0 \to \Lambda_c^+ \mu^- \bar{\nu}_\mu) \cdot \mathscr{B}(\Lambda_c \to pK^- \pi^+) \cdot \epsilon_{\text{sel}}, \tag{3.3}$$

where $\sigma_{pp}(\sqrt{s})$ denotes the pp cross-section evaluated ad the centre-of-mass energy $\sqrt{s}$; $\mathscr{L}$ represents the integrated luminosity for the considered data-taking year; f_{Λ_b} is the fragmentation fraction of a b quark to a Λ_b baryon; $\mathscr{B}$ denotes the branching fraction of the process enclosed in brackets. On the contrary, the predicted background B has been determined via an unbinned maximum likelihood linear fit to the data side-bands after the MVA cut, then integrated within the $m(pK^- \pi^+)$ peaking region. This approach results in the fastest and does not deviate from alternative methods, including exponential fit modelling the combinatorial component in the upper side-band, then extrapolated in the lower $m(pK^- \pi^+)$ region; full $m(pK^- \pi^+)$ range data fit with exponential and a sum of two Crystal-Ball functions with opposite tail parameters. Fig. 3.5.4 depicts the significance as a function of the MVA cut, superimposed to the signal and background efficiencies. The maximal significance is reached at 0.44 for the 2016 sample, corresponding to an average signal efficiency of $\sim 89\%$ and background efficiency of $\sim 19\%$. Nonetheless, the working point is taken consistently for all years at 0.5 for improved background rejection, particularly of the misidentified component. This choice is associated with a signal efficiency of $\sim 87\%$ and background efficiency of $\sim 16\%$ on the 2016 sample. Similar trends in the MVA cut optimisation have been found in other data taking years considered in this analysis.

Variable	Description
$\chi^2_{vtx}(\Lambda_c)$	χ^2 of the vertex fit to the decay of Λ_c
$\text{FD}_{\chi^2}(\Lambda_c)$	Flight Distance (FD) vector of Λ_c between its production and decay vertices

Variable	Description
$\mathrm{IP}_{\chi^2}(\Lambda_c)$	χ^2 of the Impact parameter (IP) of the Λ_c
$\mathrm{minIP}_{\chi^2}(p)$	Minimum χ^2 of the IP of p to its production vertex
$\mathrm{minIP}_{\chi^2}(\pi)$	Minimum χ^2 of the IP of π to its production vertex
$\mathrm{minIP}_{\chi^2}(K)$	Minimum χ^2 of the IP of K to its production vertex
$\mathrm{ProbNN}_K(K)$	Neural network-based probability of the particle K being identified as a kaon
$\mathrm{ProbNN}_\pi(\pi)$	Neural network-based probability of the particle π being identified as a pion
$\mathrm{ProbNN}_p(p)$	Neural network-based probability of the particle p being identified as a proton
$p_T^p + p_T^K + p_T^\pi$	Linear sum of Λ_c decay products transverse momentum

TABLE 3.5.8: Definition of input features to the MVA classifier for rejecting fake Λ_c backgrounds.
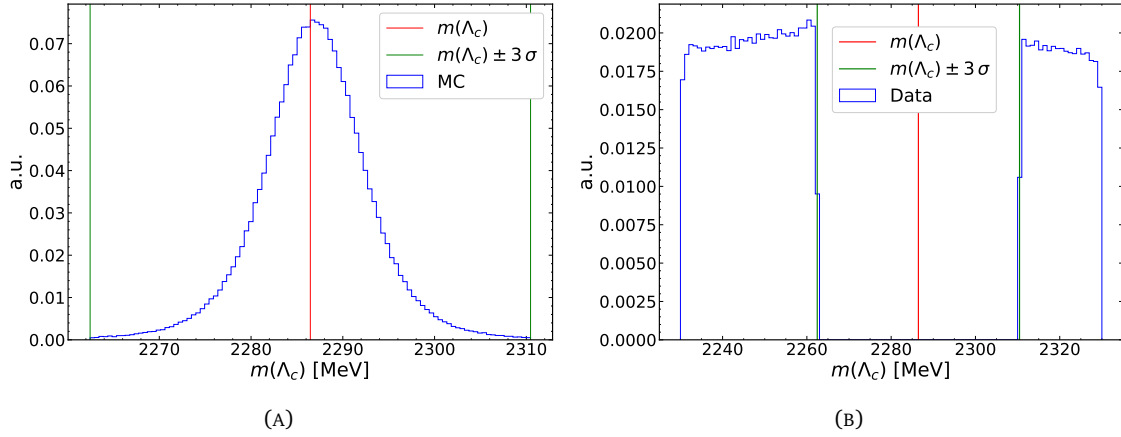
FIGURE 3.5.1: Λ_c mass distribution in selected regions for input samples in the MVA training against fake Λ_c backgrounds for 2016 $\Lambda_b^0 \to \Lambda_c^+ \mu^- \bar{\nu}_\mu$ decays: (A) the signal sample, modelled using MC simulation in the peak mass region; (B) the background component, modelled using data side-bands. The $1\,\sigma$ limit corresponds to the $8\,\mathrm{MeV}$ mass resolution for $B \to J/\Psi X$ decays.

(A) (B)
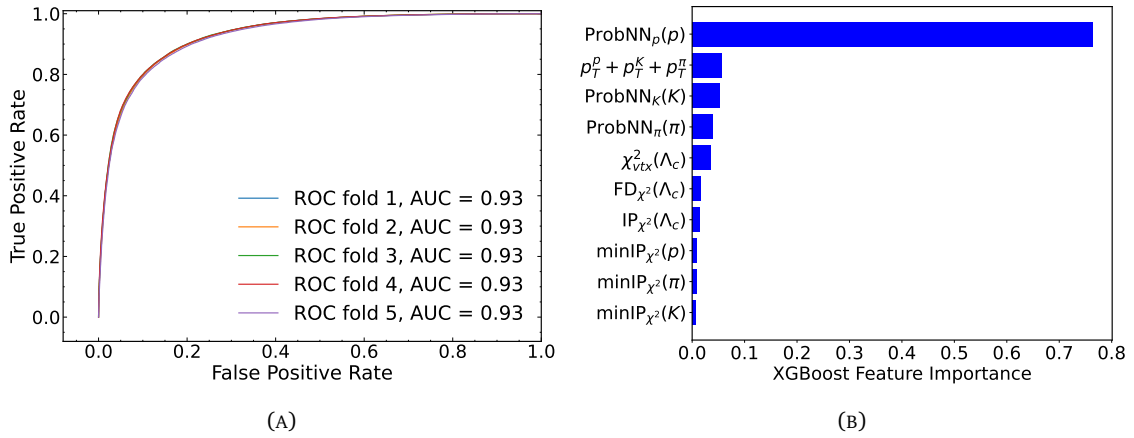
FIGURE 3.5.2: Left (A): Receiver Operator Characteristic (ROC) curves for each of the training folds with corresponding Area Under the Curve (AUC) score for an MVA classifier trained on $\Lambda_b^0 \to \Lambda_c^+ \mu^- \bar{\nu}_\mu$ decays. Right (B): input features sorted by importance score (average gain in each tree split), as evaluated in the 2016 MVA model training.
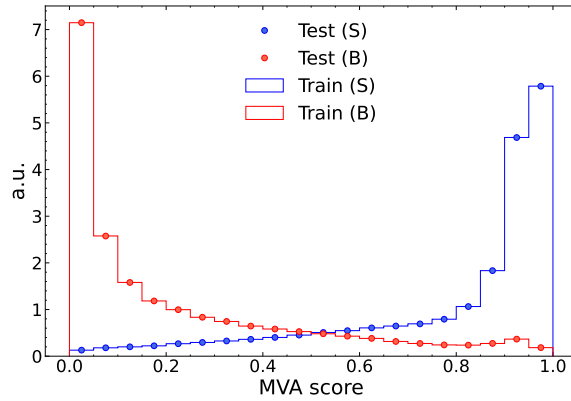
FIGURE 3.5.3: Comparison of the 2016 MVA classifier score between train (histogram) and test (points) sets drawn in red and blue, respectively.

Particle	Selection
Event level cuts	nSPDHits < 600 At least 1 Primary Vertex (PV) Hlt2XcMuXForTauB2XcMuDecision == 1
Muon	isMuon==1 (StdAllLooseMuons) $\mathrm{IP}_{\chi^2}(\mathrm{PV}) > 16$ GhostProb < 0.5 $\Delta\log\mathcal{L}(\mu - \pi) > -200$ $p > 3$ GeV
Kaons	$\Delta\log\mathcal{L}(K - \pi) > -5$ ⎫ $p_T > 250$ MeV ⎬ StdLooseKaons $\mathrm{IP}_{\chi^2}(\mathrm{PV}) > 4$ ⎭ $\Delta\log\mathcal{L}(K - \pi) > 4$ $\mathrm{IP}_{\chi^2}(\mathrm{PV}) > 9$ $p > 2$ GeV $p_T > 300$ MeV GhostProb < 0.5
Pion	$p_T > 250$ MeV ⎫ StdLoosePions $\mathrm{IP}_{\chi^2}(\mathrm{PV}) > 4$ ⎭ $\Delta\log\mathcal{L}(K - \pi) < 2$ $\mathrm{IP}_{\chi^2}(\mathrm{PV}) > 9$ $p > 2$ GeV $p_T > 300$ MeV GhostProb < 0.5
Proton	$\Delta\log\mathcal{L}(p - \pi) > -5$ ⎫ $p_T > 250$ MeV ⎬ StdLooseProtons $\mathrm{IP}_{\chi^2}(\mathrm{PV}) > 4$ ⎭ $\Delta\log\mathcal{L}(p - \pi) > 0$ $\mathrm{IP}_{\chi^2}(\mathrm{PV}) > 9$ $p > 2$ GeV $p_T > 300$ MeV GhostProb < 0.5
$\Lambda_c^+ (\to pK^-\pi^+)$	$\lvert m(pK^-\pi^+) - m(\Lambda_c^+)_{\mathrm{PDG}}\rvert < 100$ MeV ⎫ $\sum_{\mathrm{daug}} p_T > 2500$ MeV ⎬ Combination cut $\sum_{\mathrm{daug}} p_T > 2500$ MeV ⎫ $\lvert m(pK^-\pi^+) - m(\Lambda_c^+)_{\mathrm{PDG}}\rvert < 80$ MeV ⎪ χ^2/ndof (decay vertex) < 4 ⎬ Parent cut $\mathrm{FD}_{\chi^2} > 25$ ⎪ DIRA> 0.999 ⎭
$\Lambda_b^0 (\to \Lambda_c^+\mu^- \text{ or } \Lambda_c^+\mu^+)$	$m(\Lambda_c\mu) < 10.2$ GeV Combination cut $0 < m(\Lambda_c\mu) < 10$ GeV ⎫ χ^2/ndof (decay vertex) < 6 ⎬ Parent cut DIRA > 0.999 ⎭

TABLE 3.5.6: Stripping selection requirements for the signal decay $\Lambda_b^0 \to \Lambda_c^+ \mu^- \bar{\nu}_\mu$. Worth noting here that Monte Carlo filtering cuts, applied upon candidates prior to storage placement, are completely overlapping with this stripping selection flow.
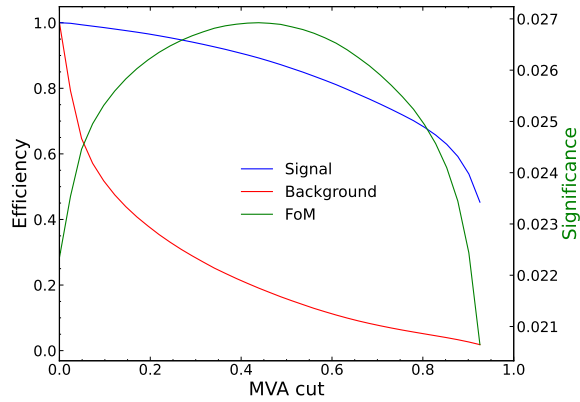
FIGURE 3.5.4: Significance of the cut on the MVA output, evaluated as Figure of Merit (FoM $= S/\sqrt{S+B}$), to reject fake Λ_c backgrounds in $\Lambda_b^0 \to \Lambda_c^+ \mu^- \bar{\nu}_\mu$ decays. Drawn as a green solid curve, the FoM is compared to the signal (blue) and background (red) efficiency as a function of the MVA cut. The chosen background suppression working point is MVA > 0.5.

3.5.5   Multivariate charged track isolation

Identifying additional particles in the event associated with the Λ_b decay is one of the strategies pursued to reject partially reconstructed physics backgrounds. We employ tools developed for the Run 1 $R(D^*)$ analysis [42], where a multivariate classifier is trained to tell particles belonging to the rest of the event from those associated to the signal $b-$hadron vertex. Fig. 3.5.5 schematically demonstrates the classification principle on Λ_b semileptonic transitions: highlighted in red, isolated tracks not belonging to the signal region; shown in green, unreconstructed extra tracks of the Λ_b decay.

Input variables include particle properties such as the track transverse momentum, the direction angle with respect to the b-hadron vertex, and quantities to assess the vertex's quality fit with the extra track(s) inclusion in the signal vertex. Except for particles already used to form the b candidate, the algorithm runs through all reconstructed tracks, identifying any extra particle likely to be associated with the signal, which gets assigned a large MVA score. The largest classification score in the event, the *isolation MVA score*, constitutes a powerful discriminating variable between the signal and the backgrounds with incorrectly unassigned final-state particles.

The classification performances of the MVA tool from Ref. [42] are also compelling in the case of baryonic Λ_b transitions, despite the sub-optimal training set comprising simulated mesonic semileptonic decays. The clear separation between signal candidates and backgrounds from feed-down and double charm, as a function of the MVA isolation score, is shown in Fig. 3.5.6. A selection cut is placed to reject candidates with an isolation score larger than 0.35 while preserving most of the signal sample.

3.6   Correction of Monte Carlo simulation

Despite the incredible sophistication of the LHCb simulation toolset, the output Monte Carlo distributions of simulated physics decays is still unmatched by the observed data. Motivations are multi-fold, ranging from overlooked detector effects to approximated physics process descriptions, including unwanted systematic effects. Consequently, it is paramount to perfect the simulated samples, particularly in high-precision measurements where the abundance of observed signal
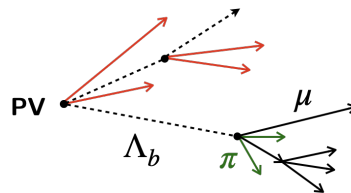
FIGURE 3.5.5: Schematic illustration of the multivariate isolation classification in Λ_b semimuonic transitions. Extra tracks associated with the Λ_b decay vertex (green) are further considered in the analysis, while those belonging to the rest of the event (red) get discarded.

yields demands meticulous control of any introduced bias. Moreover, this analysis presents the added complication of missing bits in the simulation process, relying exclusively on the response of the tracking systems (Sec. 3.4.1). Any lacking and mis-modelled information must be included while correctly reproducing data observations. Hereafter we introduce a series of dedicated data-driven procedures aimed at correcting (or modelling *ex-novo*) many aspects of the MC simulation: particle identification (Sec. 3.6.1); decay model description of $\Lambda_b^0 \to \Lambda_c^+ \ell^- \bar{\nu}_\ell$ decays (Sec. 3.6.2); production kinematics of Λ_b^0 (Sec. 3.6.3); trigger response (Sec. 3.6.4 and 3.6.5); track reconstruction (Sec. 3.6.6); response of charged isolation in $\Lambda_b^0 \to \Lambda_c^{*+} \mu^- \bar{\nu}_\mu$ (Sec. 3.6.7); kinematic agreement with the data (Sec. 3.6.8).

3.6.1 Correction to particle identification

Simulating the response of LHCb detectors devoted to the PID (RICH, calorimeters, and muon chambers) is a challenging task. Not only it implies modelling variations due to event dynamics (*i.e.* occupancy and particles kinematics), but also capturing the effect of fluctuating experimental conditions, ultimately affecting the detector performances. In addition, our reliance on tracker-only MC translates into a complete absence of any PID information (Sec. 3.4.1). Hence, a data-driven approach is followed to achieve a realistic PID modelling in simulation.

The PID emulation technique relies on the use of selected calibration samples[13] yielding low background contamination, prior to any PID requirement, as a result of basic fiducial cuts. The residual background contribution, mostly from track combinatorics, is statistically subtracted via the sPlot technique [43] from fits to the reconstructed mass of the parent particle. The efficiency

---

[13]Depending on the final state particle and the required kinematic coverage, the decay channels used as calibration samples include: $D^{*+} \to (D^0 \to K^- \pi^+)\pi^+$, $\Lambda^0 \to p\pi^-$, $J/\Psi \to \mu^+\mu^-$, $\Lambda_b^0 \to (\Lambda_c^+ \to pK^-\pi^+)\pi^-$.
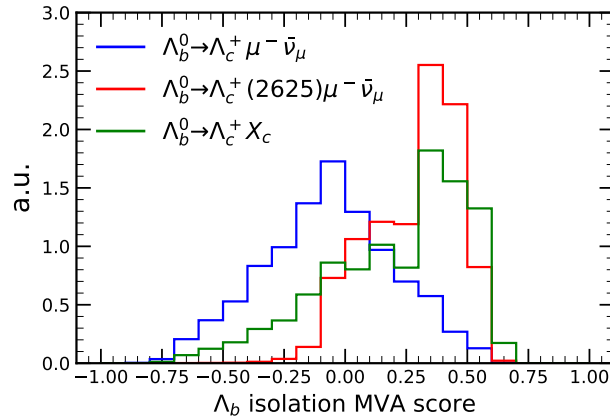
FIGURE 3.5.6: Λ_b isolation MVA output distribution for Run 2 MC simulation. Comparison between $\Lambda_b^0 \to \Lambda_c^+ \mu^- \bar{\nu}_\mu$ signal (blue) and two background channels with additional particles in the final state: feed-down $\Lambda_b^0 \to \Lambda_c^+(2625)\mu^- \bar{\nu}_\mu$ (red), double-charm $\Lambda_b^0 \to \Lambda_c^+ X_c$ (green).

of a specific particle PID selection is hence evaluated on the calibration sample, and parameterised as a function of the particle's momentum p, pseudo-rapidity η, and event occupancy `nTracks`. In the assumption of independence between the PID response of each particle species, the total per-event PID efficiency, w_{PID}, is expressed as the product of each contribution $w_{\text{PID}}^j(p^j, \eta^j, \text{nTracks})$ from the calibration sample, with j final state particle.

PID selections in this analysis mostly occur at the stripping and offline level, as summarised in Tab. 3.5.6 and Tab. 3.5.7. The corresponding PID response, detailed in bins of p, η, and `nTracks`, is shown in Fig. 3.6.1 for a specific binning choice. Albeit arbitrary, the binning is chosen to minimise the efficiency variation within each bin, possibly introducing differences between the reference and calibration samples. The total efficiency variation induced by the PID selection, as a function of phase space observables, is presented in Fig. 3.D.1.

In addition to the PID response modelling above, we explicitly resample the distribution of PID variables used as input to the MVA classifier against fake Λ_c backgrounds (Sec. 3.5.4) from the calibration sample. A direct advantage of this approach consists in preserved underlying correlations between PID variables and event kinematics.

3.6.2 Form factor correction to $\Lambda_b^0 \to \Lambda_c^+ \ell^- \bar{\nu}_\ell$

Within the LHCb software framework, b-hadron decays are generated through the `EvtGen` tool [37], which is tuned to a specified decay model to reproduce the predicted kinematics of the final state in phase space. In the case of Λ_b^0 semileptonic transitions, decay amplitudes are described in terms of hadronic FF according to the Heavy Quark Effective Theory (HQET). Nonetheless, as more precise predictions calculated on the Lattice are available to date [44, 45], we introduce a dedicated correction to the generated decay model. In fact, we expect the shape of the q^2 distribution to strongly depend on the chosen results, hence influencing the selection efficiency.

For this purpose, we perform a bi-dimensional reweighing of the $\Lambda_b^0 \to \Lambda_c^+ \ell^- \bar{\nu}_\ell$ ($\ell = \mu, \tau$) simulated samples, in bins of true q^2 and $\cos\theta_\ell$. The full expression of the decay density model, as implemented in this analysis, is provided in App. 2.D, whereas the complete set of FF parameters in the helicity formalism is introduced in Sec. 3.10.3. We closely follow Ref. [44] and limit the study to a first-order FF expansion in q^2 (Eq. 3.19), with each term corresponding to the LQCD fit result.

For each simulated event falling in a phase space bin i, a correction factor is assigned, corresponding to the ratio of predicted probability in the LQCD model and in the HQET model, prior to any cut at the generation level:

$$w_{\text{FF corr}}^i = \kappa \frac{d^2 N_{\text{LQCD}}^i}{dq^2 \, d\cos\theta_\ell} \Big/ \kappa' \frac{d^2 N_{\text{gen. lev.}}^i}{dq^2 \, d\cos\theta_\ell} \,. \tag{3.4}$$

with κ, κ' normalisation factors. The shape of the Λ_b^0 corrected mass is stable against model variations, as Fig. 3.6.3 demonstrates in the comparison between M_{corr} distributions before (HQET) and after (LQCD) enforcing the correction to the FF model for the muonic decay. Instead, the
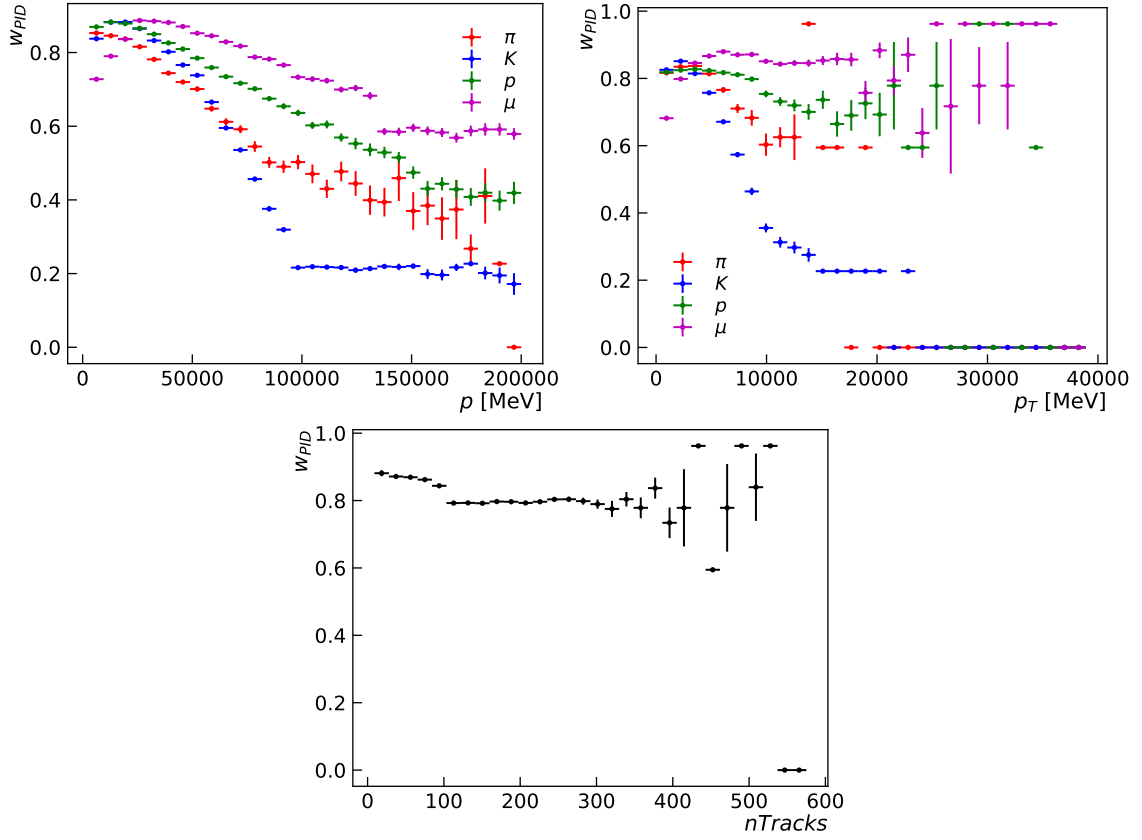
FIGURE 3.6.1: Profile of the PID correction weights for various particle species as a function of the track momentum (top left), transverse momentum (top right), and number of tracks per event (bottom) for the 2016 `MagDown` $\Lambda_b^0 \to \Lambda_c^+ \mu^- \bar{\nu}_\mu$ simulation sample.

reweighing process deeply impacts the decay kinematics, sculpting the phase space efficiency (Fig. 3.6.3) as a reflection of consistent underlying differences between the two model descriptions. A comparison between the differential density shape in phase space before and after the correction is shown in Fig. 3.6.4.

Analogous corrections can be computed for background transitions with $\Lambda_c^*(2595, 2625)$ resonances, also simulated within the heavy quark model formalism. In this case, the validity of available LQCD predictions is limited to high q^2 [46]. Consequently, we opt for a data-driven correction procedure to improve on the description of lower end of the spectrum, as detailed in App. 3.J.

3.6.3 Correction to Λ_b production kinematics

The production kinematics of Λ_b^0 baryons exhibits a strong dependence on the transverse momentum p_T, as evident in Fig. 3.6.5 from LHCb data [47]. MC simulation has not been tuned to
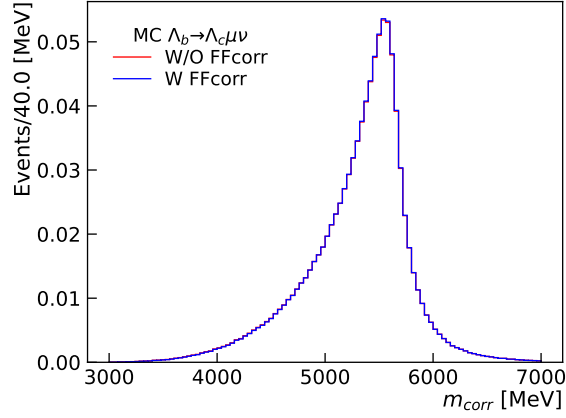
FIGURE 3.6.2: Comparison of corrected mass distributions for $\Lambda_b^0 \to \Lambda_c^+ \mu^- \bar{\nu}_\mu$ simulated decays with (blue) and without (red) the FF correction after the full selection. Only the 2016 `MagDown` sample is shown.
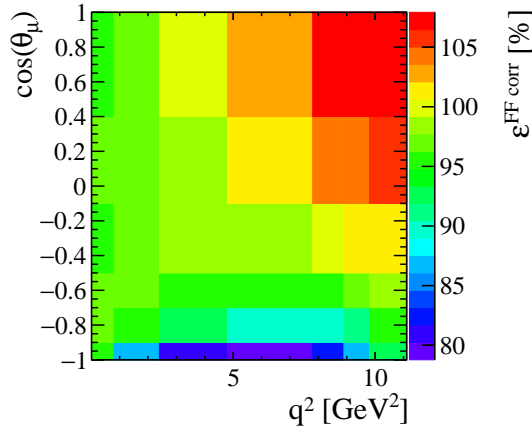
FIGURE 3.6.3: Efficiency of the correction to the Λ_b generation model as a function of the true phase space observables q^2, $\cos\theta_\mu$ for the 2016 `MagDown` signal sample, with all the simulation corrections enforced.

account for the production rate kinematic dependence, which is instead assumed to be flat. As a result, it does not accurately reproduce kinematic properties of Λ_b^0 baryons, yielding a discrepancy in both p and p_T, which impacts the total selection efficiency. We correct simulation using $\Lambda_b^0 \to (J/\Psi \to \mu^+\mu^-) p K^-$ decays since they represent a clean sample of Λ_b^0 baryons for which the trigger efficiency can be accurately modelled.

We select a clean sample of $\Lambda_b^0 \to (J/\Psi \to \mu^+\mu^-) p K^-$ in data by applying loose preselection cuts and using an optimised gradient boosting classifier to tame combinatorial backgrounds. We enforce a requirement of at least $2\,\text{GeV}$ on muons momentum and transverse momentum to isolate `L0Muon` trigger effects, as kinematics in the region below this threshold is modelled with $B^+ \to J/\Psi K^+$ decays (Sec. 3.6.4). Ultimately reflection backgrounds arising from decays with
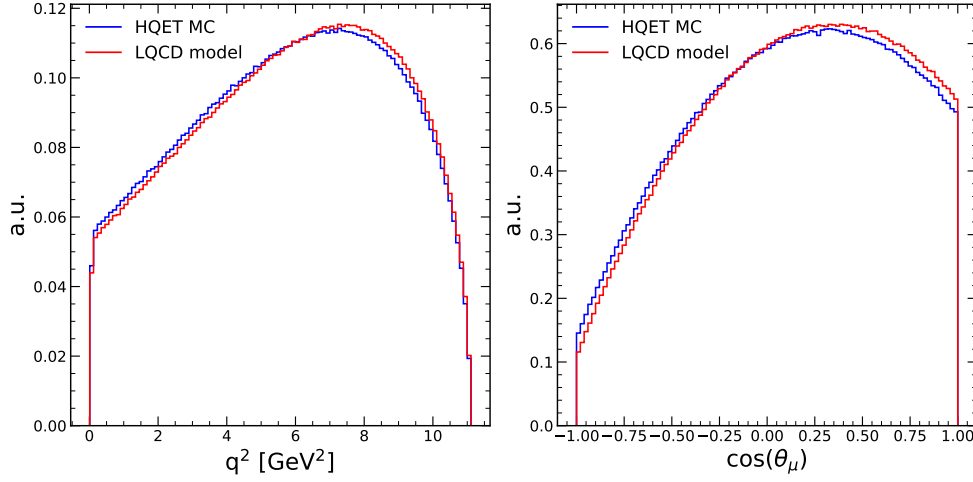
FIGURE 3.6.4: Comparison of phase space distributions for signal simulated decays with the HQET description (blue) and implemented model with LQCD FF parameters (red).
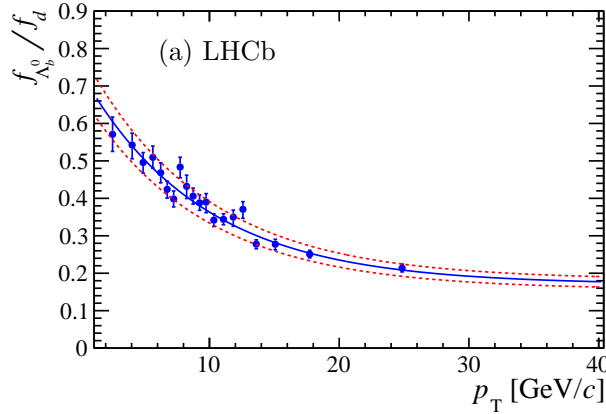
FIGURE 3.6.5: Ratio of the production rate of Λ_b baryons to B^0 mesons as a function of the p_T of the Λ_b baryon, measured by LHCb in pp collisions at $\sqrt{s} = 7\,\text{TeV}$ [47].

one or multiple hadrons wrongly tagged as a proton or kaon[14], are rejected by placing a cut on the invariant mass of the parent particle in the hypothesis of a misidentification. At this stage, the residual background contamination in the signal region is almost null, as visible from Fig. 3.6.7 showing an unbinned maximum likelihood data fit to the Λ_b^0 invariant mass. Fig. 3.6.6 illustrates the comparison between MC and data, the latter re-weighted using the `sPlot` technique [43] to remove background contributions, for fully selected $\Lambda_b^0 \to J/\Psi\,p\,K^-$ decays. We observe considerably softer data distributions than simulated ones.

---

[14]Decays of such type include: $\bar{B}_s^0 \to J/\Psi(\phi \to K^+K^-)$, $B^0 \to J/\Psi\,\pi^+K^-$, $\bar{\Lambda}_b^0 \to J/\Psi\,\bar{p}K^+$.
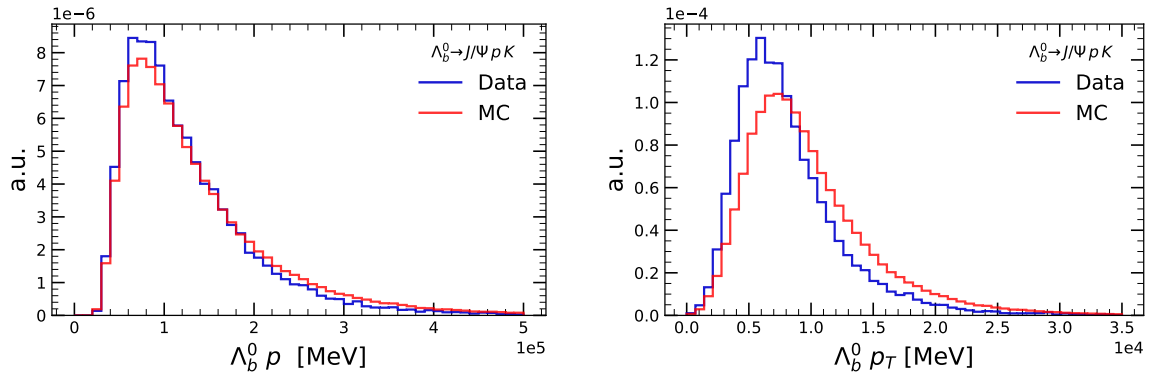
FIGURE 3.6.6: Comparison between momentum (left panel) and transverse momentum (right panel) of the Λ_b^0 between MC simulation and selected data in $\Lambda_b^0 \to J/\Psi p K^-$ decays. Distributions have been normalised to have unit area.
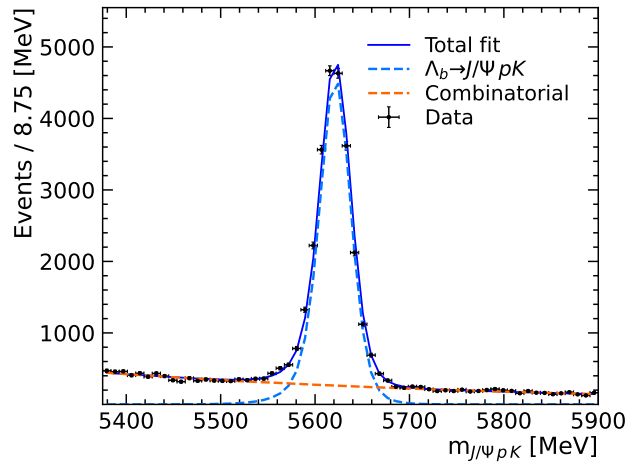
FIGURE 3.6.7: Fit to the invariant mass of $\Lambda_b^0 \to J/\Psi p K^-$ data recorded with the LHCb detector during the 2016 data-taking.

Weights correcting the simulated Λ_b^0 kinematics, $dN_{\text{Data}}/dN_{\text{MC}}$, have been retrieved from a comparison between normalised data and MC distributions in bins of $\Lambda_b^0(p, p_T)$ for each of the Run 2 years. Corrections corresponding to the 2016 sample are shown in Fig. 3.6.8, with similar trends observed in 2017 and 2018.
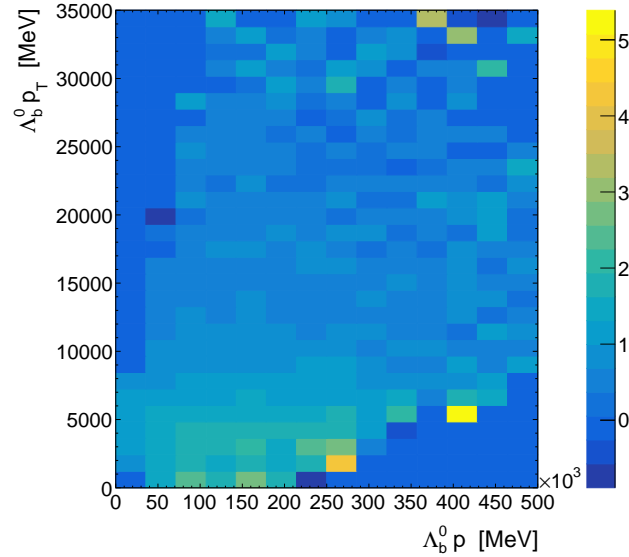
FIGURE 3.6.8: Map of kinematic weights used to correct 2016 MC simulations to account for the Λ_b^0 production kinematics, as obtained from $\Lambda_b^0 \to J/\Psi p K^-$ decays.

3.6.4 L0 trigger emulation

Two are the main components of the trigger decision we enforce at the hardware level: the first comprises a selection on the event occupancy in the scintillating pad detector, nSPD< 450, whose value is stable across data-taking years; the second consists in a condition-dependent threshold cut for the reconstructed transverse momentum of a penetrating straight track reaching the muon detection system, compatible with the hypothesis of a muon with large p_T (Sec. 3.3).

In our simulated samples, the lack of the simulated response of any detection system other than the trackers translates into the urge to model every stage of the trigger selection. Particularly for the L0Muon trigger, we separately emulate the two selection requirements with $B^+ \to (J/\Psi \to \mu^+\mu^-)K^+$ reconstructed data, in the hypothesis of perfect factorisation between them. The advantage of using these decays resides in the large signal purity obtained with loose preselection cuts and almost a 100% efficiency of the L0Muon trigger, whereby any background contamination is subtracted via the sPlot technique [43].

Firstly, the nSPD requirement effect is modelled in bins of event occupancy nTracks, with reconstructed $B^+ \to J/\Psi K^+$ decays[15] firing a L0DiMuon trigger line. This choice follows from the presence of a looser nSPD selection, nSPD< 900. The efficiency of the nSPD cut is illustrated in

---

[15]We note here that the emulation cannot be performed on fully simulated decays, as the correlation between nSPD and nTracks is not correctly reproduced in MC.

bins of `nTracks` in the left panel of Fig. 3.6.9. Before enforcing the emulation, we reweigh the incorrectly simulated `nTracks` distribution in signal tracker-only MC to match the calibration one from $B^+ \to J/\Psi K^+$ data.

The pursued approach for the emulation of the p_T cut consists of binning the efficiency of the selection requirement in muon momentum and transverse momentum (p, p_T) after the application of the nSPD cut. Similarly to the previous stage, we use $B^+ \to J/\Psi K^+$ selected data and follow a tag&probe technique. The results for the 2016 sample are shown in the right panel of Fig. 3.6.9. As a result of the significant efficiency sculpting in the lower end of the spectrum originating from the tight p_T requirement, and given the significant correlations with the phase space observables, the q^2, $\cos\theta_\mu$ distributions (Fig. 3.6.10) are heavily altered. This observation suggests the necessity of a dedicated systematic uncertainty to be assessed for the parameters of interest as a function of the muon p_T chosen threshold.
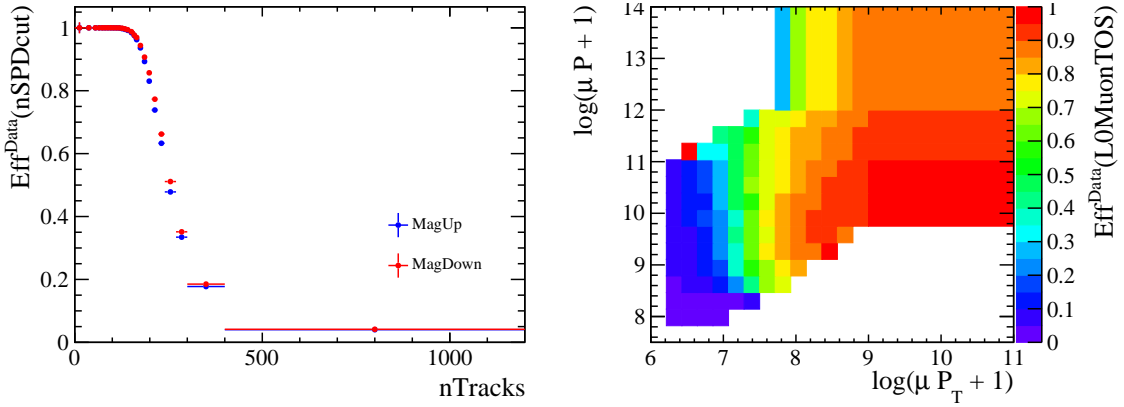
FIGURE 3.6.9: The efficiency of nSPD < 450 as function of `nTracks` (left) and efficiency of `L0MuonTOS` given nSPD < 450 as function of muon momentum and transverse momentum (right) for the 2016 sample. Both of them are obtained from $B^+ \to J/\Psi K^+$ reconstructed decays.

3.6.5 HLT1 and HLT2 trigger emulation

The reconstruction of Λ_c^+ hadronic decays is performed by requiring the logical `OR` between two trigger lines at the `HLT1` level, acting on a single track or a 2-body combination: firstly, to enforce the reconstruction of good quality tracks; secondly, to select pairs of tracks forming a good quality secondary vertex[16]. The trigger response can be modelled by reproducing the *n*-body selection of Λ_c^+ decay products on offline quantities, as both lines are triggering on signal particles (TOS).

Prior to any `HLT` related selection, Global Event Cuts (GEC) filter out the busiest events from the processing chain. The corresponding selection, which we enforce in our emulation scheme, has been summarised in Tab. 3.5.1.

---

[16]High Level Trigger selection cuts depend on a set of specified configurations, known as Trigger Configuration Key (TCK), defined at the start of each fill of the LHC.
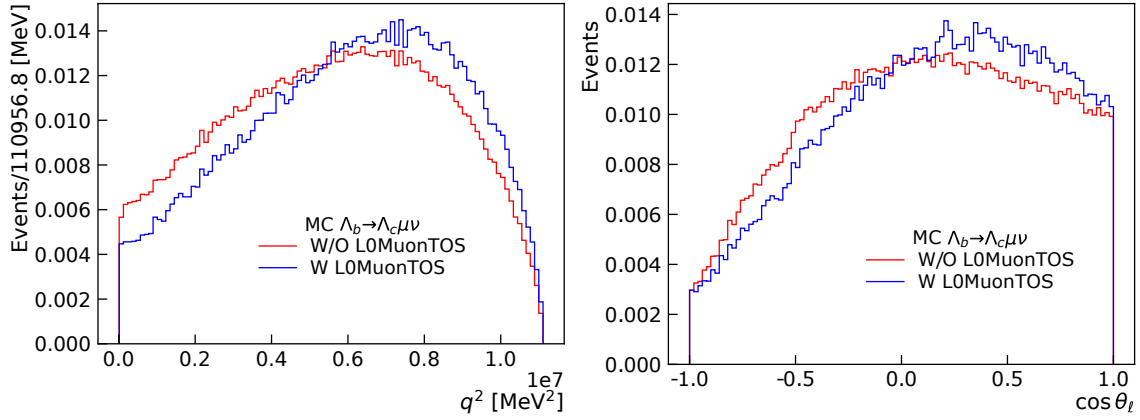
FIGURE 3.6.10: Comparison of distributions of q^2 (left) and $\cos\theta_\ell$ (right) for the $\Lambda_b^0 \to \Lambda_c^+ \mu^- \bar{\nu}_\mu$ simulation sample with (blue) and without (red) the `L0MuonTOS` requirement after the full selection (except for trigger). Only the 2016 `MagDown` sample is shown.

Another complication lies in the different track reconstruction methods employed in offline and HLT selections. The offline tracking algorithm targets the reconstruction of Long Tracks starting from Velo segments and moving to other detectors downstream (*Forward Tracking*). The HLT tracking sequence, instead, has a two-staged approach: firstly, it aims at a much faster reconstruction and momentum estimate for track preselection, therefore using as seed Velo segments matched in the TT (VeloTT tracking [48]); ultimately, the complete HLT tracking sequence is performed on the preselected set of candidates. In order to match the offline reconstruction seed with the VeloTT definition used in the HLT, we require that each Velo segment is associated with at least three hits in the TT stations. The residual difference between the two algorithms resides in the lower track reconstruction efficiency at the HLT level, by $\sim 4.2\%$ [48]. This factor has been incorporated in the trigger emulation via a random track reconstruction efficiency prescaling.

The `HLT1TrackMVA` line selection for single track candidates is summarised in Tab. 3.5.3. It makes use of a gradient boosting algorithm (MatrixNet [39]) to identify the optimal decision boundaries as a function of p_T and IP_{χ^2}. The efficiencies of the emulated trigger line, compared to the true response, are illustrated in Fig. 3.6.11 in bins of the Λ_c hadron kinematics, M_{corr} and phase space. We here note that they have been normalised to the preceding L0 trigger stage, as it is a prerequisite to run the HLT1 sequence.

The `HLT1TwoTrackMVA` trigger line imposes a set of selection cuts applied on two-track combinations, followed by quality criteria requirements on the reconstructed secondary vertex via the output of a MatrixNet-based classifier (Tab. 3.5.4). The emulated efficiencies normalised to the L0 stage, compared to the true trigger response, are shown in Fig. 3.6.12 as a function of the Λ_c kinematics and fit variables of this analysis.

Exclusive $H_b \to H_c \mu \nu$ decays are selected via the `HLT2XcMuXForTauB2XcMu` trigger line. Most of its selection requirements, applied either on a single-track or track combinations to build the Λ_b
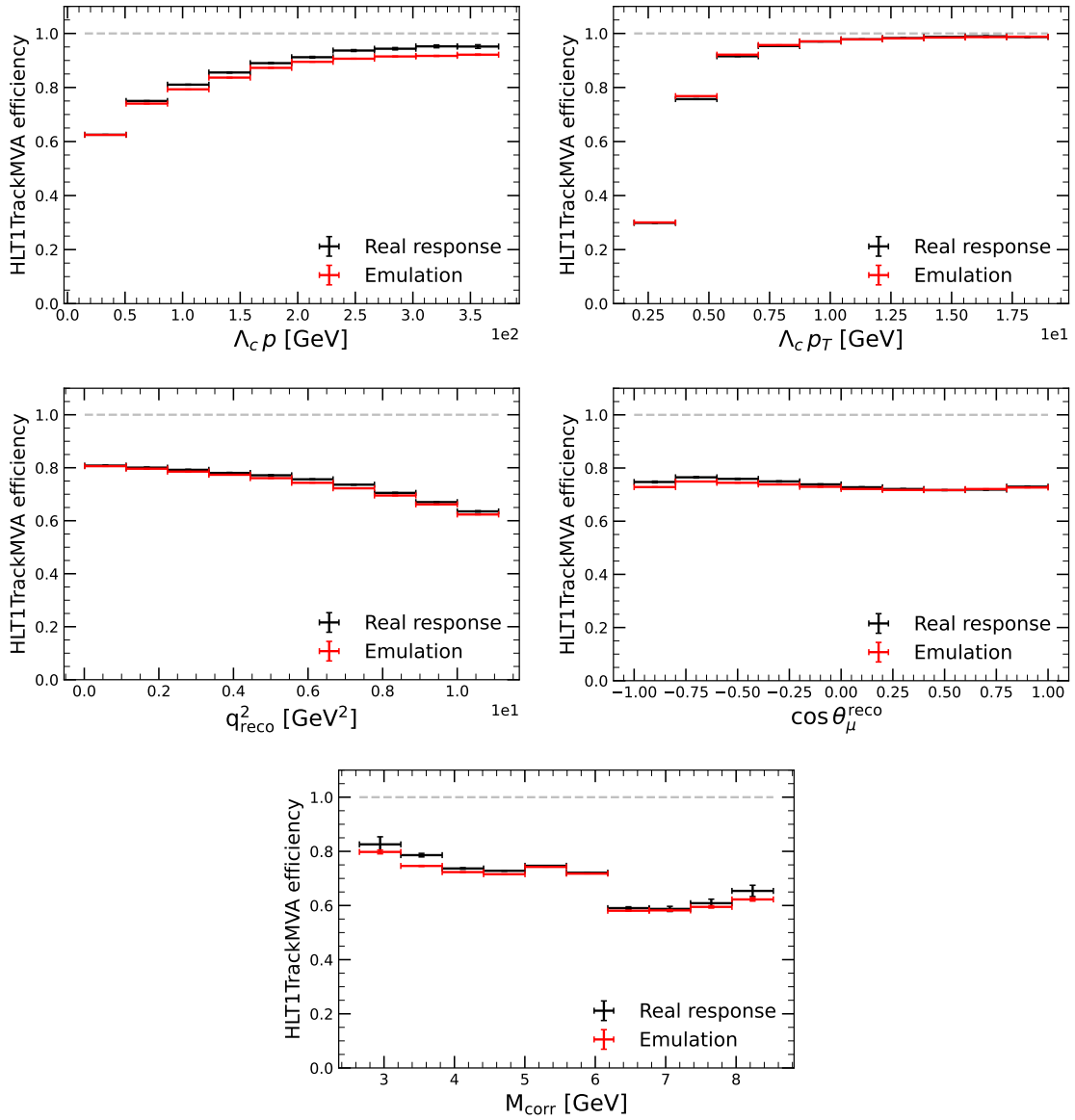
FIGURE 3.6.11: Efficiency of the `HLT1TrackMVA TOS` requirement for the real (black) and emulated (red) trigger as a function of the Λ_c^+ kinematics, corrected mass M_{corr} and phase space variables q^2, $\cos\theta_\mu$ for 2016 `MagUp` samples.

candidate, are superseded by corresponding stripping cuts, included by construction in tracker-only simulation samples. Reproducing the `HLT2` trigger condenses to a linear set of cuts, summarised in Tab. 3.5.5. The efficiencies of the emulated response, normalised to the `HLT1` stage, have been compared to the true trigger output in Fig. 3.6.13 as a function of the fit variables.
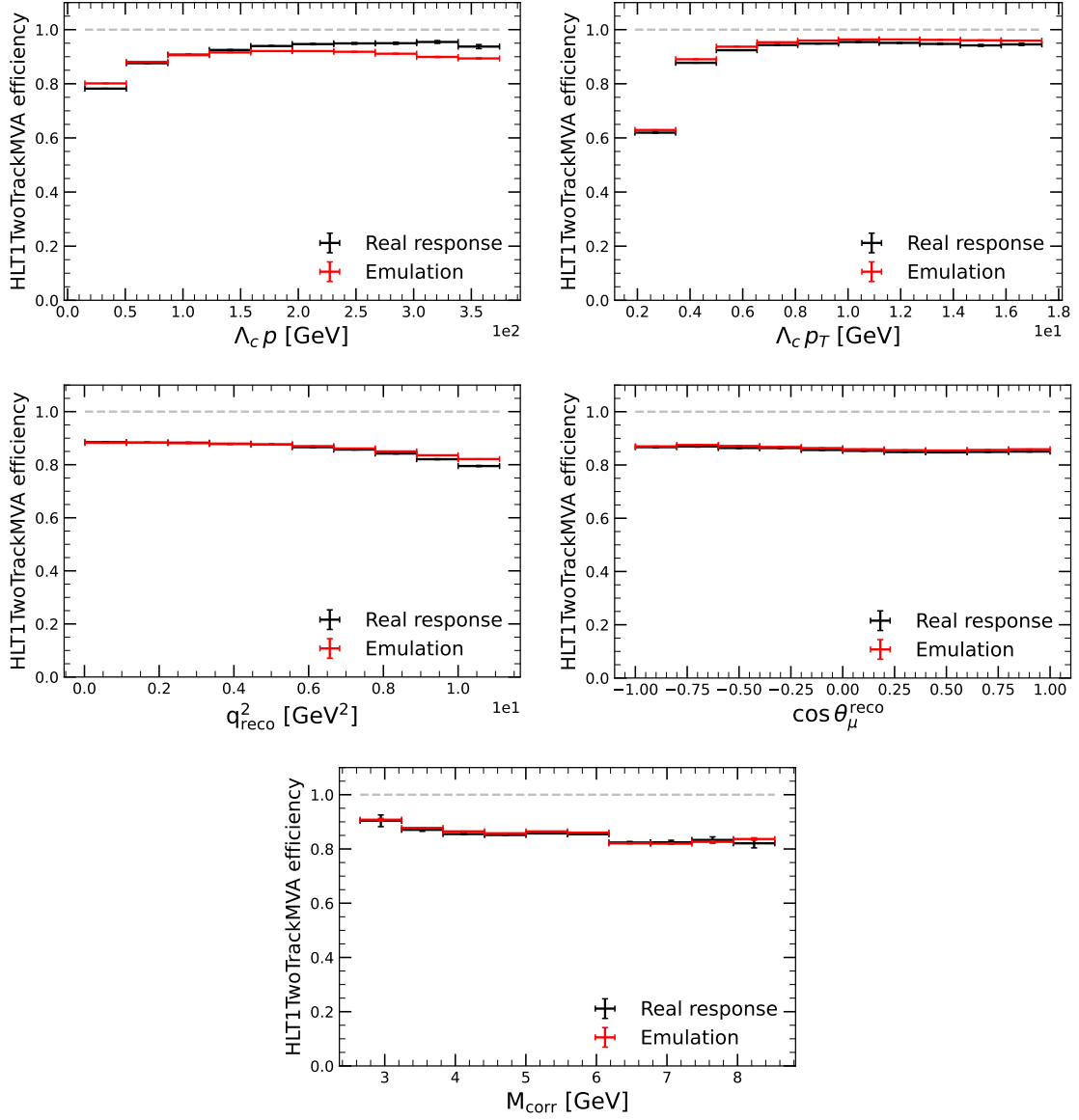
FIGURE 3.6.12: Efficiency of the `HLT1TwoTrackMVA TOS` requirement for the real (black) and emulated (red) trigger as a function of the Λ_c^+ kinematics, corrected mass M_{corr} and phase space variables q^2, $\cos\theta_\mu$ for 2016 `MagUp` samples.

3.6.6 Correction to track reconstruction

The track reconstruction process in MC samples is not perfectly aligned with data despite using identical tools, because of imperfections in the simulation of particles interaction with LHCb detector materials. Therefore, an accurate calibration is retrieved following a data-driven approach.
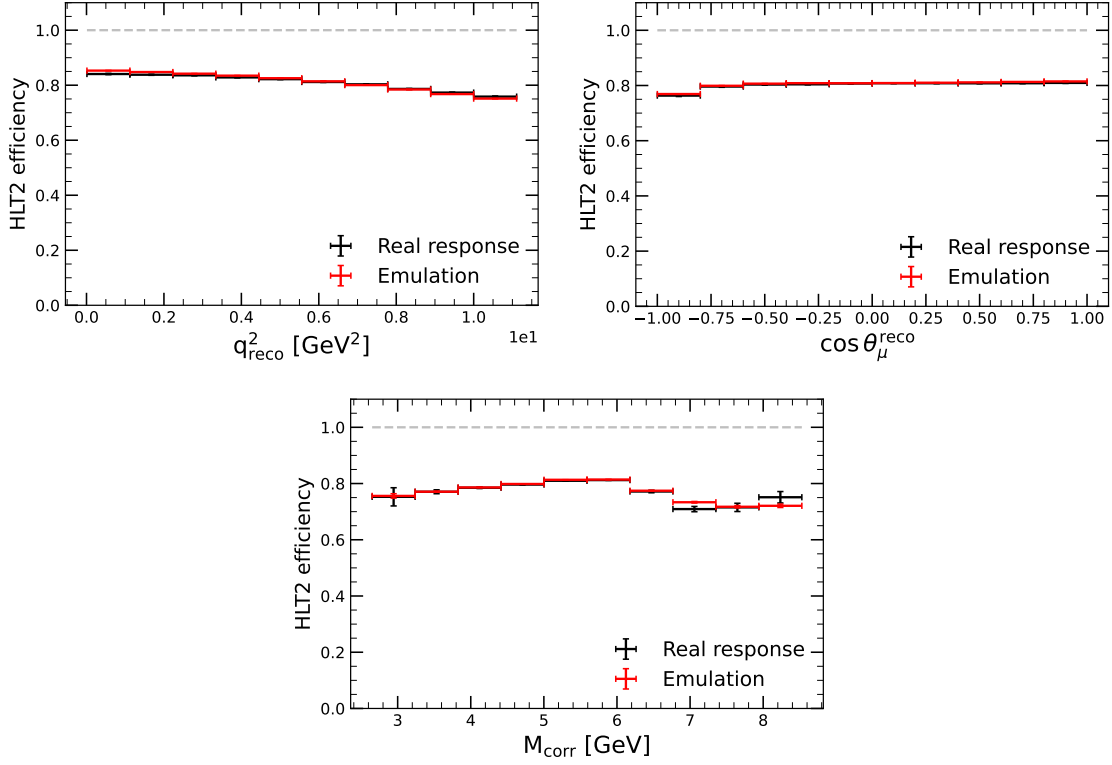
FIGURE 3.6.13: Efficiency of the `HLT2XcMuXForTauB2XcMu TOS` requirement for the real (black) and emulated (red) trigger as a function of the corrected mass M_{corr} and phase space variables q^2, $\cos\theta_\mu$ for 2016 `MagUp` samples.

For this purpose, we use the tag&probe[17] method on selected $J/\Psi \to \mu^+\mu^-$ samples from b-hadron decays to determine the track reconstruction efficiency [49]. While the tag-side muon gets fully reconstructed and identified as a track leaving hits in all the tracking sub-detectors, the probe-muon remains unbiased. Hence, the probe-muon reconstruction efficiency is determined in bins of its kinematic variables, including the pseudo-rapidity η, the momentum p, and the multiplicity of tracks in the event `nTracks`.

In the first step, MC samples are reweighed to account for residual data/MC differences in the event detector occupancy (`nSPDHits`), as it is not well reproduced in simulation. No further calibrations are needed due to the absence of track quality requirements in the offline selection flow. At this stage, the efficiency determination in bins of p and η occurs for both data and simulation. The ratio produces a set of MC correction tables per particle species:

$$w^i_{\text{track-reco}} = \frac{\epsilon^{\text{data}}_{\text{track-reco}}(\eta^i, p^i, \texttt{nTracks})}{\epsilon^{\text{MC}}_{\text{track-reco}}(\eta^i, p^i, \texttt{nTracks})}, \qquad i \in \{\mu, p, K, \pi\} \qquad (3.5)$$

---

[17]The tag&probe method is employed to determine efficiency directly from the data. Decays are selected by fully reconstructing the *tag* side first, then determining the properties of the *probe* side in an unbiased way.

Full details about the procedure are detailed in Ref. [49]. We note here that the data tracking efficiency is determined on muon particles but inherently transferred to simulated hadronic species, at the cost of considering an additional systematic uncertainty due to hadronic interactions. Secondly, the calibration range in the particle kinematics corresponds to a tighter selection in the probe particles momentum ($p > 5\,\text{GeV}$) and pseudo-rapidity ($1.9 < \eta < 4.9$) than the one adopted in this analysis. In the occurrence of tracks falling outside these kinematic boundaries, we apply the correction corresponding to the nearest bin.

The per-event tracking calibration is taken as the product of corrections applied to each track in the final state (p, K, π, μ). The resulting effect is not only minimal (close to unity) but also uniform across phase space, as illustrated for the tracking correction efficiency in Fig. 3.6.14 as a function of q^2 and $\cos \theta_\mu$ for the 2016 `MagDown` sample.
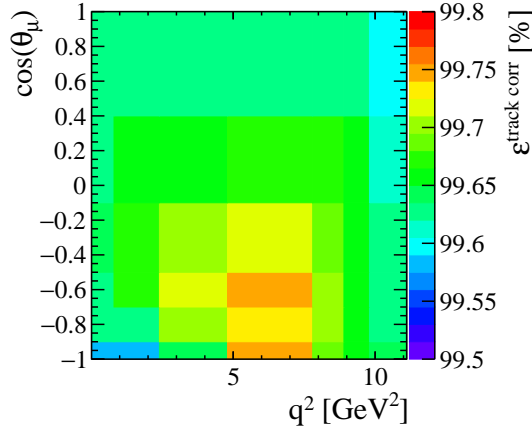
FIGURE 3.6.14: Illustration of the efficiency variation in phase space for the 2016 `MagDown` MC, arising from the correction to the track reconstruction in simulated samples.

3.6.7 Charged isolation correction in $\Lambda_b^0 \to \Lambda_c^{*+} \mu^- \bar{\nu}_\mu$

In MC simulations, we focus on modelling visible decays of excited Λ_c^{*+} states, specifically those into pairs of charged pions, due to the computational expense of simulating slow neutral pions that are not reconstructed in the analysis chain. Conversely, the contribution of neutral $\Lambda_c^{*+} \to \Lambda_c^+ \pi^0 \pi^0$ decays is significant in data, constituting $\sim 81.5\%$ of $\Lambda_c^+ (2595)$ and $\sim 45\%$ in $\Lambda_c^+ (2625)$ decays (Tab. 3.2.1).

The absence of neutral final states in the MC impacts the outcome of charged isolation compared to data, consequently affecting the modelling of background feed-down shapes. In fact, the multivariate isolation cut (described in Section 3.5.5) is highly efficient for $\Lambda_c^+ \pi^0 \pi^0$ final states given the absence of additional charged tracks, while it retains only a minor portion of $\Lambda_c^+ \pi^+ \pi^-$.

This effect is modelled with simulation by accounting for the correct proportions of neutral-to-charged Λ_c^{*+} decays. The efficiency of charged isolation for $\Lambda_b^0 \to \Lambda_c^{*+}\ell^- \bar{\nu}_\ell$ decays is rescaled by randomly selecting a portion of the non-isolated sample, assuming comparable responses between data and MC. Any possible residual differences are attributed to the exclusive use of charged Λ_c^{*+} states discarded by the isolation for modelling the fractions.

3.6.8 Multi-dimensional kinematic post-fit correction

Despite the enforced simulation correction procedures to tackle known Data/MC disagreement sources, residual mis-modelling and detector effects might still be present at this stage. To reduce this difference to a negligible level, we put in place a dedicated data-driven reweighting procedure by building a MC sample inclusive of signal and backgrounds.

Correct proportions of each channel contributing to the simulation ensemble (from now on referred to as *MC cocktail*) are determined from a first iteration of a maximum-likelihood template fit to the corrected mass M_{corr} in the integrated phase space region ($0.01 < q_{reco}^2 < 11.11$ GeV, $-1 < \cos\theta_\mu^{reco} < 1$). We neglect the sub-leading contribution of combinatorial and misidentified backgrounds, consistently below 10% for each magnet polarity and data-taking year, as its inclusion does not impact the outcome of the reweighting process. At this stage of the fit, the complete set of data/MC corrections described earlier in the manuscript has been included. For a thorough description of the fitting procedure in M_{corr}, we refer to Sec. 3.9. Fig. 3.6.15 demonstrates the residual disagreement between data (black points) and post-fit MC cocktail in 2016 `MagUp` prior to the reweighting step (red histogram), which is quantified in the lower panel in the shaded green pull histogram.

The chosen pathway to the minimisation of differences between two multidimensional distributions is given by Boosted Decision Trees, in the form of the `GBReweighter` tool [50]. In this approach, the ensemble of trees is used to identify the optimal splitting in the hyper-space of input reweighting variables by minimising a χ^2 metric, and to compute the weights. Input variables considered for the baseline training include merely the kinematics of the Λ_b decay products: momentum and transverse momentum of the muon and Λ_c candidates. The BDT-based reweighting performance is neither altered nor improved by including a richer set of training variables, *e.g.* kinematics of Λ_c products or topological quantities, significantly slowing down the training phase. In addition, isolating the training to a signal-enriched phase space region with negligible background contribution does not prove to be more effective in capturing the trend of residual discrepancies with the data. Finally, predicted event-by-event weights are assigned to each simulation sample, following a dedicated training enforced on separate data-taking years. The improved agreement with the data is illustrated in Fig 3.6.15 for 2016, `MagUp`: the corrected MC cocktail is represented by the blue histogram, while in the panel below, pulls are shown in darker green. Data/MC comparisons in additional kinematic variables are reported in Fig. 3.F.1 in App. 3.F. The effect of the correction in phase space, more pronounced in the first bins of q^2, reflects the pattern of data/MC discrepancies prior to the correction, primarily concentrated in the softer end of the momentum and transverse

momentum spectra (Fig. 3.6.16).
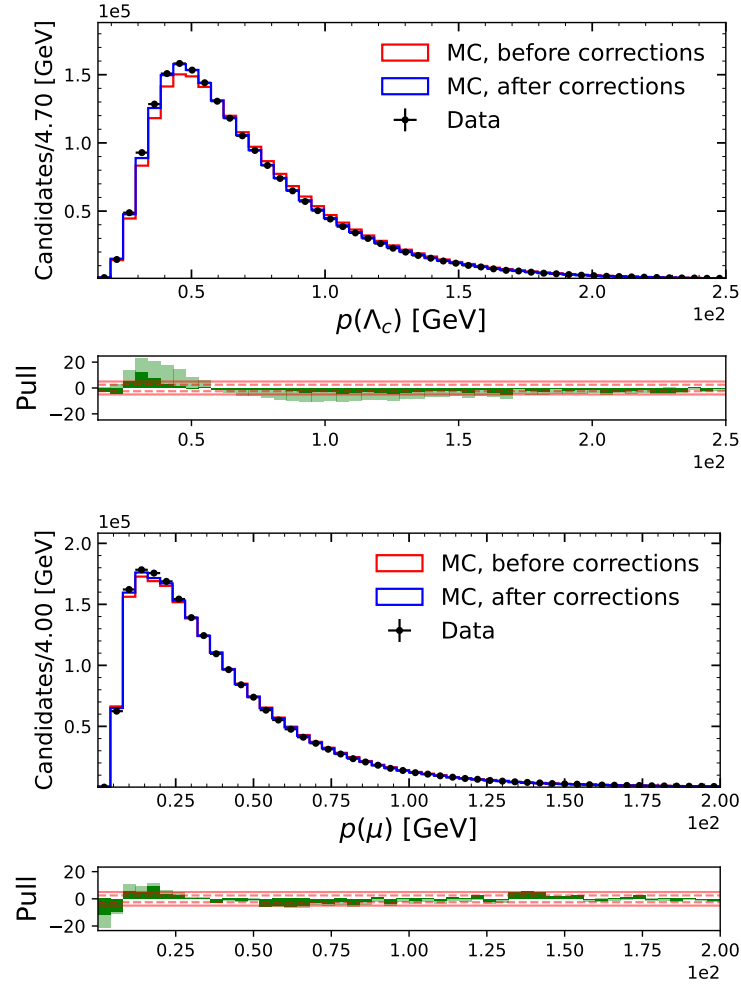
FIGURE 3.6.15: Agreement in the kinematics of the Λ_c and μ candidate between data (black points), MC cocktail before the kinematic correction (red histogram) and the same after reweighting (blue histogram). The agreement in the pre-reweighting scenario is highlighted with light green pulls, while it is in darker green for post-correction. Samples correspond to 2016 and magnet polarity `MagUp`.

3.7 Signal selection efficiencies

Requiring particle candidates to be within the LHCb detector acceptance, together with the use of tailored selection requirements, introduces a significant variation in the efficiency of the signal over the phase space variables (q^2, $\cos\theta_\mu$). Accounting for efficiency variation effects is relevant for this analysis, especially considering the fit strategy, which requires a convolution of experimental effects in the decay density model.
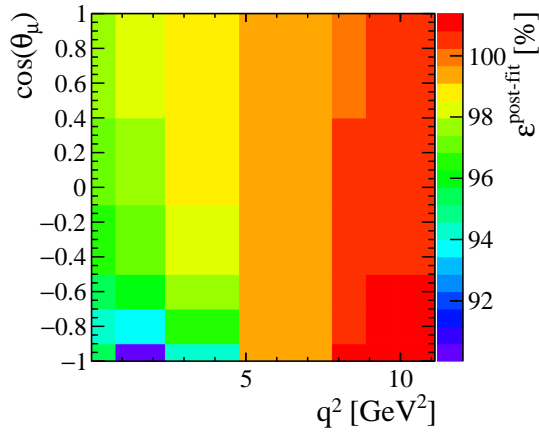
FIGURE 3.6.16: Efficiency variation in phase space for 2016 `MagUp`, as a result of the post-fit kinematic reweighting, computed with respect to the entire selection chain and accounting for all previous corrections to the MC sample.

The efficiency of signal events corresponds to the fraction of candidates recorded after the complete reconstruction and selection chain, which we evaluate as a differential function of phase space. The total efficiency (ϵ^{tot}) has been estimated as the product of conditional efficiencies[18] for each of the selection stages in bins of q^2, $\cos\theta_\mu$, and expressed as:

$$\epsilon^{\text{tot}} = \epsilon^{\text{geom}} \times \epsilon^{\text{reco}} \times \epsilon^{\text{PID}} \times \epsilon^{\text{trig}} \times \epsilon^{\text{MVA}} \times \epsilon^{\text{iso}}, \qquad (3.6)$$

where ϵ^{geom} is the efficiency of geometrical requirements; ϵ^{reco} of reconstruction; ϵ^{PID} of particle identification requirements; ϵ^{trig} of the trigger requirements; ϵ^{MVA} of the multivariate classifier cut; ϵ^{iso} of the isolation cut.

Efficiency terms of Eq. 3.6 have been modelled using simulation. Besides, we include all data-driven corrections described in Sec. 3.6.

Efficiency variations are illustrated as maps, corresponding to the data-taking year 2016 and magnet polarity `MagUp`, although compatible trends can be observed for the `MagDown` counterpart. Ultimately, we report the most relevant observable, corresponding to the total efficiency shape variation. For completeness, ancillary plots for each of the individual contributions noted in Eq. 3.6 can be found in App. 3.D.

Total efficiency

The total efficiency has been computed as the ratio between the weighted number of candidates passing the offline selection requirements and the same number obtained without any applied

---

[18]We imply here that each factor has been normalised to the preceding element in the product.

Fractional ϵ variation	2016 `MagUp`
Geometrical acceptance	$55.7 \pm 6.1\%$
Reconstruction	$38.6 \pm 4.8\%$
PID	$26.3 \pm 3.0\%$
Trigger	$124.1 \pm 20.5\%$
MVA	$21.9 \pm 3.5\%$
Isolation	$5.3 \pm 1.1\%$
Total	$155.8 \pm 10.5\%$

TABLE 3.7.1: Breakdown of fractional selection efficiency variations, evaluated for the signal decay $\Lambda_b^0 \to \Lambda_c^+ \mu^- \bar{\nu}_\mu$, 2016 `MagUp` sample.

selection. The latter is evaluated by accounting for the efficiency of filtering selections prior to the stripping stage and geometrical acceptance cuts.

Fig. 3.7.1 illustrates the total efficiency (ϵ^{tot}) variation over the phase space of true $(q^2, \cos\theta_\mu)$ for the data-taking year 2016, with compatible trends observed in 2017 and 2018. It should be noted that the efficiency normalisation is not relevant to the scope of this analysis, targeting only the shape measurement of the signal mode decay density. Therefore, only the fractional efficiency variations have been reported in Tab. 3.7.1, corresponding to $(\epsilon_{\text{max}} - \epsilon_{\text{min}})/\langle\epsilon\rangle$.

Trigger requirements, heavily impacted by the L0 stage selection acting on the muon candidate, contribute the most to the efficiency shape variation, followed immediately by the effect of geometrical acceptance cuts.
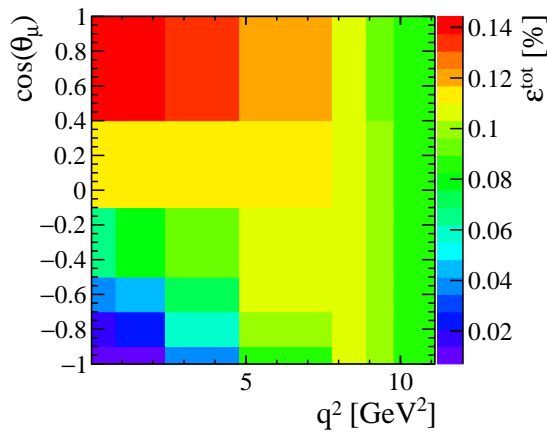
FIGURE 3.7.1: Total efficiency of selection requirements (ϵ^{tot}) for the signal decay as a function of true q^2 and $\cos\theta_\mu$ for the `MagUp` sample of 2016 data-taking.

3.8 Resolution of phase space observables

Finite resolution effects on the phase space quantities q^2 and $\cos\theta_\mu$ are incorporated in the response matrix, which models the migration probability of an event from a true bin to a reconstructed bin.

The novelty of this work consists in adopting a Gaussian Process Regression technique to improve on the resolution of phase space observables (see App. 3.E), unavoidably limited by the presence of missing momentum in the final state. The two-fold ambiguity in the solution to the Λ_b momentum, built upon the momentum conservation against the visible system (App. 3.B), is solved by selecting the closest value to the regression prediction. The achieved improvement, when compared to a linear regression-driven choice [51], is at the level of $\sim 19\%$.

The resulting response matrix is a multi-dimensional object comprising true and reconstructed phase space observables. A projection in the q^2 2D plane, relative to the signal MC sample, is illustrated in Fig. 3.8.1.
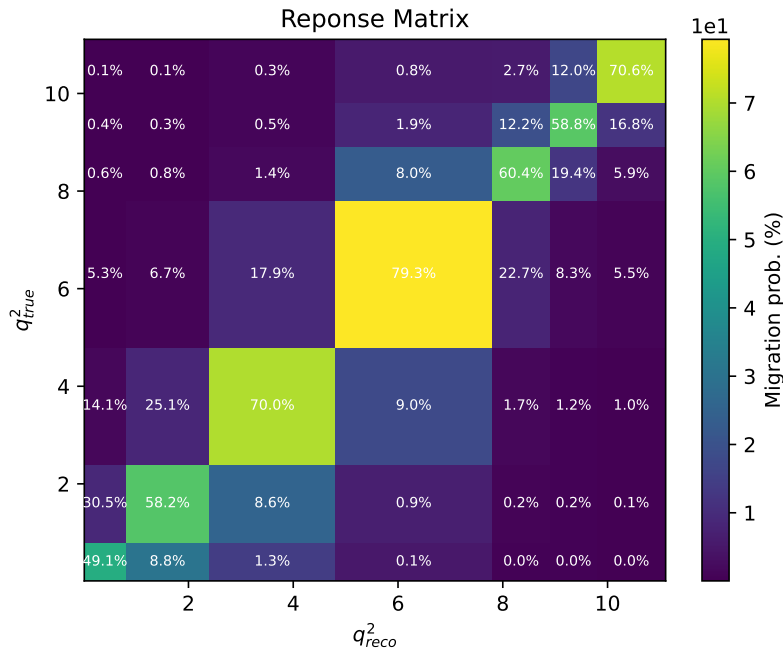
FIGURE 3.8.1: Response matrix obtained from the signal $\Lambda_b^0 \to \Lambda_c^+ \mu^- \bar{\nu}_\mu$ simulation sample, depicting the migration probability as function of reconstructed phase space observable q^2 versus the true q^2. Only the 2016 sample is shown here.

3.9 Extraction of signal phase space distribution

Following the online and offline selection and data/simulation correction stages, the signal shape is determined as a function of phase space in the next step of the analysis chain. We perform

Bin number	q^2 [GeV]	$\cos\theta_\mu$
1	(0.01, 0.80)	(−1.00, −0.90)
7	(0.80, 2.40)	(−1.00, −0.90)
13	(2.40, 4.80)	(−1.00, −0.90)
25	(7.80, 8.90)	(−1.00, −0.90)
31	(8.90, 9.80)	(−1.00, −0.90)

TABLE 3.9.1: Ignored bins of corrected mass fits for the extraction of the signal yield, together with their corresponding phase space limits.

independent maximum likelihood (ML) corrected mass fits in 42 bins of q^2, $\cos\theta_\mu$, via the fitting framework `zfit` [52] to extract the $\Lambda_b^0 \to \Lambda_c^+ \mu^- \bar{\nu}_\mu$ signal yield (*extended* ML fits). Given the absence of an analytic function to accurately describe the shape of each decay entering the fit as a component, we use the shape of each simulation template as a *pdf* (*template*, extended ML fits). The combinatorial background constitutes the only exception, as it is instead modelled in a data-driven way. A linear combination of signal and background templates represents the best approximation to the data shape, and the coefficients of the linear sum, the yields, constitute the fit parameters $\vec{\Theta}$. For every independent fit in a defined phase space region, we assume each histogram is a single measurement of a $N-$dimensional vector distributed according to a multinomial, where N is the number of bins. As the fit is extended, the total number of events is distributed according to a Poisson *pdf*, with average $E_{\text{tot}} = \sum_k E_k$. If we define the per-bin observations as O_k and expected values as E_k, then the likelihood reads as:

$$\lambda(O_k, E_k(\vec{\Theta})) = \prod_{k=1}^{N} \frac{E_k^{O_k}}{O_k!} e^{-E_k}. \tag{3.7}$$

A Poisson distribution with mean value E_k can describe the events in each bin. We retrieve the best-fit parameters from the minimisation of the function:

$$\mathscr{L}(\vec{\Theta}) = -ln\lambda = \sum_{k=1}^{N} E_k(\vec{\Theta}) - O_k \ln E_k(\vec{\Theta}). \tag{3.8}$$

The template shape uncertainty, arising from the finite size of our simulation samples, has not been included at this fit stage but is assigned as an independent systematic uncertainty (Sec. 3.11.1). Ultimately, we exclude some regions of phase space (Tab. 3.9.1), shaded in red in Fig. 3.9.1, due to extremely low signal yields, large backgrounds, and small signal efficiency. Each independent fit is performed in 80 bins of corrected mass, defined in the range $M_{\text{corr}} \in [2.5, 7.0]$ GeV, where the phase space fiducial volume has been defined in Tab. 3.5.7. A discussion regarding the binning optimisation in the variables $(q^2, \cos\theta_\mu)$ is presented in App. 3.G.
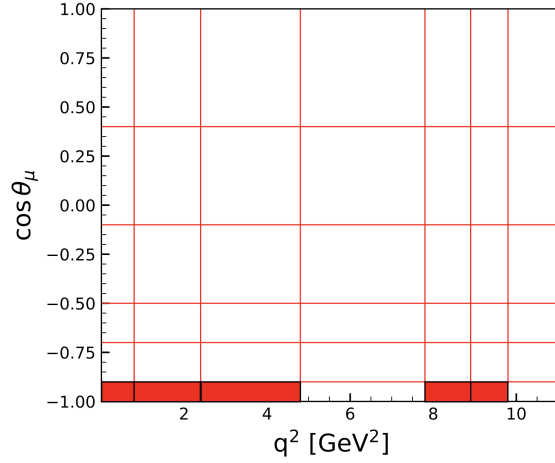
FIGURE 3.9.1: Ignored bins (red-filled areas) of corrected mass fits for the extraction of the signal yield in the phase space variables plane $(q^2, \cos\theta_\mu)$.

3.9.1 Signal and background templates

Signal shape: $\Lambda_b^0 \to \Lambda_c^+ \mu^- \bar{\nu}_\mu$

The signal shape is modelled with tracker-only MC simulation, combining magnet polarities for each data-taking year. After applying the complete trigger and offline selection, the resulting shape is modified in the reweighting stage as a consequence of MC corrections discussed at length in Sec. 3.6. In addition to the standard corrections, the signal includes the correction to the generation model to account instead for the most up-to-date Form Factors results calculated with high precision on the Lattice [44] (Sec. 3.6.2). The signal yield, $N(\Lambda_b^0 \to \Lambda_c^+ \mu^- \bar{\nu}_\mu)$, is an unconstrained parameter of the fit. The template shape in the full q^2, $\cos\theta_\mu$ range, clearly peaking at the Λ_b mass value, is shown in Fig. 3.9.2.

Λ_b^0 combinatorial background

The combinatorial background originates when a random muon, coming for example from another process in the pp collision, is combined with the Λ_c^+ particle detected from the signal decay, thus mimicking the Λ_b^0 semi-muonic transition $\Lambda_b^0 \to \Lambda_c^+ \mu^- \bar{\nu}_\mu$. We model this background in a data-driven way, using a data sample including muons and Λ_c^+ particles with the same electrical charge $\Lambda_c^+ \mu^+$, denoted as *same-sign* (SS). Figure 3.9.3 displays the corrected mass distribution of the 2016 sample after undergoing the complete set of selection cuts. Besides, we explore potential discrepancies in the combinatorial background between the SS data sample and the corresponding background in the opposite charge muon scenario, the *right-sign* data sample $\Lambda_c^+ \mu^-$ (RS). A comparison between the distributions of the $\Lambda_c\mu$ combination mass for both data samples in the regime above the Λ_b^0 mass is shown Figure 3.9.4 for the 2016 sample. As the observed ratio between the SS and RS distributions remains consistently flat across the entire range, we
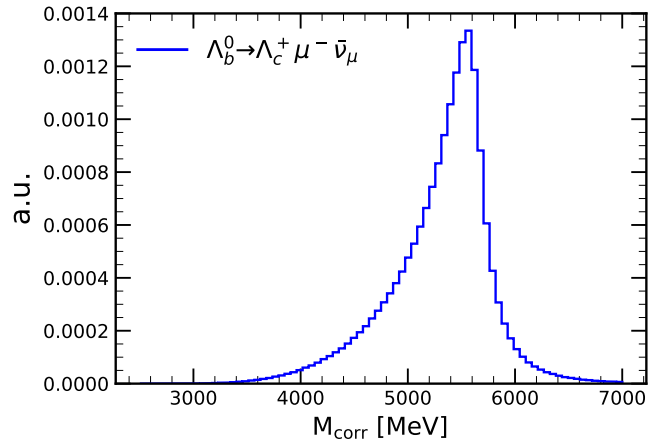
FIGURE 3.9.2: Corrected mass signal template, shown after the full offline selection and reweighing stage for the 2016, `MagUp` polarity.

conclude that the SS data sample constitutes a good proxy to estimate the shape of combinatorial background from both sources.
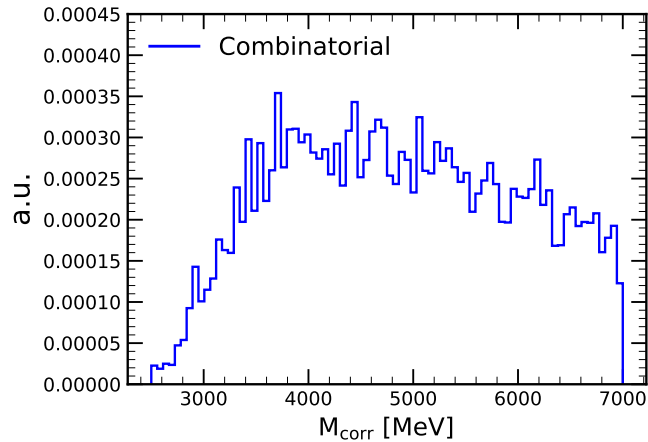
FIGURE 3.9.3: Corrected mass template for the combinatorial background modelled with the *same-sign* data sample $\Lambda_b^0 \rightarrow \Lambda_c^- \mu^- X$, shown after the full offline selection for the 2016 data-taking year.

Λ_b^0 misidentified backgrounds

In the process of particle identification, it is possible to incur into a mismatch between different particle species, mimicking one another. Specifically in this analysis context, it is the case between hadrons h^- and long-lived leptons, *i.e.* whenever a kaon or a pion is misidentified as a muon. Situations of such type, arising from a combination of wrongly identified hadrons with additional
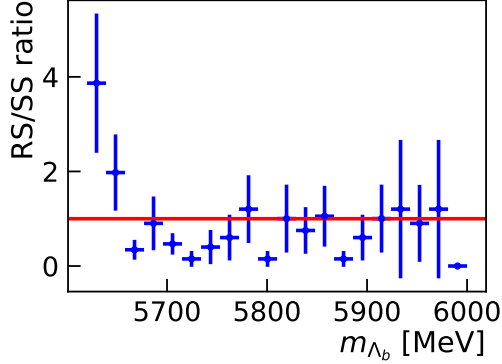
FIGURE 3.9.4: Ratio of $m(\Lambda_c \mu)$ distributions between the right-sign (RS) and same-sign (SS) data samples above the Λ_b^0 mass for the 2016 data-taking year.

unreconstructed final state X, are commonly regarded as *misidentified* backgrounds (misID) with signature $\Lambda_b^0 \to \Lambda_c^+ h^-(X)$ ($h^- \in \{K^-, \pi^-\}$). We adopt a data-driven procedure to model these contributions, subtracting them from both the RS and SS data shapes in corrected mass.

Firstly, a sample of $\Lambda_c^+ t^-$ candidates is created by eliminating any PID requirement from the selected track t^-. At this point, it is convenient to produce a set of separated sub-samples, enriched in a specific particle by imposing a dedicated trigger and PID selection, as summarised in Tab. 3.9.2: the signal $\Lambda_c^+ \mu^-$, the $\Lambda_c^+ K^-$, and the $\Lambda_c^+ \pi^-$. The difference in trigger requirements, namely in the use of `TIS` at the `L0` trigger level, is necessary to avoid introducing any bias when using the `L0` muon hardware trigger selection[19], as in the case of signal decays. As a consequence, the effect of the `TIS` selection needs to be modelled and unfolded from the misID samples just created, for which we use $B^+ \to J/\Psi K^+$ decays. The efficiency of `L0GlobalTIS` is evaluated as function of the B^+ kinematics, with transverse momentum p_T and z component of spatial momentum p_z. In addition, we unfold the PID requirements applied on the track t^- by determining the efficiency of the PID selection as function of $p, p_T, $`nTracks`, analogously to the procedure described in Sec. 3.6.1.

At this stage, the amount of misID background in fully selected data needs to be estimated. For this reason we model the efficiency of the `L0MuonTOS` trigger requirements and the muon PID misidentification rate. The first is achieved by using a tag&probe technique on $B^+ \to (J/\Psi \to \mu^+ \mu^-) K^+$ decays as function of muon p_T, while following the same strategy as above for PID mis-identification efficiency modelling.

The final misidentification background estimate is reported in Fig. 3.9.5 for the 2016 `MagDown` sample in RS data (left panel) and SS data, *i.e.* the fake Λ_b^0 contribution (right panel) in bins of corrected mass. We observe that their contribution to each data-taking year corresponds to less than a 1% effect.

---

[19]The `L0Global` line returns a positive decision whether *any* of the `L0Decision` unit (`L0Hadron`, `L0Photon`, `L0Electron`, `L0Muon`, `L0DiMuon`) is fired, being the logical `OR` between them.

$\Lambda_c^+ K^-$	$\Lambda_c^+ \pi^-$	$\Lambda_c^+ h^-$
$\Delta\log\mathfrak{L}(K-\pi) > 4$	$\Delta\log\mathfrak{L}(K-\pi) > 2$	$\Delta\log\mathfrak{L}(\mu-\{\pi, K, p\}) > 2$
`isMuon == 0`	`isMuon == 0`	`isMuon == 0`
`L0GlobalTIS == 1`	`L0GlobalTIS == 1`	`L0MuonTOS == 1`

TABLE 3.9.2: Summary of requirements enforced to perform the misidentification background estimate. The left and middle column selections are used to produce pure samples enriched in $\Lambda_c^+ K^-$ and $\Lambda_c^+ \pi^-$ final states. The selection in the right column is to estimate the total misID contribution in the signal sample.

Prompt, fake and misidentified Λ_c^+ decays

The displaced vertex requirements imposed at trigger and offline level considerably reduce the contribution from Λ_c^+s produced promptly in the *pp* collisions (*prompt*), and the combinatorial Λ_c^+ decays (*fake*). Nonetheless, a residual leakage into the signal Λ_c sample is still expected and needs to be accounted for. We perform a fit to the distribution of the logarithm of the impact parameter χ^2 ($\log \text{IP}_{\chi^2}$) for Λ_c^+ candidates after the full selection to quantify the contamination from the prompt component. The fake decays contribution is assessed by fitting the reconstructed mass of Λ_c^+ candidates, $m(\text{pK}^-\pi^+)$, after the full selection. As the observables IP_{χ^2} and $m(\text{pK}^-\pi^+)$ are uncorrelated, we perform a 1D simultaneous maximum likelihood fit to both distributions. The resulting background contribution is then subtracted from the data via the `sPlot` technique [43].

The simultaneous fit comprises three different components, *i.e.* the signal non-prompt Λ_c^+, the prompt Λ_c^+, and ultimately the fake Λ_c^+. All of them are modelled with a pdf sampled from the MC simulation ($\log \text{IP}_{\chi^2}$); instead, a double-sided Crystal Ball function is used for the first two components in the $m(\text{pK}^-\pi^+)$ fit. The fake Λ_c^+ component differs from the previous ones in the
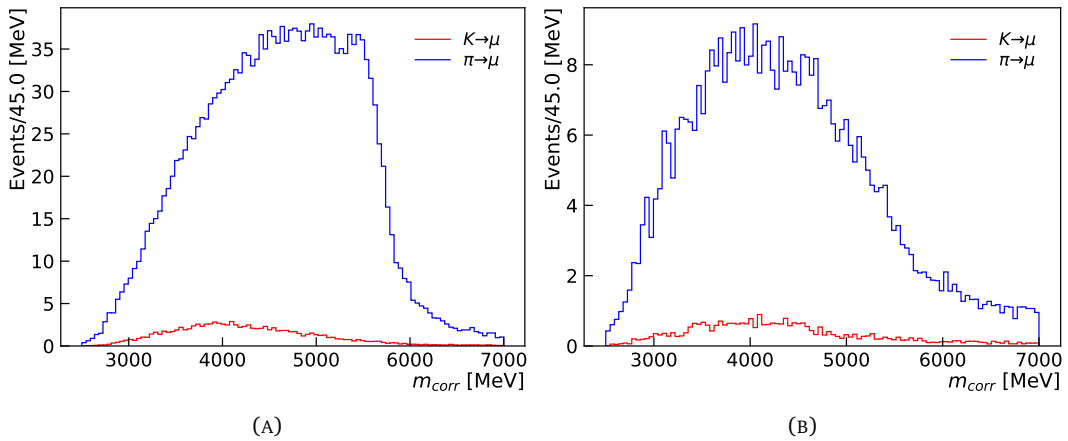
FIGURE 3.9.5: Distribution of the misidentification background in the RS (A) and SS (B) data sample in bins of corrected mass, for the $K \rightarrow \mu$ (red) and $\pi \rightarrow \mu$ (blue) scenario.

description of the $m(\mathrm{pK}^-\pi^+)$ shape, taken as an exponential function with slope parameter c. To account for possible data-MC differences, we include a shift parameter μ on the mean and a scale factor σ on the width of the reconstructed mass distribution for the signal and prompt Λ_c^+. The yields of each of the three fit components and the shape parameters c, μ, and σ are free parameters of the fit. Tab. 3.9.3 summarises the fit results for the 2016 `MagDown` data sample, hinting at a significant contribution of fake Λ_c^+ decays. Fit projections are illustrated in Fig. 3.9.6. This background is subtracted from the data with dedicated weights in the RS and SS samples. The same treatment was applied to fake lepton data to retrieve the misidentified background contribution. The impact of fake Λ_c^+ background subtraction on the corrected mass distribution on the data sample is shown in Fig. 3.9.7.

Parameter	Value	Error
$N(\text{fake } \Lambda_c^+)$	1.12×10^5	5.14×10^2
$N(\text{non-prompt } \Lambda_c^+)$	1.07×10^6	8.62×10^2
$N(\text{prompt } \Lambda_c^+)$	$-$[20]	$-$
Exponential scale factor (c)	-2.62×10^{-3}	0.13×10^{-3}
Shift parameter (μ)	$-$[20]	$-$
Scale parameter (σ)	1.100	0.001

TABLE 3.9.3: Results of the simultaneous fit to $\log \mathrm{IP}_{\chi^2}$ and mass of the Λ_c^+ candidates $m(\mathrm{pK}^-\pi^+)$ for the 2016 `MagDown` sample.

Λ_b^0 tauonic decays

The semi-tauonic decays of the Λ_b constitute a background in case of a muonic decay of the τ lepton. On one side, these decays are intrinsically suppressed due to the branching fraction $\mathrm{BR}(\tau^- \to \mu^- \bar{\nu}_\mu \nu_\tau) = (17.39 \pm 0.04)\%$ [4]. On the other side, the first level trigger, `L0Muon`, imposes a hard transverse momentum cut on the muon candidate, ruling out most of the soft(er) muons deriving from the decay of the tauon. However, they represent a non-negligible background source to be accounted for. Fig. 3.9.8 illustrates the shape of these decays, whose peak is shifted towards lower $\mathrm{M}_{\mathrm{corr}}$ values due to the presence of multiple missing neutrinos. The reweighting stage includes the model correction to account for LQCD Form Factors values (Sec. 3.6.2), tuned explicitly for $\Lambda_b^0 \to \Lambda_c^+ \tau^- \bar{\nu}_\tau$ decays. The yield of these decays, $N(\Lambda_b^0 \to \Lambda_c^+ \tau^- \bar{\nu}_\tau)$, is a free parameter of the fit. It may occur that, in some phase space bins with prevailing signal presence, the shape of this template is indistinguishable from the double-charm component, causing some fit instabilities. In this occurrence, we use only one of the two templates to determine the joint background yield to retrieve a stable fit behaviour, which by no means impacts the goal and strategy of this analysis.

---

[20]The fit result is compatible with zero.
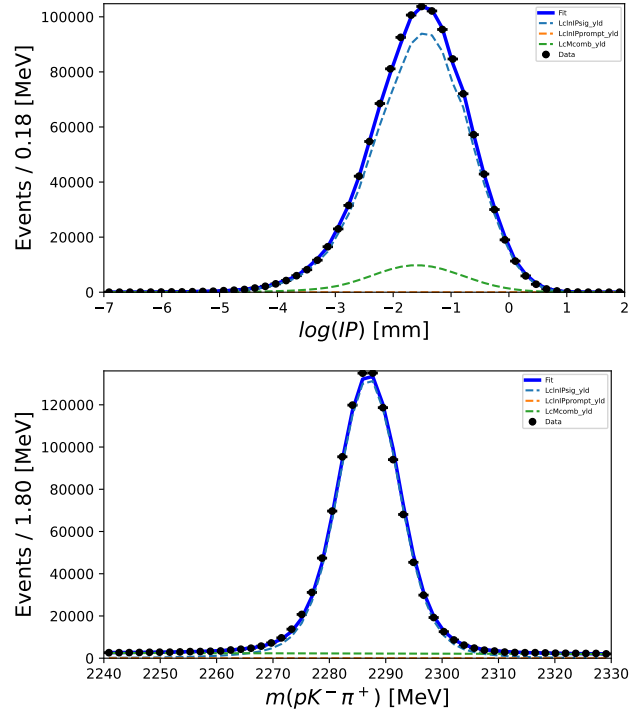
FIGURE 3.9.6: Fit projections of the simultaneous fit to the $\log \mathrm{IP}_{\chi^2}$ distribution of the Λ_c^+ candidates (left) and mass of the Λ_c^+ candidates $m(\mathrm{pK}^-\pi^+)$ (right) for the 2016 `MagDown` sample. The different components are depicted as dashed lines: blue for the signal Λ_c; orange for the prompt Λ_c; green for the fake Λ_c.
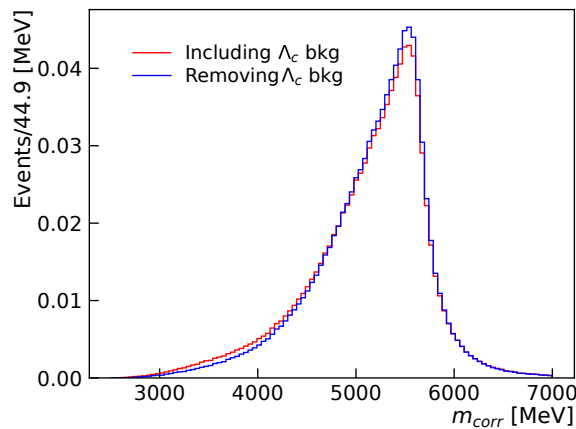
FIGURE 3.9.7: Corrected mass distribution in the 2016 data sample before (red) and after (blue) the fake Λ_c^+ background subtraction.
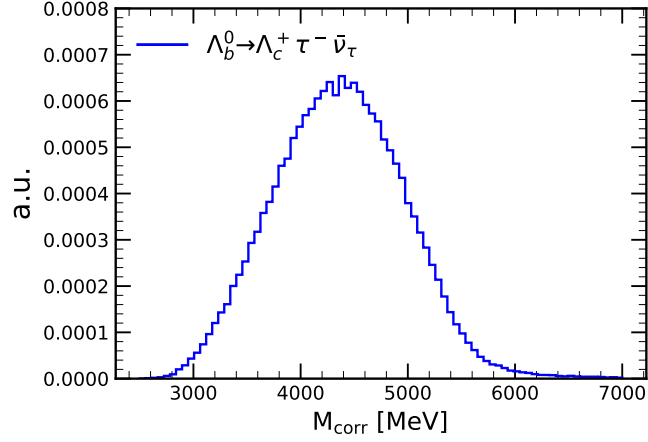
FIGURE 3.9.8: Corrected mass template for background $\Lambda_b^0 \to \Lambda_c^+ (\tau^- \to \mu^- \bar{\nu}_\mu \nu_\tau) \bar{\nu}_\tau$ decays, shown after the full offline selection and reweighing stage for the 2016, MagUp polarity.

Feed down from excited Λ_c^* decays

Decays of the type $\Lambda_b^0 \to \Lambda_c^{+*} \ell^- \bar{\nu}_\ell$ constitute the biggest contribution to the background budget, given the unreconstructed charged or neutral pions in the final state $\Lambda_c^{*+} \to \Lambda_c^+ \pi\pi$. Those slow pions are not reconstructed because of their soft energy and low associated tracking efficiency. The absence of final state particles associated with the reconstructed decay becomes an experimental advantage, as it deforms the template shape in corrected mass. Indeed, these backgrounds M_{corr} distribution is expected to be broader and to peak at lower values compared to signal decays, as demonstrated in Fig. 3.9.9 for the two biggest contributors in the muonic channel, $\Lambda_c^+(2595)$ and $\Lambda_c^+(2625)$. Although available in the set of simulated events, we do not include the shape of the tauonic decays in the corrected mass fit (with a tauon decaying into a muonic final state) as the shapes are correlated to the more abundant muon channel. Analogous reasoning affects the Λ_c lower-excited state, $\Lambda_c^+(2595)$, as it is less abundant than the decay involving $\Lambda_c^+(2625)$ (Tab. 3.2.1). Therefore, the shape of the simulated decay $\Lambda_b^0 \to \Lambda_c^+(2625)\mu^- \bar{\nu}_\mu$ is used as a proxy to model the full set of feed-down contributions. The main strategy to tackle these backgrounds takes advantage of the charged isolation technique (Sec. 3.5.5), aimed at rejecting events with identified extra tracks in the proximity of the Λ_b vertex which have not been yet associated with the signal. In addition to the usual weights to improve data/MC agreement, we place a correction on the effect of the charged isolation cut due to the intrinsic bias of our simulation, containing only $\Lambda_c^+ \to \pi^+ \pi^-$ decays (Sec. 3.6.7). The total yield of these backgrounds, $N(\Lambda_b^0 \to \Lambda_c^{+*}\ell^- \bar{\nu}_\ell)$, is a free parameter of the fit.
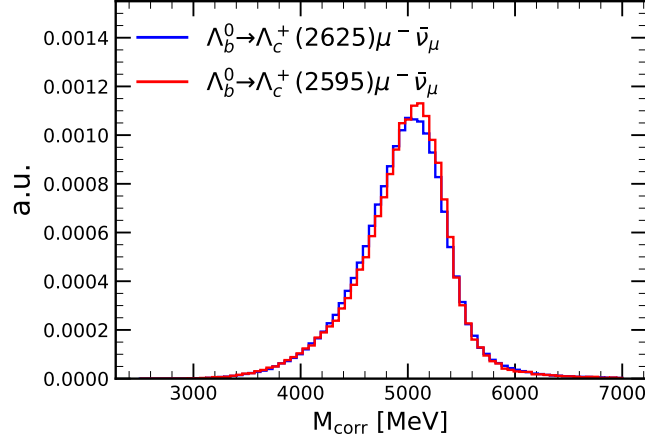
FIGURE 3.9.9: Corrected mass template for background $\Lambda_b^0 \to \Lambda_c^{+*} \mu^- \bar{\nu}_\mu$ decays, shown after the full offline selection and reweighing stage for the 2016, `MagUp` polarity.

Double-charm $\Lambda_b^0 \to \Lambda_c^+ X_c X$ decays

Decays involving two charmed hadron species in the final state are commonly regarded as *double-charm* background sources when one of the two is a Λ_c^+ and the other particle, X_c, exhibits a fully leptonic or semileptonic transition. Three-body decays with additional unreconstructed X in the final states are also possible. The X_c hadron alias denotes the full spectrum of charmed mesons. We rely on a cocktail of MC simulations to model these decays, yielding a template shape highly correlated with the Λ_b^0 tauonic channel counterpart (Fig. 3.9.10). The primary approach to curb the double-charm contribution relies on the charged isolation selection (Sec. 3.5.5). Although primarily developed for feed-down from Λ_c^+ excited states, it proves very effective also in reducing this contribution. Besides, given the soft spectrum of the muon from the X_c decay, we expect any double-charm transition to be highly suppressed by the trigger selection, just as in the Λ_b^0 tauonic decay.

3.9.2 Fit to corrected mass distribution: results

The independent corrected mass fits in bins of q^2, $\cos\theta_\mu$ have been performed separately for each data-taking year (2016, 2017, 2018), finally combining both magnet polarities. While the full set of 2016 fits has been documented in App. 3.H in Fig. 3.H.1, we illustrate an example in Fig. 3.9.11 corresponding to the phase space region with the largest contribution of Λ_b muonic decays: $q^2 \in [4.8, 7.8]\,\mathrm{GeV}^2$, $\cos\theta_\mu \in [0.4, 1.0]$. The data/fit-model agreement in fit projections of phase space variables has also been documented in App. 3.H. From each fit result we extract the signal yield, $N(\Lambda_b^0 \to \Lambda_c^+ \mu^- \bar{\nu}_\mu)$, and its related statistical uncertainty. The measured shape of the signal decay for 2016 data is illustrated in Fig. 3.9.12. White areas in the phase space plane
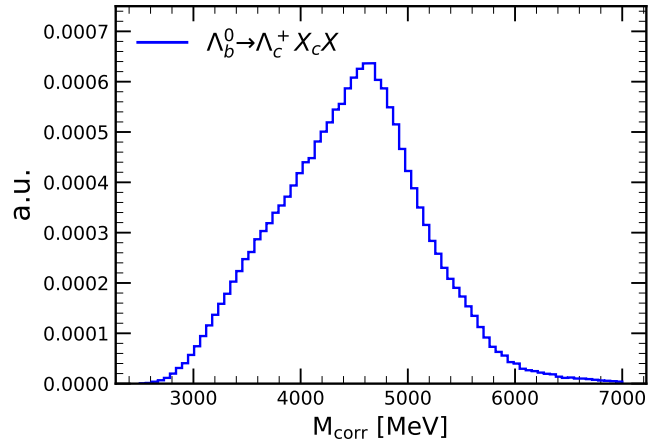
FIGURE 3.9.10: Corrected mass template for background $\Lambda_b^0 \to \Lambda_c^+ X_c X$ with a semileptonic X_c decay, shown after the full offline selection and reweighing stage for the 2016, `MagUp` polarity.

denote ignored bins, which were excluded from the analysis due to extremely low signal selection efficiency.

Any bias in the signal shape, possibly induced by a dependence of signal and background templates on New Physics encoded by the Wilson Coefficients, has been investigated and reported as systematic uncertainty in Sec. 3.11.3.
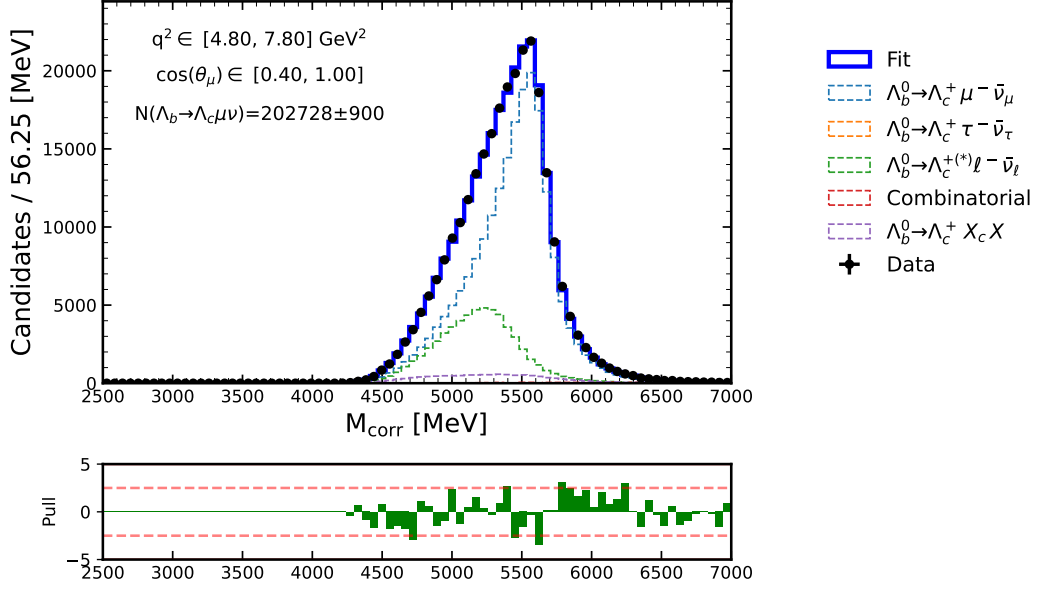
FIGURE 3.9.11: Illustration of one of the fits to the reconstructed Λ_b corrected mass in the 2016 sample, to determine the number of signal $\Lambda_b^0 \to \Lambda_c^+ \mu^- \bar{\nu}_\mu$ candidates. The phase space region here depicted corresponds to the bin with the largest contribution from signal events: $q^2 \in [4.8, 7.8] \, \text{GeV}^2$, $\cos\theta_\mu \in [0.4, 1.0]$.
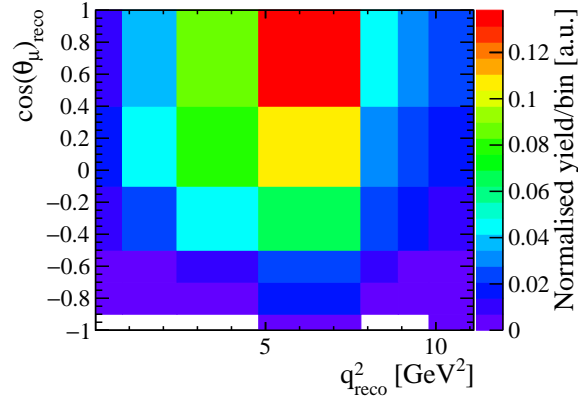
FIGURE 3.9.12: Normalised yield of the signal $\Lambda_b^0 \to \Lambda_c^+ \mu^- \bar{\nu}_\mu$ as a function of the phase space, corresponding to the 2016 sample. The blank spaces correspond to bins which have been ignored in the fitting procedure, given their extremely low statistics.

3.10 Extraction of Form Factors and Wilson Coefficients

The measurement of hadronic Form Factors and, for the first time, of muonic Wilson Coefficients in $\Lambda_b^0 \to \Lambda_c^+ \mu^- \bar{\nu}_\mu$ decays is performed following a folded fit approach. Thereby, the fit model is

constructed from the convolution of the theory prediction with experimental effects: the total selection efficiency (Sec. 3.7) and the response matrix (Sec. 3.8). Ultimately, the parameters of interest (PoI) are extracted by fitting the newly built model to the signal shape distribution, previously measured via corrected mass fits in bins of reconstructed q^2 and $\cos\theta_\mu$. The stability and robustness of the fit are enforced through an iterative approach: only the nuisance fit objects get updated at each consecutive step of the iteration with measured Form Factor values, in place of the adoption of Lattice QCD constraints, until convergence is reached. The fit is performed simultaneously over the data-taking years considered in this analysis.

While the analytic fit function is described in Sec. 3.10.1, we discuss the implementation and validation of the iterative fit procedure in Sec. 3.10.2 and 3.10.6, respectively. Ultimately, following a brief introduction on the Form Factors parameterisation in Sec. 3.10.3, fit results are presented first for Form Factors in Sec. 3.10.4, then for Wilson Coefficients in Sec. 3.10.5.

3.10.1   Fit model for q^2 and $\cos\theta_\mu$ distribution

The predicted signal decay shape across each phase space bin is described in terms of the discrete, folded fit model:

$$F\left(\vec{x}_{\text{reco}}^{i}, \vec{\Theta}\right) = \kappa \sum_{j=\text{bins}} R(\vec{x}_{\text{reco}}^{i}, \vec{x}_{\text{true}}^{j})\, \epsilon(\vec{x}_{\text{true}}^{j})\, \Delta f\left(\vec{x}_{\text{true}}^{j}, \vec{\Theta}\right) \tag{3.9}$$

where the above terms denote:

- κ, the normalisation factor;
- $\vec{x}^i = \left(q^{2\,i}, \cos\theta_\mu^{\,i}\right)$, phase space variables, either true or reconstructed;
- R^{ij}, the response matrix, function of the true and reconstructed phase space variables. It is modelled with simulation and assumed uniform across each bin;
- ϵ^j, the total selection efficiency, function of the true phase space variables. It is modelled with simulation and assumed uniform across each bin;
- $\vec{\Theta}$, parameters of interest, *i.e.* Form Factors and Wilson Coefficients;
- Δf^j, the integrated description of the decay dynamics, defined as the differential decay density integral over the true q^2, $cos\theta_\mu$:

$$\int_{q_j^2,\cos\theta_{\mu,j}} \frac{d^2\Gamma(\Lambda_b^0 \to \Lambda_c^+ \mu^- \bar{\nu}_\mu)}{dq^2\, d\cos\theta_\mu}\, dq^2\, d\cos\theta_\mu\,. \tag{3.10}$$

Taking into account the independent uncertainties on the corrected mass fit results on a bin-by-bin basis, the estimators of the PoI $\vec{\Theta}$, $\hat{\vec{\Theta}}$, can be retrieved following the method of least squares. Besides, we incorporate the prior knowledge on FF parameters from Lattice QCD or our fit results by considering a multiplicative multi-normal function $G(\vec{\Theta}_{\text{FF}})$, such that the function to minimise

becomes:

$$\chi^2(\vec{\Theta}) = -2\ln\lambda = \sum_{j=\text{bins}} \frac{(O_j - F(x_j, \vec{\Theta}))^2}{\sigma_{O_j}^2} - 2\ln G(\vec{\Theta}_{\text{FF}}), \tag{3.11}$$

where O_j is the observed signal yield shape with associated uncertainty σ_{O_j} in the bin j; $F(x_j, \vec{\Theta})$ is the fit model defined in Eq. 3.9; while

$$G(\vec{\Theta}_{\text{FF}}) = \frac{\exp\left(-(\vec{\Theta}_{\text{FF}}^c - \vec{\Theta}_{\text{FF}}) M_c^{-1} (\vec{\Theta}_{\text{FF}}^c - \vec{\Theta}_{\text{FF}})^T\right)}{(2\pi)^{n/2} |M_c|^{1/2}}. \tag{3.12}$$

The term $\vec{\Theta}_{\text{FF}}^c$ denotes the constrained value for the FF parameters, whereas M_c is the $n \times n$ covariance matrix known from external inputs.

3.10.2 Iterative fit strategy

The choice to follow an iterative, staged fit approach is two-fold. Firstly, an independent determination of FF parameters with WC set to their SM value brings the advantage of unprecedented precision, given the reduced statistical and systematic uncertainty induced by the large signal yields. Ultimately, a staged and iterative fit approach entails a reduced systematic due to the model dependency of the nuisance fit objects (Sec. 3.11.3), *i.e.* M_{corr} templates, efficiency and response matrices.

A schematic illustration of the iterative fit strategy is presented in Fig. 3.10.1. The first configuration consists of a SM fit to extract the FF parameters: the fit model includes nuisance objects (M_{corr} templates to determine the signal yields, efficiency and response matrices) constructed with FF, which are Gaussian-constrained to LQCD values. Wilson Coefficients are null in this step of the iteration, set to the SM value. Subsequent steps include updating the nuisance objects using FF values from the data fit. The procedure is repeated until convergence is reached and the PoI values stabilise. At this point, the New Physics fit takes place: we perform four individual one-dimensional likelihood profiling over the Wilson Coefficients C_{V_R}, C_T, C_{S_R}, C_{S_L} to curb correlation effects, while keeping the FF Gaussian-constrained to LQCD values. Assuming Wilks theorem is satisfied, the test statistics are distributed according to a χ^2 distribution approximated by a parabolic function around the minimum. The values corresponding to the minimum of the profiled likelihood and its variation of one unit around it yield the WC central value and uncertainty, respectively. Once generated from FF fit values, the nuisance objects are now updated using the WC fit value. The procedure is iterated until convergence is reached upon the WC parameters under the assumption that fits are more sensitive to the PoI than a variation in the nuisance objects. This hypothesis has been demonstrated with pseudo-experiments and documented in Sec. 3.11.3.
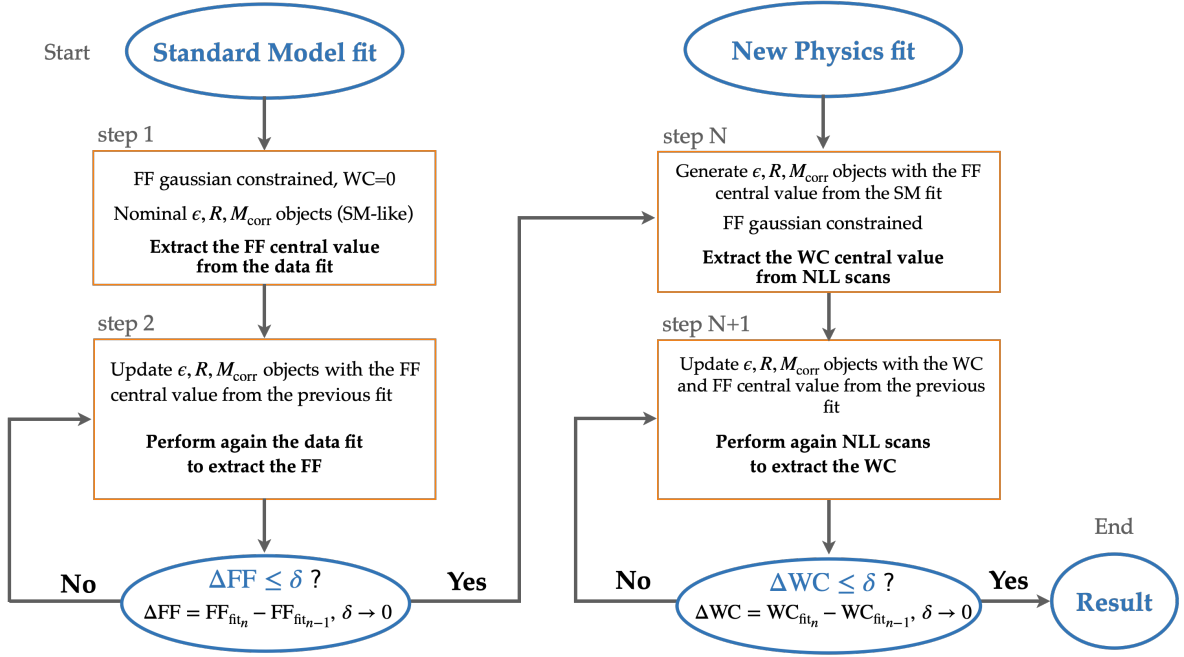
FIGURE 3.10.1: Schematic illustration of the iterative fit strategy. The transition between Standard Model and New Physics fits occurs when the observed difference in FF between two consecutive fit iterations is smaller than a δ parameter approaching zero.

3.10.3 Form Factors parameterisation

Form Factor parameters encode the non-perturbative effects of the hadronic matrix elements $\langle \Lambda_c | X | \Lambda_b \rangle$ in signal transitions for the current X. High-precision relativistic calculations are usually performed on the Lattice, although the reliability of the prediction is restricted only at high di-lepton invariant mass squared.

It is timely to introduce the Form Factor parameterisation adopted in this analysis, based on the BCL expansion [53] and corresponding to the helicity formalism described in Ref. [44, 45]. The matrix elements of the vector (Eq. 3.13), axial-vector (Eq. 3.14), scalar (Eq. 3.15), pseudo-scalar (Eq. 3.16) can be written in terms of the helicity form factors $f_0, f_+, f_\perp, g_0, g_+, g_\perp$ as follows:

$$
\begin{aligned}
\langle \Lambda_c(p',s') | \bar{c}\gamma^\mu b | \Lambda_b(p,s) \rangle = \bar{u}_{\Lambda_c}(p',s') \Bigg[& f_0(q^2)\left(m_{\Lambda_b} - m_{\Lambda_c}\right)\frac{q^\mu}{q^2} \\
& + f_+(q^2)\frac{m_{\Lambda_b} + m_{\Lambda_c}}{s_+}\left(p^\mu + p'^\mu - \left(m_{\Lambda_b}^2 - m_{\Lambda_c}^2\right)\frac{q^\mu}{q^2}\right) \\
& + f_\perp(q^2)\left(\gamma^\mu - \frac{2m_{\Lambda_c}}{s_+}p^\mu - \frac{2m_{\Lambda_b}}{s_+}p'^\mu\right) \Bigg] u_{\Lambda_b}(p,s),
\end{aligned} \tag{3.13}
$$

$$\langle \Lambda_c(p',s')|\bar{q}\gamma^\mu\gamma_5 b|\Lambda_b(p,s)\rangle = -\bar{u}_{\Lambda_c}(p',s')\gamma_5 \Bigg[g_0(q^2)(m_{\Lambda_b}+m_{\Lambda_c})\frac{q^\mu}{q^2}$$
$$+g_+(q^2)\frac{m_{\Lambda_b}-m_{\Lambda_c}}{s_-}\left(p^\mu+p'^\mu-(m_{\Lambda_b}^2-m_{\Lambda_c}^2)\frac{q^\mu}{q^2}\right)$$
$$+g_\perp(q^2)\left(\gamma^\mu+\frac{2m_{\Lambda_c}}{s_-}p^\mu-\frac{2m_{\Lambda_b}}{s_-}p'^\mu\right)\Bigg]u_{\Lambda_b}(p,s), \quad (3.14)$$

$$\langle \Lambda_c|\bar{c}b|\Lambda_b\rangle = F_0(q^2)\frac{m_{\Lambda_b}-m_{\Lambda_c}}{m_b-m_c}\bar{u}_{\Lambda_c}u_{\Lambda_b}, \quad (3.15)$$

$$\langle \Lambda_c|\bar{c}\gamma_5 b|\Lambda_b\rangle = G_0(q^2)\frac{m_{\Lambda_b}+m_{\Lambda_c}}{m_b+m_c}\bar{u}_{\Lambda_c}\gamma_5 u_{\Lambda_b}. \quad (3.16)$$

In addition to these, in the presence of non-SM-like tensor currents, matrix elements can be expressed in terms of the additional form factors h_+, $h_\perp$, $\tilde{h}_+$, $\tilde{h}_\perp$ as follows (Eq. 3.17):

$$\langle \Lambda_c|\bar{c}i\sigma^{\mu\nu}b|\Lambda_b\rangle = \bar{u}_{\Lambda_c}\Bigg[2h_+(q^2)\frac{p^\mu_{\Lambda_b}p^\nu_{\Lambda_c}-p^\nu_{\Lambda_b}p^\mu_{\Lambda_c}}{s_+}$$
$$+h_\perp(q^2)\left(\frac{m_{\Lambda_b}+m_{\Lambda_c}}{q^2}(q^\mu\gamma^\nu-q^\nu\gamma^\mu)-2(\frac{1}{q^2}+\frac{1}{s_+})(p^\mu_{\Lambda_b}p^\nu_{\Lambda_c}-p^\nu_{\Lambda_b}p^\mu_{\Lambda_c})\right)$$
$$+\tilde{h}_+(q^2)\left(i\sigma^{\mu\nu}-\frac{2}{s_-}(m_{\Lambda_b}(p^\mu_{\Lambda_c}\gamma^\nu-p^\nu_{\Lambda_c}\gamma^\mu)-m_{\Lambda_c}(p^\mu_{\Lambda_b}\gamma^\nu-p^\nu_{\Lambda_b}\gamma^\mu)+p^\mu_{\Lambda_b}p^\nu_{\Lambda_c}-p^\nu_{\Lambda_b}p^\mu_{\Lambda_c})\right)$$
$$+\tilde{h}_\perp(q^2)\frac{m_{\Lambda_b}-m_{\Lambda_c}}{q^2 s_-}\Big((m_{\Lambda_b}^2-m_{\Lambda_c}^2-q^2)(\gamma^\mu p^\nu_{\Lambda_b}-\gamma^\nu p^\mu_{\Lambda_b})-(m_{\Lambda_b}^2-m_{\Lambda_c}^2+q^2)(\gamma^\mu p^\nu_{\Lambda_c}-\gamma^\nu p^\mu_{\Lambda_c})$$
$$+2(m_{\Lambda_b}-m_{\Lambda_c})(p^\mu_{\Lambda_b}p^\nu_{\Lambda_c}-p^\nu_{\Lambda_b}p^\mu_{\Lambda_c})\Big)\Bigg]u_{\Lambda_b}. \quad (3.17)$$

The term $q = p_{\Lambda_b}-p'_{\Lambda_c}$ denotes the transferred four-momentum, while:

$$s_\pm = (m_{\Lambda_b}\pm m_{\Lambda_c})^2-q^2. \quad (3.18)$$

We approximate the FF functional form to the first-order expression in the physical limit:

$$f(q^2) = \frac{1}{1-q^2/(m_{\text{pole}}^f)^2}[a_0^f+a_1^f z^f(q^2)], \quad (3.19)$$

valid when the lattice spacing a is taken in the continuum limit ($a \rightarrow 0$), and the pion mass[21] corresponds its physical value (chiral extrapolation). The expansion parameter z^f is a parameterisation

---

[21]Equivalently, this corresponds to the mass of the light quarks $q = u$, d, s being tuned to their physical value.

of q^2, defined as[22]:

$$z^f(q^2) = \frac{\sqrt{t_+^f - q^2} - \sqrt{t_+^f - t_0}}{\sqrt{t_+^f - q^2} + \sqrt{t_+^f - t_0}},$$

(3.20)

with the constants

$$t_0 = (m_{\Lambda_b} - m_{\Lambda_c})^2,$$

(3.21)

$$t_+^f = (m_{\text{pole}}^f)^2.$$

(3.22)

The values of the pole masses, corresponding to singularities in the values of the FF, are taken from Ref. [44, 45].

The helicity formalism, here introduced to parameterise the FF, is the framework of our choice in the description of the signal differential decay density model $d^2\Gamma / (dq^2 d\cos\theta_\mu)$ (see Sec. 2.D).

3.10.4 Form Factors: fit result

This section presents the SM FF fit values and uncertainties resulting from minimising the quadratic expression formulated in Eq. 3.10.1, performed simultaneously for the Run 2 data sample. The results are expressed in terms of the helicity FF parameterisation defined in Sec. 3.10.3, with a_0 and a_1 denoting the zeroth and first order of the q^2 expansion, respectively. The floated parameters in the fit include all the FF but $a_0 g_+$, instead factorised and cancelling out with the signal shape normalisation. As a consequence, ten FF values are determined from the fit.

The corrected mass and phase space fits have been repeated twice before convergence, following the iterative procedure described in Sec. 3.10.2. Fig. 3.10.2 illustrates the post-fit agreement between the 2016 data and fit model in the phase space projections. Projections corresponding to the remaining Run 2 years (2017, 2018) are included in App. 3.I for reference.

FF central values and associated statistical uncertainties[23] from the fit are summarised in Tab. 3.10.1, with the full covariance matrix reported in Fig. 3.10.4. Given the unprecedented signal yields analysed in this work, these results are the most precise experimental FF determination to date. We note that our results are consistent with the LQCD estimate in the determination of most of the hadronic vector and axial-vector FF values. Discrepancies are instead observed in the vector/scalar currents expansion terms $a_0 f_\perp$, $a_0 f_+$, $a_1 f_0$, $a_1 f_+$. This occurrence is not an isolate case in the current experimental panorama, as demonstrated by the latest BESIII measurement [54] on $\Lambda_c^+ \to \Lambda \ell^+ \nu_\ell$ FF parameters. Fig. 3.10.3 illustrates the comparison of our unfolded decay model including the statistical uncertainty (red shaded area) with LQCD [44] (grey band) and the previous LHCb measurement [7] (blue curve) in the true q^2 and $\cos\theta_\mu$ projections. Preliminary toy studies showed good coverage of the Hessian matrix employed to determine the statistical

---

[22]The point $z = 0$ corresponds to the minimum recoil, *i.e.* $q^2 = q_{\text{max}}^2$, with the Λ_c at rest in the Λ_b rest frame.

[23]We here note that the quadratic form minimised in phase space fits (Eq. 3.10.1) includes uncertainties on the signal yield from binned fits to the corrected mass.

uncertainty of the fit. We conclude by stressing the importance of an additional LQCD-based independent determination of FF parameters to solve the pattern of deviations, which would aid the advancement of this research field.
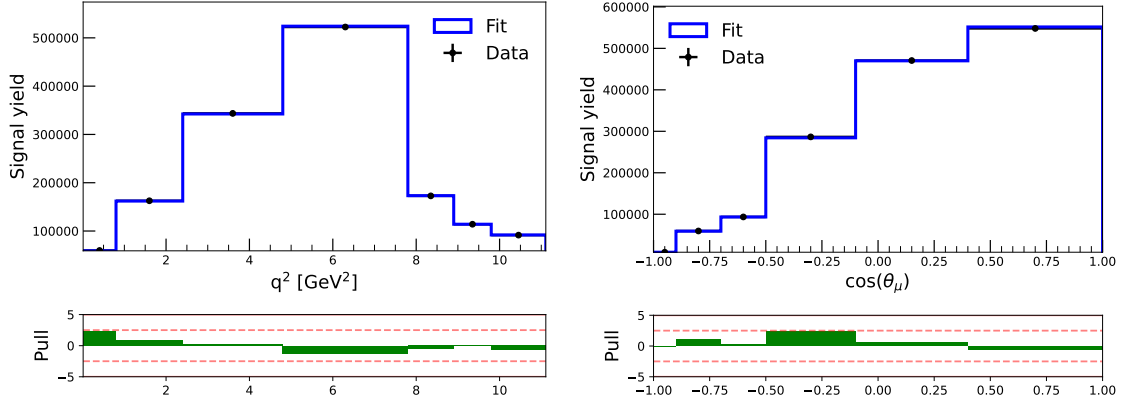
FIGURE 3.10.2: Agreement between recorded data yields (black) and fit model (blue) achieved after two iterations of the phase space fit, shown in projections of q^2 (left) and $\cos\theta_\mu$ (right) for the 2016 samples.
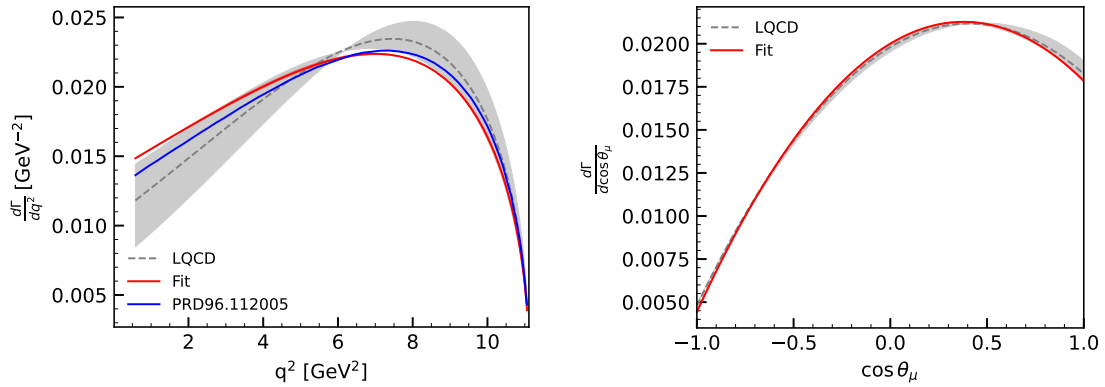
FIGURE 3.10.3: Comparison between the unfolded signal decay rate calculated with FF results including statistical uncertainty from this analysis (red shaded area), Lattice QCD FF calculations [44] (grey shaded area), and the previous FF measurement by LHCb [7] (blue curve). Top: projections in q^2; bottom: projections in $\cos\theta_\mu$.

Form Factor	Fit value $\pm \sigma_{\text{stat}}$	LQCD value $\pm \sigma_{\text{LQCD}}$ [44]
$a_0 f_0$	0.714 ± 0.010	0.74393 ± 0.00016
$a_0 f_\perp$	1.008 ± 0.010	1.0780 ± 0.0006
$a_0 f_+$	0.762 ± 0.010	0.8146 ± 0.0003
$a_0 g_0$	0.723 ± 0.011	0.73960 ± 0.00020
$a_1 f_0$	-2.36 ± 0.17	-4.65 ± 0.37
$a_1 f_\perp$	-3.07 ± 0.26	-6.42 ± 0.72
$a_1 f_+$	-2.57 ± 0.10	-4.90 ± 0.29
$a_1 g_0$	-4.26 ± 0.17	-4.37 ± 0.11
$a_1 g_\perp$	-4.29 ± 0.07	-4.46 ± 0.13
$a_1 g_+$	-4.50 ± 0.12	-4.43 ± 0.13

TABLE 3.10.1: Form Factors central value and associated statistical uncertainty, resulting from two iterations of a simultaneous Run 2 fit to the reconstructed signal shape in phase space and LQCD.
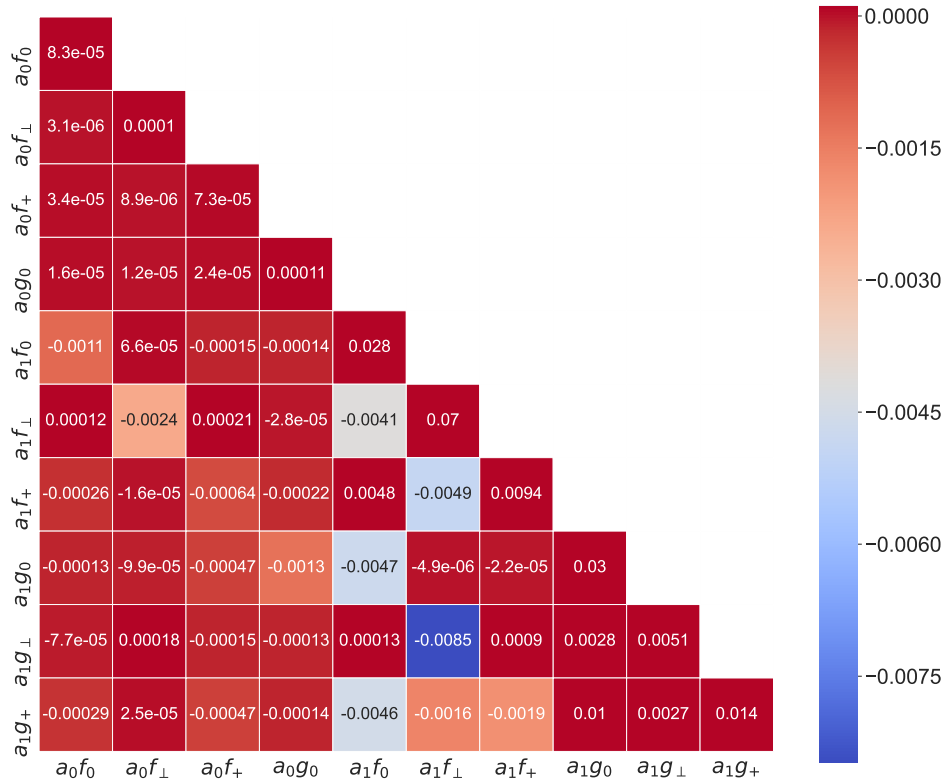
FIGURE 3.10.4: Form Factors covariance matrix, resulting from two iterations of a simultaneous Run 2 fit to the reconstructed signal shape in phase space.

3.10.5 Wilson Coefficients: fit result

At the present stage of the analysis, the central fit value of the Wilson Coefficients is unknown, masked by a blinding strategy:

$$\text{WC}_{\text{blind}} = \alpha \cdot \text{WC}_{\text{fit}} + \beta,$$

with α, β independent parameters being generated randomly in the range $[0, 100]$.

The results of the four likelihood profiles summarised in Tab. 3.10.2 and illustrated in Fig. 3.10.5 provide the current statistical sensitivity of the analysis corresponding to one standard deviation (red-shaded area). Acting as nuisance parameters of these likelihood scans, FF have been initialised with the LQCD values and Gaussian-constrained throughout the likelihood scanning procedure. While the profiles exhibit a stable behaviour and much better sensitivity in the determinations of C_{V_R} and C_T, the contrary is true for the scalar coefficients C_{S_R} and C_{S_L}. Nonetheless, we observe a large difference between the experimental sensitivity for C_{V_R} obtained here, compared to the results described in the toy studies reported in Chap. 2, when rescaled to the same integrated luminosity[24] (see *e.g.* Tab. 2.1). Some of the discrepancy should be expected, primarily because of the following differences between the two determinations, which might impact the sensitivity:

- The total efficiency, assumed uniform in the preliminary sensitivity study, is instead heavily sculpted in phase space due to the selection requirements (Fig. 3.7.1).

- The optimised binning scheme employed in this analysis (Fig. 3.G.2) does not match with the one adopted for the toys studies (see Sec. 2.G).

- The uncertainty on the signal yield distribution in phase space, in this analysis extracted from the fit to the Λ_b^0 corrected mass, is instead taken as the Poisson uncertainty of the expected number of candidates in Chap. 2. The latter is an approximation valid only under the assumption of absent background pollution, thus representing the optimistic lower limit of the real uncertainty.

- We modify fit phase space boundaries in this analysis by ignoring part of the negative $\cos \theta_\mu$ region associated with significant efficiency variations and low signal yield (Fig. 3.9.1). While this adjustment yields fit stability and no difference in the determination of the PoI, it could be a driving factor behind the enhanced sensitivity emerging from toy studies.

---

[24]We remark here that the results reported in the phenomenological study in Chap. 2 assume a signal statistics of $7.5\,\text{M}$ candidates, corresponding to the full integrated luminosity (Run 1 and Run 2) of $9\,\text{fb}^{-1}$.
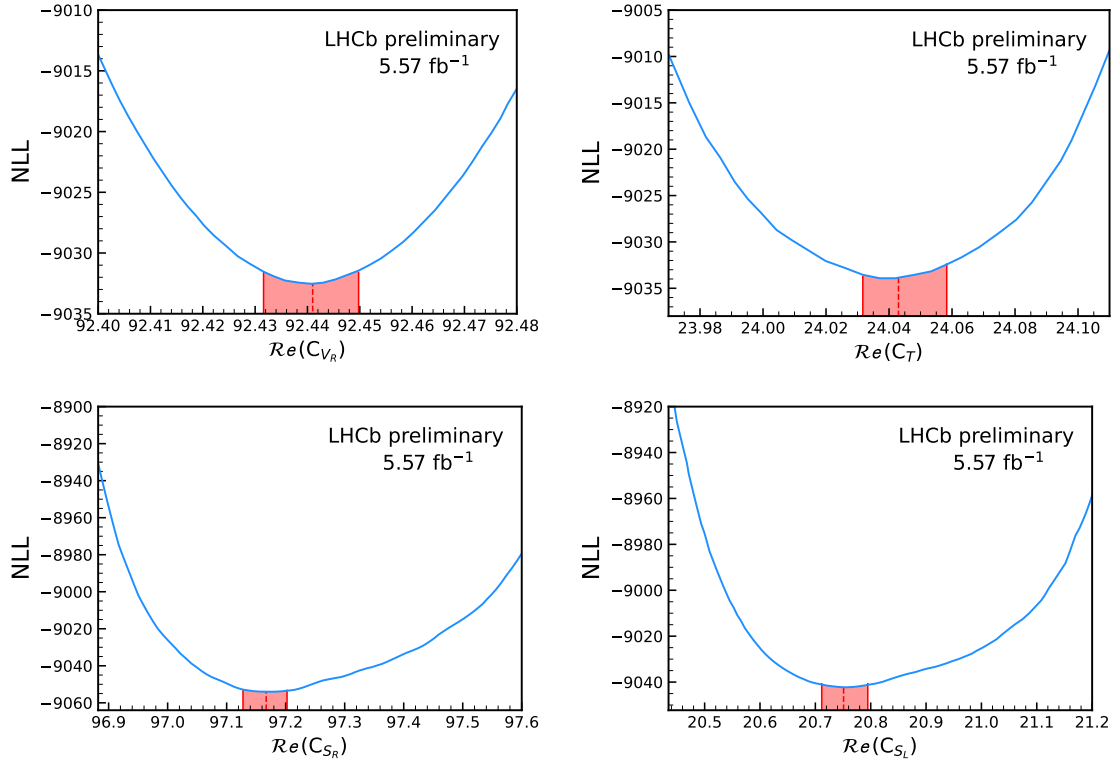
FIGURE 3.10.5: Likelihood profiling over the Wilson Coefficients C_{V_R}, C_T, C_{S_R}, C_{S_L}. The red-shaded area corresponds to one standard deviation.

Wilson Coefficient	Blind fit value $\pm\, \sigma_{\text{stat}}$
$\mathscr{R}e\left(C_{V_R}\right)$	$X^{+0.010}_{-0.010}$
$\mathscr{R}e\left(C_{T}\right)$	$X^{+0.016}_{-0.017}$
$\mathscr{R}e\left(C_{S_R}\right)$	$X^{+0.046}_{-0.040}$
$\mathscr{R}e\left(C_{S_L}\right)$	$X^{+0.055}_{-0.047}$

TABLE 3.10.2: Blind Wilson Coefficient fit values with associated statistical uncertainty, as determined from the NLL profiling over the Run 2 dataset, corresponding to $5.57\,\text{fb}^{-1}$.

3.10.6 Fit validation

A robust and unbiased fit framework translates into the ability of the fit procedure to return the true value of the PoI, given any initial setup. We test the iterative model in retrieving the Form Factor values with corrected mass fits to pseudo-data, generated according to a Standard Model-like (LQCD) or New Physics (NP) scenario, followed by a phase space fit. At the end of the iterative procedure a comparison with the underlying value of the FF, used to generate the pseudo-data, confirms or disproves the absence of biases.

The fit infrastructure is validated in the following configurations:

1. Pseudo-data generated only with the $\Lambda_b^0 \rightarrow \Lambda_c^+ \mu^- \bar{\nu}_\mu$ decay component, with FF set to LQCD values. The M_{corr} signal template is calibrated on the LQCD generation model (Sec. 3.6.2).

2. Pseudo-data generated with the signal and background decays, with FF set to LQCD values. M_{corr} templates are calibrated on the LQCD model.

3. Pseudo-data generated with the signal and background decays, with FF set to random values. M_{corr} templates are calibrated on the LQCD model.

4. Pseudo-data generated with the signal and background decays, with FF set to LQCD values. M_{corr} templates are calibrated on a model with random FF values.

For each scenario we compare the FF fit value with the one corresponding to the LQCD or NP priors, reaching good agreement in all of them (Fig. 3.10.6).
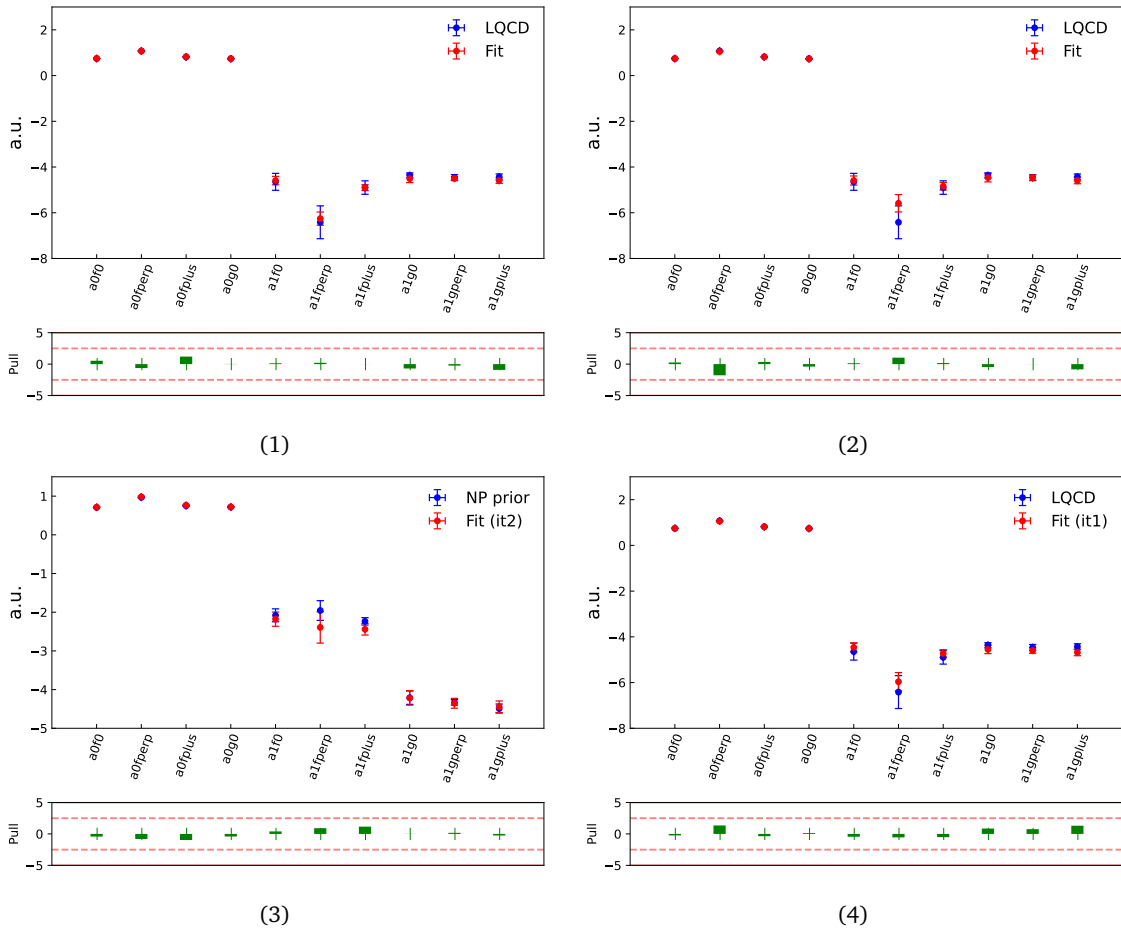
FIGURE 3.10.6: Comparison between the FF fit and prior values used in the fit validation procedure. (1): LQCD FF prior to generate signal-only pseudo-data, M_{corr} templates without background calibrated on LQCD model; (2): LQCD FF prior to generate pseudo-data, M_{corr} templates including background calibrated on LQCD model; (3): NP FF prior to generate pseudo-data, M_{corr} templates including background calibrated on LQCD model; (4): LQCD FF prior to generate pseudo-data, M_{corr} templates including background calibrated on NP model.

3.11 Systematic uncertainties

This section outlines the main systematic uncertainties associated with this analysis: effect of MC simulation size (Sec 3.11.1); inclusion of Data/MC reweighting (Sec 3.11.2); model dependency effects on fit nuisance objects (Sec 3.11.3). While this is not an exhaustive list, work is ongoing to assess the remaining systematic uncertainties, instead briefly described in Sec. 3.11.4.

3.11.1 Simulation size

The statistics of each MC simulation sample, used to generate templates in corrected mass, affects the final uncertainty on the PoI of this analysis. Its contribution can be directly evaluated via an event-by-event bootstrapping[25] of templates used to fit M_{corr} for signal and backgrounds.

Firstly, a quantitative assessment has been performed with the full MC, *i.e.* the detailed simulation, including the complete LHCb detector description. At this stage, we aim at determining the number of simulated events, which is required in order to reduce the associated systematic uncertainty σ_{sys} below the statistical uncertainty of the M_{corr} fit, σ_{stat}. We generate $N_{toys} = 100$ pseudo-experiments and fit them with bootstrapped templates. The systematic uncertainty due to the limited size of simulated samples, σ_{sys}, is defined as the standard deviation of the discrepancy in the signal yield distribution between nominal and pseudo-data M_{corr} fits.

The necessity of large statistic MC simulation is demonstrated in Fig. 3.11.2, illustrating the comparability on a per-bin level between the systematic and statistical uncertainty of corrected mass fits. A few outliers among the first bins in phase space correspond to low-statistics scenarios associated with large fluctuations in the estimated number of signal events (see also Fig. 3.G.2 for the bin numbering scheme). Given that most of those regions have been excluded from the fit (Fig. 3.9.1), this is of no concern for the analysis. Consequently, we proceed with adopting high statistics tracker-only MC simulation throughout the analysis (Sec. 3.4.1).

An equivalent systematic uncertainty assessment for tracker-only simulated samples is currently in progress.
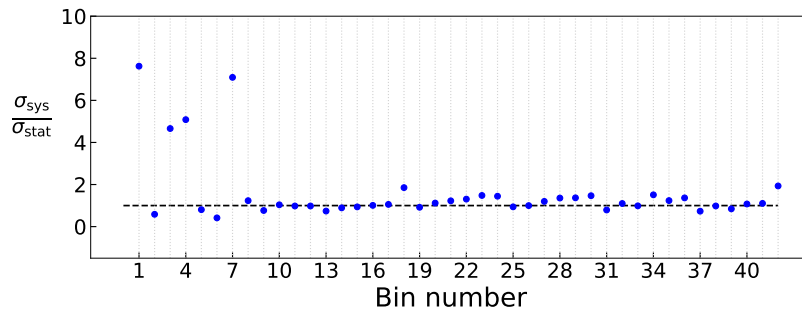
FIGURE 3.11.1: Ratio of systematic uncertainty σ_{sys}, associated with the full MC simulation size and assessed via bootstrapping, to statistical uncertainty σ_{stat} in fits to the corrected mass, as a function of the adopted binning in phase space.

3.11.2 Data/Monte Carlo agreement

One of the systematic uncertainties of this measurement pertains to the effect of the post-fit Data/MC corrections (Sec. 3.6.8), hiding a possible residual misalignment in modelling the

---

[25]Bootstrapping corresponds to a resampling technique with replacement, used to generate multiple samples from a given dataset.

detector response. We assess this contribution by performing the complete set of corrected mass and phase space fits without including the post-fit correction, next comparing the FF fit result to the nominal fit case reported in previous sections. As demonstrated in Fig. 3.11.2, the deviation of the measurement without MC corrections corresponding to two iterations (red points) from the nominal scenario (blue points) is under control for every FF parameter. Equivalent assessments on the WC fit values are ongoing.
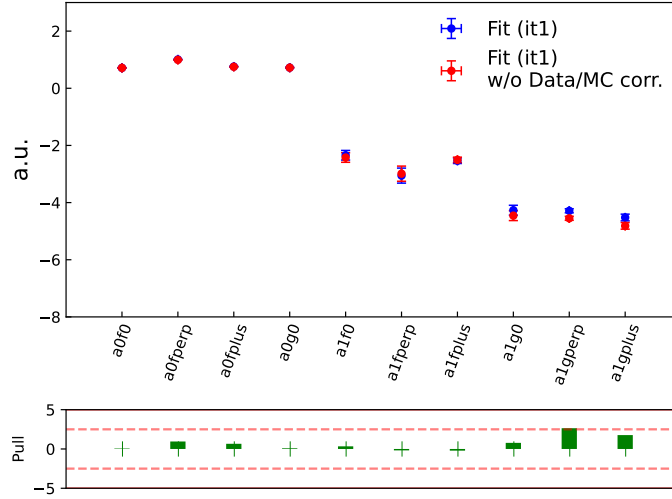
FIGURE 3.11.2: Comparison and agreement between the FF parameters retrieved in two iterative scenarios: (blue) nominal fit; (red) fit performed with templates without Data/MC post-fit kinematic weights.

3.11.3 Model dependency

The model dependency systematic uncertainty arises when the wrong model is used to produce the nuisance objects in the iterative fit process, such as the shape of the signal template (M_{corr}), efficiency ϵ, and response R matrices. We assess this contribution to the systematic budget of each PoI and for the $\Lambda_b^0 \to \Lambda_c^+ \mu^- \bar{\nu}_\mu$ signal yield, therefore defining six different *fit scenarios* and just as many estimators of the fit parameters: one for the signal number of events in M_{corr}; one for the FF ($\hat{\Theta}_{FF}$); four for the WC parameters ($\hat{\Theta}_{C_{V_R}}, \hat{\Theta}_{C_T}, \hat{\Theta}_{C_{S_R}}, \hat{\Theta}_{C_{S_L}}$). In each fit scenario we assess the bias induced by a modification in the nuisance object due to a shift in the central value of the FF or WC, by fitting pseudo-data with Run 2 statistics generated under nominal SM conditions[26]. Consequently, each fit configuration is tested under different *model scenarios* for each modified PoI value. We vary the WC parameters within the 95% confidence level from Ref. [55] while adopting the LQCD central values and associated uncertainties for the FF based on Ref. [44, 45]. Specifically for the FF and WC fit scenarios, the systematic variation is examined for the efficiency and response matrices individually and in a combined configuration to evaluate any latent correlation effects.

---

[26]Null value of the Wilson Coefficients; Form Factors set to the LQCD central values from Ref. [44, 45].

Fig. 3.11.3 shows the effect of a model variation on the corrected mass fits induced by a change in the signal template shapes after a FF and WC modification, as indicated in the legend of each panel. The systematic uncertainty, taken as the standard deviation of the difference between the signal yield in the nominal fit scenario and after the model variation, is compared to the statistical uncertainty of the fit across the phase space binning. We consistently observe that the latter dominates over the systematic budget, except for a few bins where they tend to be of comparable size. As already observed in Sec. 3.11.1, they correspond to scenarios associated with more significant instabilities in the fit due to a small signal yield value or indistinguishable background shapes. The last occurrence is resolved by adopting a common template description for multiple backgrounds, as often the case for the Λ_b tauonic decay and the double charm component.
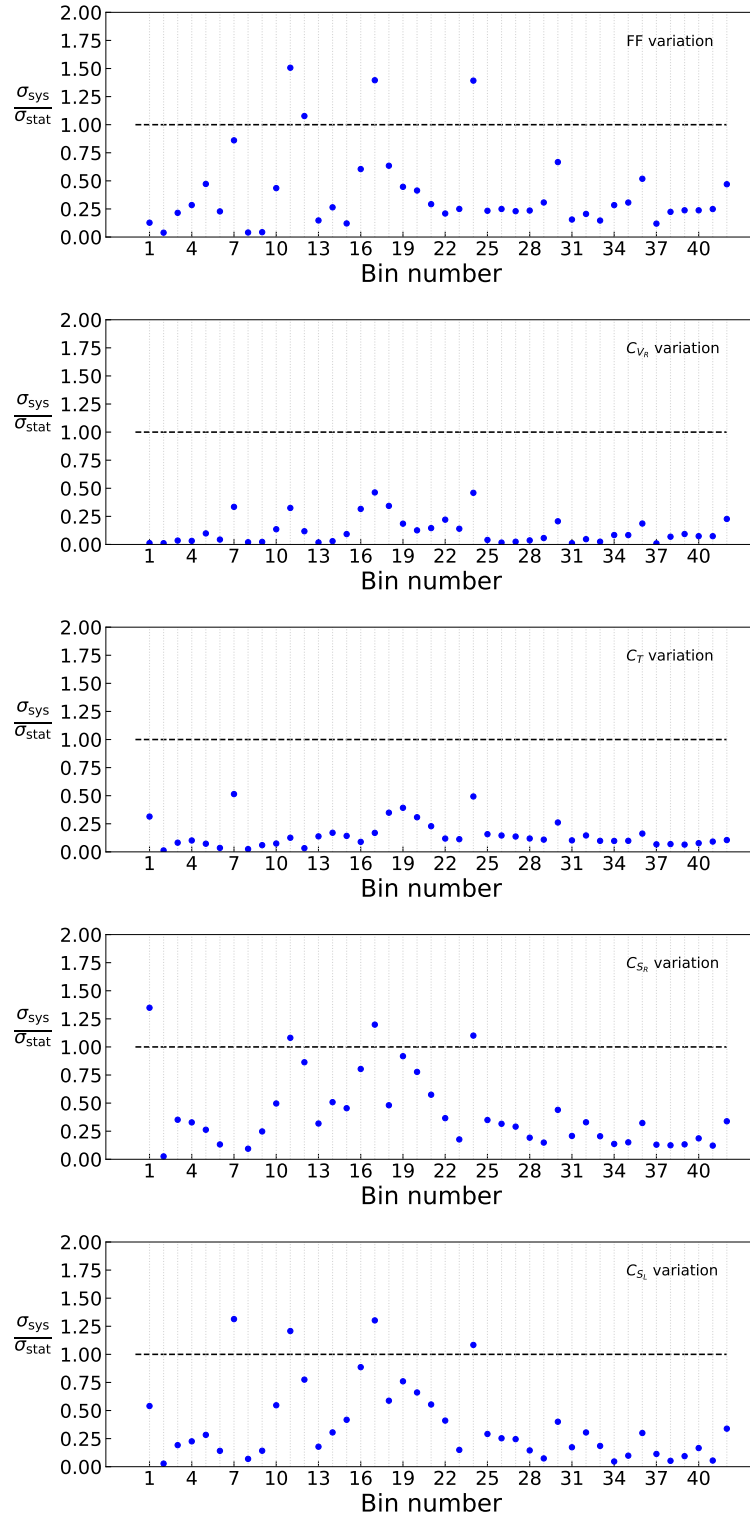
FIGURE 3.11.3: Comparison between statistical (σ_{stat}) and systematic (σ_{sys}) uncertainties in the corrected mass fit scenario as a function of the phase space binning. The systematic uncertainty is taken as the standard deviation of the signal yields discrepancy between nominal and model variation scenarios, with the latter corresponding to a change in the signal $\mathrm{M}_{\mathrm{corr}}$ template shape.

In Fig. 3.11.4, we evaluate the FF fit scenario under the FF model scenario, associated with a variation in either the efficiency (top panel), the response matrix (middle panel), or both (bottom panel). The comparison between statistical and systematic uncertainty of the fit hints at the dominant effect among the three configurations, *i.e.* the one associated with a model variation in the response matrix. Despite being the prevailing contribution, it remains equivalent to or smaller than the statistical uncertainty while showing a small interplay with the efficiency.
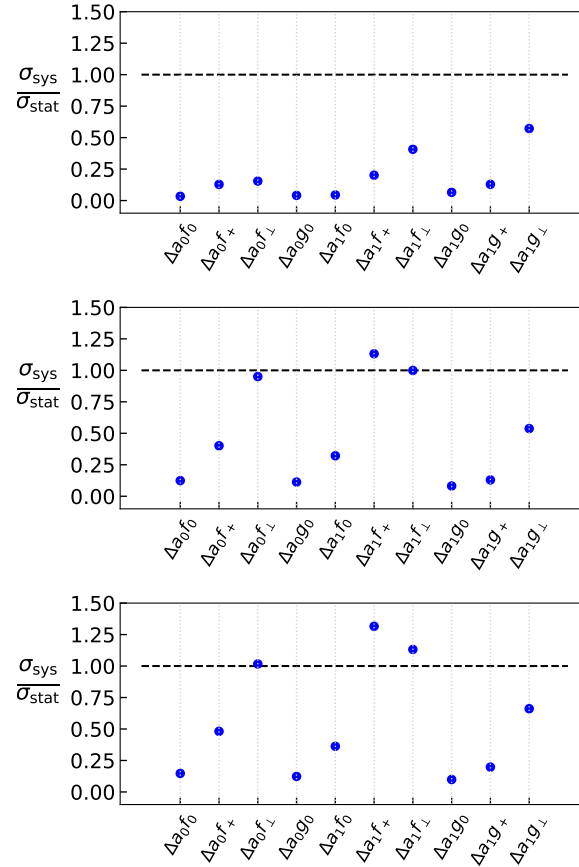
FIGURE 3.11.4: Comparison between statistical (σ_{stat}) and systematic (σ_{sys}) uncertainties in the FF fit and FF model scenario. The systematic uncertainty is taken as the standard deviation of the discrepancy in FF fit value between nominal and model variation scenarios. Three conditions are illustrated: (top) the variation is propagated only to the efficiency; (middle) the variation is propagated only to the response matrix; (bottom) the variation is injected in both efficiency and response matrices.

In Fig. 3.11.5, we assess the systematic effect in the WC fit scenario under the FF model scenario, associated with a variation in either the efficiency (top panel), the response matrix (middle panel) or both (bottom panel). The interplay between efficiency and response matrices renders an ideal situation of controlled systematics well below statistical precision.
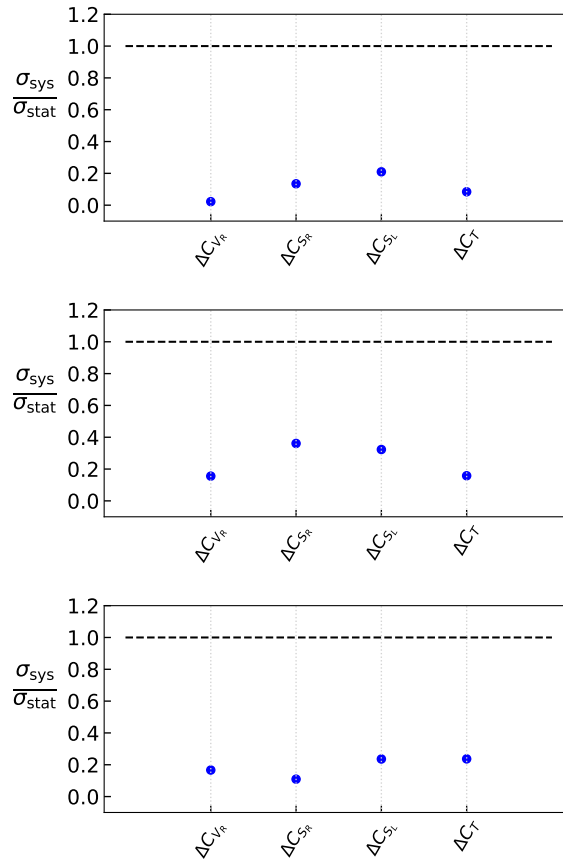
FIGURE 3.11.5: Comparison between statistical (σ_{stat}) and systematic (σ_{sys}) uncertainties in the WC fit and FF model scenario. The systematic uncertainty is taken as the standard deviation of the discrepancy in WC fit value between nominal and FF model variation scenarios. Three conditions are illustrated: (top) the variation is propagated only to the efficiency; (middle) the variation is propagated only to the response matrix; (bottom) the variation is injected in both efficiency and response matrices.

Finally, as illustrated in Fig. 3.11.6, we estimate the model dependency systematic in the WC fit scenario under a WC model variation in either the efficiency (top panel), the response matrix (middle panel), or both (bottom panel). Similarly to the preceding case, the observed values of systematic uncertainties are well below the statistical precision of the fit for all the WC values.
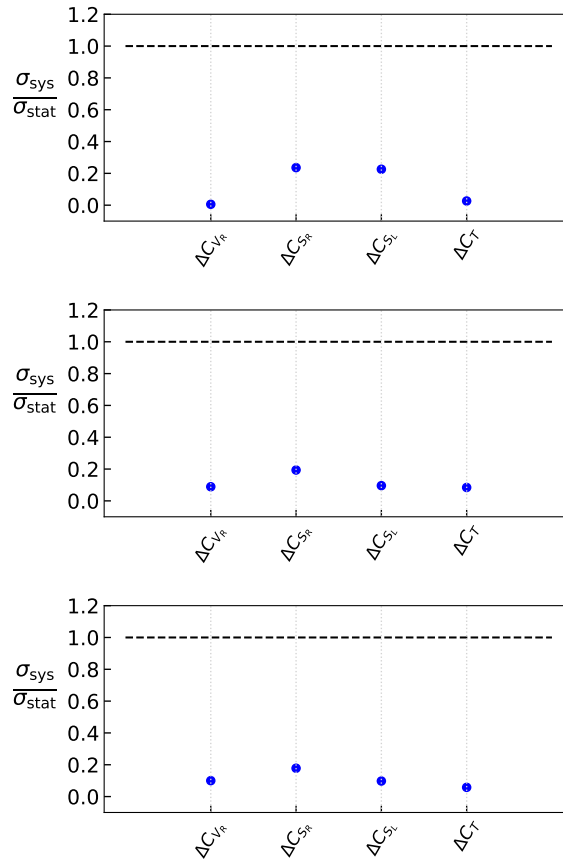
FIGURE 3.11.6: Comparison between statistical (σ_{stat}) and systematic (σ_{sys}) uncertainties in the FF fit and WC model scenario. The systematic uncertainty is taken as the standard deviation of the discrepancy in WC fit value between nominal and WC model variation scenarios. Three conditions are illustrated: (top) the variation is propagated only to the efficiency; (middle) the variation is propagated only to the response matrix; (bottom) the variation is injected in both efficiency and response matrices.

In conclusion, the examined systematic uncertainties do not pose a significant concern to this analysis.

3.11.4 Further sources of uncertainty

A set of additional sources of systematic uncertainty is currently under evaluation, reported as an exhaustive list below:

(a) Effect of using a decay model correction in ground state and excited $\Lambda_b^0 \to \Lambda_c^{(*)+} \mu^- \bar{\nu}_\mu$ decays based on LQCD calculations. The implementation of the complete differential decay density model for these transitions is discussed in Sec. 3.6.2 and App. 3.J, respectively.

(b) Impact of the choice on the truncation order in the BCL FF parameterisation of signal decays, currently corresponding to the first order in q^2 ($\sum_{n=0}^{1} a_n z^n(q^2)$). We plan to address this issue by generating pseudo-data from a *n-th* order FF description in q^2, in a model-agnostic way. This method includes sequential generation of FF parameters satisfying the unitarity condition $\sum_{n=0}^{N} a_n^2 \leq 1$. The systematic effect is assessed by performing fits to the pseudo-data with MC templates, built adopting the FF parameterisation truncation order of the nominal fit scenario. The standard deviation of the observed discrepancy in the PoI with the nominal case is taken as a measure of the associated systematic.

(c) Influence of the cut on the muon transverse momentum as performed in the L0Muon trigger line, which can be assessed by tightening the threshold value and propagating the effect through the analysis chain.

(d) Impact of the binning choice in the following Data/MC corrections:

    d.1 Tracking;

    d.2 Λ_b production kinematics;

    d.3 Particle identification;

(e) Momentum-dependent effect of tracking correction in the case of hadronic interactions with the tracking detectors material.

None of the listed systematic uncertainties is expected to provide a dominant contribution to the error budget.

3.12   Conclusions

At the time of this thesis, Λ_b^0 semileptonic decays represent a unique prerogative of the LHCb experiment to explore the flavour sector of the Standard Model. Studying the properties of these tree-level $b \to c \ell \nu_\ell$ transitions by directly measuring the Form Factor parameters and the muonic Wilson Coefficients could help to shed light on the still unsolved flavour anomalies, puzzling the physics community to date.

This work delineates the strategy and describes with minutiae the realisation of the first full angular analysis of $\Lambda_b^0 \to \Lambda_c^+ \mu^- \bar{\nu}_\mu$ decays with $5.57\,\text{fb}^{-1}$ of data collected with the LHCb detector during the Run 2 of the LHC. The measurement entails an accurate modelling of experimental effects and physics generation models, translating into a precise understanding of MC simulated samples. We have presented the state-of-the-art determination of the Form Factor parameters while demonstrating the reach of the experimental sensitivity to the muonic Wilson Coefficients. As outlined in the preceding Sections, we are currently focusing on the determination of the remaining systematic uncertainties. In addition, we plan to further ameliorate the agreement between data and simulation by including an additional correction stage based on a multi-dimensional binned reweighing. Nonetheless, we are not expecting to observe a sizeable impact on the value of the Form Factors, as demonstrated in the dedicated section of systematics evaluation.

At the moment, the blinding strategy does not allow for a showcase of the central value of the Wilson Coefficients, which will be unveiled upon approval of a dedicated internal revising committee. Given the advanced stage of the analysis, we expect the unblind phase to occur in the coming months.

Appendix

Contents

3.A Definition of analysis variables

Explicit reference is made throughout the analysis chapter to a set of variables. They have been described and reported below in Tab. 3.A.1. In the following, we will assume that X, unstable particle produced in pp-collision at the primary vertex (PV), decays in the final state $X \to a, b, \cdots$ with particles a, b corresponding to measured track objects. We refer to the decay vertex of X as secondary vertex (SV) (*e.g.* see Fig. 3.2.3).

Variable	Description
Kinematics	
$p_T(a)$	Transverse momentum of a with respect to the beam axis
m_a	Mass of a
$\mathrm{M}_{\mathrm{corr}}(X)$	Corrected mass of X
$\Delta m(a, b)$	Mass difference between a and b
Topology	
$\mathrm{FD}(X)$	Flight distance vector of X, linking its production and decay vertices
$\mathrm{FD}_{\chi^2}(X)$	χ^2 of the flight distance of X
$\mathrm{DOCA}_{\chi^2}(a, b)$	χ^2 of the distance of closest approach between a, b

Variable	Description
$\text{IP}_{\chi^2_{SV}}(a)$	Impact parameter χ^2 of track a with respect to the vertex of X
$\min \text{IP}_{\chi^2_{PV}}(X)$	Minimum impact parameter χ^2 of track X with respect to primary vertices in the event
$\text{DIRA}(X)$	Direction angle between the momentum and flight distance vectors of X

Tracks, vertices	
$\chi^2_{vtx}(X)$	χ^2 of the vertex fit to X decay
$\chi^2_{vtx}(X)/\text{ndof}$	X decay vertex fit quality
$\chi^2_{trk}(a)$	χ^2 of the track fit of a
$\chi^2_{trk}(a)/\text{ndof}$	a track fit quality
nTracks	Number of recorded tracks in the event
nSPDHits	Number of hits recorded in the SPD

Particle Identification	
$\text{isMuon}(a)$	Boolean assessing the compatibility of a with the muon hypothesis
$\Delta\log\mathfrak{L}(a-a')$	Likelihood discriminator between the particle hypotheses of a and a'
$\text{GhostProb}(a)$	Probability of a being identified as a random combination of hits
$\text{ProbNN}_{a'}(a)$	Neural network-based probability of the particle a being identified as a'
$\text{ProbNN}_{\text{ghost}}(a)$	Neural network-based probability of the particle a being identified as a random combination of hits

Data-taking	
MagUp	Upward magnet polarity configuration
MagDown	Downward magnet polarity configuration
TOS	Trigger On Signal
TIS	Trigger Independent of Signal

TABLE 3.A.1: Definition of most common LHCb variables used throughout this analysis.

3.B   Neutrino momentum reconstruction in Λ_b decays

Let us consider the signal decay $\Lambda_b^0 \to \Lambda_c^+ \mu^- \bar{\nu}_\mu$, where the Λ_c^+ decay is fully reconstructed, the missing neutrino is mass-less and the Λ_b mass is known[27]. From momentum conservation, we retrieve the following system of 4 equations:

$$\begin{cases} \sqrt{m_{\Lambda_b}^2 + \vec{P}_{\Lambda_b}^2} = \sqrt{m_{\Lambda_c \mu}^2 + \vec{P}_{\Lambda_c \mu}^2} + |\vec{P}_\nu| \\ \vec{P}_{\Lambda_b} = \vec{P}_{\Lambda_c \mu} + \vec{P}_\nu \end{cases} \tag{3.23}$$

which is unresolved, given the unknown $\vec{P}_{\Lambda_b}$ and $\vec{P}_\nu$ components.

In the hadronic environment at very forward rapidities covered by the LHCb experiment, b-hadrons are produced with a significant Lorentz boost, which can be used to constrain the kinematics. Because the flight direction of the Λ_b, $\vec{\text{FD}}_{\Lambda_b}$, is reconstructed in LHCb by measuring the direction vector linking the position of its production and decay vertices, we rewrite the system projecting on the parallel and orthogonal components relative to $\vec{\text{FD}}_{\Lambda_b}$ (Fig. 3.2.3). In this case, only the parallel component of the neutrino momentum is left undetermined. The momentum conservation against the visible system ($\Lambda_c \mu$) reads as:

$$\begin{cases} |\vec{P}_{\Lambda_b}| = P_{\Lambda_c \mu}^{\parallel} + P_\nu^{\parallel} \\ P_{\Lambda_c \mu}^{\perp} = -P_\nu^{\perp} \end{cases} \tag{3.24}$$

The solution to the unknown of the system $P_\nu^{\parallel}$, the parallel component of the neutrino momentum along the $\vec{\text{FD}}_{\Lambda_b}$ direction, is found by substitution of the quantities in Eqs. 3.24 in Eqs. 3.23:

$$P_\nu^{\parallel} = -a \pm \sqrt{r}, \tag{3.25}$$

where:

$$a = \frac{P_{\Lambda_c \mu}^{\parallel}\left(m_{\Lambda_b}^2 - m_{\Lambda_c \mu}^2 - 2 P_{\Lambda_c \mu}^{2\parallel}\right)}{2\left(P_{\Lambda_c \mu}^{2\parallel} - E_{\Lambda_c \mu}^{2\parallel}\right)} \tag{3.26a}$$

$$r = \frac{E_{\Lambda_c \mu}^2 \left(m_{\Lambda_b}^2 - m_{\Lambda_c \mu}^2 - 2 P_{\Lambda_c \mu}^{2\perp}\right)^2}{4\left(P_{\Lambda_c \mu}^{2\parallel} - E_{\Lambda_c \mu}^2\right)} + \frac{E_{\Lambda_c \mu}^2 P_{\Lambda_c \mu}^{2\perp}}{P_{\Lambda_c \mu}^{2\parallel} - E_{\Lambda_c \mu}^2}. \tag{3.26b}$$

The ambiguity in the choice of solutions for Eq. 3.25 is seldom solved by rejecting unphysical solution and requiring the positivity of the radicand r, often negative as a consequence of momentum and vertex resolution effects in the reconstruction of the visible system. When the degeneracy is

---

[27]The system of equations here reproduced can be extended to any semileptonic decay of the type $H_b \to H_c \ell \nu_\ell$. Special care is required in treating muonic decays of the τ lepton, given the three missing neutrinos in the final state. In that case, the B rest-frame approximation is the standard choice [56].

not broken, one of the two solutions is randomly chosen. Attempts have been discussed to improve the selection rate of the correct solution to a value of $\sim 70\%$ utilising a simple regression analysis on the b-hadron momentum [51].

We argue that using Gaussian Processes further ameliorates the conclusions reached in Ref. [51] and thus the momentum resolution of the Λ_b, as described in App. 3.E.

3.C MVA classifier: additional material
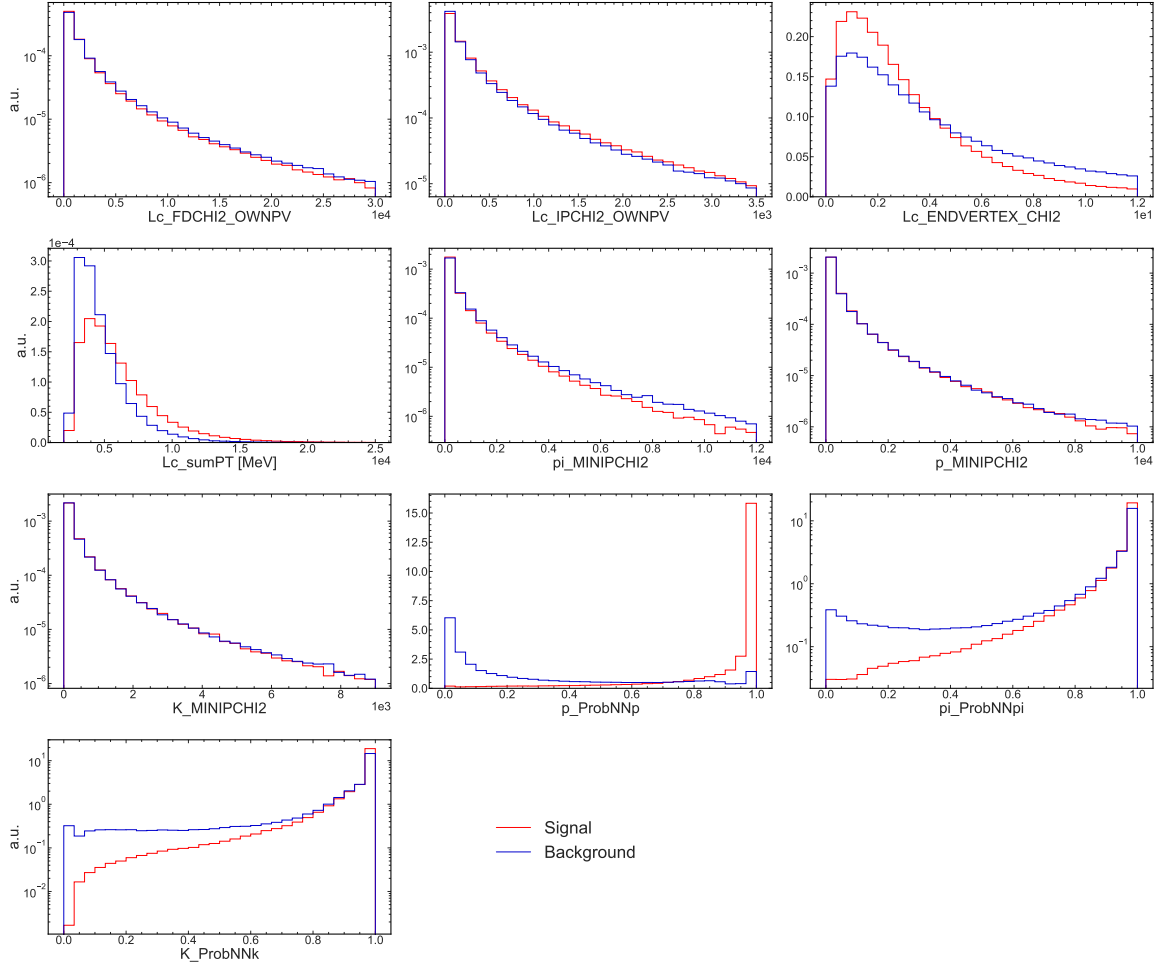
FIGURE 3.C.1: Comparison between MVA input variables distributions in MC-modelled signal (red) and data-modelled background (blue) samples.
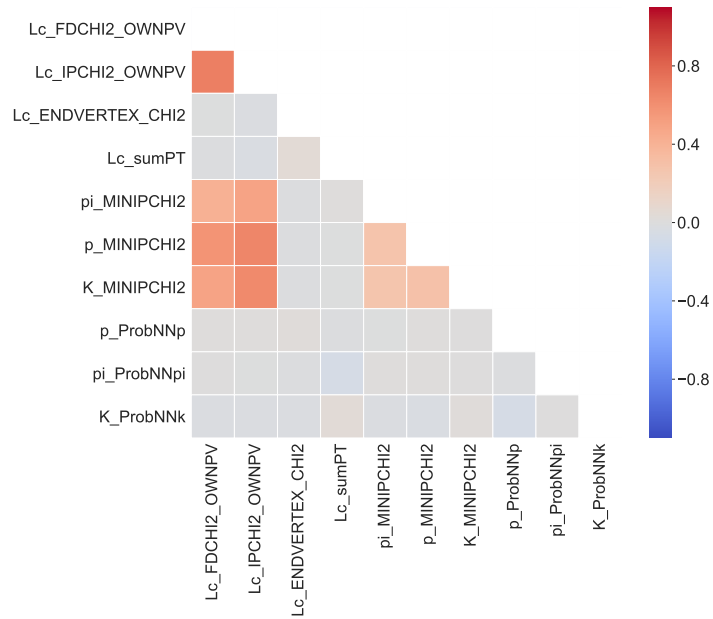
(A)
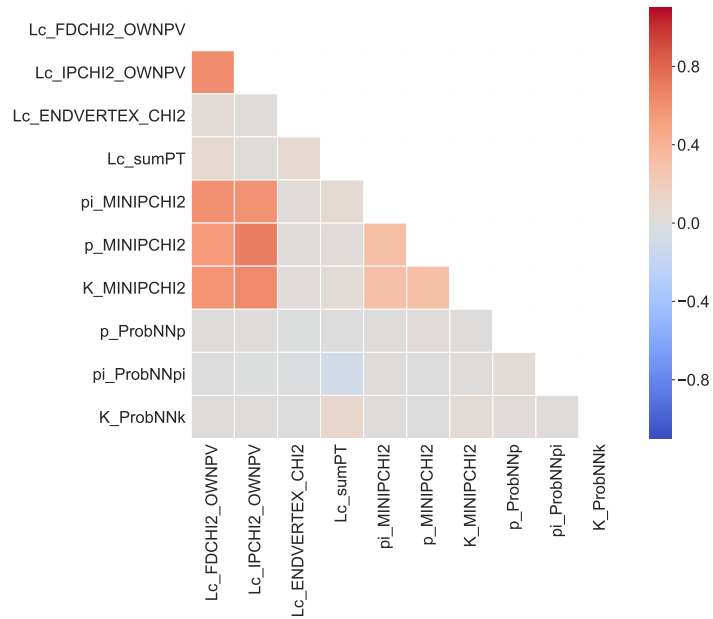
(B)

FIGURE 3.C.2: Matrix of linear correlation coefficients between input variables in the training of a MVA classifier to tame fake Λ_c backgrounds in 2016 Λ_b semi-muonic decays for: (A) data sample; (B) MC simulation.
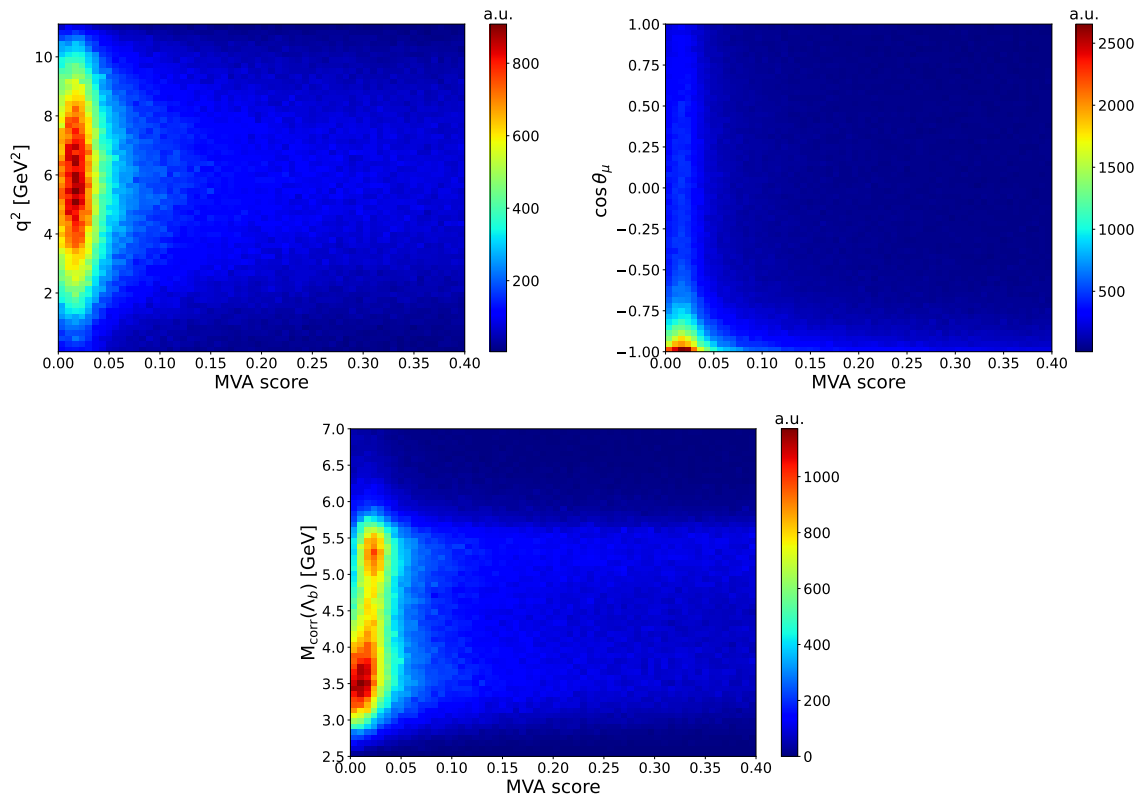
FIGURE 3.C.3: Distribution of phase space $\left(q^2, \cos\theta_\mu\right)$ and fit variables (M_{corr}) as a function of the MVA output for the 2016 data sample.
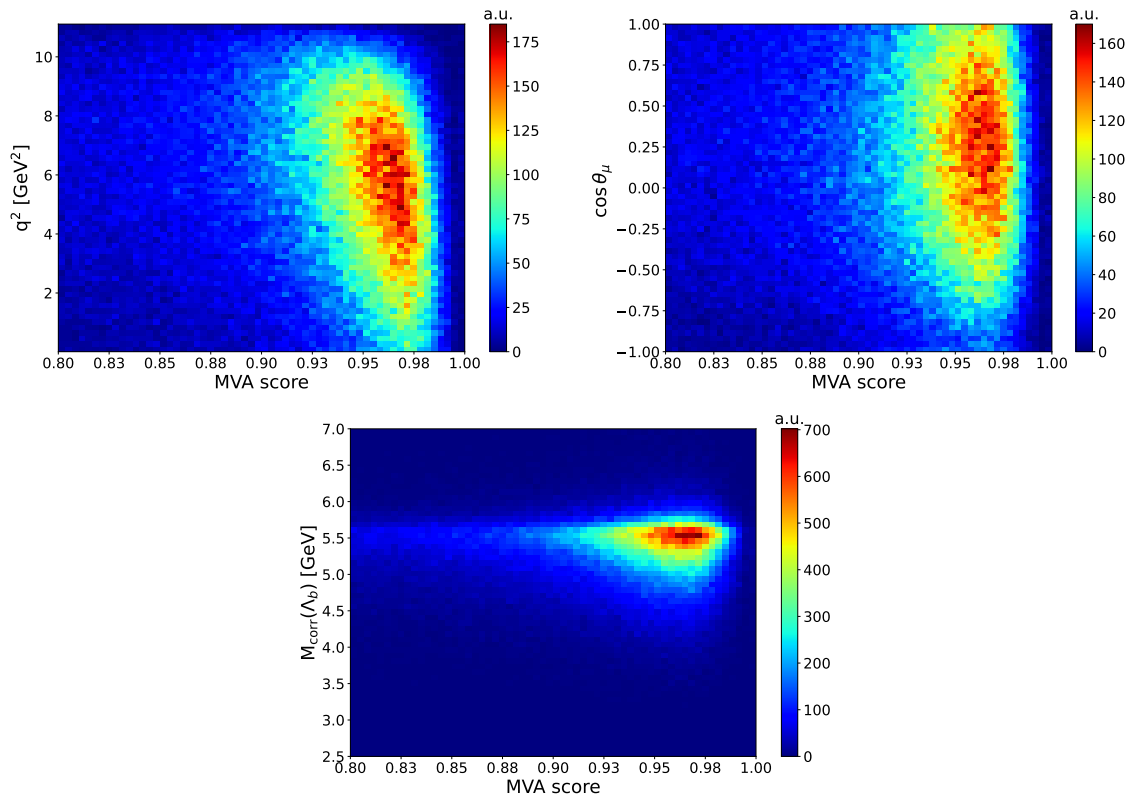
FIGURE 3.C.4: Distribution of phase space $(q^2, \cos\theta_\mu)$ and fit variables (M_{corr}) as a function of the MVA output for the 2016 MC simulation.

3.D Signal efficiency maps
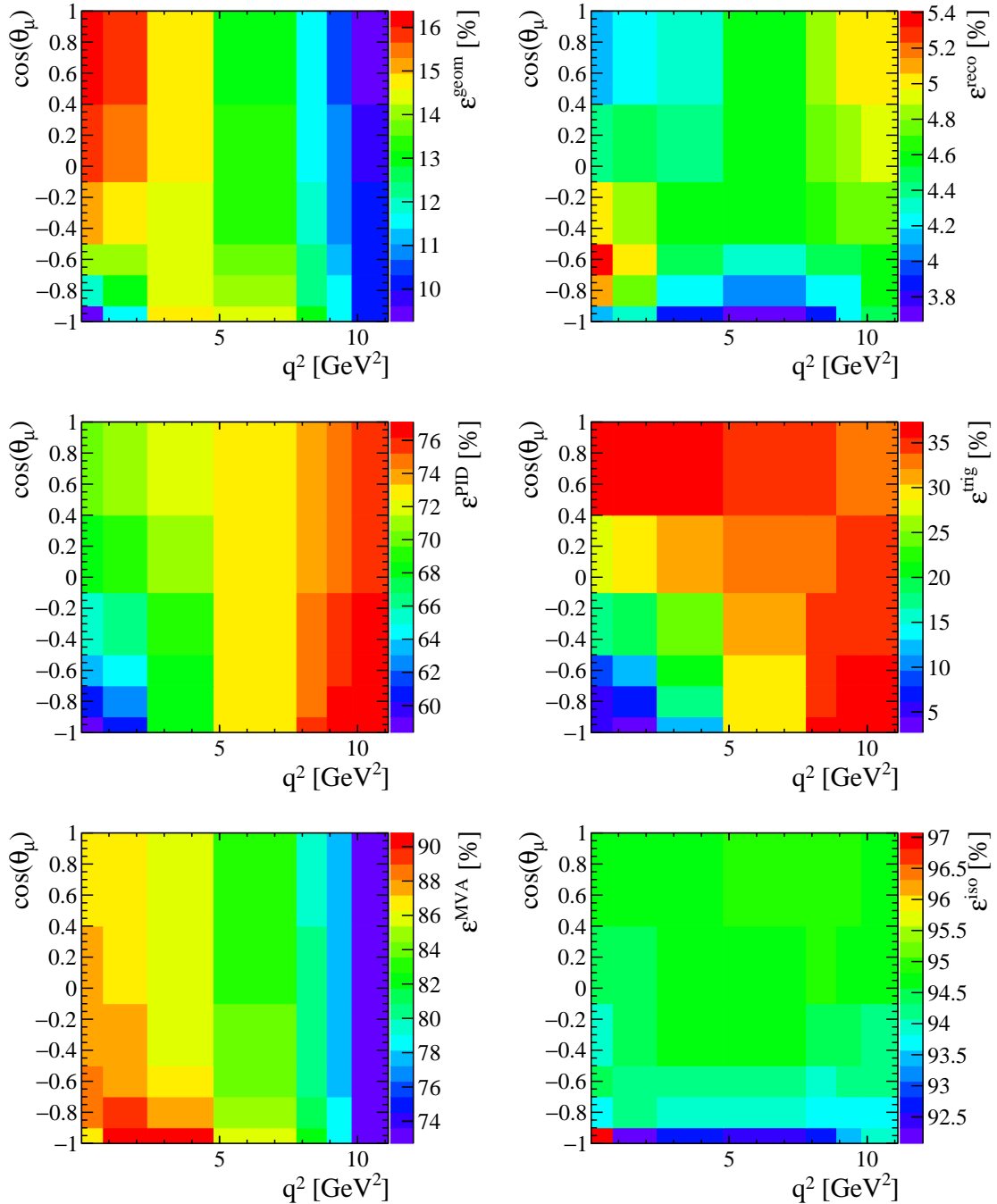
FIGURE 3.D.1: Breakdown of efficiency variations for different stages of selection requirements (from top left to bottom right: geom, reco, PID, trig, MVA, iso), evaluated for the signal decay in true phase space for the 2016 `MagUp` sample.

3.E Resolution improvement with sparse Gaussian Processes

The kinematic properties of a decay with a single unreconstructed mass-less particle can be resolved up to a quadratic ambiguity, as detailed in App. 3.B. The resolution of the phase space variables for a given reconstructed Λ_b candidate can be improved by selecting the true solution from the two possible. In many previous analyses, the choice has been made usually randomly. However, in Ref. [51], a linear regression method was used to estimate the b-hadron momentum, advancing the method that involved a random selection. This analysis resolves the quadratic ambiguity using Gaussian Process Regression (GPR), utilising the information from the reconstructed visible system.

Gaussian Process Regression is a powerful non-parametric Bayesian approach for modelling complex datasets [57]. It is particularly well-suited to make predictions with quantified uncertainties. GPR operate by placing a prior probability distribution over possible functions that could describe the data. In the context of GPR, the prior is typically taken to be Gaussian, characterised by a mean and a covariance function (also known as a kernel). Upon observing data, the GPR prior is updated to form a posterior distribution over functions, which captures our updated beliefs about the function after considering the observed data. This posterior distribution is used for making predictions: the mean of the posterior at a new input point gives the best prediction of the function, and the variance provides a measure of the uncertainty.

Despite being powerful, standard GPR scales poorly with the size of the dataset, as it requires operations on matrices whose size is determined by the number of data points. To overcome this limitation, sparse Gaussian Processes have been developed. Instead, they approximate the entire model by using only a subset of the data chosen to capture the most relevant information from the full dataset.

After testing several kernels and mean functions, we retained those that provided the best resolution between the predicted and true b-hadron momentum on the test sample. Our dataset is derived from a MC simulation of the $\Lambda_b^0 \to \Lambda_c^+ \mu^- \bar{\nu}_\mu$, focusing on the reconstructed information from the visible particles. The input features for the GP regression comprise nine variables, which encapsulate the kinematic and topological properties of the decay products:

(a) The spatial components of the Λ_c momentum vector;

(b) The spatial components of the μ momentum vector;

(c) The spatial components of the Λ_b flight distance vector.

These features are chosen to comprehensively represent the event kinematics, which is crucial for predicting the target variable, *i.e.* the true magnitude of the Λ_b spatial momentum.

The distributions and the correlation of the true and predicted magnitude of the Λ_b^0 spatial momentum for the train and test samples are shown in Fig. 3.E.1: the sparse GPR effectively predicts the target distribution while preserving the underlying correlation. We select the solution for the magnitude of the Λ_b^0 spatial momentum which is the nearest to the sparse GPR predicted

value.
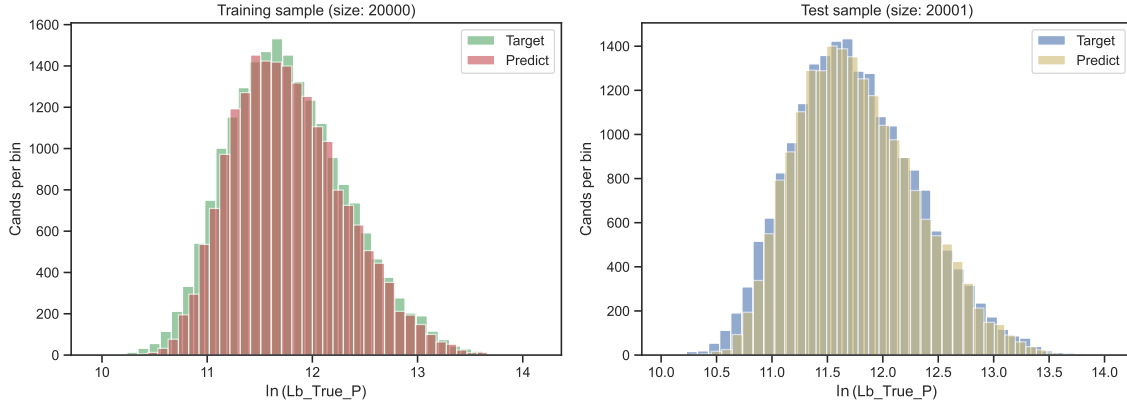
(A)
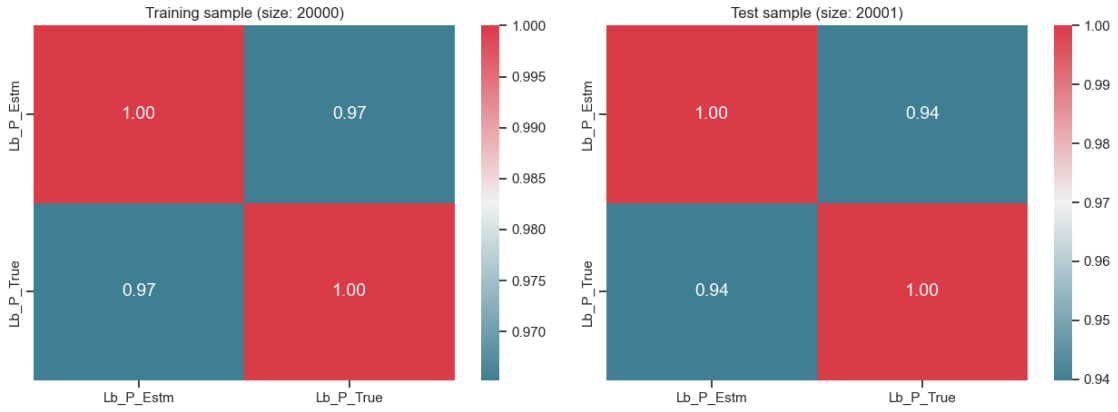
(B)

FIGURE 3.E.1: Distributions (A) and correlation (B) of true and predicted magnitude of Λ_b^0 spatial momentum for train (left) and test (right) samples, shown here for the 2016 simulation.

The sparse GPR approach significantly ameliorates the resolution in $\vec{p}_{\Lambda_b^0}$ by approximately 19 %, compared to the method outlined in Ref. [51]. This enhancement translates into an improvement of ~ 9.7 % for q^2 and ~ 7.4 % for $\cos\theta_\mu$. A comparison between this study and Ref. [51] in the fractional resolution of the phase space observables is illustrated in Fig. 3.E.2.
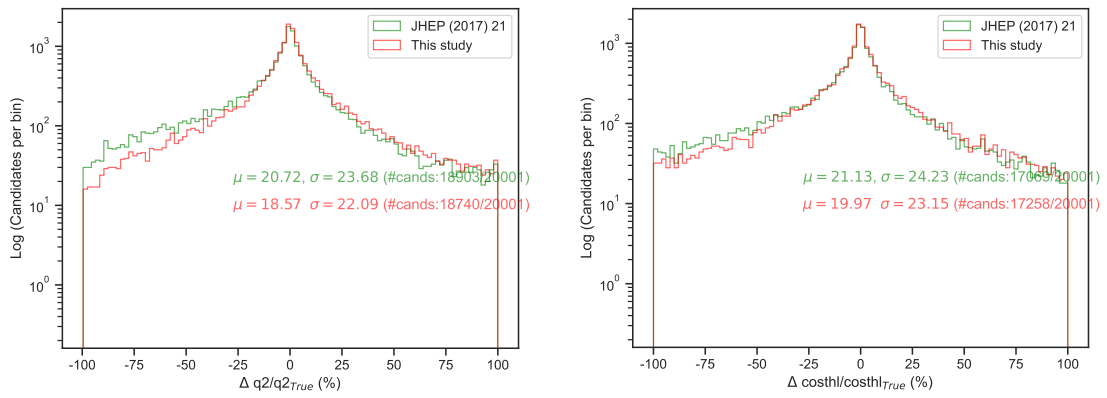
FIGURE 3.E.2: Fractional resolution of phase space variables, q^2, $\cos\theta_\mu$, comparing this study (red) with results from Ref. [51] (green) for the 2016 MC sample.

3.F Data/MC agreement after kinematic post-fit correction
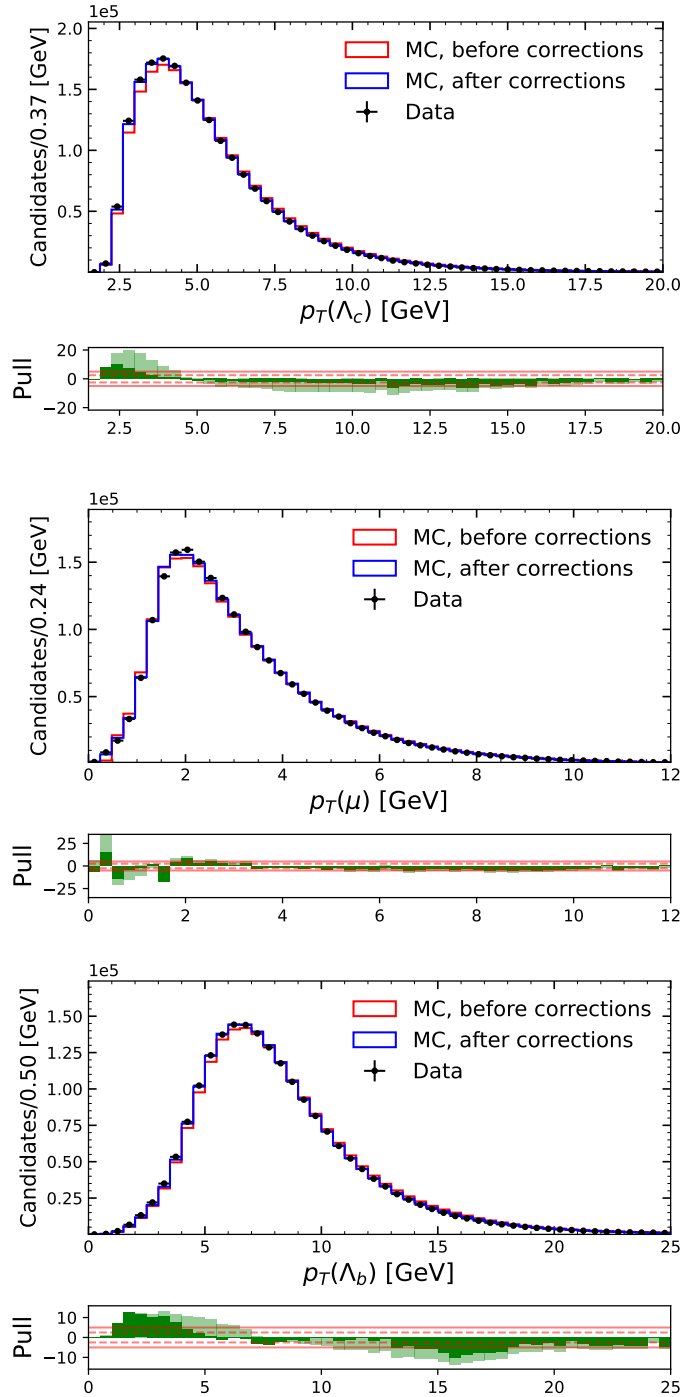
FIGURE 3.F.1
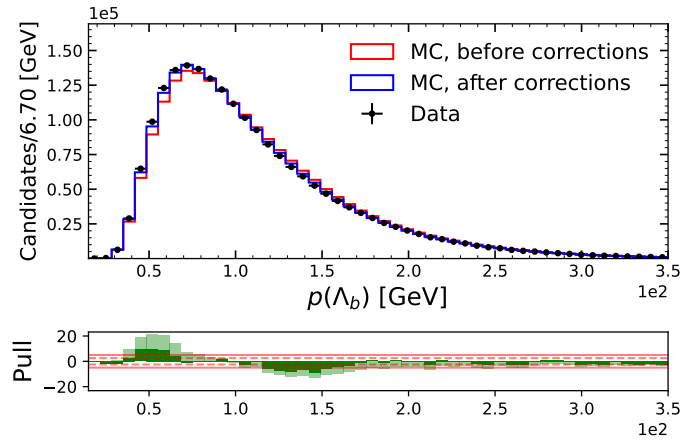
FIGURE 3.F.1: Agreement in the kinematics of the Λ_c, μ, and Λ_b candidate between data (black points), MC cocktail before the kinematic correction (red histogram) and the same after reweighting (blue histogram). The agreement in the pre-reweighting scenario is highlighted with light green pulls, while it is in darker green for post-correction. Samples correspond to 2016 and magnet polarity `MagUp`.

3.G Phase space binning optimisation

The chosen binning configuration in $(q^2, \cos\theta_\mu)$ is the result of a balanced trade-off: on one side, the aim is maximising the fit sensitivity to Wilson Coefficients, therefore increasing the number of bins along each dimension to approximate the *continuum* limit; on another side, it must be ensured each bin is large enough to incorporate sufficient statistics and yield a stable fit behaviour. We additionally account for the number of fit parameters (18 Form Factors, 4 Wilson Coefficients) to define the minimum binning divisions. The binning scheme choice has been validated with pseudo experiments, evaluating each Wilson Coefficient scenario separately. Corresponding pseudo data have been generated according to the phase space model defined in Eq. 3.9 while assuming unitary resolution and flat efficiency across phase space.

The definition of optimal bin edges in phase space has been dictated by the *absolute variation* metric, Δ, in order to identify regions associated with a large variability of the decay model:

$$\Delta_{i=\text{bin}} = \max\{\text{PDF}_i^{\text{NP}} - \text{PDF}_i^{\text{SM}}\},$$

where PDF denotes the value of the decay density (Eq. 3.9) for the New Physics (NP) or Standard Model (SM) scenarios for each of the Wilson Coefficient ($C_{V_R}, C_T, C_{S_R}, C_{S_L}$), evaluated on a number of samples $N_{\text{samples}} = 100$ with $N_{\text{bins}} = 60 \times 60$. As we observe the following:

$$\Delta(C_{V_R}) > \Delta(C_T) > \Delta(C_{S_R}) > \Delta(C_{S_L}),$$

we optimise the binning scheme for C_{V_R}, while reducing the sensitivity degradation for other coefficients. The highest absolute variation in C_{V_R} is observed in the low $\cos\theta_\mu$ high q^2 region (Fig. 3.G.1). We have probed either regular or irregular configurations with dense binning in high variability regions for the C_{V_R} scenario to accommodate the observed phase space pattern. A complete list of investigated binning schemes is reported in Tab. 3.G.1.

We generated 500 toy data samples for every Wilson Coefficient/Standard Model scenario, each with 7.5 M events equivalent to the LHC full Run 2 statistics of $\Lambda_b^0 \to \Lambda_c^+ \mu^- \bar{\nu}_\mu$ decays. Defined the sensitivity σ_k as the standard deviation from a Gaussian fit to the residuals Δ_k

$$\Delta_{k=\text{binning}} = (\text{WC}_{\text{NP}} - \text{WC}_{\text{SM}})_k,$$

with WC_i corresponding to the value extracted from a pseudo-data fit in the scenario i, the optimal choice corresponds to the binning minimising the sensitivity degradation D_k compared to the control binning (Scheme 6), where:

$$D_{k=\text{binning}}[\%] = |1 - \sigma_k/\sigma_6| \cdot 100.$$

The minimum recorded sensitivity degradation in C_{V_R}, amounting to $\sim 4\%$, corresponds to the scheme 5 (Tab. 3.G.1, Fig. 3.G.2), which is thus chosen as the reference binning configuration.
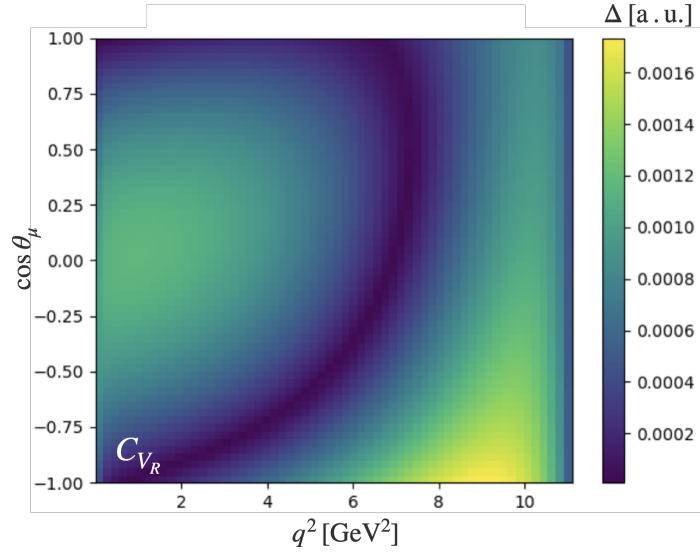
FIGURE 3.G.1: Maximum decay density model variation Δ in phase space $(q^2, \cos\theta_\mu)$ associated with a non-null value of C_{V_R}, assuming unitary resolution and flat efficiency.

Scheme number	Number of bins	Bin edges	Sensitivity degradation
1	6×4	irregular	$\sim 13\%$
2	5×5	regular	$\sim 6\%$
3	7×5	irregular	$\sim 7\%$
4	7×5	regular	$\sim 5\%$
5	7×6	irregular	$\sim 4\%$
6 (control)	40×40	regular	-

TABLE 3.G.1: Investigated binning configurations in the reconstructed q^2, $\cos\theta_\mu$ space, with corresponding sensitivity degradation in the C_{V_R} scenario.
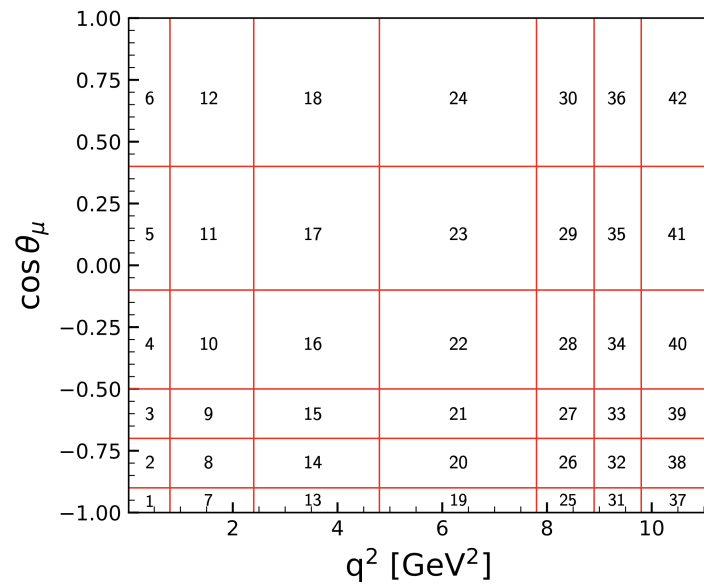
FIGURE 3.G.2: Reference binning configuration in the reconstructed $(q^2, \cos\theta_\mu)$ space adopted for this analysis.

3.H   Additional material: corrected mass fits in bins of phase space
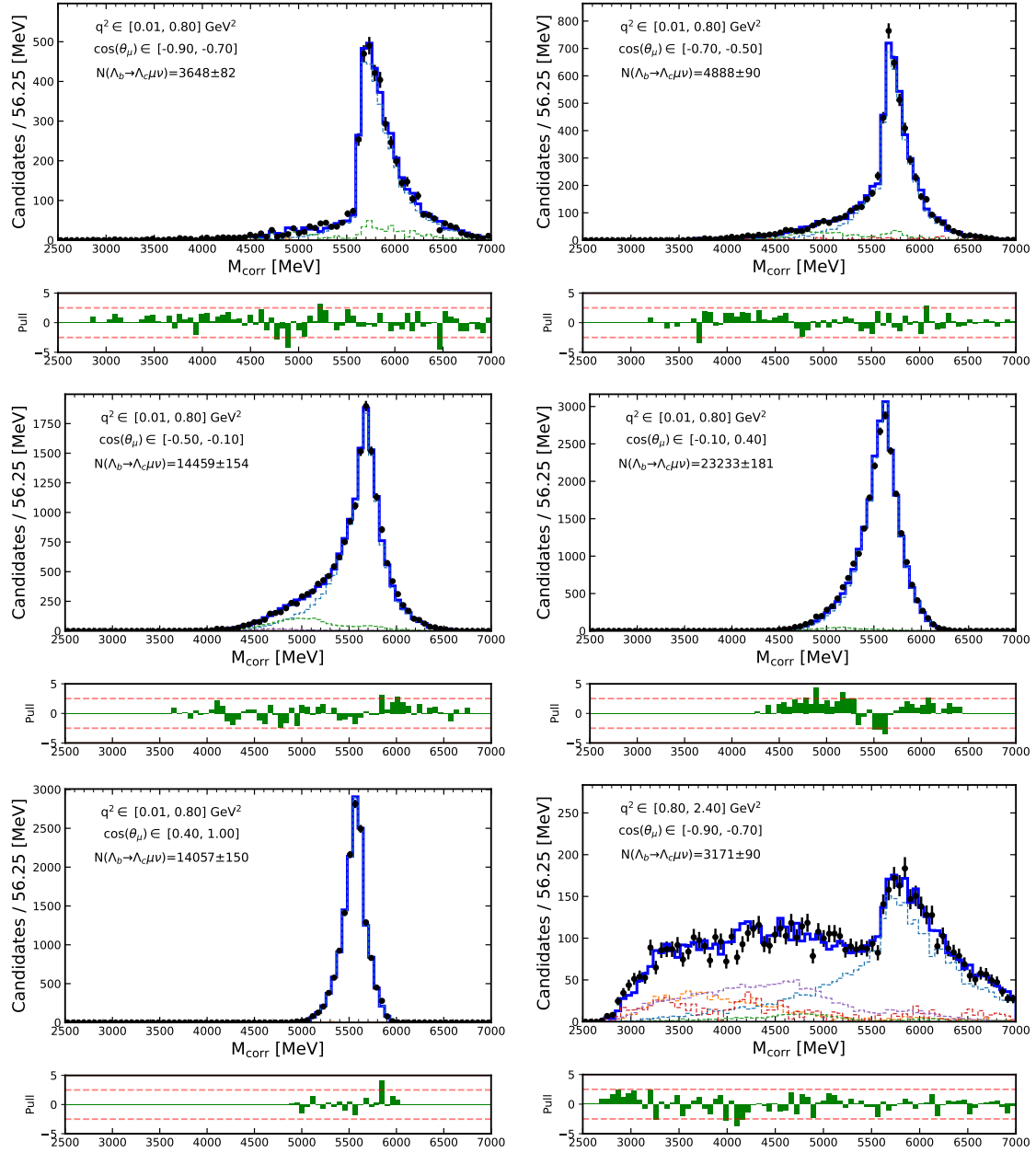
FIGURE 3.H.1
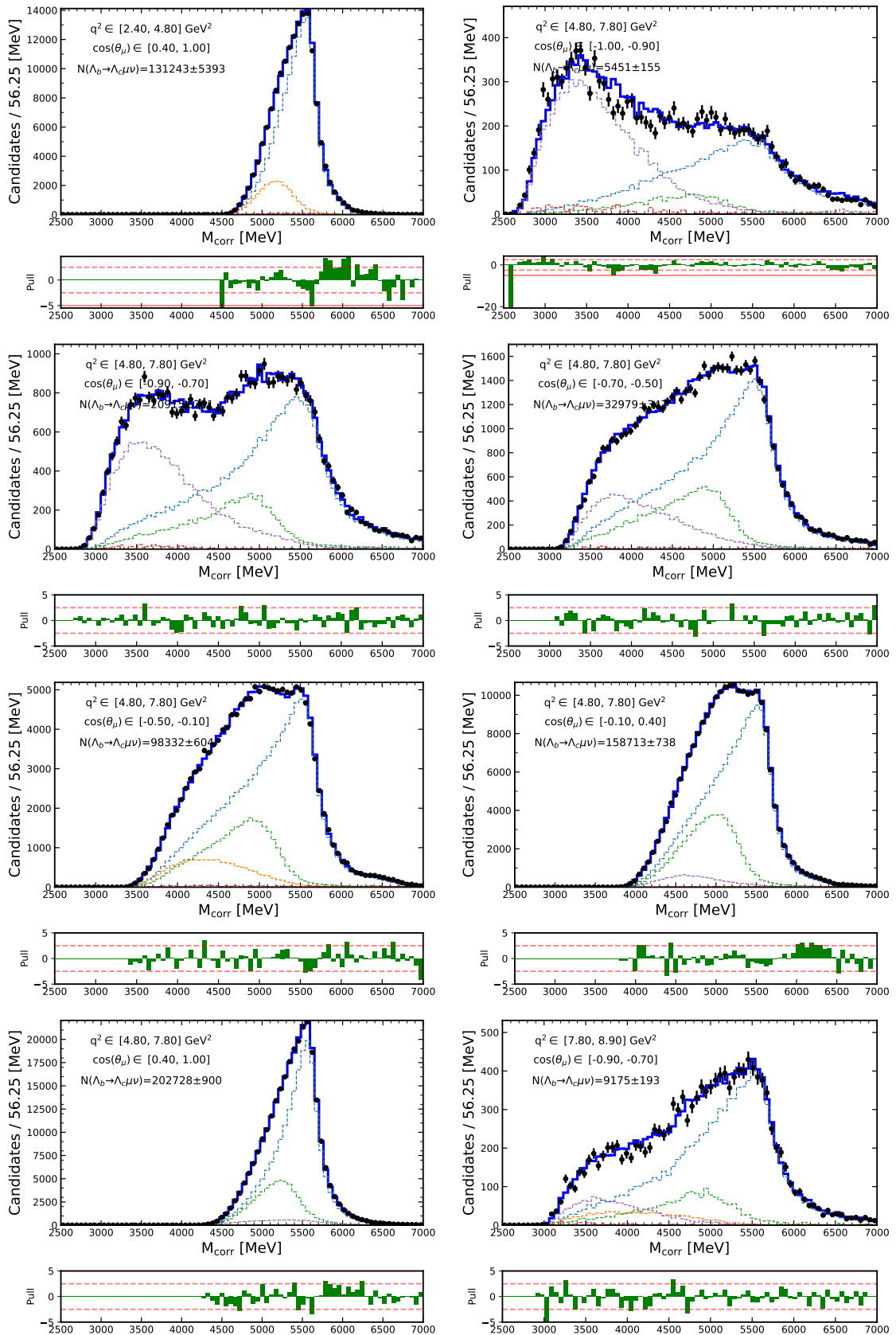
FIGURE 3.H.1
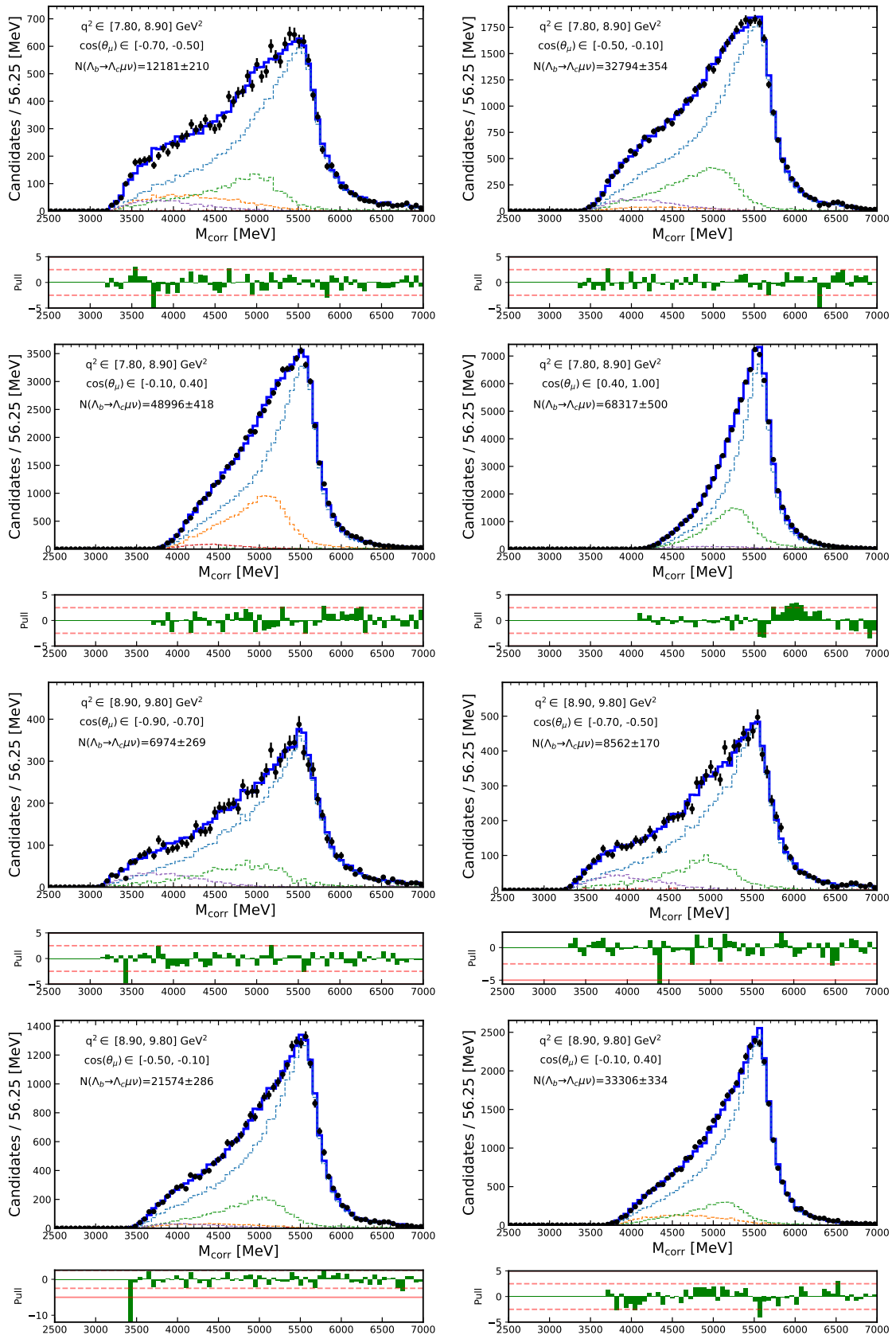
FIGURE 3.H.1
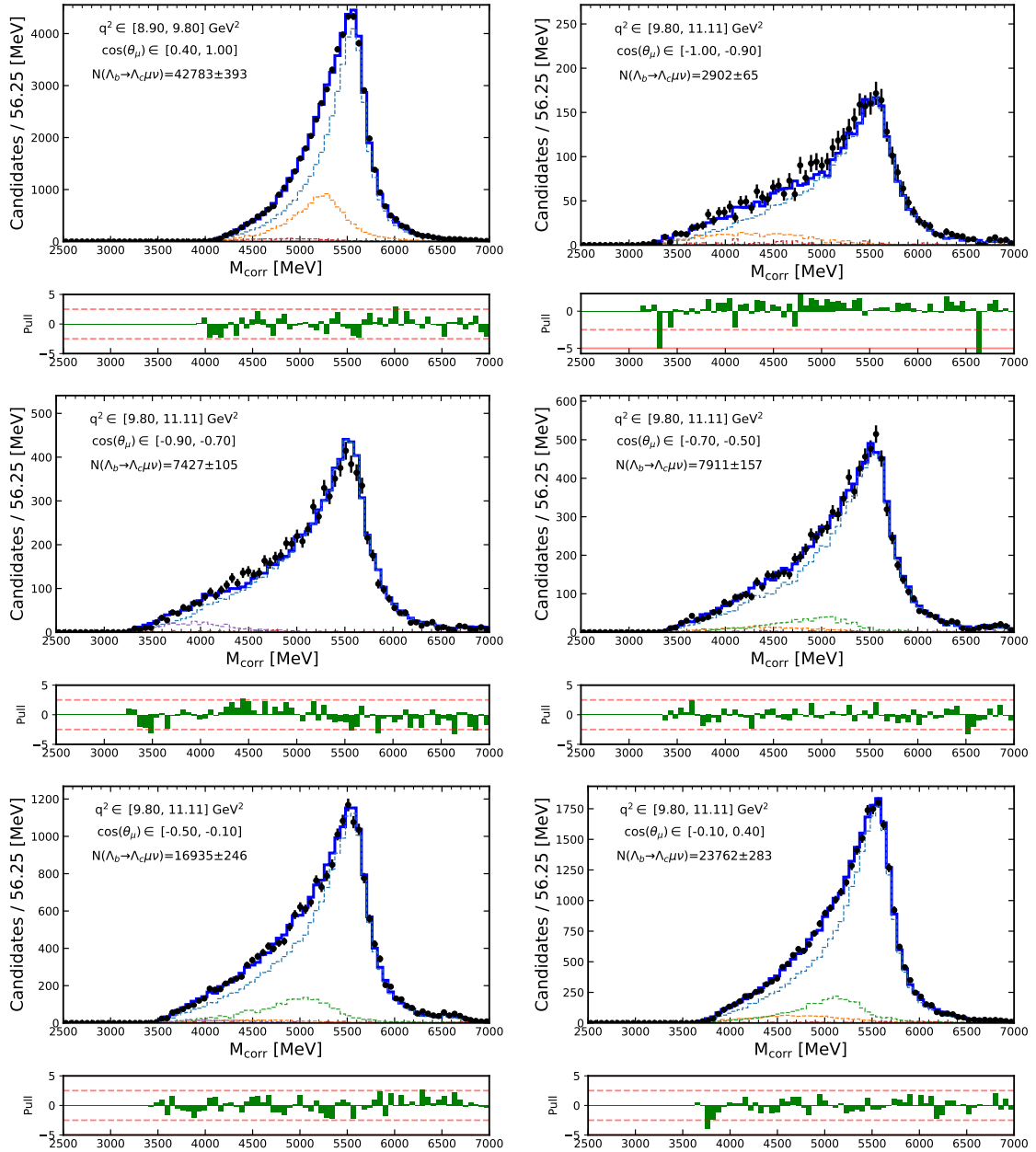
FIGURE 3.H.1
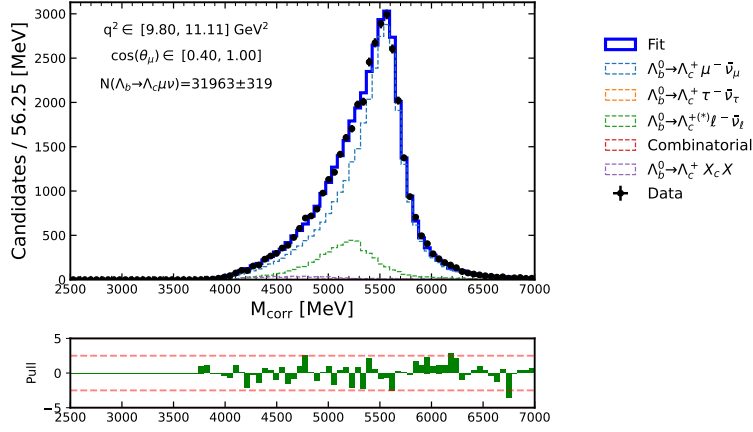
FIGURE 3.H.1

FIGURE 3.H.1: Fit to the corrected mass in bins of the covered region of reconstructed phase space variables $(q_{\text{reco}}^2, \cos\theta_\mu^{\text{reco}})$.
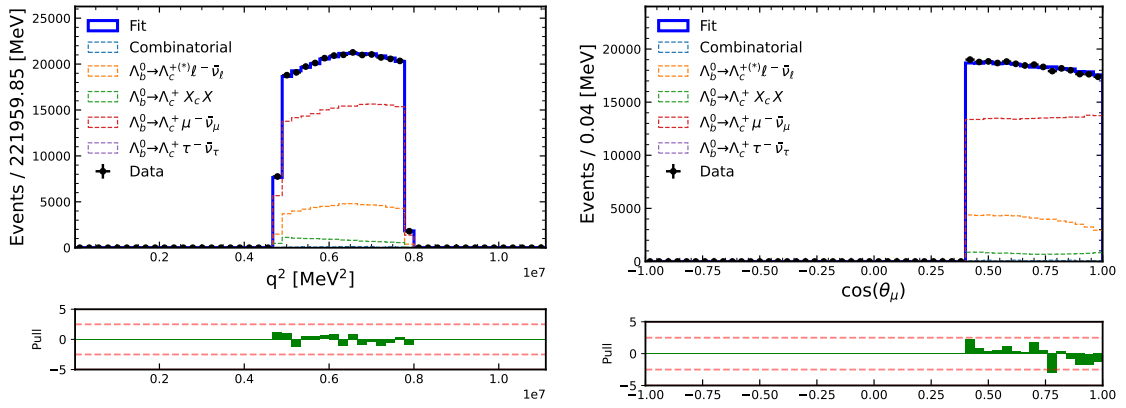
FIGURE 3.H.2: Corrected mass fit projections in bins of q_{reco}^2 and $\cos\theta_\mu^{\text{reco}}$. Defined within $q^2 \in [4.8, 7.8]\,\text{GeV}^2$, $\cos\theta_\mu \in [0.4, 1.0]$, this bin corresponds to the phase space region with the largest $\Lambda_b^0 \to \Lambda_c^+ \mu^- \bar{\nu}_\mu$ signal yield.

3.I Additional material: phase space fits
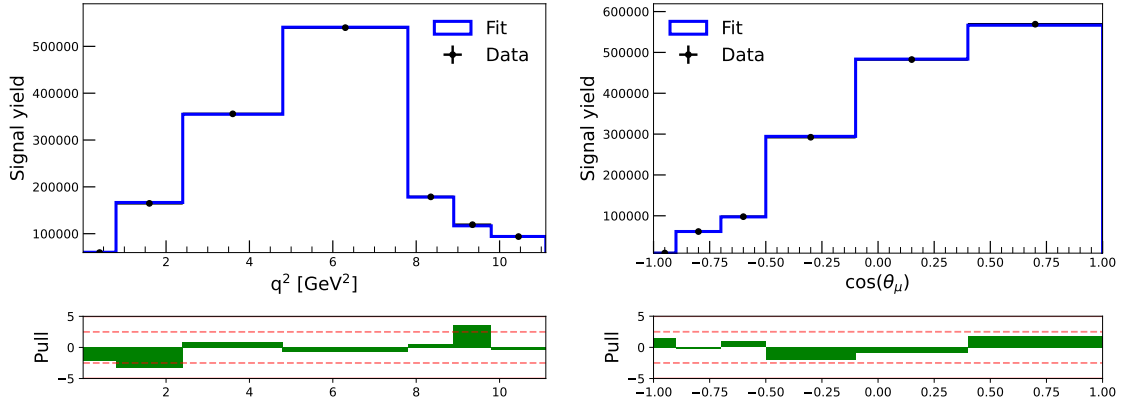
FIGURE 3.I.1: Agreement between recorded data yields (black) and fit model (blue) achieved after two iterations of the phase space fit, shown in projections of q^2 (left) and $\cos\theta_\mu$ (right) for the 2017 samples.
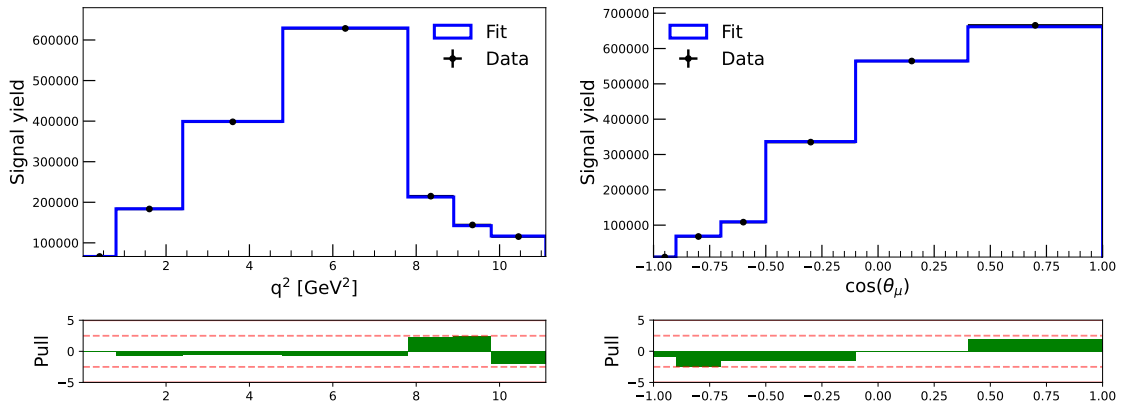
FIGURE 3.I.2: Agreement between recorded data yields (black) and fit model (blue) achieved after two iterations of the phase space fit, shown in projections of q^2 (left) and $\cos\theta_\mu$ (right) for the 2018 samples.

3.J Correction to the $\Lambda_b^0 \to \Lambda_c^{+*} \mu^- \bar{\nu}_\nu$ decay density model

Similarly to the case of ground state semileptonic decays of the Λ_b^0, also the model implementation of transitions including excited Λ_c^{+*} states follows the quark model formalism of HQET in the event generation phase. Precise LQCD predictions for FF parameters are provided in Ref. [46], however valid only in the high q^2 kinematic region ($q^2 > 8\,\text{GeV}^2$). The functional shape of the differential decay density in the lower end of phase space is consequently unreliable, as demonstrated in the comparison between the LQCD prediction and our implementation of the model (Fig. 3.J.2a for $\Lambda_c^{+*}(2595)$; Fig. 3.J.2b for $\Lambda_c^{+*}(2625)$).

(A)

(B)
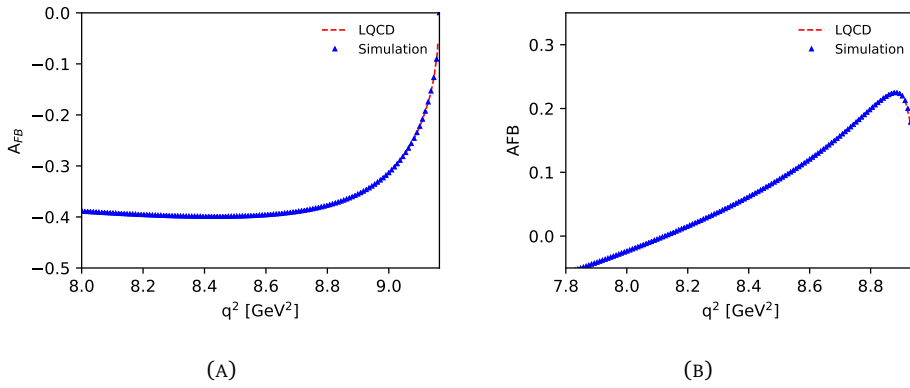
FIGURE 3.J.1: Comparison between the forward-backward asymmetry A_{FB} shape in q^2 from LQCD results [46] and from the implementation of the same model in this analysis for (A) $\Lambda_c^{+*}(2595)$ and (B) $\Lambda_c^{+*}(2625)$ states.

(A)

(B)
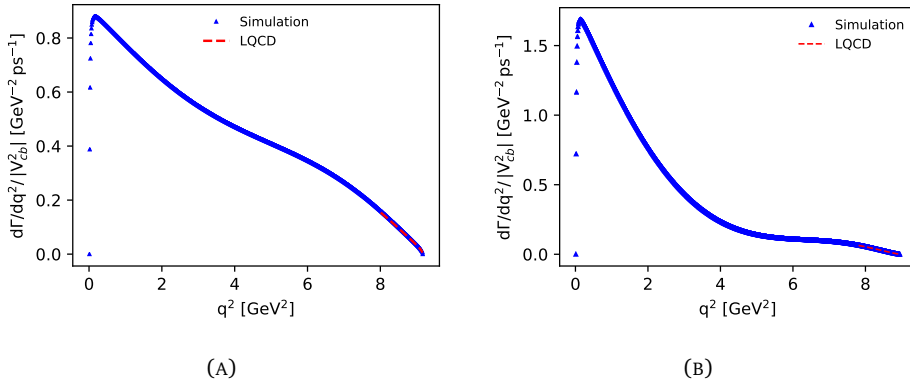
FIGURE 3.J.2: Comparison between the differential decay rate shape in q^2 from LQCD results [46] and from the implementation of the same model in this analysis for (A) $\Lambda_c^{+*}(2595)$ and (B) $\Lambda_c^{+*}(2625)$ states.

Therefore, the strategy to correct for the generated event model is hybrid. We use LQCD results to define the decay density shape in q^2, $\cos\theta_\mu$ and subsequently perform a binned fit to reconstructed $\Lambda_b^0 \to \Lambda_c^{+*} \mu^- \bar{\nu}_\mu$ data, folding efficiency of the selection and resolution effects in the model. Details

of the fit strategy are presented in Sec. 3.10.1 for signal ground state transitions, which we follow closely. In this way, extracting the FF values from the phase space fit becomes a proxy to gain a more accurate parameterisation of the decay model. Fig. 3.J.3 illustrates the resulting projections of the phase space fit to reconstructed $\Lambda_b^0 \to \Lambda_c^{+*}(2595)\mu^- \bar{\nu}_\nu$ decays for the 2016 sample.

Rather than including the decay model correction upfront, this analysis approach assesses a dedicated systematic uncertainty. It includes evaluating the induced bias in the parameters of interest, the FF and WC, induced by including the decay model correction for feed-down backgrounds. Given the model independence of the corrected mass shape, and considering the strong separation in M_{corr} between signal and decays with excited Λ_c^{*+}, the associated uncertainty is not expected to be a dominant contribution to the systematic budget.
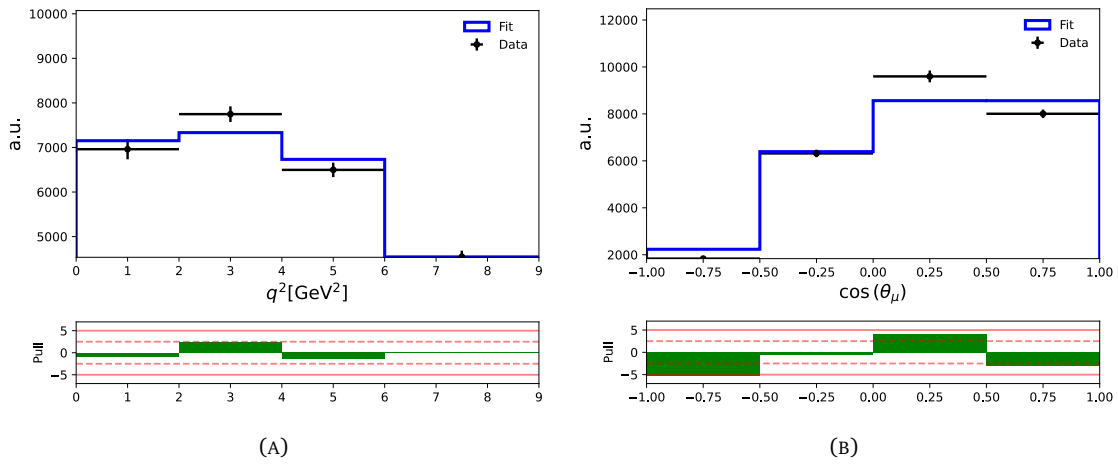
FIGURE 3.J.3: Agreement between recorded data yields (black) and fit model (blue) for $\Lambda_b^0 \to \Lambda_c^{+*}(2595)\mu^- \bar{\nu}_\nu$ decays, shown in projections of q^2 (left) and $\cos\theta_\mu$ (right) for the 2016 samples.

References

[1] R. Aaij et al. "Differential branching fraction and angular analysis of $\Lambda_b^0 \to \Lambda \mu^+ \mu^-$ decays". In: *JHEP* 06 (2015), p. 115. DOI: 10.1007/JHEP06(2015)115. arXiv: 1503.07138 [hep-ex].

[2] R. Aaij et al. "Measurement of the b-Quark Production Cross Section in 7 and 13 TeV pp Collisions". In: *Phys. Rev. Lett.* 118 (5 Feb. 2017), p. 052002. DOI: 10.1103/PhysRevLett. 118.052002. URL: https://link.aps.org/doi/10.1103/PhysRevLett.118.052002.

[3] R. Aaji et al. "Measurement of b hadron production fractions in 7 TeV pp collisions". In: *Phys. Rev. D* 85 (3 Feb. 2012), p. 032008. DOI: 10.1103/PhysRevD.85.032008. URL: https://link.aps.org/doi/10.1103/PhysRevD.85.032008.

[4] R. L. Workman et al. "Review of Particle Physics". In: *PTEP* 2022 (2022), p. 083C01. DOI: 10.1093/ptep/ptac097.

[5] S. Dambach, U. Langenegger, and A. Starodumov. "Neutrino reconstruction with topological information". In: *Nuclear Instruments and Methods in Physics Research Section A: Accelerators, Spectrometers, Detectors and Associated Equipment* 569.3 (2006), pp. 824–828. ISSN: 0168-9002. DOI: https://doi.org/10.1016/j.nima.2006.08.144. URL: https://www.sciencedirect.com/science/article/pii/S0168900206015609.

[6] R. Aaij et al. "Determination of the quark coupling strength $|V_{ub}|$ using baryonic decays". In: *Nature Physics* 11 (2015), p. 743. DOI: 10.1038/nphys3415. arXiv: 1504.01568 [hep-ex].

[7] R. Aaij et al. "Measurement of the shape of the $\Lambda_b^0 \to \Lambda_c^+ \mu^- \overline{\nu}_\mu$ differential decay rate". In: *Phys. Rev.* D96 (2017), p. 112005. DOI: 10.1103/PhysRevD.96.112005. arXiv: 1709.01920 [hep-ex].

[8] L. Koch. "A response-matrix-centred approach to presenting cross-section measurements". In: *Journal of Instrumentation* 14.09 (Sept. 2019), P09013–P09013. ISSN: 1748-0221. DOI: 10.1088/1748-0221/14/09/p09013. URL: http://dx.doi.org/10.1088/1748-0221/14/09/P09013.

[9] J. Nieves and R. Pavao. "Nature of the lowest-lying odd parity charmed baryon $\Lambda_c(2595)$ and $\Lambda_c(2625)$ resonances". In: *Phys. Rev. D* 101 (1 Jan. 2020), p. 014018. DOI: 10.1103/PhysRevD.101.014018. URL: https://link.aps.org/doi/10.1103/PhysRevD.101.014018.

[10] T. Aaltonen et al. "Measurements of the properties of $\Lambda_c(2595)$, $\Lambda_c(2625)$, $\Sigma_c(2455)$, and $\Sigma_c(2520)$ baryons". In: *Phys. Rev. D* 84 (1 July 2011), p. 012003. DOI: 10.1103/PhysRevD.84.012003. URL: https://link.aps.org/doi/10.1103/PhysRevD.84.012003.

[11] Lyndon Evans and Philip Bryant. "LHC Machine". In: *Journal of Instrumentation* 3.08 (Aug. 2008), S08001. DOI: 10.1088/1748-0221/3/08/S08001. URL: https://dx.doi.org/10.1088/1748-0221/3/08/S08001.

[12] G. Aad et al. "Observation of a new particle in the search for the Standard Model Higgs boson with the ATLAS detector at the LHC". In: *Physics Letters B* 716.1 (2012), pp. 1–29. ISSN: 0370-2693. DOI: https://doi.org/10.1016/j.physletb.2012.08.020. URL: https://www.sciencedirect.com/science/article/pii/S037026931200857X.

[13] S. Chatrchyan et al. "Observation of a new boson at a mass of 125 GeV with the CMS experiment at the LHC". In: *Physics Letters B* 716.1 (2012), pp. 30–61. ISSN: 0370-2693. DOI: https://doi.org/10.1016/j.physletb.2012.08.021. URL: https://www.sciencedirect.com/science/article/pii/S0370269312008581.

[14] *ATLAS: technical proposal for a general-purpose pp experiment at the Large Hadron Collider at CERN*. LHC technical proposal. Geneva: CERN, 1994. DOI: 10.17181/CERN.NR4P.BG9K. URL: https://cds.cern.ch/record/290968.

[15] *CMS, the Compact Muon Solenoid: technical proposal*. LHC technical proposal. Geneva: CERN, 1994. URL: https://cds.cern.ch/record/290969.

[16] *LHCb : Technical Proposal*. Geneva: CERN, 1998. URL: https://cds.cern.ch/record/622031.

[17] *ALICE: Technical proposal for a Large Ion collider Experiment at the CERN LHC*. LHC technical proposal. Geneva: CERN, 1995. URL: https://cds.cern.ch/record/293391.

[18] R. Steerenberg et al. "Operation and Performance of the Cern Large Hadron Collider During Proton Run 2". In: *Proc. 10th International Particle Accelerator Conference (IPAC'19), Melbourne, Australia, 19-24 May 2019* (Melbourne, Australia). International Particle Accelerator Conference 10. https://doi.org/10.18429/JACoW-IPAC2019-MOPMP031. Geneva, Switzerland: JACoW Publishing, June 2019, pp. 504–507. ISBN: 978-3-95450-208-0. DOI: doi:10.18429/JACoW-IPAC2019-MOPMP031. URL: http://jacow.org/ipac2019/papers/mopmp031.pdf.

[19] D Jacquet and F Follin. *Implementation and experience with luminosity levelling with offset beam*. en. 2014. DOI: 10.5170/CERN-2014-004.183. URL: http://cds.cern.ch/record/1955354.

[20] *Framework TDR for the LHCb Upgrade: Technical Design Report*. Geneva, 2012.

[21] Roel Aaij et al. "The LHCb Upgrade I". In: (2023). to appear in JINST. arXiv: 2305.10515 [hep-ex].

[22] *LHCb reoptimized detector design and performance: Technical Design Report*. Geneva, 2003.

[23] *LHCb VELO (VErtex LOcator): Technical Design Report*. Geneva, 2001.

[24] *LHCb inner tracker: Technical Design Report*. Geneva, 2002.

[25] *LHCb outer tracker: Technical Design Report*. Geneva, 2001.

[26] R. Aaij et al. "Performance of the LHCb Vertex Locator". In: *JINST* 9 (2014), P09007. DOI: 10.1088/1748-0221/9/09/P09007. arXiv: 1405.7808 [physics.ins-det].

[27] B Adeva et al. *The LHCb Silicon Tracker*. Tech. rep. On behalf of the LHCb Silicon Tracker group. Geneva: CERN, 2013. URL: https://cds.cern.ch/record/1541958.

[28] *LHCb Silicon Tracker - Material for Publications*. URL: %7Bhttps://www.physik.uzh.ch/groups/lhcb/public/material/%7D.

[29] R. Arink et al. "Performance of the LHCb Outer Tracker". In: *JINST* 9 (2014), P01002. DOI: 10.1088/1748-0221/9/01/P01002. arXiv: 1311.3893 [physics.ins-det].

[30] *LHCb RICH: Technical Design Report*. Geneva, 2000.

[31] The LHCb Collaboration et al. "The LHCb Detector at the LHC". In: *Journal of Instrumentation* 3.08 (Aug. 2008), S08005. DOI: 10.1088/1748-0221/3/08/S08005. URL: https://dx.doi.org/10.1088/1748-0221/3/08/S08005.

[32] *LHCb calorimeters: Technical Design Report*. Geneva, 2000.

[33] *LHCb muon system: Technical Design Report*. Geneva, 2001.

[34] R. Aaij et al. "Design and performance of the LHCb trigger and full real-time reconstruction in Run 2 of the LHC". In: *Journal of Instrumentation* 14.04 (Apr. 2019), P04013. DOI: 10.1088/1748-0221/14/04/P04013. URL: https://dx.doi.org/10.1088/1748-0221/14/04/P04013.

[35] R Aaij et al. "The LHCb trigger and its performance in 2011". In: *Journal of Instrumentation* 8.04 (Apr. 2013), P04022–P04022. ISSN: 1748-0221. DOI: 10.1088/1748-0221/8/04/p04022. URL: http://dx.doi.org/10.1088/1748-0221/8/04/P04022.

[36] Torbjorn Sjostrand, Stephen Mrenna, and Peter Z. Skands. "A Brief Introduction to PYTHIA 8.1". In: *Comput. Phys. Commun.* 178 (2008), pp. 852–867. DOI: 10.1016/j.cpc.2008.01.036. arXiv: 0710.3820 [hep-ph].

[37] Anders Ryd et al. "EvtGen: A Monte Carlo Generator for B-Physics". In: (May 2005).

[38] S. Agostinelli et al. "Geant4—a simulation toolkit". In: *Nuclear Instruments and Methods in Physics Research Section A: Accelerators, Spectrometers, Detectors and Associated Equipment* 506.3 (2003), pp. 250–303. ISSN: 0168-9002. DOI: https://doi.org/10.1016/S0168-9002(03)01368-8. URL: http://www.sciencedirect.com/science/article/pii/S0168900203013688.

[39] Tatiana Likhomanenko et al. "LHCb Topological Trigger Reoptimization". In: *Journal of Physics: Conference Series* 664.8 (Dec. 2015), p. 082025. DOI: 10.1088/1742-6596/664/8/082025. URL: https://dx.doi.org/10.1088/1742-6596/664/8/082025.

[40] Tianqi Chen and Carlos Guestrin. "XGBoost: A Scalable Tree Boosting System". In: *Proceedings of the 22nd ACM SIGKDD International Conference on Knowledge Discovery and Data Mining*. KDD '16. ACM, Aug. 2016. DOI: 10.1145/2939672.2939785. URL: http://dx.doi.org/10.1145/2939672.2939785.

[41] Jerome H. Friedman. "Greedy function approximation: A gradient boosting machine." In: *The Annals of Statistics* 29.5 (2001), pp. 1189–1232. DOI: 10.1214/aos/1013203451. URL: https://doi.org/10.1214/aos/1013203451.

[42] R. Aaij et al. "Measurement of the ratio of branching fractions $\mathscr{B}\left(\overline{B}^0 \to D^{*+}\tau^-\overline{\nu}_\tau\right) / \mathscr{B}\left(\overline{B}^0 \to D^{*+}\mu^-\overline{\nu}_\mu\right)$". In: *Phys. Rev. Lett.* 115 (2015), p. 111803. DOI: 10.1103/PhysRevLett.115.111803. arXiv: 1506.08614 [hep-ex].

[43] M. Pivk and F.R. Le Diberder. ": A statistical tool to unfold data distributions". In: *Nuclear Instruments and Methods in Physics Research Section A: Accelerators, Spectrometers, Detectors and Associated Equipment* 555.1–2 (Dec. 2005), pp. 356–369. ISSN: 0168-9002. DOI: 10.1016/j.nima.2005.08.106. URL: http://dx.doi.org/10.1016/j.nima.2005.08.106.

[44] William Detmold, Christoph Lehner, and Stefan Meinel. "$\Lambda_b \to p\ell^-\overline{\nu}_\ell$ and $\Lambda_b \to \Lambda_c\ell^-\overline{\nu}_\ell$ form factors from lattice QCD with relativistic heavy quarks". In: *Phys. Rev. D* 92 (3 Aug. 2015), p. 034503. DOI: 10.1103/PhysRevD.92.034503. URL: https://link.aps.org/doi/10.1103/PhysRevD.92.034503.

[45] Alakabha Datta et al. "Phenomenology of $\Lambda_b \to \Lambda_c\tau\overline{\nu}_\tau$ using lattice QCD calculations". In: *JHEP* 08 (2017), p. 131. DOI: 10.1007/JHEP08(2017)131. arXiv: 1702.02243 [hep-ph].

[46] Stefan Meinel and Gumaro Rendon. "$\Lambda_b \to \Lambda_c^*(2595, 2625)\ell^-\overline{\nu}$ form factors from lattice QCD". In: *Phys. Rev. D* 103 (9 May 2021), p. 094516. DOI: 10.1103/PhysRevD.103.094516. URL: https://link.aps.org/doi/10.1103/PhysRevD.103.094516.

[47] R. Aaij et al. "Study of the kinematic dependences of Λ_b^0 production in pp collisions and a measurement of the $\Lambda_b^0 \to \Lambda_c^+\pi^-$ branching fraction". In: *Journal of High Energy Physics* 2014.8 (Aug. 2014). ISSN: 1029-8479. DOI: 10.1007/jhep08(2014)143. URL: http://dx.doi.org/10.1007/JHEP08(2014)143.

[48] Espen Eie Bowen, Barbara Storaci, and Marco Tresch. *VeloTT tracking for LHCb Run II*. Tech. rep. Geneva: CERN, 2016. URL: https://cds.cern.ch/record/2105078.

[49] R. Aaij et al. "Measurement of the track reconstruction efficiency at LHCb". In: *JINST* 10 (2015), P02007. DOI: 10.1088/1748-0221/10/02/P02007. arXiv: 1408.1251 [hep-ex].

[50] Alex Rogozhnikov. "Reweighting with Boosted Decision Trees". In: *Journal of Physics: Conference Series* 762 (Oct. 2016), p. 012036. ISSN: 1742-6596. DOI: 10.1088/1742-6596/762/1/012036. URL: http://dx.doi.org/10.1088/1742-6596/762/1/012036.

[51] G. Ciezarek et al. "Reconstruction of semileptonically decaying beauty hadrons produced in high energy pp collisions". In: *Journal of High Energy Physics* 2017.2 (Feb. 2017). ISSN: 1029-8479. DOI: 10.1007/jhep02(2017)021. URL: http://dx.doi.org/10.1007/JHEP02(2017)021.

[52] Jonas Eschle et al. "zfit: Scalable pythonic fitting". In: *SoftwareX* 11 (2020), p. 100508. ISSN: 2352-7110. DOI: https://doi.org/10.1016/j.softx.2020.100508. URL: https://www.sciencedirect.com/science/article/pii/S2352711019303851.

[53] Claude Bourrely, Laurent Lellouch, and Irinel Caprini. "Erratum: Model-independent description of $B \to \pi l\nu$ decays and a determination of $|V_{ub}|$ [Phys. Rev. DPRVDAQ1550-7998 79, 013008 (2009)]". In: *Phys. Rev. D* 82 (9 Nov. 2010), p. 099902. DOI: 10.1103/PhysRevD.82.099902. URL: https://link.aps.org/doi/10.1103/PhysRevD.82.099902.

[54] M. Ablikim et al. "Study of $\Lambda_c^+ \to \Lambda\mu^+\nu_\mu$ and test of lepton flavor universality with $\Lambda_c^+ \to \Lambda\ell^+\nu_\ell$ decays". In: *Phys. Rev. D* 108 (3 Aug. 2023), p. L031105. DOI: 10.1103/PhysRevD.108.L031105. URL: https://link.aps.org/doi/10.1103/PhysRevD.108.L031105.

[55] Martin Jung and David M. Straub. "Constraining new physics in $b \to c\ell\nu$ transitions". In: *JHEP* 01 (2019), p. 009. DOI: 10.1007/JHEP01(2019)009. arXiv: 1801.01112 [hep-ph].

[56] Roel Aaij et al. "Measurement of the ratio of branching fractions $\mathcal{B}(\bar{B}^0 \to D^{*+}\tau^-\bar{\nu}_\tau)/\mathcal{B}(\bar{B}^0 \to D^{*+}\mu^-\bar{\nu}_\mu)$". In: *Phys. Rev. Lett.* 115.11 (2015). [Erratum: Phys.Rev.Lett. 115, 159901 (2015)], p. 111803. DOI: 10.1103/PhysRevLett.115.111803. arXiv: 1506.08614 [hep-ex].

[57] Mark Ebden. *Gaussian Processes: A Quick Introduction*. 2015. arXiv: 1505.02965 [math.ST].

Chapter 4

FunTuple: A new N-tuple algorithm for offline data processing at the LHCb experiment

Contents

4.1 Introduction

The LHCb experiment, located at Point 8 of the Large Hadron Collider (LHC) [1] at CERN, is a forward-arm spectrometer designed to study the decays of beauty and charm hadrons [2, 3]. In the initial two runs of the LHC, during 2010–2018, the experiment (mainly) collected proton-proton collision data corresponding to a total integrated luminosity of $9\,\mathrm{fb}^{-1}$. As preparations intensify for Run 3, where the LHC's instantaneous luminosity is anticipated to surge by a factor of 5 compared to the preceding runs, the LHCb experiment is poised to enhance its capabilities even further. The upgraded detector [4] and data acquisition system will allow for improved vertexing and trigger efficiency [5]. This enhancement facilitates the exploration of exceedingly rare decays [6] while also facilitating the probing of deviations from Standard Model predictions with unparalleled precision [7–9].

The advent of Run 3 data acquisition presents significant hurdles for the LHCb data processing framework. Notably, the data volume from LHCb's Run 3 is projected to surge by over 15 times

compared to prior runs [10]. Consequently, management of petabytes of processed data and effectively incorporating distributed computing resources present significant challenges [11, 12]. In light of these challenges, a comprehensive redesign of both the trigger and offline data processing pipelines is imperative [10, 11]. This paper concentrates on the offline data processing pipeline, specifically highlighting the development of a novel algorithm called `FunTuple` facilitating analysis of Run 3 data and beyond.

In the initial LHC runs, LHCb's trigger and offline reconstruction frameworks, `Moore` [13] and `Brunel` [14], operated independently from the `DaVinci` framework [15] employed for offline data processing. Besides executing offline event selection, the `DaVinci` framework was used to process and store data for subsequent analysis. This function was accomplished via the `DecayTreeTuple` algorithm [16], [1] which recorded specific set of observables into output files. In this approach, the separation of trigger and offline frameworks implied that the equivalence between trigger-computed observables and those analysed offline was not guaranteed. Furthermore, in response to the forthcoming data processing challenges in Run 3, the LHCb experiment has significantly enhanced the performance of the trigger reconstruction algorithms, resulting in the retirement of the `Brunel` package responsible for offline reconstruction [19]. Consequently, there's a pressing need to develop new offline algorithms to accommodate upstream changes.

To overcome these hurdles, a strategic choice was made to leverage tools developed from the trigger system within the offline software framework. This led to the development of a new algorithm, `FunTuple`, which is tailored for processing Run 3 and Run 4 data. The `FunTuple` algorithm introduces enhancements to the previous workflow. Firstly, it guarantees the consistency between trigger-computed observables and those subjected to offline analysis. Secondly, it offers users the flexibility to efficiently tailor the list of recorded observables, an important feature given the expected surge in data volume for Run 3 and Run 4. This algorithm is configured with a robust suite of tools designed for the second stage of the LHCb trigger system, known as Throughput Oriented (`ThOr`) functors [20–22]. These functors are designed to deliver high-speed and efficient performance in the trigger's demanding throughput environment and are adept at computing topological and kinematic observables. `FunTuple` utilises these functors to compute a diverse range of observables and writes a `TTree` in the `ROOT` N-tuple format. [2] The N-tuple format is widely used in the High Energy Physics community to store flattened data in a tabular format [24]. Furthermore, the algorithm's lightweight design ensures simplified maintenance and seamless knowledge transfer. As depicted in Fig.4.1.1, the `FunTuple` algorithm plays a central role, bridging the gap between the offline data processing stage (`Sprucing`) and the subsequent user analysis stages[25]. In the `Sprucing` stage, the data is slimmed and skimmed before being saved to disk as part of the offline data processing workflow. The placement of `FunTuple` underscores its critical role in LHCb's analysis productions [26], facilitating the storage of experiment-acquired data in a format suitable for subsequent offline analysis.

---

[1]There were also alternative Python based algorithms like `Bender` [17, 18] for Run 1/2 data processing.

[2]There are plans in the future to write `ROOT` `RNTuple`, which has been designed to address performance bottlenecks and shortcomings of `ROOT` current state of the art `TTree` [23].
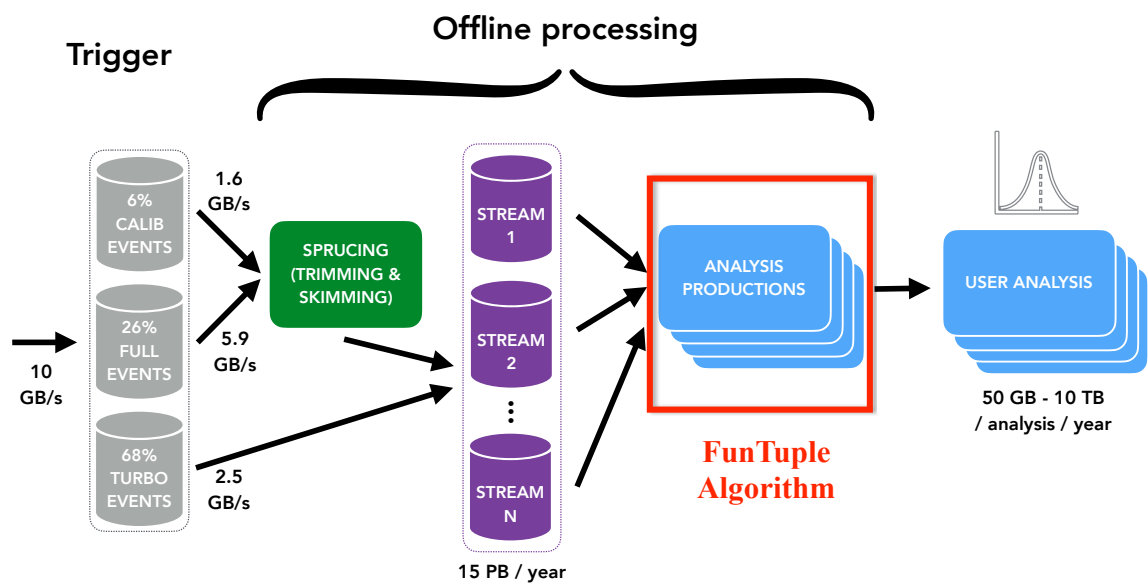
FIGURE 4.1.1: Data flow diagram for Run 3 data processing showing the placement of the FunTuple algorithm. Figure adapted from Ref. [25].

4.2   Design and interface

`FunTuple`, short for **Fun**ctional n**Tuple**, is an novel algorithm integral to the LHCb experiment's data processing infrastructure. It is a C++ [27] class built upon the `Gaudi` functional framework [28], and it offers a user-friendly `Python` [29] interface. The flexibility of the `FunTuple` algorithm lies in its templated design, allowing it to accommodate various types of input data. As a result, it is available in the three distinct flavours `FunTuple_Particles`, `FunTuple_MCParticles` and `FunTuple_Event` hereafter described.

The `FunTuple_Event` algorithm processes input data comprising of reconstructed or simulated events, where each event represents a single LHC bunch crossing. It acquires event-level information (for example the number of charged particles in the event), using thread-safe `ThOr` functors that are specialised C++ classes developed for utilisation in the second stage of the LHCb trigger system [20, 21, 30]. The algorithm then stores this extracted information from `ThOr` functors in a `ROOT` N-tuple file. The `FunTuple_Particles` algorithm functions on reconstructed events and identifies specific reconstructed decays by utilising the decay-finding algorithm `DecayFinder` [22] explained in Section 4.2.1. It further retrieves essential details regarding parent and children particles (for example magnitude of the transverse moment) through `ThOr` functors and records this information in a ROOT file. Similarly, the `FunTuple_MCParticles` algorithm shares similarities with `FunTuple_Particles`, but it processes simulated events instead, and captures information about simulated decays. For an illustrative representation of the data flow encompassing these three algorithmic approaches, refer to Fig. 4.2.1. Each aspect of the data-flow diagram is further elaborated in the following sections.

The instantiation of the three flavours of the `FunTuple` algorithm in `Python` is exemplified in Listings 4.1– 4.3. As depicted, the user is required to provide the `name` and `tuple_name` attributes for all three flavours. The `name` attribute defines the algorithm's name and the name of the corresponding `TDirectory` in the output ROOT file. On the other hand, the `tuple_name` attribute defines the name of the `TTree` in the ROOT file. The `fields` attribute can only be defined for `FunTuple_Particles` and `FunTuple_MCParticles` and is used to select specific decays within an event and define the corresponding `TBranches` in the output file. For a detailed exploration of this attribute, see Section 4.2.1. The `variables` attribute is used to specify the observables to be computed for each event or decay. In the case of `FunTuple_Event`, only event-level observables can be defined. Conversely, for `FunTuple_Particles` and `FunTuple_MCParticles`, both decay-level and event-level observables can be specified. The latter is achieved by defining an optional `event_variables` attribute. It is worth noting that the `FunTuple` algorithm automatically writes certain event information, such as the run and event numbers,[3] to the output file by default. For a more comprehensive discussion on the `variables` attribute, refer to Section 4.2.2. Finally, the `inputs` attribute refers to the Transient Event Store (TES) location, indicating the data pertaining to a given event cycle that will be processed by the algorithm. Subsequently, the processed information is stored in the output ROOT file, which is further elaborated on in Section 4.2.3.

---

[3]Both run and event numbers are used to uniquely identify an event in the LHC experiments.
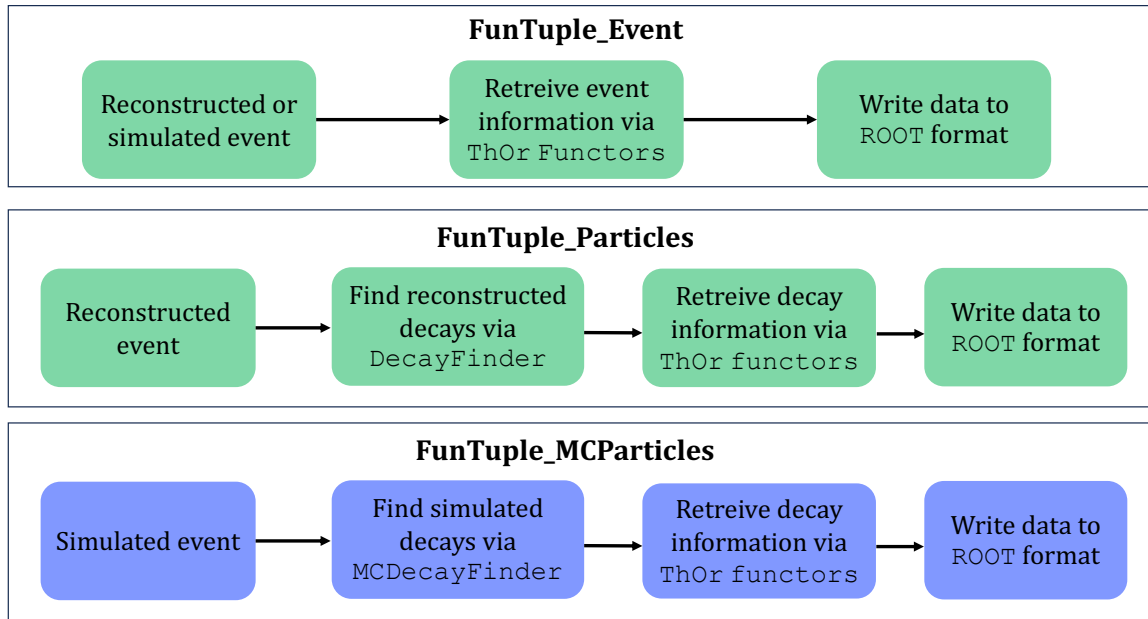
FIGURE 4.2.1: Data flow diagram for the three flavours of `FunTuple` algorithm.

The `FunTuple` algorithm also incorporates several essential counters to monitor the data processing. These counters include tracking the number of processed events, the count of non-empty events for each selected particle, and the tally of events with multiple candidates for each chosen particle. Upon completing the data processing, the results of these counters are displayed to the users. To ensure effective error handling, the algorithm employs a custom error handling class that inherits from the `StatusCode` class implemented in `Gaudi`. This custom implementation enables the algorithm to raise specific exceptions in targeted scenarios. For example, if a particular `ThOr` functor encounters difficulties and cannot compute an observable for a given event, the algorithm raises an exception to promptly notify the user of the issue. Additionally, the `FunTuple` algorithm takes measures to validate the input attributes both on the Python and C++ sides, ensuring the correctness of the provided data. Moreover, the development process includes the creation of several tests and examples, see Section 4.2.4.

4.2.1 Finding decays in an event

To isolate a particular decay process within an event and select a particle within the decay chain, the user is required to provide a `fields` attribute to either the `FunTuple_Particles` or the `FunTuple_MCParticles` instance. The `fields` attribute takes the form of a string dictionary. Here, the `key` corresponds to the particle alias, serving as a prefix to label the `TBranch` in the resulting output file. On the other hand, the associated `value` denotes the decay descriptor employed to filter and select the particles participating in a distinct reconstructed or simulated decay process. A practical illustration of the `fields` attribute configuration is shown in Listing 4.2.

LISTING 4.1: FunTuple_Particles instance

```python
# import FunTuple to run over
    reconstructed particles
from FunTuple import
    FunTuple_Particles

# define instance of FunTuple
data_tuple = FunTuple_Particles(
    name="TDirectoryName",
    tuple_name="TTreeName",
    fields=fields,
    variables=variables,
    event_variables=event_variables
    ,
    inputs=reco_data_TES_location)
```

LISTING 4.2: FunTuple_MCParticles instance

```python
# import FunTuple to run over
    simulated particles
from FunTuple import
    FunTuple_MCParticles

# define instance of FunTuple
data_tuple = FunTuple_MCParticles(
    name="TDirectoryName",
    tuple_name="TTreeName",
    fields=fields,
    variables=variables,
    event_variables=event_variables
    ,
    inputs=mc_data_TES_location)
```

LISTING 4.3: FunTuple_Event instance

```python
# import FunTuple to run over
    reconstructed or simulated event
from FunTuple import FunTuple_Event

# define instance of FunTuple
data_tuple = FunTuple_Event(
    name="TDirectoryName",
    tuple_name="TTreeName",
    variables=event_variables)
```

LISTING 4.2: Example definition of the `fields` attribute.

```python
# define fields to select decays in an event
# key: alias of the particle used as a prefix to name the TBranch
# value: decay descriptor syntax select particles
fields = {
    "Bplus": "[B+ ->  (J/psi -> mu+ mu-) [K+]CC ]CC",
    "Jpsi" : "[B+ ->  ^(J/psi -> mu+ mu-) [K+]CC ]CC",
    "kaons": "[B+ ->  (J/psi -> mu+ mu-) ^[K+]CC ]CC",
}
```

A correct syntax for the decay descriptor is crucial in the selection of the particles within a given decay process. A straightforward decay descriptor such as `"B+ -> J/psi K+"` is employed to select all decays of a B^+ meson into a J/ψ meson and a K^+ meson. For the inclusion of charge-conjugate decays, users can encapsulate the decay descriptor in square brackets and append the `CC` keyword, such as `"[B+ -> J/psi K+]CC"`. This syntax covers both $B^+ \rightarrow J/\Psi K^+$ and $B^- \rightarrow J/\Psi K^-$ decays. Alternatively, the `[]CC` notation can also be used around an individual particle, e.g., `"B+ -> J/psi [K+]CC"`, encompassing both $B^+ \rightarrow J/\Psi K^+$ and $B^- \rightarrow J/\Psi K^-$ decays.[4] To target a specific particle within a decay, the caret symbol (`^`) is employed. For instance, `"B+ -> J/psi ^K+"` selects the K^+ meson, while excluding the caret symbol selects the parent particle. In cases of identical particles in the final state, the `FunTuple` algorithm ensures distinct C++ objects for each identical particle instance. For example, `"B+ -> ^pi+ pi- pi+"` and `"B+ -> pi+ pi- ^pi+"` would choose two distinct instances of a π^+. In the context of simulations, the `FunTuple_MCParticles` algorithm utilises the `LoKi` decay finder [31]. This finder offers the flexibility to incorporate various arrow types within the decay descriptor syntax [31, 32]. Each arrow type allows users to selectively include simulated particles based on distinct criteria. For instance, the `=>` arrow type signifies the inclusion of arbitrary number of additional photons stemming from final state radiation of charged particles when matching the decay.

Given the distinct event models for reconstructed and simulated events, the `FunTuple` algorithm employs two separate `Gaudi` tools for decay identification. Specifically, `FunTuple_Particles` relies on the `Gaudi` tool [33] `DecayFinder`, while `FunTuple_MCParticles` utilises the `MCDecayFinder` tool [34]. Both of these tools utilise the `boost` library [35, 36] to parse decay descriptors. The names of particles used in the decay descriptor, along with their associated properties, are stored in the LHCb conditions database (`CondDB`) [37], and are retrieved through the `ParticlePropertySvc` [38] service.

4.2.2 Retrieve event and decay information

To extract essential information related to either the event or individual particles within a decay chain, users are required to furnish the `variables` or `event_variables` attribute to `FunTuple`. The `variables` attribute functions as a python dictionary in which the `key` corresponds to the particle name previously defined in the `fields` attribute in the previous section. The corresponding `value` is an instance of a `FunctorCollection`, which acts as a collection of `ThOr` functors, effectively resembling a dictionary itself, with the `key` representing the variable name and the `value` denoting a `ThOr` functor. Within the context of the `FunTuple` algorithm, these `ThOr` functors are just-in-time (JIT) compiled and employed on the particle instance to retrieve the desired information. Notably, a key labelled `ALL` holds a special significance within the definition of the `variables`. Any `FunctorCollection` associated with the `ALL` key is applied to all particles specified in the `fields` attribute. In contrast, the `event_variables` attribute takes the form of an instance of `FunctorCollection`. The enclosed `ThOr` functors are designed to provide information

---

[4]The charge-violating decays are often reconstructed at LHCb to serve as proxies for the study of sources of background.

at the event level. The specifics of how to define the `variables` and `event_variables` attributes are illustrated in Listing 4.3.

The `FunTuple` algorithm utilises the flexibility inherent in `ThOr` functors to extract a diverse array of information from the event. These functors are adaptable enough to accept multiple reconstructed objects as input, enabling the computation of associated information. For instance, consider the functor designed to calculate the flight distance of a particle. To achieve this, the functor takes both the reconstructed primary vertices and the reconstructed particle as input arguments. The usage of this specific functor (`BPVFD`) is shown in Listing 4.3. These functors can also undergo various mathematical operations. Furthermore, the output from one `ThOr` functor can be passed as input to other `ThOr` functors through a mechanism known as *composition*. This proves particularly advantageous when users seek to compute an observable that relies on the outcomes of other observables. All these functionalities are harnessed to provide users with an range of observables via a pre-defined `FunctorCollection` instance, which is intended for use in conjunction with `FunTuple`. An illustrative example is the `SelectionInfo` collection, which gathers the functors employed to store the trigger configuration key (TCK) and the event's trigger line decision. Listing 4.4 outlines the definition of this collection, with its application showcased in Listing 4.3.

In this listing, the `SelectionInfo` collection is designed to take two main inputs: the type of selection, which can be any of the three stages (`Hlt1`, `Hlt2`, or `Sprucing`), and a list of trigger or Sprucing lines. In response, it generates a `FunctorCollection` that incorporates two functors: `F.TCK` for storing TCK information and `F.DECISION` for storing the trigger decision of the specified selection line. Such collections do not expose the users to the technical intricacies involved in retrieving the requested information. In this particular case, the involved functors require the `DecReport` object, which is obtained from the `DaVinci` framework via the `get_decreports` function. Furthermore, users maintain the flexibility to add, merge or remove observables within these collections, enabling them to create their customised collections. Multiple collections have been developed and continue to be actively expanded, accompanied by relevant unit tests within the `DaVinci` framework.

4.2.3 Writing of retrieved information

The `ThOr` functors, utilised for retrieving reconstructed or truth-level information, are capable of encapsulating data in a diverse range of formats. These functors can return basic C++ types, but they can also yield complex objects pertaining to the LHCb software framework. Subsequently, the extracted information is recorded within the ROOT file, where each `TBranch` corresponds to an scalar observable. In this context, the `FunTuple` framework provides extensive support for various variable types, expanding beyond the fundamental C++ types. These encompass three-vectors, four-vectors, matrices of both symmetric and non-symmetric nature with arbitrary dimensions, containers spanning arbitrary dimensions, as well as `std::optional<T>` constructs and `std::map<std::string, T>` structures. Here, `T` signifies any of the supported types. As of

LISTING 4.3: Example definition of the `variables` and `event_variables` attributes.

```python
# import ThOr functor library
import Functors as F
# import the FunctorCollection library
import FunTuple.functorcollections as FC
# import function to get TES location of PVs
from PyConf.reading import get_pvs

# variables for "Bplus" defined in the "fields"
b_vars = FunctorCollection()
# store the flight distance of candidate B relative to the primary
    vertex that best aligns with the origin of candidate B.
pvs = get_pvs()
b_vars["BPVFD"] = F.BPVFD(pvs)

# variables for "Kaons" defined in the "fields"
kaon_vars = FunctorCollection()
kaon_vars["PT"] = F.PT

# variables for "ALL" particles defined in "fields"
all_vars = FunctorCollection()
all_vars["ETA"] = F.ETA

# define decay-level variables
variables = {
  "Bplus": b_vars,
  "Kaons": kaon_vars,
  "ALL": all_vars,
}

# define event-level variables,
# for example number of primary vertices
# and add FunctorCollection "SelectionInfo"
# that stores trigger configuration key (TCK) and
# decisions of "Hlt1LineName" trigger line
event_variables = FunctorCollection()
event_variables["nPVs"] = F.nPVs
evt_variables += FC.SelectionInfo(selection_type="Hlt2",
    trigger_lines=["Hlt1LineName"])

```

LISTING 4.4: Definition of the `SelectionInfo` collection.

```python
from GaudiConf.LbExec import HltSourceID
import Functors as F
from PyConf.reading import get_decreports

def SelectionInfo(*,
  selection_type: HltSourceID,
  trigger_lines: list[str]) -> FunctorCollection:
  """
  Event-level collection for tupling trigger/Sprucing information.

  Args:
      selection_type (HltSourceID): Name of the selection type i.e.
    "Hlt1" or "Hlt2" or "Spruce". Used as branch name prefix when
    tupling and as source ID to get decision reports.
      trigger_lines (list(str)): List of line names for which the
    decision is requested.

  Returns:
      FunctorCollection: Collection of functors to tuple trigger/
    Sprucing information.
  """

  # get selection type
  selection_type = HltSourceID(selection_type)

  # get decreports
  dec_report = get_decreports(selection_type)

  # check that the code ends with decision
  trigger_lines = [s + "Decision" if not s.endswith("Decision") else
    s for s in trigger_lines]

  # create trigger info dictionary
  trigger_info = FunctorCollection({
      selection_type.name + "_TCK": F.TCK(dec_report),
      l: F.DECISION(dec_report, l) for l in trigger_lines
  })
  return trigger_info
```

the preparation of this document, the `FunTuple` algorithm uses the `GaudiTupleAlg` tool [38] to write the information to the ROOT file.

4.2.4   Test suite and examples

The `FunTuple` "package" includes a comprehensive set of examples for users as well as a dedicated test suite based on `pytest` [39]. The unit as well as "physics" tests are designed to evaluate various functionalities of the algorithm, ensuring its reliability. Furthermore, an application test goes with each and single example job run in continuous integration to guarantee the correct functionality at all times.

4.3   Interface with other `Gaudi` algorithms

In the LHCb framework, the execution of multiple algorithms within the offline data processing pipeline is a common necessity. Notable examples of such algorithms encompass the `DecayTreeFitter`[40], which fits complete decay chains with optional primary vertex constraints or mass constraints on intermediary states; the `MCTruthAndBkgCatAlg` algorithm [22], which is used to extract truth-level information from reconstructed objects in simulations; the `ParticleCombiner` algorithm [22], for combining basic particles into composite entities; among others. These algorithms can be employed in conjunction with the `FunTuple` algorithm to process and store data. A practical illustration of `FunTuple` in synergy with `DecayTreeFitter` and `MCTruthAndBkgCat` is presented in Listing 4.5.

In this listing, the `DecayTreeFitter` and `MCTruthAndBkgCat` algorithms operate on reconstructed $B^+ \to J/\Psi K^+$ decays. Under the hood, both algorithms construct a relation table linking the reconstructed object with a related object that holds pertinent information. For `MCTruthAndBkgCat`, the related object is the associated simulation object, harbouring truth-level information; conversely, for `DecayTreeFitter`, the related object corresponds to the output of the decay tree fitting process. To extract the relevant information, the reconstructed object is mapped to the related object, and the `ThOr` functor is applied to the related object. This entire process is executed within the `__call__` method of both the `MCTruthAndBkgCat` and `DecayTreeFitter` algorithms. For example, in Listing 4.5, calling `MCTRUTH(F.FOURMOMENTUM)` establishes a mapping between the reconstructed $B^+ \to J/\Psi K^+$ decay and the corresponding simulation object. Subsequently, the `F.FOURMOMENTUM` functor is employed on the simulation object to retrieve the true four-momentum of the B+ meson. A similar approach is followed for the `DTF(F.FOURMOMENTUM)`, with the distinction that the four-momentum of the B^+ meson is stored following the decay tree fit, incorporating mass constraint on the J/ψ meson and primary vertex constraint.

The interaction between `FunTuple` and other `Gaudi` algorithms is fortified by a fail-safe mechanism. When either of the algorithms encounters failure, such as the absence of corresponding truth-level information or unsuccessful decay tree fitting, the `ThOr` functors and `FunTuple` are equipped to handle the situation. If the `ThOr` functor returns data of floating-point type, the `FunTuple` algorithm

automatically records Not a Number (`NaN`) in the ROOT file. Conversely, if the `ThOr` functor returns an integral type, the invalid value needs to be explicitly defined using the `F.VALUE_OR` functor, exemplified in Listing 4.5.

4.4 Summary and conclusions

This paper introduces the `FunTuple` algorithm, designed to support offline data processing for the LHCb experiment during Run 3 and subsequent runs. Its primary purpose is to facilitate the storage of experiment-acquired data in the `ROOT` format, optimising it for subsequent offline analysis. Currently, the algorithm plays a vital role in various early measurement analyses of LHCb data collected during the Run 3 data taking period. An example of the processed data using `FunTuple` is displayed in Fig. 4.4.1, showcasing the reconstructed mass of the $J/\psi \to \mu^-\mu^+$ decay from LHCb data gathered in 2022 during commissioning [41]. Built upon the `Gaudi` functional framework, this algorithm showcases an accessible `Python` interface. It accommodates storage of both event-level and decay-level information, and supports processing of both reconstructed and simulated events.
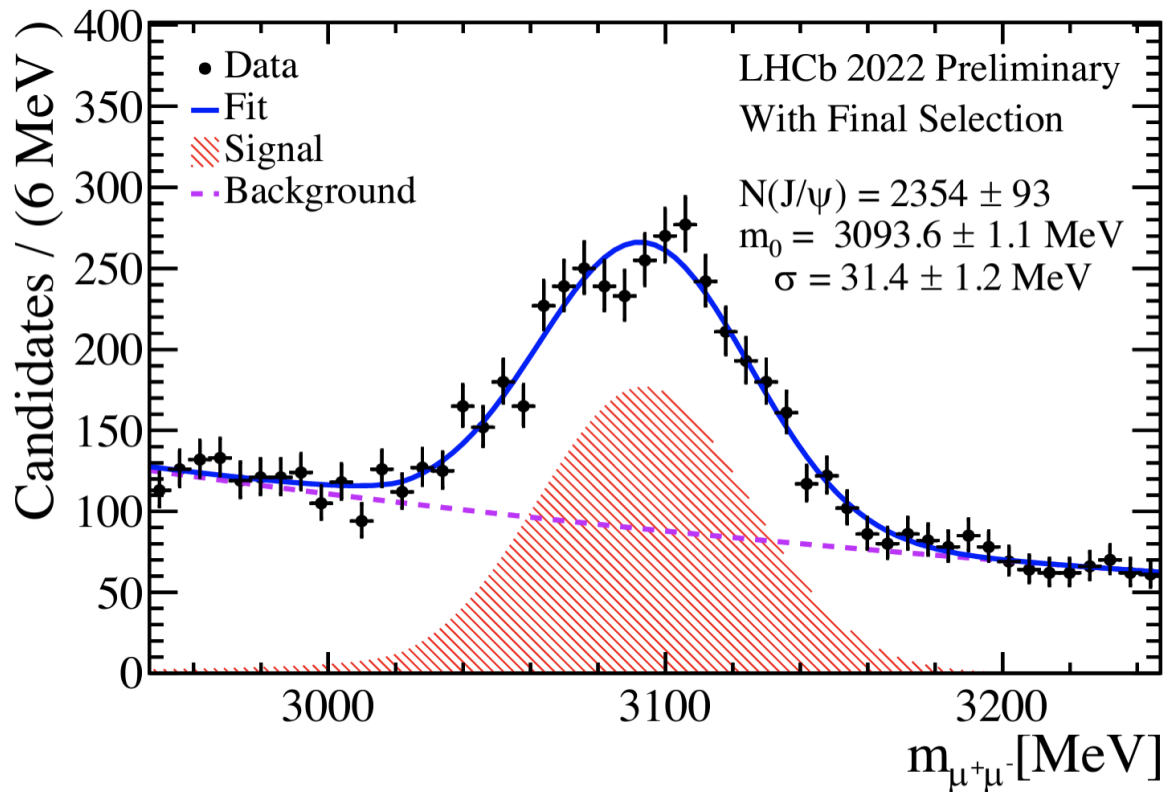
FIGURE 4.4.1: Invariant mass of the $(\mu^-\mu^+)$ system showing the J/ψ peak for LHCb data collected during the Run 3 commissioning data taking period in 2022 [41].

LISTING 4.5: Usage of truth-matching (MCTruthAndBkgCat) and decay tree fitting (DecayTreeFitter) algorithms in conjunction with FunTuple.

```python
from DecayTreeFitter import DecayTreeFitter
from DaVinciMCTools import MCTruthAndBkgCat

# get the TES location of the input data with
# reconstructed "B+ -> J/psi K+" decays
input_data = get_particles(f"/Event/HLT2/BToJpsiK/Particles")

# define an instance of MCTruthAndBkgCat algorithm for truth-
    matching.
# Arguments include:
# - name: User-specified name
# - input_data: TES location of the input data
MCTRUTH = MCTruthAndBkgCat(name="MCTRUTH", input_data=input_data)

#define an instance of DecayTreeFitter for fitting the decay chain
# Arguments include:
# - name: User-specifed name
# - (optional) mass_constraint: Mass constraint on intermediate
    state (in this instance J/psi(1S))
# - (optional) input_pvs: TES location of reconstructed primary
    vertices to apply primary vertex constraint
# - input_data: TES location of the input data
DTF = DecayTreeFitter(name="DTF", mass_constraints=["J/psi(1S)"],
    input_pvs=pvs, input_data=input_data)

# define the B candidate variables to be passed to FunTuple
# Note: The "F.VALUE_OR" functor specifies an invalid value to be
    written to ROOT file in the case of no corresponding truth-level
     information. For functors returning floating point types such
    as components of F.FOURMOMENTUM, this is automatically chosen to
     be "NaN" by FunTuple
b_vars = FunctorCollection()
# add truth-level information
b_vars["TRUE_ID"] = F.VALUE_OR(0) @ MCTRUTH(F.PARTICLE_ID)
b_vars["TRUE_FOURMOM"] = MCTRUTH(F.FOURMOMENTUM)
# add decay tree fitter information
b_vars["DTF_FOURMOM"] = DTF(F.FOURMOMENTUM)
```

Of particular importance is its ability to ensure equivalence between trigger-computed observables and those subjected to offline analysis. This achievement is made possible through the integration of the `ThOr` functors, adept at computing topological and kinematic observables. Furthermore, users also have substantial flexibility, enabling them to personalise the range of observables stored within the `ROOT` file. The algorithm is also thoroughly validated through a series of unit-tests and `pytest` tests to ensure its reliability. In conclusion, the unique attributes of the `FunTuple` algorithm establish it as a robust tool for offline data processing at the LHCb experiment making it essential for Run 3 and beyond.

References

[1] "LHC Machine". In: *JINST* 3 (2008). Ed. by Lyndon Evans and Philip Bryant, S08001. DOI: 10.1088/1748-0221/3/08/S08001.

[2] A. A. Alves Jr. et al. "The LHCb detector at the LHC". In: *JINST* 3.LHCb-DP-2008-001 (2008), S08005. DOI: 10.1088/1748-0221/3/08/S08005.

[3] R. Aaij et al. "LHCb detector performance". In: *Int. J. Mod. Phys.* A30 (2015), p. 1530022. DOI: 10.1142/S0217751X15300227. arXiv: 1412.6352 [hep-ex].

[4] Roel Aaij et al. "The LHCb Upgrade I". In: (2023). to appear in JINST. arXiv: 2305.10515 [hep-ex].

[5] Roel Aaij et al. "A comprehensive real-time analysis model at the LHCb experiment". In: *JINST* 14 (2019), P04006. DOI: 10.1088/1748-0221/14/04/P04006. arXiv: 1903.01360 [hep-ex].

[6] R. Aaij et al. "Measurement of the $\mathscr{B}_s^0 \to \mu^+\mu^-$ decay properties and search for the $\mathscr{B}^0 \to \mu^+\mu^-$ and $\mathscr{B}_s^0 \to \mu^+\mu^-\gamma$ decays". In: *Phys. Rev.* D105 (2022), p. 012010. DOI: 10.1103/PhysRevD.105.012010. arXiv: 2108.09283 [hep-ex].

[7] R. Aaij et al. "Measurement of *CP*-averaged observables in the $\mathscr{B}^0 \to K^{*0}\mu^+\mu^-$ decay". In: *Phys. Rev. Lett.* 125 (2020), p. 011802. DOI: 10.1103/PhysRevLett.125.011802. arXiv: 2003.04831 [hep-ex].

[8] R. Aaij et al. "Test of lepton flavour universality using $\mathscr{B}^0 \to D^{*-}\tau^+\nu_\tau$ decays, with hadronic τ channels". In: *Phys. Rev.* D108 (2023), p. 012018. DOI: 10.1103/PhysRevD.108.012018. arXiv: 2305.01463 [hep-ex].

[9] R. Aaij et al. "Measurement of the ratio of branching fractions $\mathscr{R}(D^*)$ and $\mathscr{R}(D^0)$". In: (2023). submitted to Phys. Rev. Lett. arXiv: 2302.02886 [hep-ex].

[10] N. Skidmore, E. Rodrigues, and P. Koppenburg. "Run-3 offline data processing and analysis at LHCb". In: *PoS* EPS-HEP2021 (2022), p. 792. DOI: 10.22323/1.398.0792.

[11] *Computing Model of the Upgrade LHCb experiment*. Geneva, 2018.

[12] A. Tsaregorodtsev et al. "DIRAC3: The new generation of the LHCb grid software". In: *J. Phys. Conf. Ser.* 219 (2010), p. 062029. DOI: 10.1088/1742-6596/219/6/062029.

[13] *Moore project*. https://gitlab.cern.ch/lhcb/Moore. [Online; accessed 19-Aug-2023].

[14] *Brunel project*. https://gitlab.cern.ch/lhcb/Brunel. [Online; accessed 19-Aug-2023].

[15] *DaVinci project*. https://gitlab.cern.ch/lhcb/DaVinci. [Online; accessed 19-Aug-2023].

[16] *Analysis project*. https://gitlab.cern.ch/lhcb/Analysis/-/tree/v22r7?ref_type=tags. [Online; accessed 19-Aug-2023].

[17] I. Belyaev et al. *Python-based Physics Analysis Environment for LHCb*. https://inspirehep.net/literature/928906. Oct. 2004.

[18] *Bender project*. https://gitlab.cern.ch/lhcb/Analysis/-/tree/v22r7?ref_type=tags. [Online; accessed 19-Aug-2023].

[19] Florian Reiss. *Real-time alignment procedure at the LHCb experiment for Run 3*. http://cds.cern.ch/record/2846414. 2023.

[20] *ThOr Functors*. https://lhcbdoc.web.cern.ch/lhcbdoc/moore/master/selection/thor_functors.html. [Online; accessed 02-Nov-2022].

[21] Niklas Nolte. *A Selection Framework for LHCb's Upgrade Trigger*. https://cds.cern.ch/record/2765896. Presented 22 Feb 2021. 2020.

[22] *Rec project*. https://gitlab.cern.ch/lhcb/Rec. [Online; accessed 19-Aug-2023].

[23] Javier Lopez-Gomez and Jakob Blomer. "RNTuple performance: Status and Outlook". In: *J. Phys. Conf. Ser.* 2438.1 (2023), p. 012118. DOI: 10.1088/1742-6596/2438/1/012118. arXiv: 2204.09043 [physics.data-an].

[24] R. Brun and F. Rademakers. "ROOT: An object oriented data analysis framework". In: *Nucl. Instrum. Meth. A* 389 (1997). Ed. by M. Werlen and D. Perret-Gallix, pp. 81–86. DOI: 10.1016/S0168-9002(97)00048-X.

[25] *RTA and DPA dataflow diagrams for Run 1, Run 2, and the upgraded LHCb detector*. https://cds.cern.ch/record/2730181. 2020.

[26] *Analysis Production project*. https://lhcb-analysis-productions-preview.web.cern.ch/. [Online; accessed 19-Aug-2023].

[27] *Standard C++, version C++17*. https://isocpp.org/. [Online; accessed 19-Aug-2023].

[28] G. Barrand et al. "GAUDI - A software architecture and framework for building HEP data processing applications". In: *Comput. Phys. Commun.* 140 (2001), pp. 45–55. DOI: 10.1016/S0010-4655(01)00254-5.

[29] *Python Software Foundation. Python Language Reference, version 3.9*. https://www.python.org/. [Online; accessed 19-Aug-2023].

[30] Peilian Li. "Real-time analysis in Run 3 with the LHCb experiment". In: *PoS* EPS-HEP2021 (2022), p. 829. DOI: 10.22323/1.398.0829.

[31] *LoKi framework*. https://twiki.cern.ch/twiki/bin/view/LHCb/FAQ/LoKiNewDecayFinders. [Online; accessed 19-Aug-2023].

[32] *Grammar in short: Arrows*. https://twiki.cern.ch/twiki/bin/view/LHCb/FAQ/LoKiNewDecayFinders#Arrows. [Online; accessed 16-Sept-2022]. 2022.

[33] Marco Clemencic et al. "Recent Developments in the LHCb Software Framework Gaudi". In: *Journal of Physics: Conference Series* 219 (May 2010), p. 042006. DOI: 10.1088/1742-6596/219/4/042006.

[34] *LHCb project*. https://gitlab.cern.ch/lhcb/LHCb. [Online; accessed 19-Aug-2023].

[35] *Boost.Regex 7.0.1*. https://www.boost.org/doc/libs/1_80_0/libs/regex/doc/html/index.html. [Online; accessed 19-Aug-2023].

[36] Hartmut Kaiser Joel de Guzman. *Qi - Writing Parsers*. https://www.boost.org/doc/libs/1_80_0/libs/spirit/doc/html/spirit/qi.html. [Online; accessed 16-Sept-2022]. 2011.

[37] *LHCb Conditions Database*. https://gitlab.cern.ch/lhcb-conddb. [Online; accessed 19-Aug-2023].

[38] *Gaudi framework*. https://gitlab.cern.ch/lhcb/Gaudi. [Online; accessed 19-Aug-2023].

[39] Holger Krekel et al. *pytest*. https://docs.pytest.org/en/7.1.x/. 2004. URL: https://github.com/pytest-dev/pytest.

[40] Wouter D. Hulsbergen. "Decay chain fitting with a Kalman filter". In: *Nucl. Instrum. Meth.* A552 (2005), pp. 566–575. DOI: 10.1016/j.nima.2005.06.078. arXiv: physics/0503191 [physics].

[41] *Jpsi2MuMu 2022 mass figure*. https://cds.cern.ch/record/2867664. 2022.

Part II

Neutrino physics at the High Energy Frontier

Chapter 5

Observation of collider muon neutrinos with the SND@LHC experiment

Contents

We report the direct observation of muon neutrino interactions with the SND@LHC detector at the Large Hadron Collider. A data set of proton-proton collisions at $\sqrt{s} = 13.6\,\text{TeV}$ collected by SND@LHC in 2022 is used, corresponding to an integrated luminosity of $36.8\,\text{fb}^{-1}$. The search is based on information from the active electronic components of the SND@LHC detector, which covers the pseudo-rapidity region of $7.2 < \eta < 8.4$, inaccessible to the other experiments at the collider. Muon neutrino candidates are identified through their charged-current interaction topology, with a track propagating through the entire length of the muon detector. After selection cuts, 8 ν_μ interaction candidate events remain with an estimated background of 0.076 events, yielding a significance of seven standard deviations for the observed ν_μ signal.

5.1 Introduction

The use of the Large Hadron Collider (LHC) as a neutrino factory was first envisaged about 30 years ago [1–3] in particular for the then undiscovered ν_τ [4]. Those studies suggest a detector intercepting the very forward flux ($\eta > 7$) of neutrinos (about 5% have τ flavour) from b and c decays [5]. The physics potential of a detector to study neutrinos was underlined in Ref. [6]. The

role of an off-axis setup, which enhances the neutrino flux from charmed particle decays, was emphasised in Ref. [7].

Proton-proton (*pp*) collisions at a center-of-mass energy of 13.6 TeV during LHC Run 3, with an expected integrated luminosity of 250 fb^{-1}, will produce a high-intensity beam yielding $O(10^{12})$ neutrinos in the far forward direction with energies up to a few TeV [8].

Neutrinos allow precise tests of the Standard Model (SM) [9–12] and are a probe for new physics [13, 14]. Measurements of the neutrino cross section in the last decades were mainly performed at low energies. The region between 350 GeVand 10 TeV is currently unexplored [15].

SND@LHC [16] was designed to perform measurements with high-energy neutrinos (100 GeVto a few TeV) produced at the LHC in the pseudo-rapidity region $7.2 < \eta < 8.4$. It is a compact, standalone experiment located in the TI18 unused LEP transfer tunnel (480 m away of the ATLAS interaction point, IP1[17]) where it is shielded from collision debris by around 100 m of rock and concrete. The detector is capable of identifying all three neutrino flavours with high efficiency.

The detector was installed in TI18 in 2021 during the Long Shutdown 2 and has collected data since the beginning of the LHC Run 3 in April 2022. The experiment will run throughout the whole Run 3, during which a total of two thousand high-energy neutrino interactions of all flavours are expected to occur in the detector target.

In this paper, we report the detection of ν_μ charged-current (CC) interactions using only data that was taken by the electronic detectors in 2022.

Recently the observation of neutrino interactions in a complementary pseudo-rapidity region ($\eta > 8.8$) has also been reported with the analysis of the 2022 data by the FASER Collaboration [18].

5.2 Detector

The SND@LHC detector consists of a hybrid system with a ~ 830 kg target made of tungsten plates interleaved with nuclear emulsions and electronic trackers, followed by a hadronic calorimeter and a muon system (see Figure 5.2.1). The electronic detectors provide the time stamp of the neutrino interaction, preselect the interaction region, tag muons and measure the electromagnetic and hadronic energy, while the emulsion detectors provide excellent vertex reconstruction.

A left-handed coordinate system is used, with z along the nominal collision axis and pointing away from IP1, x pointing towards the center of the LHC, and y vertically aligned and pointing upwards.

The detector consists of three parts: the veto system, the target section, and the hadronic calorimeter and muon system.

The veto system is located upstream of the target region and comprises two parallel planes, located 4.3 cm apart, of scintillating bars read out on both ends by silicon photomultipliers (SiPMs). Each plane consists of seven $1 \times 6 \times 42$ cm^3 stacked bars of EJ-200 scintillator [19]. The number of

photons generated by a minimum-ionising particle crossing 1 cm scintillator is of the order of 10^4. The bars are wrapped in aluminized BoPET foil to ensure light tightness and therefore isolate them from light in adjacent bars. This system is used to tag muons and other charged particles entering the detector from the IP1 direction.

The target section contains five walls. Each wall consists of four units of emulsion cloud chambers (ECC [20]) and is followed by a scintillating fibre (SciFi [21]) station for tracking and electromagnetic calorimetry.
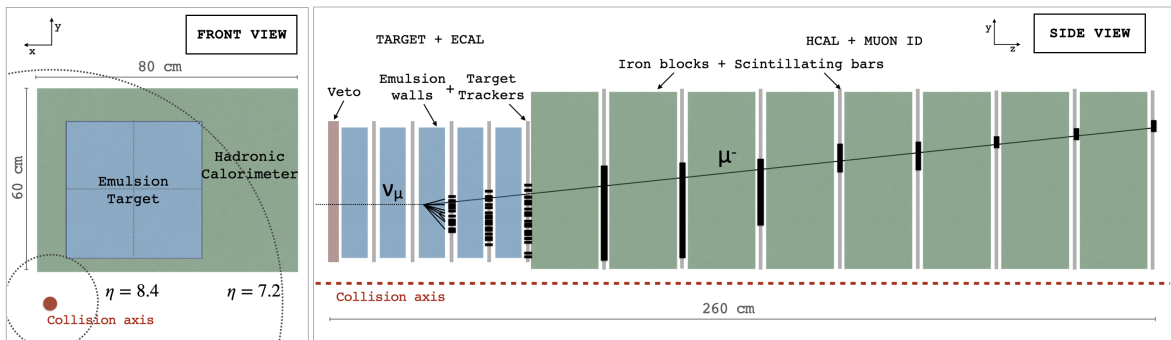
FIGURE 5.2.1: Schematic layout of the SND@LHC detector front view (left) and side view (right). The side view includes an illustration of a ν_μ charged-current interaction in the target with a hadronic shower sampled in the emulsion target, target trackers, and hadronic calorimeter, and a muon track visible in the muon system.

The sub-micrometric spatial resolution of the nuclear emulsions allows for very efficient tracking of all the charged particles produced in high energy neutrino interactions, despite their small angular separation due to the large boost. This also allows for efficient tracking of the tau lepton and its decay vertex which in turn is a key element in the identification of tau leptons and hence the tagging of tau neutrino interactions.

Each ECC unit is a sequence of 60 nuclear emulsion films, $19.2 \times 19.2 \, \text{cm}^2$ and approximately 300 µm, interleaved with 59 tungsten plates, 1 mm thick. Its weight is approximately 41.5 kg, adding up to about 830 kg for the total target mass.

Each SciFi station consists of two $40 \times 40 \, \text{cm}^2$ planes, alternating x and y views. Each view comprises six densely packed staggered layers of 250 µm diameter polystyrene-based scintillating fibres read out by SiPM arrays. The single particle spatial resolution in one view is of order of $\sim 150 \, \text{µm}$ and the time resolution for a particle crossing both x and y views of one plane is about 250 ps.

The muon system and hadronic calorimeter consists of two parts: upstream (US), the first five stations, and downstream (DS), the last three stations (see Figure 5.2.1). Each US station consists of 10 stacked horizontal scintillator bars of $82.5 \times 6 \times 1 \, \text{cm}^3$, similar to the veto detector, resulting in a coarse y view. A DS station consists of two layers of thinner $82.5 \times 1 \times 1 \, \text{cm}^3$ bars arranged

in alternating x and y views, allowing for a spatial resolution in each view of less than 1 cm. The time resolution for a single DS detector bar is ~ 120 ps. The eight scintillator planes are interleaved with 20 cm thick iron blocks. In combination with SciFi, the muon system and hadronic calorimeter acts as a coarse sampling calorimeter ($\sim 9.5\,\lambda_{\text{int}}$ in the US detector), providing the energy measurement of hadronic jets. The finer spatial resolution of the DS detector allows for the identification of muon tracks exiting the detector.

All signals exceeding preset thresholds are read out by the front-end electronics and clustered in time to form events. A software noise filter is applied to the events online, resulting in negligible detector deadtime or loss in signal efficiency. Events satisfying certain topological criteria, such as the presence of hits in several detector planes, are read out at a rate of around 5.4 kHz at the highest instantaneous luminosity achieved in 2022 of $2.5 \times 10^{34}\,\text{cm}^{-2}\,\text{s}^{-1}$.

5.3 Dataset and simulated samples

In this paper, we analyse the data collected during 2022, with pp collisions at center of mass energy of 13.6 TeV. The delivered integrated luminosity during this period, as estimated by the ATLAS Collaboration[17, 22], was 38.7 fb^{-1}, of which 36.8 fb^{-1} were recorded, corresponding to a detector uptime of 95%. The data set comprises a total of 8.3×10^9 events.

The analysis developed for the first observation of ν_μ CC interactions from LHC collisions is conducted solely using the data from the electronic detectors, as information from the emulsion target is currently being processed.

In SND@LHC the dominant CC process occurring for ν_μs is deep inelastic scattering (CCDIS), given the high energy of neutrinos within the detector acceptance [8]. The signature of these interactions includes an isolated muon track in the muon system, associated with a hadronic shower detected in the SciFi and hadronic calorimeter. In Figure 5.2.1 the distinctive topology of ν_μ CCDIS interactions is shown.

Neutrino production in pp collisions at the LHC is simulated with the FLUKA Monte Carlo code [23, 24]. DPMJET3 (Dual Parton Model, including charm) [25, 26] is used for the pp event generation, and FLUKA performs the particle propagation towards the SND@LHC detector with the help of a detailed simulation of LHC accelerator elements [27]. FLUKA also takes care of simulating the production of neutrinos from decays of long-lived products of the pp collisions and of particles produced in re-interactions with the surrounding material. GENIE [28] is then used to simulate neutrino interactions with the detector material. The propagation of particles through the TI18 tunnel and the SND@LHC detector is simulated with GEANT4. A total of around 160 thousand simulated neutrino events and 30 million background events were generated for the analysis described in this publication.

Given the total mass of the tungsten target during the 2022 run (~ 800 kg), about 157 ± 37 ν_μ CCDIS interactions are expected in the full target in the analysed data set, where the range in the

expectation is given by the difference between the predictions of the ν_μ flux at SND@LHC using DPMJET3 and SIBYLL obtained in Ref.[29].

5.4 Analysis

Observing the rare neutrino signal over the prevailing background implies adopting a selection with strong rejection power, designed to yield a clean set of events.

The signal selection proceeds in two steps. The first step aims at identifying events happening in a fiducial region of the target, while rejecting backgrounds due to charged particles entering from the front and sides of the detector. Cuts are applied on the hit multiplicity in the veto and SciFi planes to select events that are located in the 3rd or 4th target wall and consistent with a neutral particle interaction. The exclusion of events starting in the two most upstream target walls enhances the rejection power for muon-induced backgrounds, while excluding events starting in the most downstream wall ensures the neutrino-induced showers are sampled by at least two SciFi planes. The average SciFi channel and DS bar number are used to discard events with hits at the edges of detectors' sensitive areas, resulting in a fiducial cross-sectional area in the xy plane
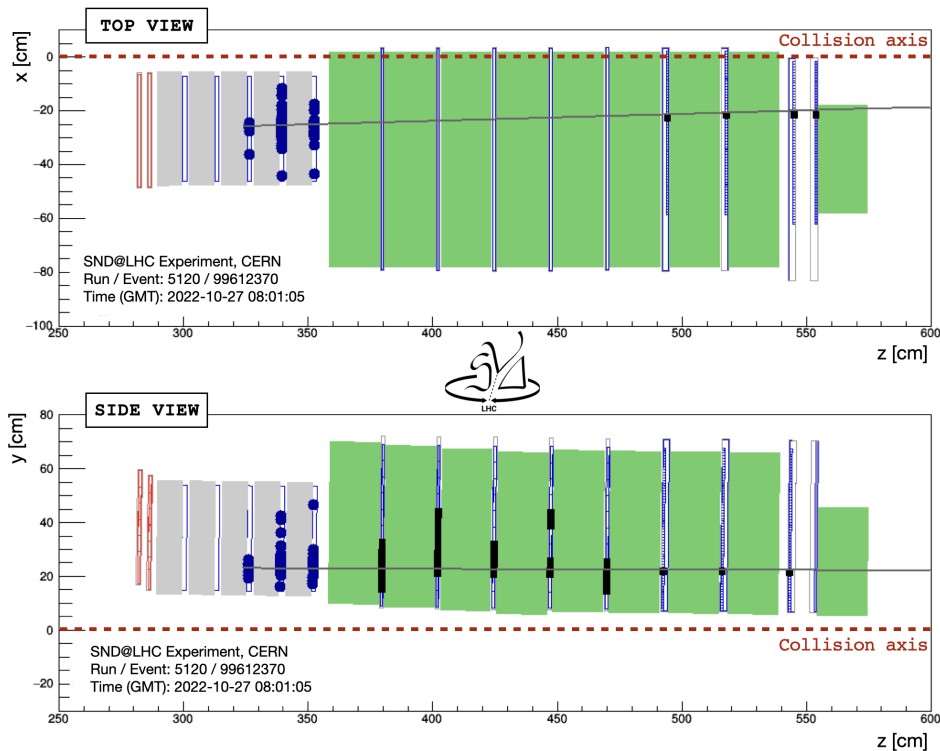
FIGURE 5.4.1: Display of a ν_μ CC candidate event. Hits in the SciFi, and hadronic calorimeter and muon system are shown as blue markers and black bars, respectively, and the line represents the reconstructed muon track.

of $25 \times 26\,\mathrm{cm}^2$. The efficiency of fiducial region cuts on simulated neutrino interactions in the target is 7.5%.

The second step selects signal-like signature patterns using a cut-based procedure. ν_μ CCDIS interactions are associated to a large hadronic activity in the calorimetric system, with a clean outgoing muon track reconstructed in the muon system, and hit time distribution consistent with an event originating from the IP1 direction. The muon track is defined by a set of muon system hits in a straight-line pattern spanning at least three detector planes in both zx and zy views. Events with a large number of hits in the muon system are rejected to ensure cleanly reconstructed tracks.

The achieved reduction factor on the data for the total selection (fiducial and neutrino identification cuts) amounts to 1.0×10^9, while the overall efficiency on the ν_μ CCDIS Monte Carlo sample is 2.9%.

As a result of the full selection, 8 ν_μ CCDIS candidates are identified, while 4.5 are expected. The contribution of other neutrino flavours and neutral current interactions to the selected sample is less than 1% of the expected ν_μ CCDIS yield. One of the selected candidates is shown in Figure 5.4.1. The distribution of the number of hits in the SciFi detector for the selected events is consistent with the neutrino signal expectation, as shown in Figure 5.5.1.

5.5   Background

Muons reaching the detector location are the main source of background for the neutrino search. They can either enter in the fiducial volume without being vetoed and generate showers via bremsstrahlung or deep inelastic scattering, or interact in the surrounding material and produce neutral particles that can then mimic neutrino interactions in the target.

The estimate of the penetrating muon background is based on the expected flux in the fiducial volume and on the inefficiency of detector planes used as veto: the veto system and the two most upstream SciFi planes.

The muon flux at the detector location is estimated by the CERN SY-STI team with simulations of proton-proton interactions at IP1 and the transport of the resulting charged pions and kaons along the LHC straight section until their decay using FLUKA [23, 24]. The simulation includes both the effects of the accelerator optics and of the material traversed by the particles before reaching the detector. The muons are recorded at a scoring plane, $1.8 \times 1.8\,\mathrm{m}^2$, located about 70 m upstream of SND@LHC, 419 m from IP1. The transport of muons from the scoring plane to the detector and their interactions along the way are modelled with a GEANT4 simulation of SND@LHC and its surroundings.

The FLUKA simulation consists of 50 million pp collisions with LHC Run 3 beam conditions and a downward crossing angle of $-160\,\mu\mathrm{rad}$ on the vertical plane, corresponding to the collider configuration in 2022.

The expected muon flux in the fiducial area used in the present analysis ($25 \times 26\,\mathrm{cm}^2$) is $1.69 \times 10^4\,\mathrm{cm}^{-2}/\mathrm{fb}^{-1}$. The measured rate in the same area during the 2022 run amounts to $(2.07 \pm 0.01\,(stat) \pm 0.10\,(sys)) \times 10^4\,\mathrm{cm}^{-2}/\mathrm{fb}^{-1}$, in good agreement with predictions, thus validating the Monte Carlo simulation [30]. The corresponding total number of muons integrated in $36.8\,\mathrm{fb}^{-1}$ therefore amounts to 5.0×10^8, with 4.0×10^8 muons expected.

The inefficiency of the veto system planes is estimated from data by using good quality tracks reconstructed in the SciFi detector and validated with a track segment in the DS detector. The tracks are extrapolated to the veto detector fiducial volume. All tracks are identified as muons due to the large number of interaction lengths traversed; tracks entering the detector from the downstream end are excluded by timing measurements. For the first period of data taking amounting to $23.1\,\mathrm{fb}^{-1}$, the applied time alignment procedure was relatively rough, leading to some physical
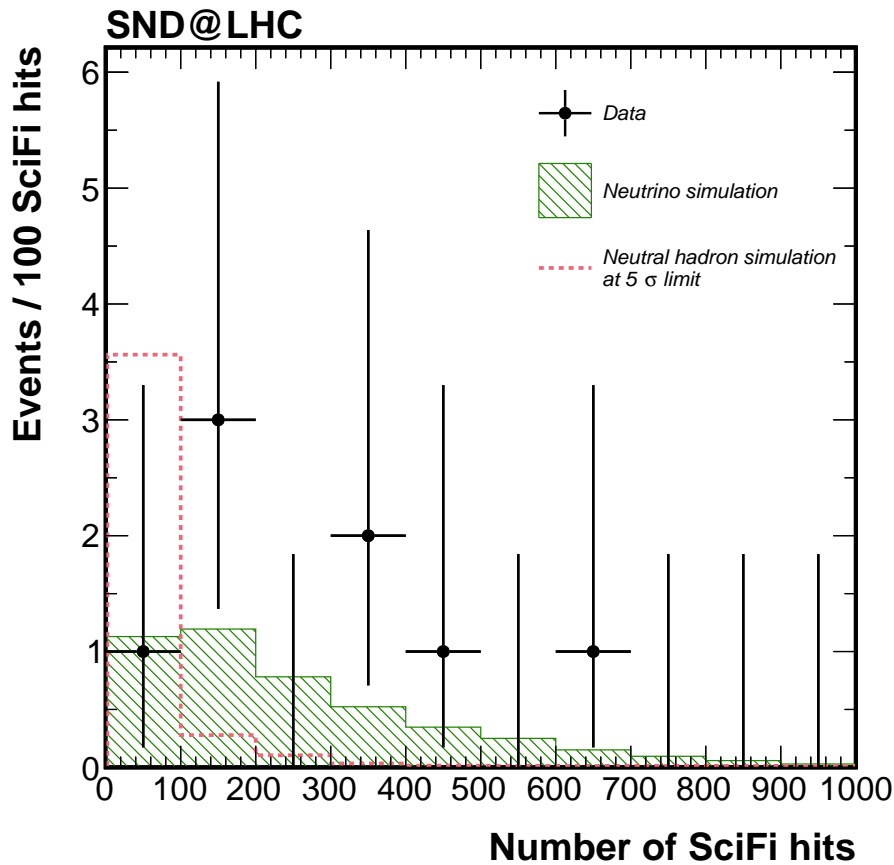
FIGURE 5.5.1: Distribution of SciFi hits for candidate events, along with the expectation from the neutrino signal. The dashed line shows the background-only hypothesis scaled up to a deviation from the nominal expectation at a level of five standard deviations. The vertical bars represent 68.3% confidence intervals of the Poisson means.

events being split into two different recorded events. If one of the two does not contain enough hits to pass the online noise filter, this results in an apparent inefficiency of the detector. Therefore, for this period the measured inefficiency of a single plane is 8×10^{-4}, dominated by this effect.

The problem was fixed at the end of October 2022 and the single-plane inefficiency dropped to 4×10^{-5} [31]. With the same method we have also estimated the inefficiency of the coincidence of the two veto detector planes, amounting to

7.1×10^{-4} in the first period ($23.1\,\mathrm{fb}^{-1}$) and 2.5×10^{-6} in the second period ($13.7\,\mathrm{fb}^{-1}$). The measured inefficiency of the double layer does not scale as the square of the single plane. The apparent correlation between the inefficiency of the two veto detector planes may be due to tracking imperfections in the inefficiency measurement or residual effects of the noise filter, both of which are expected to improve in the future. The overall veto system inefficiency during the 2022 run therefore amounts to 4.5×10^{-4}.

The SciFi detector inefficiency is estimated with a similar method used for the veto detector, using reconstructed SciFi tracks confirmed with a DS track and hits in the veto system. The presence of all SciFi stations is not required in the reconstruction, therefore the inefficiency of the first or second SciFi stations can be extracted. The inefficiency found for each station is 1.1×10^{-4}.

The combined inefficiency of the veto system and the two most upstream SciFi planes is therefore 5.3×10^{-12}, thus making the background induced by muons entering the fiducial volume negligible.

Neutral particles (mainly neutrons and K^0_L's) originating from primary muons interacting in rock and concrete in front of the detector can potentially mimic a neutrino interaction since they do not leave any incoming trace in the electronic detectors, and can create a shower in the target associated with a DS track produced by punch-through or decay-in-flight $\pi^{\pm}$ and $K^{\pm}$. Although they are mainly rejected due to accompanying charged particles originating from the primary muon interaction, they constitute the main background source for the neutrino search.

PYTHIA v6.4 [32] was used to simulate interactions of μ^{+} and μ^{-} on protons or neutrons at rest using the muon spectrum expected at the detector location. These events are placed along the muon flight direction according to the material density, and the secondary particles are transported by GEANT4 in the detector surroundings. Neutral particles induced by muon DIS interact in the rock and concrete and only a small fraction of the particles leaves the tunnel wall and enters the detector. The energy spectrum of neutral hadrons entering the detector is shown in Figure 5.5.2, where the suppression achieved by rejecting events in which accompanying charged particles produce hits in the veto detector is also shown.

To estimate the yield of neutral particles passing the event selection criteria, we simulate the highest energy neutral hadrons entering the target region in a given muon DIS interaction using GEANT4 [33]. The events are simulated with energies within [5, 200] GeV and uniformly distributed across the front face of the detector's target. As shown in Figure 5.5.2, the rate of neutral-hadron events with energies above 100 GeV is heavily suppressed by using the veto system to tag the accompanying charged particles (most often the scattered muon). Below 5 GeV the minimum

ionizing particles resulting from the neutral hadron interactions do not have enough energy to produce a track exiting the downstream end of the detector.

As can be seen in Figure 5.5.1, the lower energy of the neutral hadrons compared to the neutrino signal results in fewer hits in SciFi. We note that while this variable has not been used to reduce the neutral-hadron contamination in the present analysis, it is shown to be a powerful discriminant against this background.

The background yield after the selection amounts to $(7.6 \pm 3.1) \times 10^{-2}$ and is dominated by neutrons and K_L^0s. The systematic uncertainty of 40% on the expected background yield is the combined effect of three sources. Since the neutral hadrons are produced in interactions of muons in the rock, we take as the uncertainty on the muon flux the 22% difference between the simulated and measured flux of muons traversing detector. To estimate the impact of the hadron interaction model on the selection efficiency of these background events, we compare the results of simulations using two GEANT4 physics lists, QSGP_BERT_HP_PEN and FTFP_BERT, corresponding to two
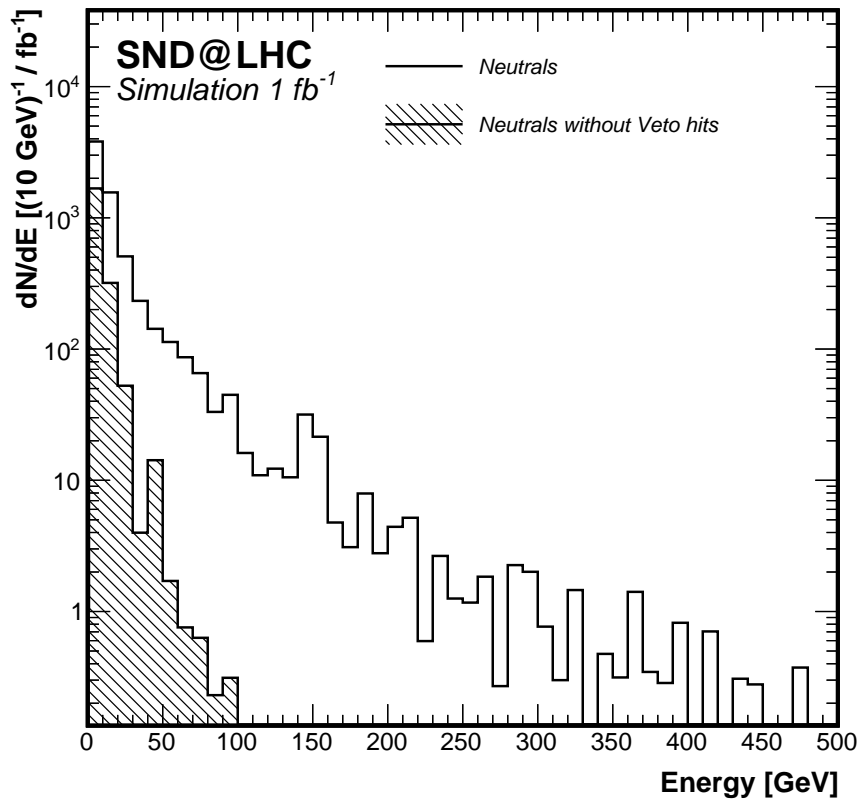
FIGURE 5.5.2: Energy spectrum of neutral hadrons produced by muon interactions in the rock and concrete entering the SND@LHC acceptance. The shaded area shows the spectrum after rejecting events with hits in the veto detector.

rather different hadron-nucleus interaction models, which differ by 22%. Finally, the contribution to the systematic uncertainty due to the available statistics in the simulations is 25%.

5.6 Significance evaluation

The significance of the observation of 8 candidates with an expected background yield of 7.6×10^{-2} is quantified in terms of the exclusion of the null hypothesis, defined by setting the neutrino signal strength, μ to zero.

The one-sided profile likelihood ratio test $\lambda(\mu)$ was used as test statistic. The significance is evaluated by comparing $\lambda_{data}(\mu = 0)$ with the sampling distribution of $\lambda(\mu = 0)$. The likelihood, which includes a Gaussian factor to account for the background uncertainties, is

$$\mathscr{L} = \mathrm{Poisson}(n \,|\, \mu s + \beta) \, \mathrm{Gauss}(\beta \,|\, b, \sigma_b)$$

where n is the number of observed events, s is the expected number of signal events and β is the number of background events given by the Gaussian model, having a mean value b and an uncertainty σ_b.

The implementation of the method based on RooStats[34] results in a p-value of 1.48×10^{-12}, corresponding to an exclusion of the background-only hypothesis at the level of 7.0 standard deviations.

5.7 Conclusions

A search for high energy neutrinos originating from pp collisions at $\sqrt{s} = 13.6\,\mathrm{TeV}$ is presented using data taken by the electronic detectors of SND@LHC. We observe 8 candidate events consistent with ν_μ CC interactions. Our muon-induced and neutral-hadron backgrounds for the analysed data set amount to $(7.6 \pm 3.1) \times 10^{-2}$ events, which implies an excess of ν_μ CC signal events over the background-only hypothesis of seven standard deviations.

References

[1]   A. De Rújula and R. Ruckl. "Neutrino and muon physics in the collider mode of future accelerators". In: *SSC Workshop: Superconducting Super Collider Fixed Target Physics*. May CERN-90-10-V-2, 1984, pp. 571–596. DOI: 10.5170/CERN-1984-010-V-2.571.

[2]   A. De Rújula, E. Fernandez, and J.J. Gomez-Cadenas. "Neutrino fluxes at future hadron colliders". In: *Nucl. Phys. B* 405 (1993), pp. 80–108. DOI: 10.1016/0550-3213(93)90427-Q.

[3]   François Vannucci. *Neutrino physics at LHC/SSC*. Tech. rep. LPNHE-93-03. Paris: Univ. Paris, Aug. 1993. URL: https://cds.cern.ch/record/253670.

[4]   *Large Hadron Collider Workshop: Aachen, Germany 4 - 9 Oct 1990*. Jarlskog, G and Rein, D. TH 3892: CERN, 1990. DOI: 10.5170/CERN-1990-010-V-2. URL: http://cds.cern.ch/record/215298.

[5]   S. Buontempo et al. *CMS-XSEN: LHC Neutrinos at CMS. Experiment Feasibility Study*. Tech. rep. Geneva: CERN, Mar. 2018. arXiv: 1804.04413. URL: https://cds.cern.ch/record/2309742.

[6]   N. Beni et al. "Physics Potential of an Experiment using LHC Neutrinos". In: *J. Phys. G* 46.11 (2019), p. 115008. DOI: 10.1088/1361-6471/ab3f7c. arXiv: 1903.06564 [hep-ex].

[7]   N. Beni et al. "Further studies on the physics potential of an experiment using LHC neutrinos". In: *J. Phys. G* 47.12 (2020), p. 125004. DOI: 10.1088/1361-6471/aba7ad. arXiv: 2004.07828 [hep-ex].

[8]   C. Ahdida et al. *SND@LHC- Scattering and Neutrino Detector at the LHC*. Tech. rep. CERN-LHCC-2021-003, LHCC-P-016. https://cds.cern.ch/record/2750060/files/LHCC-P-016.pdf. Geneva: CERN, 2021.

[9]   R. Brock et al. "Handbook of perturbative QCD: Version 1.0". In: *Rev. Mod. Phys.* 67 (1995), p. 157. URL: https://doi.org/10.1103/RevModPhys.67.157.

[10] J.M. Conrad, M.H. Shaevitz, and T. Bolton. "Precision measurements with high-energy neutrino beams". In: *Rev. Mod. Phys.* 70 (1998), p. 1341. URL: https://doi.org/10.1103/RevModPhys.70.1341.

[11] J.A. Formaggio and G.P. Zeller. "From eV to EeV: Neutrino Cross Sections Across Energy Scales". In: *Rev. Mod. Phys.* 84 (2012), p. 1307. URL: https://doi.org/10.1103/RevModPhys.84.1307.

[12] G. De Lellis, P. Migliozzi, and P. Santorelli. "Charm physics with neutrinos". In: *Phys. Rept.* 399 (2004), p. 227. URL: https://doi.org/10.1016/j.physrep.2004.07.005.

[13] D. Marfatia, D.W. McKay, and T.J. Weiler. "New physics with ultra-high-energy neutrinos". In: *Phys. Lett. B* 748 (2015), p. 113. URL: https://doi.org/10.1016/j.physletb.2015.07.002.

[14] C.A. Argüelles et al. "New opportunities at the next-generation neutrino experiments I: BSM neutrino physics and dark matter". In: *Reports on Progress in Physics* 83 (2020), p. 124201. URL: https://doi.org/10.1088/1361-6633/ab9d12.

[15] M. Bustamante et al. "Extracting the Energy-Dependent Neutrino-Nucleon Cross Section above 10 TeV Using IceCube Showers". In: *Phys. Rev. Lett.* 122 (2019), p. 041101. URL: https://doi.org/10.1103/PhysRevLett.122.041101.

[16] SND@LHC Collaboration. *SND@LHC: The Scattering and Neutrino Detector at the LHC*. 2023. arXiv: 2210.02784 [hep-ex].

[17] ATLAS Collaboration. "Luminosity determination in pp collisions at $\sqrt{s} = 8$ TeV using the ATLAS detector at the LHC". In: *Eur. Phys. J. C* 76.12 (2016), p. 653. DOI: 10.1140/epjc/s10052-016-4466-1. arXiv: 1608.03953 [hep-ex].

[18] H. Abreu et al. *First Direct Observation of Collider Neutrinos with FASER at the LHC*. 2023. arXiv: 2303.14185 [hep-ex].

[19] ELJen. *EJ-200*. https://eljentechnology.com/products/plastic-scintillators/ej-200-ej-204-ej-208-ej-212. accessed January 22, 2022.

[20] Akitaka Ariga et al. "Nuclear Emulsions". In: *Particle Physics Reference Library: Volume 2: Detectors for Particles and Radiation*. Ed. by Christian Wolfgang Fabjan and Herwig Schopper. Elsevier, 2020, pp. 383–438. DOI: 10.1007/978-3-030-35318-6_9.

[21] LHCb Collaboration. *LHCb Tracker Upgrade Technical Design Report*. Tech. rep. CERN-LHCC-2014-001, LHCB-TDR-015. Geneva: CERN, 2014. URL: http://cds.cern.ch/record/1647400.

[22] ATLAS Collaboration. *Luminosity determination in pp collisions at $\sqrt{s} = 13$ TeV using the ATLAS detector at the LHC*. Dec. 2022. arXiv: 2212.09379 [hep-ex].

[23] G. Battistoni et al. "Overview of the FLUKA code ". In: *Annals of Nuclear Energy* 82 (2015), pp. 10–18.

[24] C. Ahdida et al. "New Capabilities of the FLUKA Multi-Purpose Code". In: *Front. in Phys.* 9 (2022), p. 788253. DOI: 10.3389/fphy.2021.788253.

[25] Stefan Roesler, Ralph Engel, and Johannes Ranft. "The Monte Carlo event generator DPMJET-III". In: *Advanced Monte Carlo for radiation physics, particle transport simulation and applications. Proceedings, Conference, MC2000, Lisbon, Portugal, October 23-26, 2000*. 2000, p. 1033. DOI: 10.1007/978-3-642-18211-2_166. arXiv: hep-ph/0012252 [hep-ph]. URL: http://www-public.slac.stanford.edu/sciDoc/docMeta.aspx?slacPubNumber=SLAC-PUB-8740.

[26] A. Fedynitch. "Cascade equations and hadronic interactions at very high energies". In: *CERN-THESIS-2015-371 https://cds.cern.ch/record/2231593* (2015).

[27] V. Boccone et al. "Beam-machine Interaction at the CERN LHC". In: *Nucl. Data Sheets* 120 (2014), pp. 215–218. DOI: 10.1016/j.nds.2014.07.050.

[28] C. Andreopoulos et al. "The GENIE Neutrino Monte Carlo Generator". In: *Nucl. Instrum. Meth. A* 614 (2010), p. 87. DOI: 10.1016/j.nima.2009.12.009. arXiv: 0905.2517 [hep-ph].

[29] Felix Kling and Laurence J. Nevay. "Forward neutrino fluxes at the LHC". In: *Phys. Rev. D* 104.11 (2021), p. 113008. DOI: 10.1103/PhysRevD.104.113008. arXiv: 2105.08270 [hep-ph].

[30] S. Ilieva. *Muon flux measurement with electronic detectors*. Tech. rep. CERN-SND@LHC-ANA-2023-002. In preparation. Geneva: CERN, 2023.

[31] T. Ruf. *SciFi Veto detector inefficiency*. Tech. rep. CERN-SND@LHC-ANA-2023-003. In preparation. Geneva: CERN, 2023.

[32] Torbjorn Sjostrand, Stephen Mrenna, and Peter Z. Skands. "PYTHIA 6.4 Physics and Manual". In: *JHEP* 05 (2006), p. 026. DOI: 10.1088/1126-6708/2006/05/026. arXiv: hep-ph/0603175 [hep-ph].

[33] S. Agostinelli et al. "GEANT4: A Simulation toolkit". In: *Nucl. Instrum. Meth. A* 506 (2003), p. 250. DOI: 10.1016/S0168-9002(03)01368-8.

[34] Lorenzo Moneta et al. "The RooStats Project". In: *PoS* ACAT2010 (2010). Ed. by T. Speer et al., p. 057. DOI: 10.22323/1.093.0057. arXiv: 1009.1003 [physics.data-an].

Part III

The Intensity Frontier

Chapter 6

Sensitivity of the SHiP experiment to light dark matter

Contents

Dark matter is a well-established theoretical addition to the Standard Model supported by many observations in modern astrophysics and cosmology. In this context, the existence of weakly interacting massive particles represents an appealing solution to the observed thermal relic in the Universe. Indeed, a large experimental campaign is ongoing for the detection of such particles in the sub-GeV mass range. Adopting the benchmark scenario for light dark matter particles produced in the decay of a dark photon, with $\alpha_D = 0.1$ and $m_{A'} = 3m_\chi$, we study the potential of the SHiP experiment to detect such elusive particles through its Scattering and Neutrino detector (SND). In its 5-years run, corresponding to $2 \cdot 10^{20}$ protons on target from the CERN SPS, we find that SHiP will improve the current limits in the mass range for the dark matter from about 1 MeV to 300 MeV. In particular, we show that SHiP will probe the thermal target for Majorana candidates in most of this mass window and even reach the Pseudo-Dirac thermal relic.

6.1 Introduction

One of the main challenges in particle physics today is figuring out the microscopic identity and the cosmological origin of dark matter (DM). The theoretical landscape is broad and it spans over many orders of magnitude in the mass/coupling parameter space. A compelling idea to explore is DM as a thermal relic of the early universe. The canonical example of this scenario is the Weakly Interacting Massive Particle (WIMP), a particle in the GeV-TeV mass range interacting with the visible sector via weak-sized interactions. Searches for WIMPs are in full swing [1, 2]: however, the interesting parameter space goes beyond that has been explored in the past decade: thermal DM can be as heavy as 100 TeV or as light as a few keV. Recently, a lot of attention has been directed towards light DM (LDM) in the keV-GeV mass range [3].

Direct detection has traditionally employed the Migdal Effect [4] using liquid Argon [5, 6] or liquid Xenon [7–10], while a novel strategy based on silicon devices has allowed to design new experiments optimised for sub-GeV DM, as SENSEI [11]. Since current DM direct detection experiments searching for elastic nuclear recoils rapidly lose sensitivity once the candidate mass drops below a few GeV [1, 12], experiments at the intensity frontier represent an alternative yet appealing route and play an important role in this quest [3]. Fixed target experiments represent the prototype for such searches, although other collider experiments might be relevant in the same parameter space, as showed by the mono-photon searches at BaBar [13] and Belle II [14].

In particular, neutrino fixed target experiments could efficiently search for LDM via signatures of DM scattering with electrons and/or nuclei in their near detectors [15–26].

Here we present the sensitivity of the SHiP scattering and neutrino detector (SND), to LDM. We focus on the hypothesis that the DM couples to the SM through the exchange of a massive vector mediator, dubbed in the literature dark photon, and we have considered the cleanest signature given by the LDM-electron scattering. The scattering with nuclei, both coherent and deep inelastic scattering, although plagued by a larger neutrino background, might be an alternative detection strategy and will be the subject of a forthcoming dedicated analysis.

In a proton beam dump experiment signal yields are largely reduced as the interaction with the dark photon A' is probed twice, if compared to electron fixed target experiments which make use of search strategies based on missing energy, such as NA64 [27], or missing momentum, such as the LDMX proposal [28]. Indeed, the LDM detection is achieved through its scattering within the downstream detector. Hence, the expected LDM yield scales as $\epsilon^4 \alpha_D$ (ϵ being the interaction strength of the dark photon to SM particles and α_D the LDM-A' coupling), where a factor ϵ^2 comes from production and another $\epsilon^2 \alpha_D$ is due to detection. This has to be compared to the ϵ^2 scaling of typical missing energy/momentum experiments, which prove however to be not sensitive to LDM coupling constant α_D. Due to their higher penetrating power and enhancements from meson decay reactions and/or strong interactions, proton beams are characterised by dark photon production rates larger than the ones achievable in electron beams of comparable intensity, which in part compensate for the detection suppression factor.

The potential to directly probe the dark sector mediator coupling α_D, together with a wider sensitivity which encompasses other viable dark matter models, shows to a large extent the complementarity between the two approaches. This is even a more pressing aspect in the light of a possible discovery, as in general the observation of an excess alone is not sufficient to claim a discovery of a Dark matter particle. Indeed, intensity frontier probes do not depend on whether the particle χ produced through prompt DP decay is DM or not, as the only necessary ingredient is its stability concerning the target-detector distance. The observed excess might have an instrumental origin rather than a genuine New Physics (NP) effect. This applies also to the constraints that the SHiP experiment can place. With this regard, invaluable contribution could come from complementary DM observations from a cosmic source to unequivocally probe its thermal origin. In addition, since the SHiP experiment has a direct sensitivity to LDM interactions, we anticipate the possibility to use the time of flight measurement to uncontroversially discriminate massive NP particles from the SM neutrino background.

The paper is organised as follows: in Section 6.2 we give a brief presentation of the model focusing on the main motivations. After introducing the SHiP experiment in Section 6.3, we discuss the relevant production and detection mechanisms, in Section 6.4. The detailed analysis of the neutrino background is the topic of Section 6.5. We then pass to the discussion of the signal reviewing the main processes taken into account in our simulation. Finally, we show the main results on the sensitivity reach of the SHiP experiment in Section 6.6 and we give our conclusions in Section 6.7.

6.2 Vector Portal

Thermal freeze-out can naturally explain the origin of the DM relic density for a sub-GeV particle provided the interaction with the visible sector is mediated by a new light force carrier [2, 29]. Here, we will consider as benchmark model the dark photon (DP) [30] vector portal where the DP A'_μ, is the gauge boson of a new dark gauge group $U(1)_D$ kinetically mixed with the photon, and a scalar χ charged under $U(1)_D$ that serves as a DM candidate. Then, the low-energy effective Lagrangian describing the DM reads

$$\mathscr{L}_{\rm DM} = \mathscr{L}_{A'} + \mathscr{L}_\chi \tag{6.1}$$

where:

$$\mathscr{L}_{A'} = -\frac{1}{4}F'_{\mu\nu}F'^{\mu\nu} + \frac{m_{A'}^2}{2}A'^\mu A'_\mu - \frac{1}{2}\epsilon F'_{\mu\nu}F^{\mu\nu}, \tag{6.2}$$

where ϵ is the DP-photon kinetic mixing parameter and $m_{A'}$ is the mass of the DP while:

$$\mathscr{L}_\chi = \frac{ig_D}{2}A'^\mu J^\chi_\mu + \frac{1}{2}\partial_\mu\chi^\dagger\partial^\mu\chi - m_\chi^2\chi^\dagger\chi, \tag{6.3}$$

where $J_\mu^\chi = \left[(\partial_\mu \chi^\dagger)\chi - \chi^\dagger \partial_\mu \chi\right]$, g_D is the $U(1)_D$ gauge coupling and m_χ is the mass of the dark matter particle. The region of the parameter space relevant for χ searches at beam-dump facilities corresponds to $m_{A'} > 2m_\chi$ and $g_D \gg \epsilon e$ which implies $BR(A' \to \chi \chi^\dagger) \sim 1$.

In case χ is DM, precise measurements of the temperature anisotropies of the cosmic microwave background (CMB) radiation significantly constraint the parameter space. In particular, they rule out Dirac fermions with mass below 10 GeV as a thermal DM candidate and more in general every DM candidate that acquires its relic abundance via s-wave annihilation into SM particles [31, 32]. Hence, a complex scalar dark matter candidate χ is safe from such constraints as well as a Majorana or Pseudo-Dirac fermion. Tighter bounds come instead from the Planck measurement of the effective number of neutrino species N_{eff} [32] and rule out the minimal DP model considered here if the complex scalar is lighter than 9 MeV [33].

In order to show the region of parameter space relevant for thermal freeze-out, we will present the SHiP sensitivity in the (m_χ, Y) plane where Y is defined as:

$$Y \equiv \epsilon^2 \alpha_D \left(\frac{m_\chi}{m_{A'}}\right)^4, \qquad \alpha_D = \frac{g_D^2}{4\pi}. \tag{6.4}$$

In the assumption $m_{A'} > 2m_\chi$, the parameter Y is linked to the DM annihilation cross section via the formula [34]:

$$\sigma(\chi \bar{\chi} \to f \bar{f}) v \propto \frac{8\pi v^2 Y}{m_\chi^2}, \tag{6.5}$$

where v is the relative velocity between the colliding DM particles.

6.3 The SHiP experiment

The Search for Hidden Particles (SHiP) experiment has been proposed as a general-purpose experiment [35] at the CERN Super-Proton-Synchrotron (SPS), addressed to explore the high-intensity frontier for NP searches, thus complementing the LHC research program [35]. It is particularly targeted at the observation of long-lived weakly interacting particles of mass below 10 GeV/c^2, foreseen in many Standard Model (SM) extensions. The use of a beam-dump facility [36] will result in a copious flux of charmed hadrons, from which not only hidden sector particles originate [37], but also tau neutrinos and their corresponding anti-particles. Therefore, being also a neutrino factory, SHiP will perform a wide neutrino physics program, as well as a first direct observation of the tau anti-neutrino, which represents the last particle to be directly observed to complete the SM framework. The SHiP Scattering Neutrino Detector (SND) is an apparatus designed for LDM particles searches, since it exploits an optimised combination of a dense target and high-granularity scattering detector, being it based on nuclear emulsion technology. In Fig. 6.3.1 a sketch of the experimental facility as currently implemented in the official simulation framework of the experiment FairShip [38] is shown. A synthetic overview of the simulated processes within FairShip and corresponding simulation software is reported in Tab. 6.3.1.
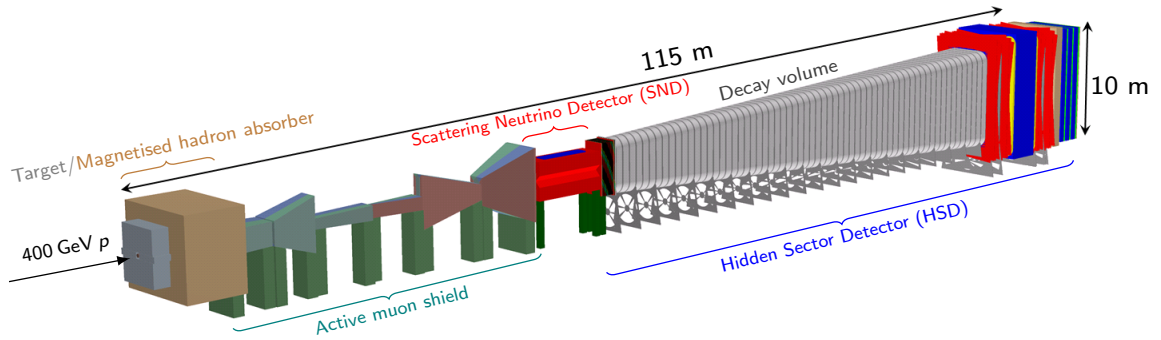
FIGURE 6.3.1: Overview of the SHiP experimental layout.
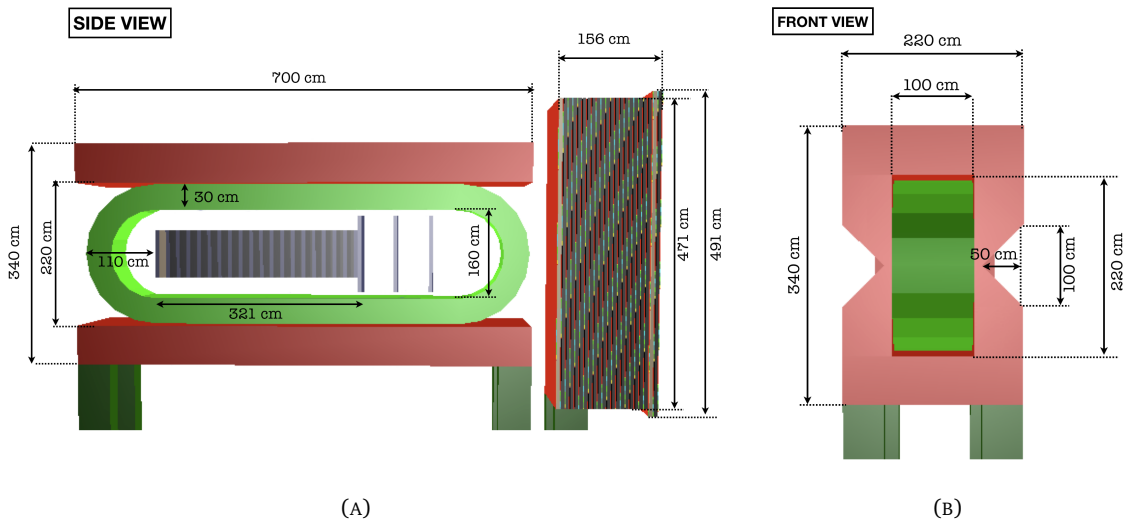
FIGURE 6.3.2: Side (a) and front (b) views of the Scattering Neutrino Detector layout adopted for this study, with a detail of the magnet (red) and of the coil (green).

A 400 GeV/c proton beam will be delivered onto a thick heavy-metal hybrid target, specifically designed to maximise the charm production yield and thus hidden sector particles and tau neutrino yields. Over five years of SPS operations, a total of 2×10^{20} protons on target (*p.o.t.*) collisions will be delivered, where each proton spill will have nominally 4×10^{13} *p.o.t.*. A hadron stopper follows the beam-dump target, with the goal to absorb the SM particles produced in the beam interaction. In addition, a series of sweeping magnets, referred to as Muon Shield [39], act as a deflecting device for the residual muons, further cleaning the flux of particles from leftover backgrounds to hidden sector particles and neutrino searches.

The SND, shown in Fig. 6.3.2 in the setup adopted for this study, is located downstream of the muon sweeper. Placed in a magnetised region of 1.2 Tesla in the horizontal direction and perpendicular to the beam axis [40], it consists of a $(90 \times 75 \times 321)$ cm^3 high-granularity tracking device which exploits the Emulsion Cloud Chamber (ECC) technique developed by the OPERA experiment [41],

which was successfully used for tau neutrino detection [42, 43]. Each elementary unit of the modular detector, called brick (Fig. 6.3.3), consists of alternating 56 lead plates of 1 mm thickness, passive material to increase the interaction probability, and 57 nuclear emulsion films of 0.3 mm thickness, acting as tracking detector with micro-metric accuracy. It is worth noting that the brick also functions as a high-granularity sampling calorimeter with more than five active layers for every radiation length X_0 over a total thickness of $10 X_0$ [44]. The ECC technology is also particularly efficient in the e/π^0 separation. The Compact Emulsion Spectrometer (CES), made up of a sequence of emulsion films and air gaps, is attached immediately downstream of the brick for electric charge measurement for particles not reaching the spectrometer. Despite the magnetic field, electron charge measurement is not possible due to early showering happening within the brick and the consequent information loss. The resulting weight of each ECC brick is approximately 8.3 kg, adding up to ~ 8 tons for the whole SND. The bricks are then assembled to shape 19 walls of ~ 50 units each, alternated with planes of electronic detector, called Target Tracker (TT), planes. For the time being, we consider the SciFi detector [45] as a feasible TT technological option. The TT additionally provide the time stamp of the event and help in linking the emulsion tracks to those reconstructed in the spectrometer and the muon system downstream of the SND. These features make the SND perfectly tailored for neutrino physics using all three flavours, as well as detection of light dark matter particles scattering off of electrons and nuclei of the SND.

An approximately 50 m long vacuum decay vessel is positioned downstream of the SND. The proposed facility is completed with a Hidden Sector Detector (HSD), equipped with calorimeters and muon detectors for the identification of long-lived Beyond Standard Model (BSM) particles.

Simulation	Software
SHiP detector: geometry and transport	`GEANT4` [46]
Proton on target collisions	`PYTHIA v8.2` [47]
Heavy flavour cascade production	`PYTHIA v6.4` [48]
Neutrino interactions	`GENIE` [49]

TABLE 6.3.1: Details of the different steps of the simulation process within the FairShip framework and corresponding employed software.

6.4   Light dark matter production and detection

At a proton beam dump, DP can be abundantly produced in several channels:

1. *Light meson decay*: proton collisions on a heavy target result in a copious flux of outgoing mesons. Hence, DP may be produced in radiative decays of neutral mesons, whereas a final state photon converts into a DP. The production cross-section is proportional to ϵ^2 and the relevant contributions come from the lightest mesons, because of decay modes with photons with relatively high branching ratio: π^0, η, ω [15].
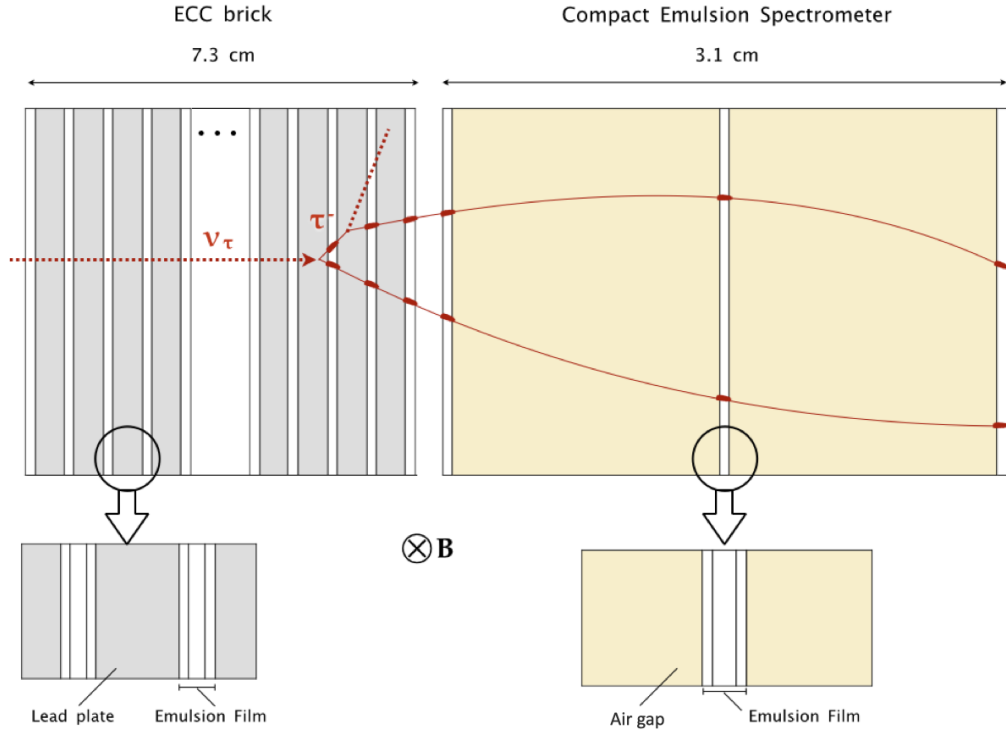
FIGURE 6.3.3: Schematic illustration of the basic unit of the Scattering Neutrino Detector and the ECC brick: on the left, emulsion films interleaved with lead plates; on the right, the Compact Emulsion Spectrometer.

2. *Proton bremsstrahlung*: being a charged particle surrounded by its own electromagnetic field, the proton radiates low-frequency and/or quasi-collinear photons with high probability when it undergoes a scattering process. Vector states like DP mediators can then be generated via radiative process $pA \rightarrow pAA'$ [50] in proton interactions with the target nuclei.

3. *Direct perturbative QCD production*: it corresponds to the dominant production mechanism for higher masses ($m_{A'} \gtrsim 1\,\text{GeV}$). At the lowest order in the strong interaction, DP are produced through the quark-antiquark annihilation process $q\bar{q} \rightarrow A'$ [15]. At higher orders, one can also have the associated production with a jet, according to the the quark-gluon scattering process $qg \rightarrow qA'$, and with multiple jets.

In addition, secondary leptons produced in the dump can contribute to the flux of photons, and thereby of DPs, by different re-scattering processes occurring within the target. Such lepton-induced processes are usually sub-dominant at a proton beam dump. However, they are not completely negligible, as nicely shown in a the dedicated analysis [51], and might be relevant in scenarios in which the New Physics does not couple with colour particles. We do not include them in this work. Therefore, our estimates should be considered conservative in this regard. The minimal DP model can be probed by the SHiP experiment through the direct detection of LDM elastic

scattering process off of the electrons and nuclei of the SND (Fig. 6.4.1) For the majority of the
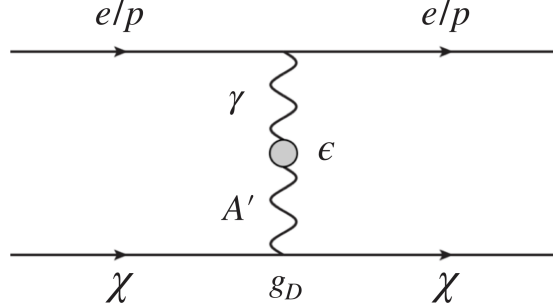
FIGURE 6.4.1: Light dark matter interaction processes which can be probed by the SHiP experiment within the Scattering Neutrino Detector, *i.e.* elastic scattering off electrons ($\chi\, e^- \to \chi\, e^-$) and off protons ($\chi\, p \to \chi\, p$).

events $\chi\, e^- \to \chi\, e^-$, the scattered electron is sufficiently energetic to generate an electromagnetic shower within the brick. Given that the ECC device acts as a high-granularity sampling calorimeter, it is thus possible to reconstruct the electron and measure its energy. Furthermore any activity in the proximity of the primary vertex can be spotted down to 100 MeV or below, thanks to the micrometrical position resolution of the nuclear emulsion device and the high sampling rate. These features translate into capability to accurately identify and tackle background events to LDM searches, as further described in Sec. 6.5. As a consequence, LDM scattering events can be distinguished from a large neutrino-induced background.

An estimate of the order of magnitude of the expected yield of LDM interactions at SHiP can be determined as follows. The number of LDM-electron scattering events in the SND detector is given by the standard formula

$$\mathcal{N}_{\text{LDM}} = \sigma(\chi\, e^- \to \chi\, e^-) \cdot \frac{\phi}{A_{\text{SND}}} \cdot N_{e^-}, \tag{6.6}$$

where N_{e^-} is the numbers of scattering centres, *i.e.* the electrons in the detector, ϕ is the flux of incident LDM particles and A_{SND} represents the transverse area in (x, y) of the SND. The elastic LDM-electron scattering cross section is roughly given by

$$\sigma(\chi\, e^- \to \chi\, e^-) \simeq \frac{4\,\pi\,\alpha\,\alpha_D\,\epsilon^2}{m_{A'}^2}. \tag{6.7}$$

The flux ϕ mainly depends on the specific value of the DP mass which in turn determines the relative importance of the different production mechanisms. For example, for $m_{A'} \ll m_\pi$, LDM production in the beam dump is dominated by pion decays. In this case and under the assumption that all the primary proton impinging on the target will eventually interact in the beam dump, ϕ can be written as

$$\phi \simeq 2 \cdot N_{p.o.t} \cdot \lambda_{\pi^0} \cdot \epsilon^2 \cdot \mathcal{A}_{\text{geo}}. \tag{6.8}$$
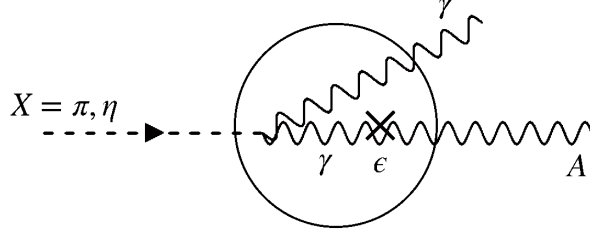
FIGURE 6.4.2: Effective vertex for the decay process $X \to \gamma A'$, $X = \pi^0, \eta$.

In Eq. (6.8), $N_{p.o.t.}$ is the total number of $p.o.t.$ delivered in the five years of data-taking; λ_{π^0} denotes the multiplicity of π^0s per $p.o.t.$; $\mathscr{A}_{\text{geo}}$ embeds the geometrical acceptance of the SND to LDM interaction vertices, corresponding to an angular coverage $|(\theta_x, \theta_y)| \leq (12, 10)$ mrad from the proton beam dump. If considering an average value of $\lambda_{\pi^0} \sim 6$ as provided by the simulation of prompt proton-nucleon collisions with Pythia[1] [47], a geometrical acceptance $A_{geo} \sim 30\%$ and if assuming a coupling close to the current experimental constraints $\epsilon \sim 5 \times 10^{-5}$ for a 10 MeV-DP and $\alpha_D \sim 0.1$, the expected number of LDM candidates foreseen in SHiP is $\sim 1.3 \times 10^4$.

We used MadDump [52] as the principal tool for the simulation of signal events. Its general philosophy and all the technical details are outlined in Ref. [52]. We generate the event samples at the particle level and apply the selection criteria on the recoil electrons without taking into account other detector effects besides the geometrical acceptance. This is consistent with what has been done in the estimate of the background event rate. Since the target length is way larger than the proton interaction length in the material, we assume all of them to interact within the beam dump. In the following, we give further details for each production mechanism.

6.4.1 Meson decay

The relevant parameter space within the reach of the SHiP SND corresponds to $m_{A'} > 2m_\chi$ and $g_D \gg \epsilon e$. Indeed, in this scenario, the DP decays almost entirely into DM after travelling a very short distance, maximising the DM flux reaching the SHiP SND. The decay rate for light mesons decaying into dark photons is then dominated by the formation of an on-shell dark photon which decays promptly into dark matter, $BR(A' \to \chi\bar{\chi}) \simeq 1$. The production process is then well described by an effective Lagrangian with mesons as dynamical degrees of freedom leading to interaction vertices like $X\gamma A'$ ($X = \pi^0, \eta$, see Fig. 6.4.2) and $\omega\pi^0 A'$. The corresponding branching ratios scale with ϵ^2 and are given by:

$$\frac{\text{BR}(\pi^0, \eta, \eta' \to \gamma A')}{\text{BR}(\pi^0, \eta, \eta' \to \gamma\gamma)} \simeq 2\,\epsilon^2 \left(1 - \frac{m_{A'}^2}{m_{\pi^0,\eta,\eta'}^2}\right)^3 \tag{6.9}$$

$$\frac{\text{BR}(\omega \to \pi^0 A')}{\text{BR}(\omega \to \pi^0 \gamma)} \simeq \epsilon^2 \left(m_\omega^2 - m_\pi^2\right)^{-3} \left[(m_{A'}^2 - (m_\pi + m_\omega)^2)(m_{A'}^2 - (m_\pi - m_\omega)^2)\right]^{3/2}. \tag{6.10}$$

---

[1]We use Pythia(v8.230) and simulate events under the flag *SoftQCD:Inelastic*.

An interested reader can find useful insights about the formulas above in [16, 53, 54]. The full simulation process is performed in three steps:

  i. production of the input meson fluxes originating from the incoming protons impinging and interacting within the target (beam dump)

  ii. generation of DM fluxes from the BSM meson decays in the relevant DM mass range

  iii. generation of the corresponding $DM - e^-$ scattering events within the detector acceptance and the selection criteria.

MadDump provides a unified framework to handle the last two steps, in which all the new physics content is involved. The main source of uncertainties comes from the meson fluxes. Indeed, the description of the proton-nucleus interactions is highly non-trivial and experimental data are available only for a limited collection of energies and nuclear targets. Phenomenological and data-driven parametrisations for the distributions of the light mesons have been proposed in the literature [55]. An alternative strategy is provided by Monte Carlo programs like `Pythia` [47]. Recently, `Pythia(8)` results have been compared with existing experimental data for the inclusive production of π^0 and η mesons in pp collisions [56]. A fairly good agreement has been found for mesons with high momentum and within middle-high rapidity range (where the Feynman variable $0.025 < x_F < 0.3$), which represent the bulk of our events in acceptance.

Furthermore, secondary interactions of hadrons in the beam-dump target may affect the particle multiplicities, which in turn may increase the LDM yields and impact the sensitivity reach of the experiment. It is thus important to estimate the so-called cascade effects [57]. As the main input for the lightest mesons (π^0, η) we use the fluxes generated with `GEANT4(v10.3.2)` within the FairShip software framework, which takes into account the secondary interactions adapting what has been used in Ref. [58]. We also consider samples of mesons from primary proton-nucleon interactions generated with `Pythia`, as a reference to assess the impact of the cascade. For the ω, we rely on the `Pythia` samples only.

In Tables 6.4.1, 6.4.2 and 6.4.3, we report a selection of results for π^0 and η, comparing the FairShip and `Pythia` samples. An important parameter in the FairShip simulation is the energy cut-off E_{cut} applied to the particles produced at each interaction vertex: particles with energy less than E_{cut} are removed from the list of those considered for new interactions within the target. We report the result for $E_{cut} > 500\,\text{MeV}$. Primary proton-proton interactions, as generated with `Pythia`, give an average particle multiplicity per *p.o.t.* of $N_{\pi^0}/p.o.t. = 6$ and $N_\eta/p.o.t. = 0.8$, for π^0 and η respectively. From the samples of mesons generated with FairShip, we get $N_{\pi^0}/p.o.t. = 42$ and $N_\eta/p.o.t. = 5.5$. Therefore, we observe that secondary interactions occurring within the beam-dump target greatly increase the particle multiplicities and, in turn, lead to a rise of the DM yield by the same amount. However, this does not translate directly into an enhancement of the signal yield in the SND. Indeed, in order to produce a detectable scattering event one should take into account

  • the geometrical acceptance,

- the path travelled within the detector,

- the cross section for the scattering process.

We consider separately the effect due to the geometrical acceptance, defining an effective number of mesons per *p.o.t.* $N_X^{\text{eff}}/p.o.t.$ as the average number of mesons of species X per *p.o.t.* which produce a DM particle impinging on the detector surface. For different $m_{A'}$ values, we report in Tables 6.4.2 and 6.4.3 our estimate of $N_{\pi^0}^{\text{eff}}/p.o.t.$ and $N_{\eta}^{\text{eff}}/p.o.t.$ as estimated with `Pythia` and FairShip. The comparison shows that the increase due to the cascade is around $50 - 70\%$. The explanation is that the secondary particles mainly populate the soft part of the spectrum, as it is clearly shown in the left panels of Fig. 6.4.3 and Fig. 6.4.4 which have to be compared with the corresponding right panels describing the spectrum from prompt yields. Moreover, the cross section for the elastic LDM-e^- scattering grows with the energy of the incoming dark-matter particle before saturating to a constant behaviour [59]. Hence, we expect that scattering events initiated by LDM particles produced in secondary interactions, being softer, will be less probable. This is clearly demonstrated by the last two columns in Tables 6.4.2 and 6.4.3 in which we report the final signal yields N_s (corresponding to the benchmark point $\alpha_D = 0.1$ and $m_{A'} = 3m_\chi$ and $\epsilon = 10^{-4}$) due to FairShip and `Pythia` samples respectively. From the comparison, we see that the impact of the secondary interactions is reduced to that given by the geometrical acceptance only. In conclusion, our finding is that for π^0, the cascade modestly affects ($\sim 15 - 40\%$) the signal event yields within the detector volume, while for η it is negligible.

meson	$N_{\pi^0}/p.o.t.$ FairShip	$N_{\pi^0}/p.o.t.$ `Pythia`
π^0	42	6
η	5.5	0.8

TABLE 6.4.1: Average particle multiplicities per *p.o.t.* in 400 GeV proton collisions as estimated with FairShip, applying a cut-off $E_{\text{cut}} > 500$ MeV on secondary particles, and with `Pythia`, for primary interactions only.

$m_{A'}$ (MeV)	$N_{\pi^0}^{\text{eff}}/p.o.t.$ (FairShip)	$N_{\pi^0}^{\text{eff}}/p.o.t.$ (`Pythia`)	N_s (FairShip)	N_s (`Pythia`)
10	1.2	0.80	$1.7 \cdot 10^4$	$1.3 \cdot 10^4$
30	1.1	0.72	$8.6 \cdot 10^3$	$7.3 \cdot 10^3$
60	0.70	0.46	$2.0 \cdot 10^3$	$1.8 \cdot 10^3$
90	0.24	0.15	$3.1 \cdot 10^2$	$2.5 \cdot 10^2$
120	0.013	0.0083	7.4	6.7

TABLE 6.4.2: Comparison between π^0 samples generated using FairShip (with an energy cut of $E_{\text{cut}} > 500$ MeV in secondary vertices) and `Pythia`. $N_{\pi^0}^{\text{eff}}/p.o.t.$ is the effective number of π^0s per p.o.t. producing LDM particles within the geometrical acceptance. N_s is the signal yield for the benchmark point $\alpha_D = 0.1$ and $m_{A'} = 3m_\chi$ and $\epsilon = 10^{-4}$ corresponding to $2 \cdot 10^{20} p.o.t.$

$m_{A'}$ (MeV)	$N_\eta^{\text{eff}}/p.o.t.$ (FairShip)	$N_\eta^{\text{eff}}/p.o.t.$ (Pythia)	N_s (FairShip)	N_s (Pythia)
10	0.15	0.10	$1.1 \cdot 10^3$	$8.1 \cdot 10^2$
130	0.13	0.092	25	24
250	0.099	0.059	1.6	1.5
370	0.033	0.020	$1.16 \cdot 10^{-1}$	$1.15 \cdot 10^{-1}$
520	0.00020	0.00012	$1.9 \cdot 10^{-4}$	$1.8 \cdot 10^{-4}$

TABLE 6.4.3: Comparison between η samples generated using FairShip (with an energy cut of $E_{\text{cut}} > 500\,\text{MeV}$ in secondary vertices) and `Pythia`. $N_{\pi^0}^{\text{eff}}/p.o.t.$ is the effective number of ηs per p.o.t. which give raise to LDM particles within the geometrical acceptance. N_s is the LDM yield for the benchmark point $\alpha_D = 0.1$ and $m_{A'} = 3m_\chi$ and $\epsilon = 10^{-4}$ corresponding to $2 \cdot 10^{20} p.o.t.$
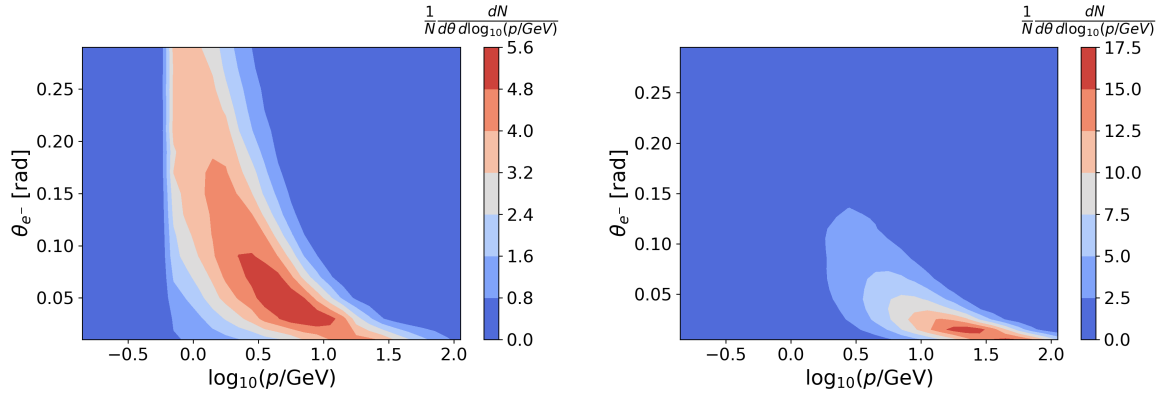
FIGURE 6.4.3: 2D contour plot of the momentum (p) and the production angle (θ) correlation for π^0s produced in the collisions of 400 GeV protons hitting the SHiP beam-dump target. Left: simulation with FairShip including π^0 production in the interactions of secondary hadrons with the target nuclei. Right: simulation of the prompt proton-nucleon π^0 production with `Pythia`.
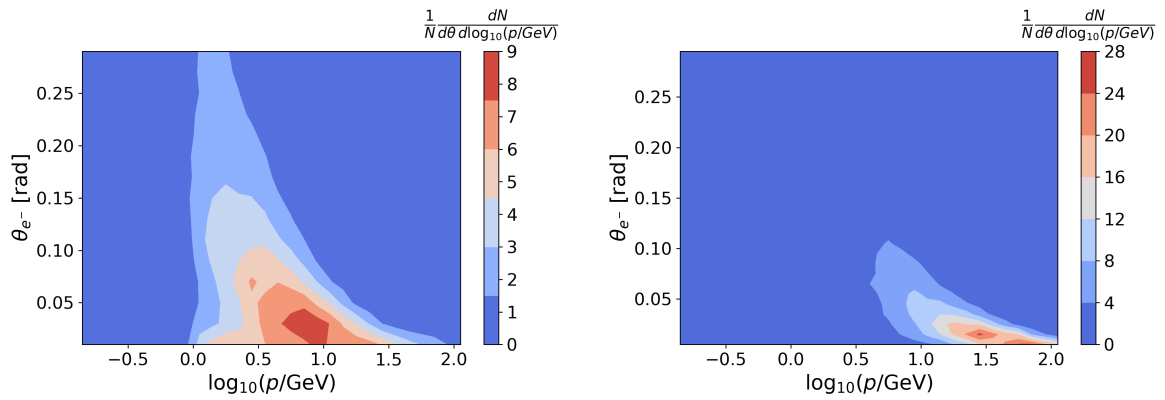
FIGURE 6.4.4: 2D contour plot of the momentum (p) and the production angle (θ) correlation for the ηs produced in the collisions of 400 GeV protons hitting the SHiP beam-dump target. Left: simulation with FairShip including η production in the interactions of secondary hadrons with the target nuclei. Right: simulation of the prompt proton-nucleon η production with Pythia.

6.4.2 Proton Bremsstrahlung

In the mass range $500 \, \text{MeV} \lesssim m_{A'} \lesssim 1 \, \text{GeV}$, the production of A' is dominated by the proton bremsstrahlung mechanism. The photon emission cross section is indeed enlarged in the collinear direction so that a sizeable fraction of A' is produced within the geometrical acceptance for an on-axis detector as the SND ($\sim 20\%$). In this limit, the process can be described by a generalisation of the Fermi-Williams-Weizsäcker method [60–62], based on the assumption that the $p - N$ scattering is dominated by the exchange in the 1^{--} channel. We extend MadDump include the bremsstrahlung from the primary protons. Following Refs. [50, 63], we parametrise the four-momentum vector of the emitted A' as $p_{A'} = (E_{A'}, p_T \cos(\phi), p_T \sin(\phi), zP)$, with $E_{A'} = zP + (p_T^2 + m_{A'}^2)/(2zP)$, where P is the momentum of the incident proton, z is the fraction of the proton momentum carried by the outgoing A', p_T is the momentum perpendicular to the beam momentum and ϕ is the azimuthal angle. We generate unweighted A' events according to the differential production rate

$$\frac{d^2 N_{A'}}{dz \, dp_T^2} = \frac{\sigma_{pA}(s')}{\sigma_{pA}(s)} F_{1,p}^2(m_{A'}^2) w_{ba}(z, p_T^2), \tag{6.11}$$

where $s' = 2 m_p (E_p - E_{A'})$, $s = 2 m_p E_p$ and the photon splitting function is

$$w_{ba}(z, p_T^2) = \frac{\epsilon^2 \alpha}{2\pi H} \left[\frac{1 + (1 - z)^2}{z} - 2z(1 - z) \left(\frac{2m_p^2 + m_{A'}^2}{H} - z^2 \frac{2m_p^4}{H^2} \right) \right.$$
$$\left. + 2z(1 - z)(1 + (1 - z)^2) \frac{m_p^2 m_{A'}^2}{H^2} + 2z(1 - z)^2 \frac{m_{A'}^4}{H^2} \right],$$

with $H = p_T^2 + (1 - z)m_{A'}^2 + z^2 m_p^2$. In the above formula, $F_{1,p}$ is the time-like proton form-factor, as provided by the parameterisation in Ref. [64]. It effectively incorporates off-shell mixing with vector mesons such as ρ and ω, corresponding to a resonance effect around $m_{A'} \sim 770 \, \text{MeV}$ [65]. In Ref. [63], the authors compare the description of the peak region by adopting the time-like proton form factors and by adding by hand the vector mixing within an on-shell computation, finding small deviations in the peak region. Assessing the size of this uncertainty is beyond the scope of this work.

The next steps of the simulation, namely the decay $A' \to \chi \bar{\chi}$ and the $\chi - e^-$ scattering in the SND, are handled by standard MadDump functions. The whole process has been integrated into the new MadDump mode `bremsstrahlung-interaction`.

The normalisation of the flux of the original A' is given by the integral of the differential production rate eq. (6.11) in the validity range of the equivalent photon approximation, given by the kinematical conditions

$$E_p, E_{A'}, E_p - E_{A'} \gg m_p, m_{A'}, |p_T|. \tag{6.12}$$

Following Refs. [50, 63, 66], we adopt $z \in [0.1, 0.9]$. For a relatively high energy experiment such as SHiP, the minimum DP energy E_P corresponds then to $\sim 40 \, \text{GeV}$ and we can set its
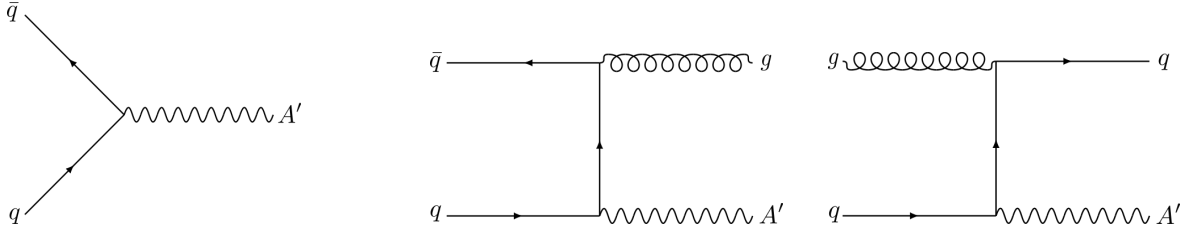
FIGURE 6.4.5: Main tree-level partonic QCD contributions: Drell-Yan-like production (left panel), associated production with the emission of extra QCD radiation (right panel).

maximum transverse momentum p_T to 4 GeV, i.e. an order of magnitude less. We expect electron bremsstrahlung to be sub-dominant as discussed for example in [66, 67]. As for the cascade effects, extra dark photons may arise from the bremsstrahlung of secondary charged hadrons. Similarly to what happens in the case of mesons, the picture is complicated by the impact of the geometrical acceptance and the convolution with the scattering cross section. For the case the proton undergoes a chain of elastic proton-nucleon collisions, so that it retains all of its initial energy, we can make a rough estimate by means of the following simplified calculation. Let p_{el} be the probability that the incoming proton undergoes an elastic scattering interaction with a nucleon in the target and p_{brem} the probability of a dark photon produced in the proton bremsstrahlung. Under the assumption that p_{brem} does not depend much on the number of previous elastic collisions, the probability that a dark photon is produced in this chain is

$$p = p_{brem} \left(1 + p_{el} \times p_{el} + p_{el} \times p_{el} \times p_{el} + \dots \right) = p_{brem} \sum_{n=0}^{\infty} p_{el}^n = p_{brem} \frac{1}{1-p_{el}}. \tag{6.13}$$

At the energy of SHiP, $p_{el} \simeq 0.25$ so that we estimate a mild increment of $\sim 30\%$. In the following, we keep the conservative estimate based only upon the bremsstrahlung of the primary protons.

6.4.3 QCD prompt production

QCD parton processes become relevant for $m_{A'} \gtrsim 1\,\text{GeV}$, at the edge where perturbation theory starts to become reliable. Indeed, at scales $\lesssim 1\,\text{GeV}$ the strong coupling α_s is $O(1)$ and the description of the hadrons in terms of constituent partons is spoiled by the confinement. In the attempt of estimating the relative importance of this production mechanism, we have tried to push the perturbative computation down to $m_{A'} \sim 300\,\text{MeV}$. The main tree-level diagrams correspond to the Drell-Yan-like production and the associated production with QCD radiation, Fig. 6.4.5. The latter allows for smaller $m_{A'}$ values since the characteristic scale of the process, given by the transverse momentum of the emitted parton, can be kept to be higher than the Λ_{QCD} scale. A minimum cut on the p_T of the QCD radiation is physically required to tame infrared singularities. The cross section diverges logarithmically up to scales of order $O(\Lambda_{QCD})$, when perturbation theory eventually breaks down. The transverse momentum cut-off is a severe requirement for an on-axis

set-up as SHiP, due to its small angular acceptance. We find that even for relatively small values of the cut-off, $p_T \sim 800 \, \text{MeV}$, the production rate is not sufficient to produce a significant yield of LDM within the geometrical acceptance. Therefore, we focus only on Drell-Yan-like production. We rely on `MadGraph5`(v.2.66) [68], which is integrated in MadDump as it is based on the former package, for the generation of the events, and we use the `NNPDF2.3LO` [69, 70] set as our choice of the proton parton distribution function (PDF). In the normalisation of the number of produced LDM particles, we effectively take into account nuclear effects in the following way

$$N_{\text{LDM}} = 2 \times \frac{\sigma_{pA \to \chi \bar{\chi}}}{\sigma_{pA \to \text{all}}} \times N_{p.o.t.} = 2 \times \frac{A \sigma_{pp \to \chi \bar{\chi}}}{A^{0.71} \sigma_{pp \to \text{all}}} \times N_{p.o.t.} = 2 \times A^{0.29} \times \frac{\sigma_{pp \to \chi \bar{\chi}}}{\sigma_{pp \to \text{all}}} \times N_{p.o.t.} \,,$$

where $A = A_{\text{Molybdenum}} = 96$; the nuclear rescaling as $A^{0.71}$ is taken from Ref. [71] and $\sigma_{pp \to \text{all}} = 40 \, \text{mb}$ [72].

In this case, the characteristic scale of the process coincides with $m_{A'}$. As mentioned before, we cannot use scales $\lesssim 1 \, \text{GeV}$, where both the strong coupling and PDF are ill-defined from the perturbative point of view. To push our projection into the sub-GeV range, we adopt the following prescription: we set both the re-normalisation scale μ_R (at which the strong coupling constant is evaluated) and the factorisation scale μ_F (at which the PDF is evaluated) to a fixed value chosen to be $\mu_R = \mu_F = 1.5 \, \text{GeV}$, the lowest scale variation point associated to open charm production.

6.5 Background estimate

Neutrinos emerging from the beam-dump target and interacting in the SND are the relevant background source to the detection of LDM elastic scattering, whenever the topology at the primary vertex consists of a single outgoing charged track, an electron. The expected background yield for five years of data-taking has been estimated by means of the `GENIE` [49] Monte Carlo software, supplied with the spectrum of neutrinos produced at the beam dump as simulated with `Pythia v6.4.28` within FairShip and including secondary production, for the generation of the following neutrino interactions in the whole kinematic phase space:

- *Elastic scattering* (EL) of $\nu_e(\bar{\nu}_e)$, $\nu_\mu(\bar{\nu}_\mu)$ off the electrons of the SND, which is a source of irreducible background as it shares the same topology of LDM elastic interactions:

$$\nu_\ell + e^- \to \nu_\ell + e^- \,.$$

- *Resonant scattering* (RES) of $\nu_e(\bar{\nu}_e)$ off nucleons A(n, p):

$$\nu_e(\bar{\nu}_e) + A \to e^-(e^+) + \Delta^{+/++} \,,$$

$$\nu_e(\bar{\nu}_e) + A \to e^-(e^+) + (N^* \to \text{inv}) \,.$$

- *Deep Inelastic scattering* (DIS) of $\nu_e(\bar{\nu}_e)$ off nucleons A, representing background when only the electron track at the primary vertex is reconstructed because of unidentified hadrons:

$$\nu_e(\bar{\nu}_e) + A \to e^-(e^+) + X \,.$$

- *Quasi-elastic scattering* (QE) of $\nu_e(\bar{\nu}_e)$, with the primary proton undetected because it is below the energy threshold:

$$\nu_e + n \to e^- + p \,,$$
$$\bar{\nu}_e + p \to e^+ + n \,.$$

Charged current interactions of $\nu_\ell\,(\bar{\nu}_\ell)$ with $\ell = \mu, \tau$ do not represent a concern because they are easily discernible from LDM events by reconstructing the charged lepton produced in the final state. Electron decay modes of the τ lepton are a negligible background source, since an early decay of the parent track ($\sim 1\%$ occurrence) leading to an undetected τ would occur with less than a per-mill probability. In addition, we do not consider $\nu_\tau\,(\bar{\nu}_\tau)$ elastic scattering processes as background, due to the suppression resulting from the combination of smaller flux ϕ_{ν_τ} (~ 1 order of magnitude smaller than ϕ_{ν_e} and ~ 2 orders of magnitude smaller than ϕ_{ν_μ}) and cross section . The whole ν spectrum is made to interact within the SND and the surrounding materials. Moreover, for this study we assume the detection efficiency to be unitary [73]. The simulated sample of neutrinos undergoes a two-steps selection procedure, in order to be tagged as residual background. First, only interactions occurring within geometrical acceptance and associated with a single charged final state track, an electron, are selected: ν vertices are further considered in the analysis only if located inside the SND volume, whereas all the out-coming charged tracks are inspected in order to assess their visibility in the nuclear emulsion medium. The visibility threshold depends crucially on the exploited tracking device technology; for this study we assume 170 MeV/c for the protons, 100 MeV/c for the other charged particles including the electrons. These are derived as benchmark values from the OPERA experiment, where charged-particle reconstruction is possible only if two consecutive straight track segments, before and after a lead plate, are found to be in agreement [74]. A further handle considered here for signal against background discrimination is the presence of neutral particles, *e.g.* photons or π^0s, nearby the interaction vertex, since it is not foreseen in any LDM elastic scattering event.

The second step of the event identification procedure consists of a kinematic selection in the energy E_e and polar angle with respect to the incoming neutrino/LDM direction θ_e of the scattered electron. For the elastic case, these quantities are constrained by the kinematic relation $E_e\,\theta_e^2 \leq 2\,m_e$, valid in the regime $E_{in} \gg m_e, m_\chi$, where E_{in} is the energy of the incident neutrino/LDM particle. In order to choose the energy and angle ranges for the selection, an optimisation procedure is performed,

aiming at maximising the following significance:

$$\Sigma = \frac{S}{\sqrt{\sigma_{\text{stat}}^2 + \sigma_{\text{sys}}^2}} = \frac{S}{\sqrt{B + \sum\limits_{\substack{i \in [\text{EL, QE, RES, DIS}] \\ \ell \in [\nu_e, \nu_\mu, \bar{\nu}_e, \bar{\nu}_\mu]}} \left(\kappa_{i\ell} B_{i\ell}\right)^2}}, \qquad (6.14)$$

where S denotes the signal yield, while $B_{i\ell}$ are the individual contributions to the background yield B per interaction category and neutrino flavour, each of them weighted by a factor $\kappa_{i\ell}$ accounting for the systematic uncertainty. We have focused on the relevant systematics, arising from the uncertainty on the neutrino cross sections (assumed flavour-independent, κ_i) and on the incoming neutrino flux produced at the beam dump (interaction-independent, $\tilde{\kappa}_\ell$), so that we have assumed $\kappa_{i\ell} = \sqrt{\kappa_i^2 + \tilde{\kappa}_\ell^2}$. As for the former, we assume the following: 5% for DIS [75], 18% for RES [76], 8% for QE [77], while we neglect the uncertainty on the EL cross section that is well known within the SM [78]. As for the uncertainty on the incoming neutrino flux, this will be well constrained by an independent measurement of the abundant CC-DIS interactions occurring within the SHiP detector (expected $\sim 10^6$ for $\nu_{e,\mu}$). Since the corresponding cross section is lepton-universal and known within $\sim 5\%$ accuracy down to E_ν of 2.5 GeV [75], we assume it to be the driving systematic uncertainty on the neutrino flux. While SHiP is capable of disentangling ν_μ from $\bar{\nu}_\mu$ interactions by measuring the charge of the primary muon, thus providing a different estimate for ν_μ and $\bar{\nu}_\mu$ fluxes, with regard to electron species it will measure a combination of the lepton and anti-lepton initiated events. As the relative abundance of ν_e and $\bar{\nu}_e$ produced at the beam dump can be assessed, the individual fluxes can be estimated accordingly. For neutrino energies below 2.5 GeV we double the uncertainty on the flux assuming them to be at 10%.

Since the signal yield S depends on the mass hypothesis placed on the LDM candidate and thus on the DP, we adopt the most-general assumption of maximising the experimental sensitivity with respect to the broadest possible range of masses. Therefore, S is given as the average of the signal yields for three DP mass hypotheses: 50 MeV, 250 MeV and 500 MeV.

The selection optimisation strategy is based on a grid-search method and proceeds as follows:

- an energy window $[E_{\min}, E_{\max}]$ is identified, according to the signal events distributions;

- in the given energy range, the significance Σ values are determined in uniform angular intervals of 5 mrad spread;

- the selection ranges, corresponding to the maximum Σ, are chosen for the analysis.

As shown in Fig. 6.5.1, signal events are mostly concentrated at energies below 10 GeV. Two energy windows have thus been considered: $[1, 5]$ GeV and $[1, 10]$ GeV, where the lower cut is placed as a minimum requirement for the recoil electron to produce a detectable electromagnetic shower within the ECC brick. The motivation to consider an additional tighter energy range resides in the opportunity to further suppress the high energetic components of the neutrino background, as illustrated in Fig. 6.5.2 which shows the relevant EL and QE contributions. DIS and RES processes are not shown since they exhibit signatures with higher multiplicities of charged tracks at the

	ν_e	$\bar{\nu}_e$	ν_μ	$\bar{\nu}_\mu$	all
Elastic scattering on e^-	68	41	60	38	207
Quasi - elastic scattering	9	9			18
Resonant scattering	-	5			5
Deep inelastic scattering	-	-			-
Total	77	55	60	38	230

TABLE 6.5.1: Expected neutrino background yield to light dark matter elastic scattering search in the SHiP experiment, corresponding to 2×10^{20} delivered *p.o.t.* The current estimate is the result of a combined geometrical, topological and kinematical selection, aimed at identifying only interactions occurring within the Scattering Neutrino Detector with one visible track in the final state being an electron. Tracks under a defined visibility threshold are discarded ($p < 100$ MeV/c for charged, $p < 170$ MeV/c for protons). A kinematic cut in $E_e \in [1, 5]$ GeV and $\theta_e \in [10, 30]$ mrad of the scattered electron is chosen as result of the signal significance optimisation procedure and determines the final number of background events. We refer to the Sec. 6.5 for further details on the analysis and the associated uncertainties.

primary vertex.

The results of the optimisation are reported in Fig. 6.5.3, showing indeed a preference for the tighter energy window $E_e \in [1, 5]$ GeV and an angular range $\theta_e \in [10, 30]$ mrad.

The corresponding background yield estimate is reported in Table 6.5.1.

Neutrino elastic scattering processes, involving either electronic and muonic species, represent the dominant background source and are to some degree irreducible, since they share the same topology as the signal.

With regard to quasi-elastic ν_e and $\bar{\nu}_e$ interactions, a small but non-negligible contribution is observed. The process $\nu_e n \to e^- p$ mimics the signal when the proton at the primary vertex is not identified, because of the 170 MeV/c threshold. Improvements in the proton identification efficiency with dedicated techniques, including Machine Learning clustering algorithms, will be the subject of future studies. When considering anti-neutrinos, events as $\bar{\nu}_e p \to e^+ n$ are topologically irreducible since we assume for the present study the neutron to be undetectable within the SND. This effect compensates the larger (by a factor of ~ 3) neutrino flux, thus making the two contributions comparable.

In the case of resonant neutrino scattering, the outgoing electron is often accompanied by a further charged track, which helps discriminating between background and signal. Nevertheless, some topologically irreducible interactions are present as well:

$$\bar{\nu}_e p \to e^+ N^*, \qquad N^* \to \Lambda^0 K^0_{L/S},$$

where the $K^0_{L/S}$ is considered undetectable within the SND for this study. Future improvements lie in the employment of combined information of ECC and TT, coming from the linking of the emulsion tracks with those reconstructed in the electronic tracking system. Moreover, some final

(A) $m_{A'} = 50$ MeV, production from π^0 decays.

(B) $m_{A'} = 250$ MeV, production from η decays.

(C) $m_{A'} = 500$ MeV, production from proton bremsstrahlung.
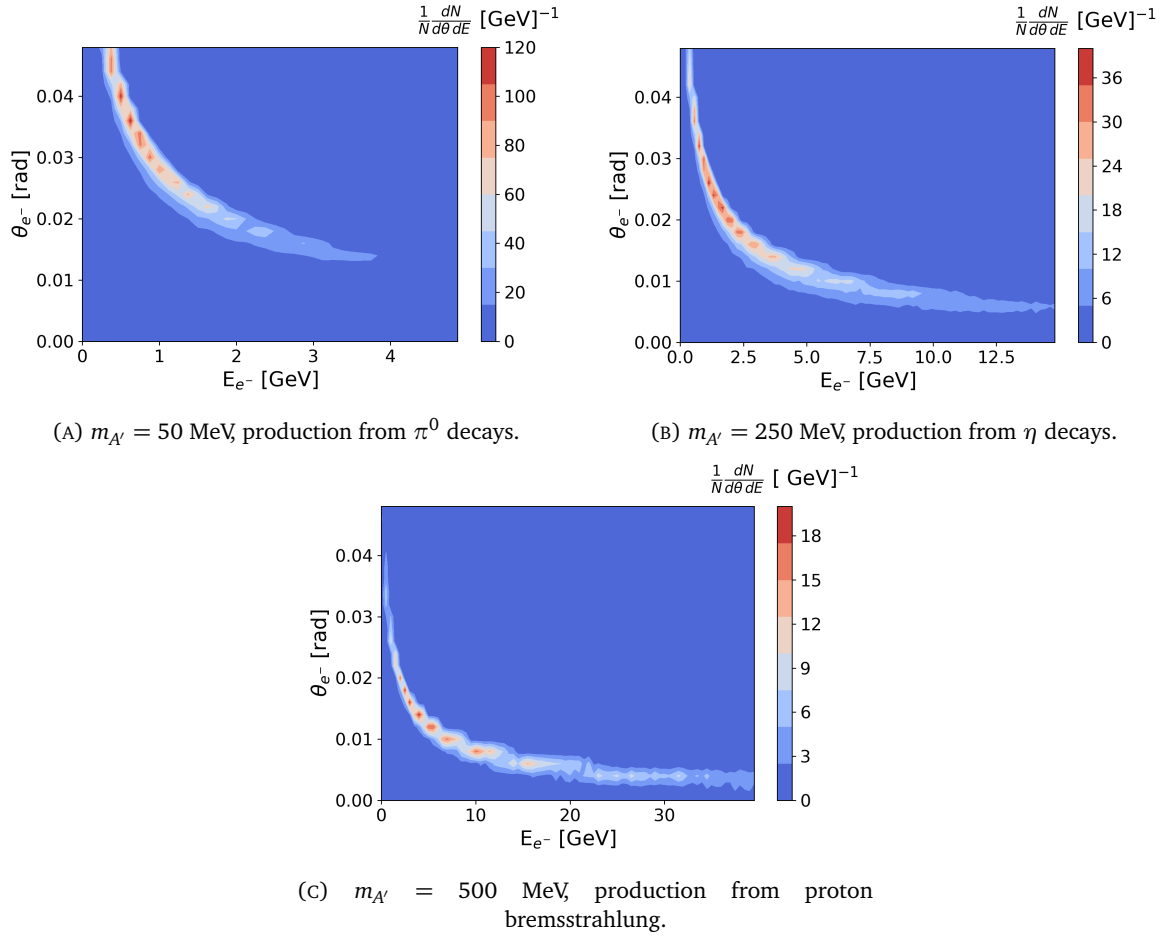
FIGURE 6.5.1: 2D-contour plot in the energy-polar angle plane of the recoil electron in LDM-e^- scattering for three different mass DP candidates: (a) 50 MeV, (b) 250 MeV, (c) 500 MeV. The colour range is expressed in arbitrary units. A clear correlation is observed between the mass of the DP candidate and the electron energy-angle spectrum: the higher is the mass the smaller the recoil angle and the higher the associated energy. In the mass range we are interested in, most of the signal lies in the energy region below 10 GeV.

states with the pattern $e^+ (n) \gamma$ contribute, when the emitted photon is too soft to be identified via the reconstruction of the electron-positron pairs from its conversion.

The contribution from neutrino deep inelastic scattering processes is, on the contrary, negligible, as a consequence of the high rejection power observed on these event categories, which exhibit a topology with a high multiplicity of charged tracks.

In the eventuality of an observed excess in the number of events, SHiP may collect data in a bunched beam mode, exploiting the time of flight measurement to separate massive particles like LDM from neutrinos.

(A) Sum of the EL $\nu_\ell\,(\bar{\nu}_\ell)$ scattering contributions ($\ell = e, \mu$).

(B) Sum of the QE $\nu_e(\bar{\nu}_e)$ scattering contributions.
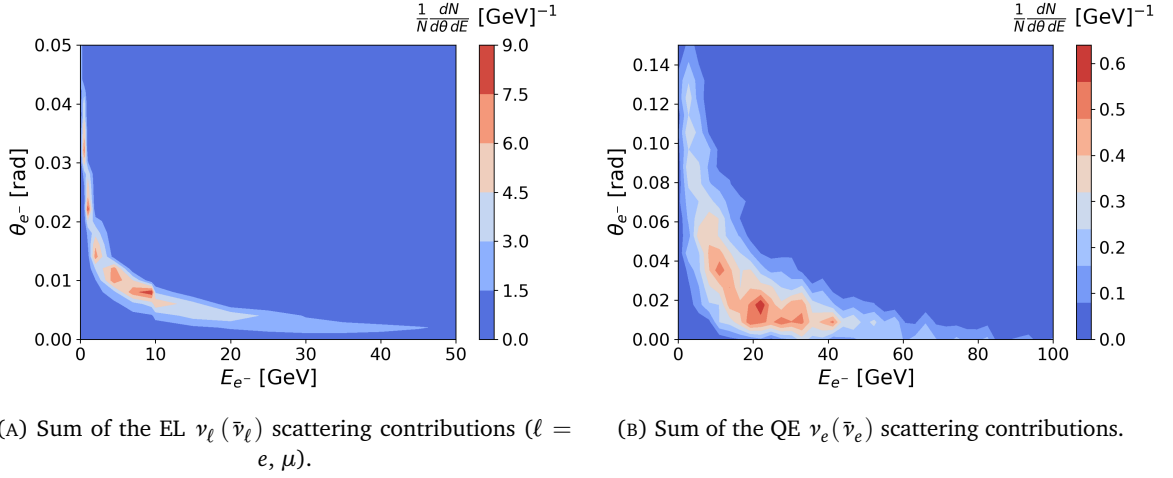
FIGURE 6.5.2: 2D plot of the scattered electron energy E_{e^-} Vs. angle θ_{e^-} for the relevant background sources from neutrino and anti-neutrino species: (a) EL scattering from $\nu_\ell\,(\bar{\nu}_\ell)$ being $\ell = e, \mu$; (b) QE scattering from $\nu_e\,(\bar{\nu}_e)$.

6.6 Sensitivity

Once the significance of Eq. (6.14) is maximised, the optimal energy and angle ranges are employed to determine the yields of signal and background, following a cut-and-count procedure, per each fixed value of the mediator mass $m_{A'}$. The 90% confidence level (C.L.) exclusion limits on the ϵ coupling at fixed mass $m_{A'}$ are then retrieved by adopting a single-tail Poissonian statistics. Statistical and systematic uncertainties are combined as reported after Eq. (6.14).

In Fig. 6.6.1, we report our projection for the SHiP SND exclusion limit at 90% C.L. in the $m_\chi - Y$ plane of the dark-photon model. As stated above, we consider the benchmark scenario $\alpha_D = 0.1$ and $m_\chi = m_{A'}/3$. In Fig. 6.6.2, we separate the contributions given by the different production mechanisms. In the low mass range $m_\chi \lesssim 150$ MeV, the main contribution comes from the decay of the lightest mesons. π decays dominate the A' yield up to masses close to the $m_\pi \to \gamma A'$ kinematic threshold. When approaching this threshold, the decay rate rapidly closes due to the steep suppression given by the phase space factor and with further increasing m_χ mass the $\eta \to \gamma A'$ starts to dominate. The contribution of the ω is subdominant in the whole available mass range, which justifies *a posteriori* the fact that we do not include in our analysis A' production from decays of heavier meson like the η'.

We find that the contribution due to pQCD is very small in the mass region explored. By varying the factorisation scale in the range 800 MeV $< \mu_F < 3$ GeV, we estimate the uncertainty associated with missing higher orders to be about 15% on the signal yield within acceptance. We believe that this is an underestimation of the uncertainty as at next-to-leading order the process starts to receive radiative corrections proportional to the strong coupling constant at a scale close to Λ_{QCD}, and new production channels open. While we do not expect that this will lead to a sizeable impact

(A) Grid values for $E_e \in [1, 5]$ GeV.

(B) Grid values for $E_e \in [1, 10]$ GeV.
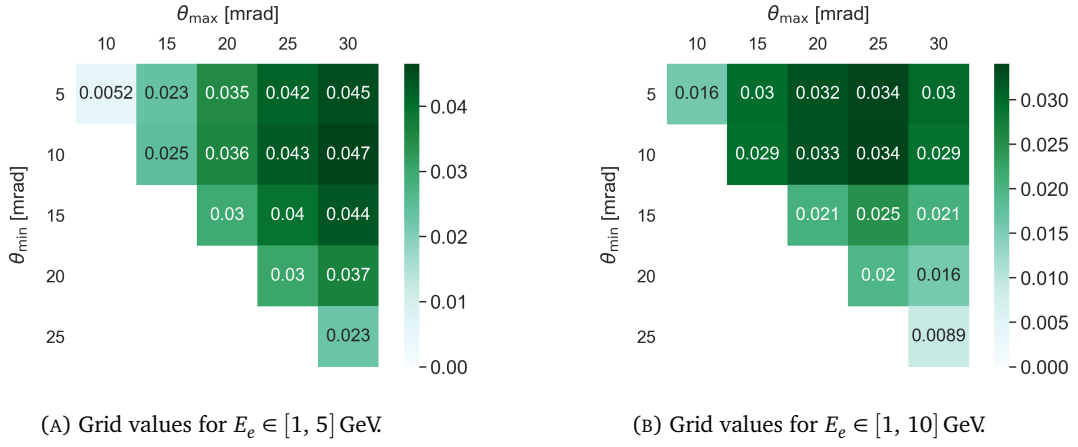
FIGURE 6.5.3: Grid-search optimisation of the significance Σ as a function of the angular cut for a fixed energy window. The left axis represents the lower cut value for θ_e whereas the upper axis is the higher one. The plots in the two panels share the same normalisation. The best selection corresponds to the tighter energy window (a) and the angular range $[10, 30]$ mrad.

on the sensitivity, neglecting it leads anyway to a conservative estimate of the signal; hence, we have not considered the contribution of pQCD in our final result.

In the mass range $1\,\text{MeV} < m_\chi < 300\,\text{MeV}$, the SHiP upper limit fairly improves the current strongest experimental limits (BaBar [13], Na64 [27]), even by more than an order of magnitude in the central region ($5\,\text{MeV} < m_\chi < 100\,\text{MeV}$). In this range and for the benchmark point under investigation, SHiP will cover the still unexplored parameter space corresponding to the solution of the relic density given by a scalar LDM. In the range $3\,\text{MeV} < m_\chi < 300\,\text{MeV}$, SHiP will reach the thermal target for a Majorana candidate. Furthermore, it will exceed the thermal target for a Pseudo-Dirac candidate for masses around $10\,\text{MeV} < m_\chi < 40\,\text{MeV}$.

We notice that for $m_\chi \lesssim 5\,\text{MeV}$ the SHiP line saturates. In this region, the dark matter mass starts to become negligible and the selection requirements affect similarly the signal and the background. The rise in the signal production rate due to a lower mass is then balanced by a smaller fraction of events passing the kinematics selection, leading to the observed flatten sensitivity in the small mass range. The distinctive peak at $m_\chi \simeq 257$ GeV corresponds to the $\rho - \omega$ resonant region, which is effectively taken into account by the time-like proton form factors used in the modelling of the proton bremsstrahlung mechanism.

In Fig. 6.6.3, the comparison between the SHiP sensitivity reach and that of other concurrent experiments clearly shows strengths and the complementarity offered by the proposed experimental scenario. Indeed the SHiP experiment will place constraints in unexplored regions of parameters space by exploiting a high intensity proton beam dump at $400\,\text{GeV}$ and a micrometrical resolution tracking capability with the ECC. Thus, it offers a diverse approach to this NP search with respect to other experimental scenarios including direct searches and electron beam-line technologies.
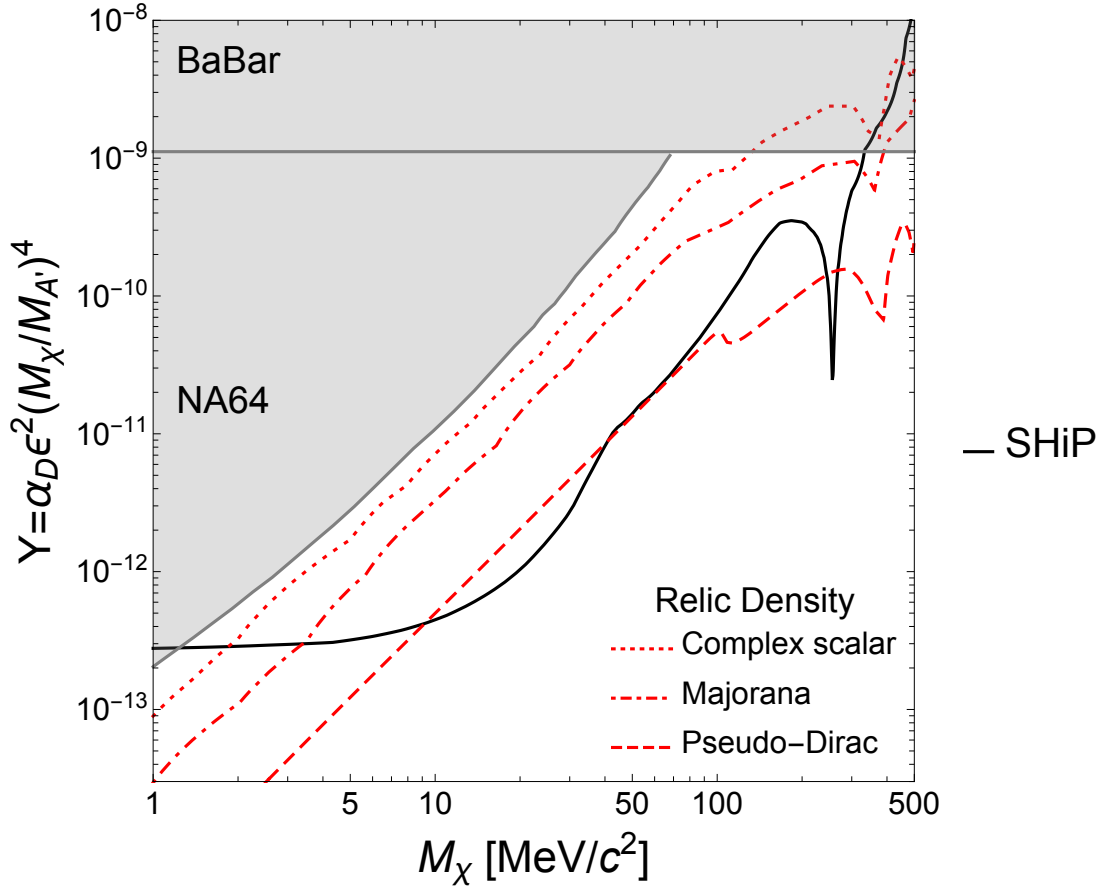
FIGURE 6.6.1: SHiP SND exclusion limit at $90\% CL$ relative to a A' decaying into $\chi\bar{\chi}$ pairs for the benchmark point $\alpha_D = 0.1$ and $m_{A'} = 3\, m_\chi$. The current strongest experimental limits are also shown (BaBar [13], NA64 [27]), together with the three thermal relic lines corresponding to the scalar and the Majorana [3], and the Pseudo-Dirac DM [79] hypothesis.

6.7 Conclusions

Light dark matter particles χ with masses in the sub-GeV region represent an appealing scenario for the explanation of the observed thermal relic density in the Universe. In this work, we have studied the potential offered by the SHiP SND to reveal LDM which couple to SM particles via a new gauge force mediated by a vector boson, A'. We have assumed the simplest DP model, with coupling g_D to χ and A' kinetically mixed with the SM photon with mixing parameter ϵ. We have focused on the relevant scenario for the SHiP SND: $m_{A'} > 2m_\chi$ and $g_D \gg \epsilon e$. Our main result is that for DM masses in $[1, 300]$ MeV the SHiP experiment will reach an unexplored region of the parameter space. For the benchmark point considered, the sensitivity of the SHiP SND is even below the thermal relic line corresponding to a Majorana DM candidate in the mass window $[3, 300]$ MeV and it will reach the target for a Pseudo-Dirac candidate within $[15, 30]$ MeV. Our analysis is based
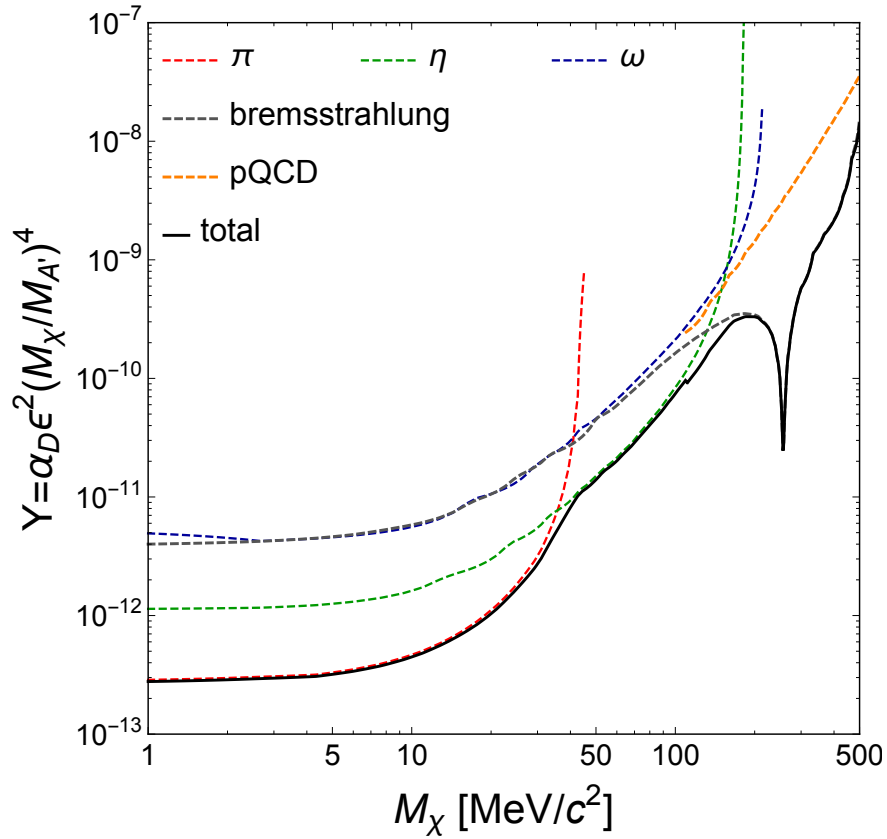
FIGURE 6.6.2: SHiP SND exclusion limit at $90\% CL$ relative to a A' decaying into $\chi\bar{\chi}$ pairs for the benchmark point $\alpha_D = 0.1$ and $m_{A'} = 3m_\chi$. The contributions from the different production mechanisms are reported separately.

on a robust simulation framework for both the signal and the background which includes the relevant physical processes propagated within the detector. In particular, interactions of secondary particles in the beam-dump target have been taken into account in the neutrino background modelling, assuming unitary detection efficiency. As for the signal, we have consistently adopted 100% detection efficiency within the selection requirements and we have studied the impact of the cascade effect on meson multiplicities and the resulting dark matter production yield. We have observed that the impact of the cascade is quite modest and affects mainly the low masses.

In this work, we have focused on the elastic $\chi e \rightarrow \chi e$ signature detectable within the SHiP Scattering and Neutrino Detector. Other signatures, as the elastic scattering with nuclei, may lead to an improvement of the sensitivity. We leave their study to forthcoming works. In our case, then the main background sources arise from elastic $\nu_\ell / \bar{\nu}_\ell$-electron and quasi-elastic $\nu_e / \bar{\nu}_e$ scattering. We have considered the region $E_e \in [1, 5]$ GeV and $\theta_e \in [10, 30]$ mrad, where e is the recoil electron. We have found that about 230 neutrino events survive the selection requirements, for 2×10^{20} *p.o.t.* corresponding to 5 years of data-taking.

We conclude by mentioning that, should an excess of events be observed, a time of flight measurement of particles scattering within the SND might represent a smoking gun to discriminate LDM from neutrino events, thus leading to an inarguable discovery.
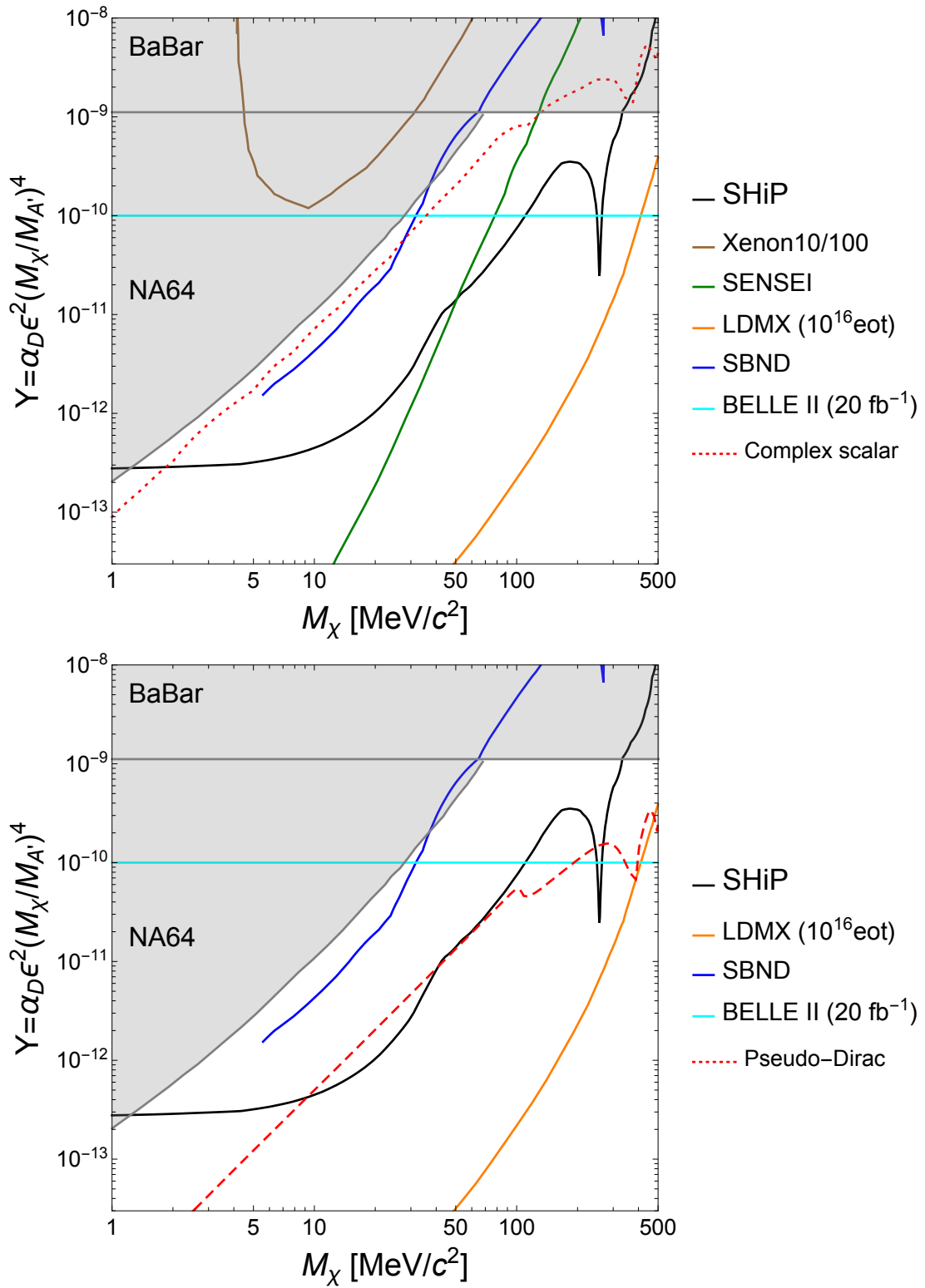
FIGURE 6.6.3: Comparison of existing and projected limits among the SHiP and other experiments as taken from Ref. [80] for scalar (top panel) and Pseudo-Dirac dark matter (bottom panel).

References

[1]   Marc Schumann. "Direct Detection of WIMP Dark Matter: Concepts and Status". In: *J. Phys. G* 46.10 (2019), p. 103003. DOI: 10.1088/1361-6471/ab2ea5. arXiv: 1903.03026 [astro-ph.CO].

[2]   Patrick J. Fox. "TASI Lectures on WIMPs and Supersymmetry". In: *PoS* TASI2018 (2019), p. 005.

[3]   Marco Battaglieri et al. "US Cosmic Visions: New Ideas in Dark Matter 2017: Community Report". In: (2017). arXiv: 1707.04591 [hep-ph].

[4]   Masahiro Ibe et al. "Migdal Effect in Dark Matter Direct Detection Experiments". In: *JHEP* 03 (2018), p. 194. DOI: 10.1007/JHEP03(2018)194. arXiv: 1707.07258 [hep-ph].

[5]   P. Agnes et al. "Low-Mass Dark Matter Search with the DarkSide-50 Experiment". In: *Phys. Rev. Lett.* 121 (8 Aug. 2018), p. 081307. DOI: 10.1103/PhysRevLett.121.081307. URL: https://link.aps.org/doi/10.1103/PhysRevLett.121.081307.

[6]   G. Angloher et al. "Results from 730 kg days of the CRESST-II Dark Matter Search". In: *Eur. Phys. J. C* 72 (2012), p. 1971. DOI: 10.1140/epjc/s10052-012-1971-8. arXiv: 1109.0702 [astro-ph.CO].

[7]   Rouven Essig et al. "First Direct Detection Limits on Sub-GeV Dark Matter from XENON10". In: *Phys. Rev. Lett.* 109 (2 July 2012), p. 021301. DOI: 10.1103/PhysRevLett.109.021301. URL: https://link.aps.org/doi/10.1103/PhysRevLett.109.021301.

[8]   E. Aprile et al. "Dark Matter Search Results from a One Ton-Year Exposure of XENON1T". In: *Phys. Rev. Lett.* 121.11 (2018), p. 111302. DOI: 10.1103/PhysRevLett.121.111302. arXiv: 1805.12562 [astro-ph.CO].

[9]   Carla Macolino. "DARWIN: direct dark matter search with the ultimate detector". In: *J. Phys. Conf. Ser.* 1468.1 (2020). Ed. by Masayuki Nakahata, p. 012068. DOI: 10.1088/1742-6596/1468/1/012068.

[10]   Xiangyi Cui et al. "Dark Matter Results From 54-Ton-Day Exposure of PandaX-II Experiment". In: *Phys. Rev. Lett.* 119.18 (2017), p. 181302. DOI: 10.1103/PhysRevLett.119.181302. arXiv: 1708.06917 [astro-ph.CO].

[11]   Michael Crisler et al. "SENSEI: First Direct-Detection Constraints on Sub-GeV Dark Matter from a Surface Run". In: *Phys. Rev. Lett.* 121 (6 Aug. 2018), p. 061803. DOI: 10.1103/PhysRevLett.121.061803. URL: https://link.aps.org/doi/10.1103/PhysRevLett.121.061803.

[12]   Leszek Roszkowski, Enrico Maria Sessolo, and Sebastian Trojanowski. "WIMP dark matter candidates and searches—current status and future prospects". In: *Rept. Prog. Phys.* 81.6 (2018), p. 066201. DOI: 10.1088/1361-6633/aab913. arXiv: 1707.06277 [hep-ph].

[13] J. P. Lees et al. "Search for Invisible Decays of a Dark Photon Produced in e^+e^- Collisions at BaBar". In: *Phys. Rev. Lett.* 119.13 (2017), p. 131804. DOI: 10.1103/PhysRevLett.119.131804. arXiv: 1702.03327 [hep-ex].

[14] W. Altmannshofer et al. "The Belle II Physics Book". In: *PTEP* 2019.12 (2019). Ed. by E. Kou and P. Urquijo. [Erratum: PTEP 2020, 029201 (2020)], p. 123C01. DOI: 10.1093/ptep/ptz106. arXiv: 1808.10567 [hep-ex].

[15] Brian Batell, Maxim Pospelov, and Adam Ritz. "Exploring Portals to a Hidden Sector Through Fixed Targets". In: *Phys. Rev.* D80 (2009), p. 095024. DOI: 10.1103/PhysRevD.80.095024. arXiv: 0906.5614 [hep-ph].

[16] Patrick deNiverville, Maxim Pospelov, and Adam Ritz. "Observing a light dark matter beam with neutrino experiments". In: *Phys. Rev.* D84 (2011), p. 075020. DOI: 10.1103/PhysRevD.84.075020. arXiv: 1107.4580 [hep-ph].

[17] Patrick deNiverville, David McKeen, and Adam Ritz. "Signatures of sub-GeV dark matter beams at neutrino experiments". In: *Phys.Rev.* D86 (2012), p. 035022. DOI: 10.1103/PhysRevD.86.035022. arXiv: 1205.3499 [hep-ph].

[18] R. Dharmapalan et al. "Low Mass WIMP Searches with a Neutrino Experiment: A Proposal for Further MiniBooNE Running". In: (2012). arXiv: 1211.2258 [hep-ex].

[19] Brian Batell et al. "Leptophobic Dark Matter at Neutrino Factories". In: (2014). arXiv: 1405.7049 [hep-ph].

[20] Davison E. Soper et al. "Scattering of Dark Particles with Light Mediators". In: (2014). arXiv: 1407.2623 [hep-ph].

[21] Bogdan A. Dobrescu and Claudia Frugiuele. "GeV-scale dark matter: production at the Main Injector". In: *Journal of High Energy Physics* 02 (2015), p. 019. DOI: 10.1007/JHEP02(2015)019. arXiv: 1410.1566 [hep-ph].

[22] Pilar Coloma et al. "Dark matter beams at LBNF". In: *Journal of High Energy Physics* 04 (2016), p. 047. DOI: 10.1007/JHEP04(2016)047. arXiv: 1512.03852 [hep-ph].

[23] Claudia Frugiuele. "Probing sub-GeV dark sectors via high energy proton beams at LBNF/-DUNE and MiniBooNE". In: *Phys. Rev.* D96.1 (2017), p. 015029. DOI: 10.1103/PhysRevD.96.015029. arXiv: 1701.05464 [hep-ph].

[24] Patrick deNiverville and Claudia Frugiuele. "Hunting sub-GeV dark matter with NOνA near detector". In: (2018). arXiv: 1807.06501 [hep-ph].

[25] Gabriel Magill et al. "Millicharged particles in neutrino experiments". In: (2018). arXiv: 1806.03310 [hep-ph].

[26] A. A. Aguilar-Arevalo et al. "Dark Matter Search in Nucleon, Pion, and Electron Channels from a Proton Beam Dump with MiniBooNE". In: (2018). arXiv: 1807.06137 [hep-ex].

[27] D. Banerjee et al. "Dark matter search in missing energy events with NA64". In: *Phys. Rev. Lett.* 123.12 (2019), p. 121801. DOI: 10.1103/PhysRevLett.123.121801. arXiv: 1906.00176 [hep-ex].

[28] Torsten Åkesson et al. "Light Dark Matter eXperiment (LDMX)". In: (Aug. 2018). arXiv: 1808.05219 [hep-ex].

[29]   Brian Batell et al. "Flavor-specific scalar mediators". In: *Phys. Rev.* D98.5 (2018), p. 055026. DOI: 10.1103/PhysRevD.98.055026. arXiv: 1712.10022 [hep-ph].

[30]   Bob Holdom. "Two U(1)'s and Epsilon Charge Shifts". In: *Phys. Lett.* 166B (1986), pp. 196–198. DOI: 10.1016/0370-2693(86)91377-8.

[31]   Tongyan Lin, Hai-Bo Yu, and Kathryn M. Zurek. "On Symmetric and Asymmetric Light Dark Matter". In: *Phys.Rev.* D85 (2012), p. 063503. DOI: 10.1103/PhysRevD.85.063503. arXiv: 1111.0293 [hep-ph].

[32]   P. A. R. Ade et al. "Planck 2015 results. XIII. Cosmological parameters". In: *Astron. Astrophys.* 594 (2016), A13. DOI: 10.1051/0004-6361/201525830. arXiv: 1502.01589 [astro-ph.CO].

[33]   Paul Frederik Depta et al. "BBN constraints on the annihilation of MeV-scale dark matter". In: *JCAP* 04 (2019), p. 029. DOI: 10.1088/1475-7516/2019/04/029. arXiv: 1901.06944 [hep-ph].

[34]   Eder Izaguirre et al. "Analyzing the Discovery Potential for Light Dark Matter". In: *Phys. Rev. Lett.* 115.25 (2015), p. 251301. DOI: 10.1103/PhysRevLett.115.251301. arXiv: 1505.00011 [hep-ph].

[35]   M. Anelli et al. "A facility to Search for Hidden Particles (SHiP) at the CERN SPS". In: (2015). arXiv: 1504.04956 [physics.ins-det].

[36]   C. Ahdida et al. "The experimental facility for the Search for Hidden Particles at the CERN SPS". In: *Journal of Instrumentation* 14.03 (2019), P03025–P03025. DOI: 10.1088/1748-0221/14/03/p03025. URL: https://doi.org/10.1088%2F1748-0221%2F14%2F03%2Fp03025.

[37]   C. Ahdida et al. "Sensitivity of the SHiP experiment to Heavy Neutral Leptons". In: *JHEP* 04 (2019), p. 077. DOI: 10.1007/JHEP04(2019)077. arXiv: 1811.00930 [hep-ph].

[38]   "FairShip". In: *https://github.com/ShipSoft/FairShip* (). URL: https://github.com/ShipSoft/FairShip.

[39]   A. Akmete et al. "The active muon shield in the SHiP experiment". In: *Journal of Instrumentation* 12.05 (2017), P05011–P05011. DOI: 10.1088/1748-0221/12/05/p05011. URL: https://doi.org/10.1088%2F1748-0221%2F12%2F05%2Fp05011.

[40]   C. Ahdida et al. "The magnet of the scattering and neutrino detector for the SHiP experiment at CERN". In: *Journal of Instrumentation* 15.01 (Jan. 2020), P01027–P01027. DOI: 10.1088/1748-0221/15/01/p01027. URL: https://doi.org/10.1088%2F1748-0221%2F15%2F01%2Fp01027.

[41]   R. Acquafredda et al. "The OPERA experiment in the CERN to Gran Sasso neutrino beam". In: *Journal of Instrumentation* 4.04 (2009), P04018–P04018. DOI: 10.1088/1748-0221/4/04/p04018. URL: https://doi.org/10.1088%2F1748-0221%2F4%2F04%2Fp04018.

[42]   N. Agafonova et al. "Discovery of τ Neutrino Appearance in the CNGS Neutrino Beam with the OPERA Experiment". In: *Phys. Rev. Lett.* 115 (12 Sept. 2015), p. 121802. DOI: 10.1103/PhysRevLett.115.121802. URL: https://link.aps.org/doi/10.1103/PhysRevLett.115.121802.

[43] N. Agafonova et al. "Final Results of the OPERA Experiment on ν_τ Appearance in the CNGS Neutrino Beam". In: *Phys. Rev. Lett.* 120.21 (2018), p. 211801. DOI: `10.1103/PhysRevLett.121.139901,10.1103/PhysRevLett.120.211801`. arXiv: `1804.04912 [hep-ex]`.

[44] N. Agafonova et al. "Final results of the search for $\nu_\mu \to \nu_e$ oscillations with the OPERA detector in the CNGS beam". In: *Journal of High Energy Physics* 2018.6 (2018). ISSN: 1126-6708. DOI: `10.1007/JHEP06(2018)151`.

[45] T. Kirn et al. "SciFi – A large scintillating fibre tracker for LHCb". In: *Nuclear Instruments and Methods in Physics Research Section A: Accelerators, Spectrometers, Detectors and Associated Equipment* 845 (2017), pp. 481–485. ISSN: 0168-9002. DOI: `https://doi.org/10.1016/j.nima.2016.06.057`. URL: `http://www.sciencedirect.com/science/article/pii/S016890021630599X`.

[46] S. Agostinelli et al. "Geant4—a simulation toolkit". In: *Nuclear Instruments and Methods in Physics Research Section A: Accelerators, Spectrometers, Detectors and Associated Equipment* 506.3 (2003), pp. 250–303. ISSN: 0168-9002. DOI: `https://doi.org/10.1016/S0168-9002(03)01368-8`. URL: `http://www.sciencedirect.com/science/article/pii/S0168900203013688`.

[47] Torbjörn Sjöstrand et al. "An Introduction to PYTHIA 8.2". In: *Comput. Phys. Commun.* 191 (2015), pp. 159–177. DOI: `10.1016/j.cpc.2015.01.024`. arXiv: `1410.3012 [hep-ph]`.

[48] Torbjörn Sjöstrand, Stephen Mrenna, and Peter Skands. "PYTHIA 6.4 physics and manual". In: *Journal of High Energy Physics* 2006.05 (May 2006), pp. 026–026. ISSN: 1029-8479. DOI: `10.1088/1126-6708/2006/05/026`. URL: `http://dx.doi.org/10.1088/1126-6708/2006/05/026`.

[49] C. Andreopoulos et al. "The GENIE neutrino Monte Carlo generator". In: *Nuclear Instruments and Methods in Physics Research Section A: Accelerators, Spectrometers, Detectors and Associated Equipment* 614.1 (2010), pp. 87–104. ISSN: 0168-9002. DOI: `https://doi.org/10.1016/j.nima.2009.12.009`. URL: `http://www.sciencedirect.com/science/article/pii/S0168900209023043`.

[50] Johannes Blümlein and Jürgen Brunner. "New Exclusion Limits on Dark Gauge Forces from Proton Bremsstrahlung in Beam-Dump Data". In: *Phys. Lett.* B731 (2014), pp. 320–326. DOI: `10.1016/j.physletb.2014.02.029`. arXiv: `1311.3870 [hep-ph]`.

[51] Andrea Celentano et al. "New production channels for light dark matter in hadronic showers". In: *Phys. Rev. D* 102.7 (2020), p. 075026. DOI: `10.1103/PhysRevD.102.075026`. arXiv: `2006.09419 [hep-ph]`.

[52] Luca Buonocore et al. "Event generation for beam dump experiments". In: *Journal of High Energy Physics* 2019.5 (May 2019), p. 28. ISSN: 1029-8479. DOI: `10.1007/JHEP05(2019)028`. URL: `https://doi.org/10.1007/JHEP05(2019)028`.

[53] Yonatan Kahn et al. "DAEδALUS and dark matter detection". In: *Phys. Rev.* D91.5 (2015), p. 055006. DOI: `10.1103/PhysRevD.91.055006`. arXiv: `1411.1055 [hep-ph]`.

[54] S. Gardner, R. J. Holt, and A. S. Tadepalli. "New Prospects in Fixed Target Searches for Dark Forces with the SeaQuest Experiment at Fermilab". In: *Phys. Rev.* D93.11 (2016), p. 115015. DOI: 10.1103/PhysRevD.93.115015. arXiv: 1509.00050 [hep-ph].

[55] M. Bonesini et al. "On Particle production for high-energy neutrino beams". In: *Eur. Phys. J.* C20 (2001), pp. 13–27. DOI: 10.1007/s100520100656. arXiv: hep-ph/0101163 [hep-ph].

[56] Babette Döbrich, Joerg Jaeckel, and Tommaso Spadaro. "Light in the beam dump - ALP production from decay photons in proton beam-dumps". In: *Submitted to: J. High Energy Phys.* (2019). arXiv: 1904.02091 [hep-ph].

[57] Hans Dijkstra and Thomas Ruf. "Heavy Flavour Cascade Production in a Beam Dump". In: (Dec. 2015). URL: https://cds.cern.ch/record/2115534.

[58] C. Ahdida et al. "Measurement of the muon flux for the SHiP experiment". In: (Jan. 2020). arXiv: 2001.04784 [physics.ins-det].

[59] Luca Buonocore, Patrick deNiverville, and Claudia Frugiuele. "The hunt for sub-GeV dark matter at neutrino facilities: a survey of past and present experiments". In: (Dec. 2019). arXiv: 1912.09346 [hep-ph].

[60] E. Fermi. "On the Theory of the impact between atoms and electrically charged particles". In: *Z. Phys.* 29 (1924), pp. 315–327. DOI: 10.1007/BF03184853.

[61] E. J. Williams. "Nature of the high-energy particles of penetrating radiation and status of ionization and radiation formulae". In: *Phys. Rev.* 45 (1934), pp. 729–730. DOI: 10.1103/PhysRev.45.729.

[62] C. F. von Weizsäcker. "Radiation emitted in collisions of very fast electrons". In: *Z. Phys.* 88 (1934), pp. 612–625. DOI: 10.1007/BF01333110.

[63] Patrick deNiverville et al. "Light dark matter in neutrino beams: Production modeling and scattering signatures at MiniBooNE, T2K, and SHiP". In: *Phys. Rev. D* 95 (3 2017), p. 035006. DOI: 10.1103/PhysRevD.95.035006. URL: https://link.aps.org/doi/10.1103/PhysRevD.95.035006.

[64] Amand Faessler, M. I. Krivoruchenko, and B. V. Martemyanov. "Once more on electromagnetic form factors of nucleons in extended vector meson dominance model". In: *Phys. Rev.* C82 (2010), p. 038201. DOI: 10.1103/PhysRevC.82.038201. arXiv: 0910.5589 [hep-ph].

[65] David E. Morrissey and Andrew Paul Spray. "New Limits on Light Hidden Sectors from Fixed-Target Experiments". In: *Journal of High Energy Physics* 06 (2014), p. 083. DOI: 10.1007/JHEP06(2014)083. arXiv: 1402.4817 [hep-ph].

[66] D. Gorbunov, A. Makarov, and I. Timiryasov. "Decaying light particles in the SHiP experiment: Signal rate estimates for hidden photons". In: *Phys. Rev.* D91.3 (2015), p. 035027. DOI: 10.1103/PhysRevD.91.035027. arXiv: 1411.4007 [hep-ph].

[67] Asher Berlin et al. "Dark Sectors at the Fermilab SeaQuest Experiment". In: *Phys. Rev.* D98.3 (2018), p. 035011. DOI: 10.1103/PhysRevD.98.035011. arXiv: 1804.00661 [hep-ph].

[68] Johan Alwall et al. "MadGraph 5 : Going Beyond". In: *Journal of High Energy Physics* 06 (2011), p. 128. DOI: 10.1007/JHEP06(2011)128. arXiv: 1106.0522 [hep-ph].

[69] Richard D. Ball et al. "Parton distributions with LHC data". In: *Nucl. Phys.* B867 (2013), pp. 244–289. DOI: 10.1016/j.nuclphysb.2012.10.003. arXiv: 1207.1303 [hep-ph].

[70] Richard D. Ball et al. "Parton distributions with QED corrections". In: *Nucl. Phys.* B877 (2013), pp. 290–320. DOI: 10.1016/j.nuclphysb.2013.10.010. arXiv: 1308.0598 [hep-ph].

[71] Sergey Alekhin et al. "A facility to Search for Hidden Particles at the CERN SPS: the SHiP physics case". In: *Rept. Prog. Phys.* 79.12 (2016), p. 124201. DOI: 10.1088/0034-4885/79/12/124201. arXiv: 1504.04855 [hep-ph].

[72] M. Tanabashi et al. "Review of Particle Physics". In: *Phys. Rev. D* 98.3 (2018), p. 030001. DOI: 10.1103/PhysRevD.98.030001.

[73] A. Alexandrov et al. "Improving the detection efficiency in nuclear emulsion trackers". In: *Nucl. Instrum. Meth. A* 776 (2015), pp. 45–49. DOI: 10.1016/j.nima.2014.12.063.

[74] N. Agafonova et al. ""New results on $\nu_\mu \to \nu_\tau$ appearance with the OPERA experiment in the CNGS beam"". In: *Journal of High Energy Physics* 2013.11 (2013), p. 36. ISSN: 1029-8479. DOI: 10.1007/JHEP11(2013)036. URL: https://doi.org/10.1007/JHEP11(2013)036.

[75] Q. Wu et al. "A Precise measurement of the muon neutrino-nucleon inclusive charged current cross-section off an isoscalar target in the energy range $2.5 < E(\nu) < 40$ GeV by NOMAD". In: *Phys. Lett. B* 660 (2008), pp. 19–25. DOI: 10.1016/j.physletb.2007.12.027. arXiv: 0711.1183 [hep-ex].

[76] A. A. Aguilar-Arevalo et al. "Measurement of neutrino-induced charged-current charged pion production cross sections on mineral oil at $E_\nu \sim 1$ GeV". In: *Phys. Rev. D* 83 (5 Mar. 2011), p. 052007. DOI: 10.1103/PhysRevD.83.052007. URL: https://link.aps.org/doi/10.1103/PhysRevD.83.052007.

[77] V Lyubushkin et al. "A Study of quasi-elastic muon neutrino and antineutrino scattering in the NOMAD experiment". In: *Eur. Phys. J. C* 63 (2009), pp. 355–381. DOI: 10.1140/epjc/s10052-009-1113-0. arXiv: 0812.4543 [hep-ex].

[78] J. A. Formaggio and G. P. Zeller. "From eV to EeV: Neutrino cross sections across energy scales". In: *Rev. Mod. Phys.* 84 (3 Sept. 2012), pp. 1307–1341. DOI: 10.1103/RevModPhys.84.1307. URL: https://link.aps.org/doi/10.1103/RevModPhys.84.1307.

[79] Michael Duerr et al. "Invisible and displaced dark matter signatures at Belle II". In: *JHEP* 02 (2020), p. 039. DOI: 10.1007/JHEP02(2020)039. arXiv: 1911.03176 [hep-ph].

[80] R. Alemany et al. "Summary Report of Physics Beyond Colliders at CERN". In: (Feb. 2019). Ed. by J. Jaeckel, M. Lamont, and C. Vallée. arXiv: 1902.00260 [hep-ex].

Chapter 7

Conclusions

The requirement to address the limitations of the Standard Model (SM) with the absence of New Physics (NP) evidence at the TeV energy scale motivates the pursuit of diversified, novel research approaches within the scientific community. Following the same intention, this PhD work has been devoted to the exploration of complementary searches for physics beyond the SM.

Firstly, we have presented comprehensive efforts completed in high-precision and flavour physics with the LHCb experiment by studying semileptonic baryon tree-level transitions at the phenomenological and experimental levels. To begin with, we carried out sensitivity studies to assess the achievable experimental precision on Wilson Coefficients (WC) of NP operators with the analysis of the angular decay distribution of $\Lambda_b^0 \to \Lambda_c^+ \mu^- \bar{\nu}_\mu$ decays, in two different scenarios addressing distinct two and three-body final states of the Λ_c^+. We concluded that competitive constraints with the world's best determinations could be reached on the WC parameters. Therefore, we have proceeded with the experimental measurement of the normalised angular distribution of signal $\Lambda_b^0 \to (\Lambda_c^+ \to pK^-\pi^+)\mu^- \bar{\nu}_\mu$ transitions, with Run 2 data of the LHCb experiment, to look out for possible signs of NP. The analysis has yielded the most precise experimental determination of the hadronic Form Factors of signal Λ_b^0 transitions. At the same time, we have delivered on the experimental sensitivity to the WC. The value of the WC parameters, and therefore the assessment of NP content in Λ_b^0 semimuonic decays, will be unveiled following internal peer review. The result will be an impactful input to interpret current deviations from Lepton Flavour Universality in $b \to c\ell^- \bar{\nu}_\ell$ tree-level decays.

In addition to this work, we have contributed substantially to the offline data-processing framework of the LHCb experiment after the implemented detector and trigger updates. The effort has resulted in the realisation of a novel infrastructure, named `FunTuple`, to facilitate and optimise the storage process of LHCb data from Run 3 to future data-taking campaigns.

In the quest for alternative searches for NP, we focused on the TeV-energy neutrinos produced in the forward rapidity from pp collisions at CERN, offering the potential for measurements in a so far unexplored phase space. We have discussed the analysis performed using data collected with the SND@LHC experiment during Run 3 of the Large Hadron Collider. We have observed eight muon neutrino candidates, resulting in a statistical significance of seven standard deviations over the background-only hypothesis. This measurement demonstrates the feasibility of a high-energy

neutrino physics program at CERN, paving the way for various NP investigations and stress tests of the SM.

Finally, we have explored the potential offered by a high intensity, beam dump experiment proposal like SHiP to probe signatures of Feebly Interacting Particles, possibly solving the mystery of the origin of Dark Matter (DM). We have studied the scenario involving the scattering of light DM particles off electrons of a heavy target, assuming a simple extension of the SM and production mechanism from a vector force carrier. We have established that the SHiP experiment will cover an unexplored region of parameters, extending the current limits by at least one order of magnitude. This assessment played a critical role in the approval process of the SHiP proposal, resulting into a positive decision during the last days of completion of this manuscript.

In this quest to understand the mechanisms governing our Universe, one thing is sure: an abundance of opportunities is awaiting exploration. We must endure the investigation, remaining confident that the effort will lead us to the next revolutionary discovery in particle physics.

List of Figures

List of Tables